DISSERTATION
submitted to the
Combined Faculties for the Natural Sciences and for Mathematics
of the Ruperto-Carola University of Heidelberg, Germany
for the degree of
Doctor of Natural Sciences

presented by
Dipl. Phys. KERSTIN ELLEN KRALL
born in Schlema

day of oral exam: January 23, 2013

Laboratory Investigations of Air-Sea Gas Transfer under a Wide Range of Water Surface Conditions

Referees:
Prof. Dr. BERND JÄHNE
Prof. Dr. WERNER AESCHBACH-HERTIG

Abstract: Transfer velocities of 5 sparingly soluble gases were measured in two different wind wave tanks at wind speeds between u_{10}=1.2 m/s and 67 m/s. Two different gas analysis techniques were used, FT-IR and UV spectroscopy. Additionally, a method was developed that allows the parallel measurement of gas transfer velocity and the solubility. The fast 'controlled leakage' method for the measurement of gas transfer velocities was found to be not precise enough to measure Schmidt number exponents and transfer velocities in the Aeolotron.

Gas transfer velocities measured spanned more than 3 orders of magnitude, lying between 0.5 cm/h and 1100 cm/h. At lower wind speeds, measured in the Heidelberg Aeolotron, the change of the Schmidt number exponent from 2/3 for a smooth to 1/2 for a wavy water surface was confirmed. A surfactant, which inhibits wave growth, was used in 3 of the 7 experiments. For all surfactant conditions, the change of the Schmidt number exponent spanned a wide range of wind speeds with the mid-point at u_{10} =4.5 m/s for a clean, and at 9 m/s for a surface film covered water surface. It was confirmed that the mean square slope is suitable for the description of the transition of the Schmidt number exponent. The facet model could not reproduce the measured transfer velocities. The transfer velocities measured were found to scale very poorly with the commonly used parameter wind speed u_{10}. The correlation between the mean square slope of the water surface and the transfer velocities was found to be good, except at the lowest mean square slopes.

In the Kyoto high speed wind-wave tank, the effect of strong wave breaking and bubble entrainment on the gas transfer velocity was studied. Gas transfer velocities were split up into a purely wave induced part and a part caused by bubbles and wave breaking. The measured gas transfer velocities were found to be up to 350 % larger than expected from waves alone at the highest wind speed. Three empirical parameterizations were tested on the bubble induced part, two successfully.

Zusammenfassung: In zwei verschiedenen Wind-Wellen-Kanälen wurden Gastransfergeschwindigkeiten von 5 wenig löslichen Gasen bei Windgeschwindigkeiten zwischen u_{10}=1.2 m/s und 67 m/s gemessen. Zwei verschiedene Gasanalyse-Methoden, die FT-IR- und die UV-Spektroskopie wurden benutzt. Desweiteren wurde eine Methode zur parallelen Messung der Gastransfergeschwindigkeit und der Löslichkeit entwickelt. Die schnelle 'Controlled Leakage' Methode wurde als nich präzise genug zur Messung des Schmidtzahlexponenten und von Gastransfergeschwindigkeiten im Aeolotron nachgewiesen.

Die gemessenen Gastransfergeschwindigkeiten liegen zwischen 0.5 cm/h und 1100 cm/h und überspannen damit einen Bereich von mehr als 3 Größenordnungen. Bei niedrigen Windgeschwindigkeiten, die im Heidelberger Aeolotron gemessen wurden, konnte der Umschlag des Schmidtzahlexponenten von 2/3 bei einer glatten auf 1/2 bei einer rauhen Wasseroberfläche nachgewiesen werden. Ein Oberflächenfilm, der die Entstehung von Wellen behindert, wurde in 3 der 7 Experimente eingesetzt. Der Umschlag des Schmidtzahlexponenten erstreckt sich über einen weiten Bereich von Windgeschwindigkeiten bei allen Oberflächenbedingungen, wobei der Mittelpunkt bei u_{10} =4.5 m/s bei sauberer und bei 9 m/s bei filmbedeckter Wasseroberfläche liegt. Es wurde nachgewiesen, dass die mittlere quadratische Neigung zur Beschreibung des Umschlags des Schmidtzahlexponenten geeignet ist. Das Facettenmodell konnte die gemessenen Gastransfergeschwindigkeiten nicht reproduzieren. Die Transfergeschwindigkeiten skalieren schlecht mit dem üblicherweise benutzten Parameter Windgeschwindigkeit u_{10}. Die Korrelation zwischen der mittleren quadratischen Neigung der Wasseroberfläche und den Transfergeschwindigkeiten ist sehr gut, ausgenommen bei den niedigsten mittleren quadratischen Neigungen.

Im Hochgeschwindigkeits-Wind-Wellen-Kanal in Kyoto wurde der Einfluss von brechenden Wellen und Blaseneinschlag auf die Transfergeschwindigkeit untersucht. Die gemessenen Transfergeschwindigkeiten wurden in einen wellenbedingten und einen blasen- und wellenbrechenbedingten Anteil aufgespaltet. Die gemessenen Gastransfergschwindigkeiten liegen bis zu 350 % über denen die bei welliger Oberfläche bei der höchsten Windgeschwindigkeit erwartet werden. Drei empirische Parameterisierungen wurden am blaseninduzierten Anteil getestet, zwei davon erfolgreich.

Contents

1. Introduction **1**
- 1.1. Objectives of this Study . . . 3
- 1.2. Structure of this Thesis . . . 3

2. Theory **5**
- 2.1. Transport Mechanisms . . . 5
  - 2.1.1. Diffusion . . . 5
  - 2.1.2. Turbulence . . . 8
- 2.2. Air-Sea Gas Transfer . . . 9
  - 2.2.1. The Boundary Layer . . . 9
  - 2.2.2. The Logarithmic Wind Profile . . . 11
  - 2.2.3. Concentration and Velocity Profiles . . . 11
  - 2.2.4. The Schmidt Number . . . 12
  - 2.2.5. Transfer Resistances . . . 12
  - 2.2.6. Gas Transfer Models . . . 14
  - 2.2.7. Surfactants . . . 21
  - 2.2.8. Gas Transfer at Extreme Wind Speeds . . . 22
- 2.3. Absorption Spectroscopy . . . 23
  - 2.3.1. FT-IR Spectroscopy . . . 24
  - 2.3.2. UV Absorption Spectroscopy . . . 27

3. Method **29**
- 3.1. The Box Model . . . 29
- 3.2. Measuring the Leak Rate . . . 30
  - 3.2.1. Small Leaks: Closed System . . . 31
  - 3.2.2. Large Leaks: Open System . . . 31
- 3.3. Measuring Gas Transfer Velocities . . . 32
  - 3.3.1. The $\dot{\mathbf{c}}_\mathbf{a}$ Method . . . 32
  - 3.3.2. The Classic Evasion Method . . . 36
- 3.4. Measuring the Solubility . . . 37

4. Experiments **39**
- 4.1. The Wind-Wave Tanks . . . 39
  - 4.1.1. The Heidelberg Aeolotron . . . 39
  - 4.1.2. The Kyoto High Speed Wind-Wave Tank . . . 40
  - 4.1.3. Comparison of the Wind-Wave Tanks . . . 41
- 4.2. Chemicals . . . 42
  - 4.2.1. Tracers Used in the Aeolotron . . . 42
  - 4.2.2. Surfactant used in the Aeolotron . . . 43
  - 4.2.3. Tracers used in the Kyoto High Speed Tank . . . 43
- 4.3. Experimental Conditions . . . 44
  - 4.3.1. Aeolotron . . . 45

4.3.2. Kyoto High Speed Wind-Wave Tank 47
4.4. Experimental Setup 49
4.4.1. Setup at the Aeolotron 49
4.4.2. Setup at the Kyoto High Speed Wind-Wave Tank 51
4.5. Oxygenator Performance 54
4.5.1. Estimating the Time Constant of the Equilibration 55

5. Data Processing **59**
5.1. Preprocessing 59
5.1.1. Preprocessing the UV Spectroscopic Data 59
5.1.2. Preprocessing the FT-IR Spectroscopic Data 61
5.2. Calculating Absorbances 62
5.2.1. UV Spectroscopy 63
5.2.2. FT-IR Spectroscopy 64
5.3. Calculating Transfer Velocities and Schmidt Number Exponents 69
5.3.1. FT-IR Spectroscopy in the Heidelberg Aeolotron 69
5.3.2. Transfer Velocities 69
5.3.3. Schmidt Number Exponents 70
5.3.4. Transfer Velocities in the Kyoto High-Speed Wind Wave Tank 71

6. Calibration of the FT-IR Spectrometers **79**
6.1. General Principle 79
6.2. Determining the Concentration 80
6.3. Calibration Factors 80
6.3.1. CHF_3 80
6.3.2. N_2O 81
6.3.3. C_2HF_5 82
6.3.4. CF_4 82
6.3.5. Overview of Calibration Factors 83
6.4. Uncertainties 83
6.4.1. Uncertainty of the Input Concentration 83
6.4.2. Choice of Reference Spectrum 84
6.4.3. Statistical Errors 85
6.4.4. Uncertainty of the Calibration Factors 86
6.4.5. Summary of the Errors 86

7. Results **89**
7.1. Homogeneity of the Air Side Concentration in the Aeolotron 89
7.2. Leak Rates in the Aeolotron 92
7.3. Solubility 94
7.3.1. Uncertainties of the Measured Solubilities 96
7.4. Gas Exchange at Low to Medium Wind Speeds 96
7.4.1. Wind Speed, Friction Velocity and Mean Square Slope 96
7.4.2. Transfer Velocities 98
7.4.3. Schmidt Number Exponents 100
7.4.4. Carbon Dioxide Equivalent Transfer Velocities 102
7.4.5. Validation of the Facet Model 105
7.4.6. Comparison with Previously Measured Values 110
7.4.7. Uncertainties of Gas Exchange at Low to Medium Wind Speeds 115

7.5. Gas Exchange Velocities at High Wind Speeds 118
7.5.1. Measured Transfer Velocities 119
7.5.2. Comparison between Heidelberg and Kyoto Gas Transfer Velocities . . . 122
7.5.3. Enhancement of Gas Transfer at Highest Wind Speeds 123
7.5.4. A Model for Gas Transfer at High Wind Speeds 130
7.5.5. Uncertainties 132

8. Conclusion and Outlook **135**

A. Appendix **137**
A.1. A Numerical Model for Calculating Concentration Time Series 137
A.2. Water Side FT-IR Reference Spectra 137
A.3. More on Calibration of the FT-IR Spectrometers 137
A.3.1. Calibration Curves with Error Bars 137
A.3.2. Alternative Calibrations 139
A.3.3. Statistical Errors 140
A.4. Numerical Results 141
A.4.1. Aeolotron 141
A.4.2. Kyoto High-Speed Wind Wave Tank 144

Bibliography **147**

1. Introduction

Gas Exchange between the Ocean and the Atmosphere

Interactions between the oceans and the atmosphere have increasingly come into focus of climate scientists in recent years. Gases, momentum and heat are exchanged between air and sea. The ocean was identified as the largest sink of atmospheric carbon dioxide. In 2008, the net carbon uptake of the ocean was 2.3 ± 0.6 Pg, see Khatiwala et al. [2009]. There are major uncertainties in the estimations of the greenhouse gas uptake of the ocean, warranting research into the mechanisms governing the exchange of trace gases across the air sea boundary. The gas transfer velocity, along with the net gas flux, is commonly used to describe the gas transfer process. It is influenced by a multitude of environmental factors, see figure 1.1. Notable are the waves, created by the wind. In the presence of waves, the gas transfer is enhanced by a factor of three, compared to a flat water surface, see Jähne [2009]. The enlargement of the water surface due to the waves alone can not explain this enhancement. Gas transfer is limited by a merely 30 to 200 μm thick diffusive sublayer at the water surface, see Münsterer [1996]. Therefore, increasing the turbulence in the boundary layer by waves, increases the gas transfer velocity. Surface films, in turn, dampen waves and limit wave growth, in turn diminish gas transfer. Wurl et al. [2011] shows, that biogenic surface films are abundant, especially in the tropical oceans, making them an important parameter influencing the gas transfer velocity. Bubbles, created by breaking waves influence the gas transfer in two different ways. On the one hand, they increase the water surface available for gas exchange. On the other hand they generate additional turbulence when they rise through the water column and burst through the water surface. Bubble effects are usually studied in tipping bucket tanks, see Asher et al. [1996], with water jets, see Mischler [2010] or with aeration devices, see De Leeuw and Leifer [2002]. Studies of bubbles generated by breaking waves on the open ocean are sparse, and mostly limited to bubble size spectra, without measurement of gas transfer velocities.

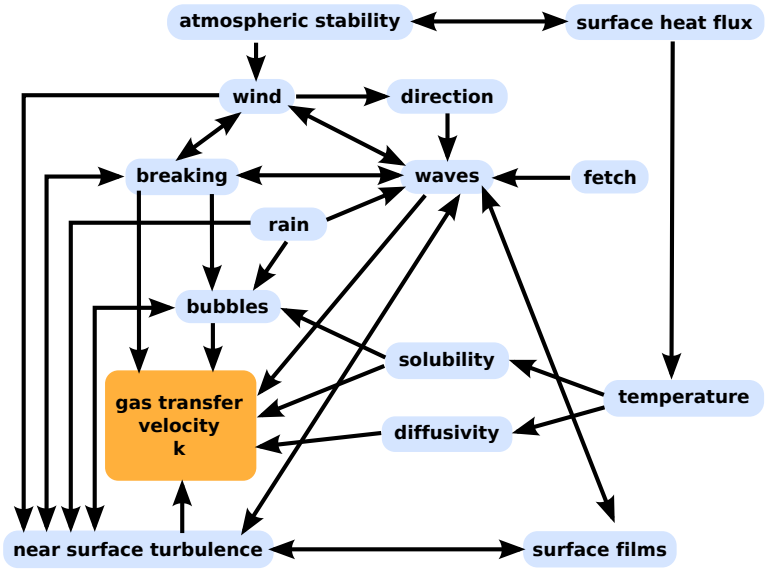

Figure 1.1.: Framework of factors influencing the transfer velocity of sparingly soluble gases across the air-sea interface. Modified after McGillis [2012].

Knowledge about forcing factors other than wind speed is incomplete. The only exception are some empirical gas transfer models which include bubbles, see for instance Dani et al. [2007] for single bubbles or Woolf et al. [2007] for bubble plumes. The complexity of the multitude of interactions at the water surface is oftentimes simplified to only include the wind speed and the tracer's diffusivity, see for instance Liss and Merlivat [1986], Nightingale et al. [2000] and Wanninkhof et al. [2009] as well as figure 1.2. These simple, empirical wind speed – gas transfer relationships work well for getting rough estimates of the gas transfer velocity, but they fail to catch the intricate interactions between the physical processes at play. Detailed studies of the physical mechanisms will give insight into gas exchange processes and improve the modeling of the gas transfer velocities and fluxes.

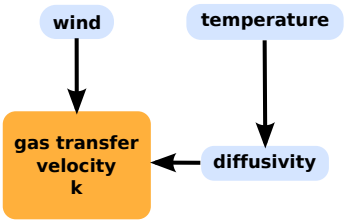

Figure 1.2.: Simplified framework of factors influencing the gas transfer velocities used in most empirical parameterizations.

Extreme Wind Speeds

The total number of tropical cyclones is in the order of 50 per year, see Webster et al. [2005]. Depending on location and strength, a tropical cyclone is referred to by names such as hurricane, typhoon or cyclonic storm. They are all characterized by heavy rain, a low pressure center, a center warmer than its surroundings, and wind speeds exceeding 33 m/s. Hurricanes, as tropical cyclones will be referred to in this thesis, can only develop over water warmer than 26.5 ^{o}C.

Due to the severe environmental conditions within such a storm system, including strong winds, rain, hail and large waves, measurements of gas transfer velocities directly on the ocean are extremely difficult. Therefore, the effect of tropical cyclones on air-sea gas transfer is not well understood. The authors of one study, McNeil and D'Asaro [2007], managed to model one and measure two gas transfer velocities at hurricane strength wind speed using unmanned buoys. After the passage of three hurricanes, one of category 3 and two of category 4 in the year 1995 over the Sargasso sea, Bates et al. [1998] found an increase in summertime sea to air flux of CO_2 of 55 % compared to non hurricane years. This shows the significance of the influences of hurricanes on the global fluxes of gases across the water surface.

With global warming, predictions of future hurricane activity is difficult. On one hand, the sea surface temperature is expected to increase, see Xie et al. [2010]. As evaporation of sea water is the fuel of tropical storm systems, this should increase hurricane number and intensity when larger areas warm enough for hurricane formation are available. However, at the same time wind shear also increases in the regions where hurricanes form, see Vecchi and Soden [2007]. High wind shear disrupts growing storm systems' circulations and hinders hurricane development. A model study of the net effect of both factors in the north-east Atlantic has been done by Bender et al. [2010] and comes to the conclusion, that the overall amount of hurricanes will decrease by 20 to 30 % in a warming climate, while the amount of hurricanes in the highest categories 4 and 5 will increase by 80 to 100 %. Hurricanes will play an important role in warmed climate, too, and their effect on gas transfer needs to be studied more thoroughly.

1.1. Objectives of this Study

Due to the mentioned difficulties in measuring gas transfer at the open ocean, lab experiments are preferred. Wind-wave tanks are ideal places to study the physical parameters influencing gas transfer. Wind-wave tanks allow to set and tune the environmental parameters, so that the process in question can be studied in great detail. One process in the focus of this work was the change in boundary conditions from a flat to a wavy water surface with and without surface films and its influence on the gas transfer velocity. The second focus lay on the almost unstudied regime of hurricane strength wind speed including bubble mediated gas transfer.

Experiments at two wind-wave tanks were performed, with one of them, the Kyoto high speed wind-wave tank being capable of producing hurricane wind speeds. The other, the Heidelberg Aeolotron, was favorable for the surface film experiments as well as the study of the changing boundary conditions. Due to the Aeolotron's annular shape, the surface film stays on the water surface throughout the duration of the experiments. The facet model, a physics based model that describes the change in the boundary conditions from a flat to a wavy water surface was to be tested, for the first time including the effects of surface films. For the high wind speed regime, empirical parameterizations describing effects of bubble entrainment on the gas transfer velocity were to be tested.

Two different spectroscopic gas analysis techniques, UV and Fourier Transform Infrared Spectroscopy (FT-IR) were to be applied and adapted to the respective requirements to measure the concentrations of trace gases. Gas transfer rates were to be measured using a mass balance, which integrates over the whole water surface without spatial resolution. The applicability of one very fast mass balance method, the controlled leakage method developed by Degreif [2006] in a small wind-wave tank, was to be tested in the much larger Aeolotron.

Knowledge of physico-chemical parameters of trace gases, such as the temperature dependency of their solubility and diffusion coefficient in water, is often insufficient. A method was to be developed that allows the measurement of the solubility of a tracer.

The improved understanding of air-sea gas transfer with boundary conditions varying between a flat and a wavy water surface, and the first systematic study of gas transfer velocities in the hurricane wind speed regime gained from this work will be another step on the path to a comprehensive physics based gas transfer model.

1.2. Structure of this Thesis

In chapter 2, the theoretical basis for gas exchange including the physical mechanisms of diffusion and turbulence as well as models for gas exchange will be given. The theoretical foundations of the absorption spectroscopy in the UV and IR wavelength range is also discussed in chapter 2. The box model and the derivation of the methods used to measure parameters needed for the understanding of experiments such as the tracers' solubilities and the leak rate will be part of chapter 3. There, three methods to measure the gas transfer velocities will be discussed, too. A description of the wind-wave tanks as well as the experiments performed will follow in chapter 4. The spectra measured during the experiments need to be evaluated with respect to tracer concentration. The basics of the data processing will be explained in chapter 5. For the measurements with the IR setup, a calibration, detailed in chapter 6 is needed, that yields the tracer concentrations. The results are discussed in chapter 7.

Most of the chapters are split up into two parts. One part comprises a low to medium wind speed regime including the change in boundary conditions, surface films and concentration measurements using Fourier Transform Infrared Spectroscopy in the Heidelberg Aeolotron. The sec-

ond part consists of the gas exchange measurements at high wind speeds using UV spectroscopy in the Kyoto high speed wind-wave tank.

2. Theory

First, a general mathematical description of the transport mechanisms diffusion and turbulence will be given. These will then be applied to the special question of transport of momentum and concentration across the air-water interface. A discussion of the models, which are used to describe air-water gas transfer will follow. Finally, the physical basis for ultraviolet spectroscopy and Fourier Transform Infrared Spectroscopy, the methods of gas analysis in this work, will be given.

2.1. Transport Mechanisms

Transfer of mass across the air-sea interface is caused by a difference in concentration. Involved transport processes are diffusion and turbulent convection, with turbulence being the more effective one far from the interface. As turbulence can not penetrate the interface, turbulent structures must be reduced in size and effectiveness close to the interface. Here, diffusion is the limiting factor for transport. Both transport phenomena will be looked at in this section.

2.1.1. Diffusion

Fick's first law postulates that the diffusive flux density $\vec{j}$ of an admixture of a substance goes from regions with high concentration c to regions with low concentration,

$$\vec{j} = -D\nabla c, \tag{2.1}$$

or, in one dimension,

$$j = -D\frac{\partial c}{\partial x}. \tag{2.2}$$

D denotes the diffusivity, a tracer specific property. This means, that the flux of particles is in opposite direction to the concentration gradient meaning, that diffusion tends to balance concentration differences.

In macroscopic terms, it is evident that the flux density j must be proportional to the concentration difference, or

$$j = k\Delta c, \tag{2.3}$$

with the proportionality constant k which has the unit of a velocity and is therefore called the transfer velocity.

In an air mixture, the diffusivity D_a is dependent on temperature T and pressure p,

$$D_a \approx \frac{T^{3/2}}{p}, \tag{2.4}$$

see Cussler [2009]. The inverse proportionality between the diffusion and the pressure can be seen easily when the free path length for molecular motion is considered, which gets the longer the smaller the pressure is. According to kinetic gas laws, the kinetic energy E_{kin} and thus the mean velocity of particles $\overline{v}$ is proportional to the temperature, i.e. $E_{\mathrm{kin}} \propto \overline{v}^2 \propto T$. And the larger the

velocity of a particle, the more efficient diffusion is. Diffusion D_w of spherical particles in water is described by the Stokes-Einstein equation, see Einstein [1905],

$$D_w = \frac{k_B T}{6\pi\,\eta\,r}, \tag{2.5}$$

with the Boltzmann constant k_B, the dynamic viscosity of water η and the radius of the spherical particle r. As water is incompressible, the pressure does not have an effect on the diffusion in water. Because most molecules are not spheres, equation 2.5 is only an approximation. More reliable in yielding correct diffusion coefficients are empirical parameterizations, which must be obtained experimentally for each chemical compound.

Fick's first law can also be applied to heat and momentum,

$$\vec{j}_h = -\frac{\kappa}{\rho c}\nabla(\rho c T) \tag{2.6}$$

$$\vec{j}_m = -\nu\nabla(\rho v) \tag{2.7}$$

with the following naming conventions:

$\vec{j}$	$[\frac{kg}{m^2\,s}]$	mass flux density
D	$[\frac{m^2}{s}]$	diffusion coefficient
c	$[\frac{kg}{m^3}]$	concentration
$\vec{j}_h$	$[\frac{J}{m^2\,s}]$	heat flux
κ	$[\frac{W}{m\,K}$=$\frac{kg\,m}{s^3\,K}]$	thermal conductivity
T	$[K]$	temperature
ρ	$[\frac{kg}{m^3}]$	density
$\vec{j}_m$	$[\frac{kg\,m}{s}\frac{1}{m^2\,s}]$	momentum flux
ν	$[\frac{m^2}{s}]$	kinematic viscosity
v	$[\frac{m}{s}]$	velocity

The continuity equation describes the transport of mass when no sources or sinks for mass exist,

$$\frac{dc}{dt} + \nabla\vec{j} = 0. \tag{2.8}$$

Combining the continuity equation with Fick's first law, equation 2.1, yields Fick's second law,

$$\frac{dc}{dt} = -\nabla\vec{j} = \nabla(D\nabla c). \tag{2.9}$$

Assuming a spatially and temporally constant diffusion constant D, this equation can be written as

$$\frac{dc}{dt} = D\nabla^2 c. \tag{2.10}$$

In one dimension, equation 2.10 simplifies to

$$\frac{dc}{dt} = D\frac{d^2 c}{dx^2} \tag{2.11}$$

which can be solved easier. As an example, a delta peak of a substance is assumed to be at position $x = 0$ at time $t = 0$. Then, the solution of the one dimensional diffusion equation 2.11 is a Gaussian function,

$$c(x,t) = \frac{C_0}{\sqrt{4\,\pi\,D\,t}}\,\exp\left(-\frac{x^2}{4\,D\,t}\right) \tag{2.12}$$

with an integration constant C_0. Figure 2.1a shows equation 2.12 for seven different times for a substance with a diffusion coefficient of D=1. Figure 2.1b shows the same, but for a tracer with a diffusion coefficient of D=5. With time, the distribution of concentration broadens in space and the maximum of concentration gets lower. A higher diffusion constant broadens the distribution faster. But the spreading of the concentration is not uniform in time, it gets slower as time progresses. Note that the time scale in figure 2.1 is exponential. The time doubles with every subsequent curve.

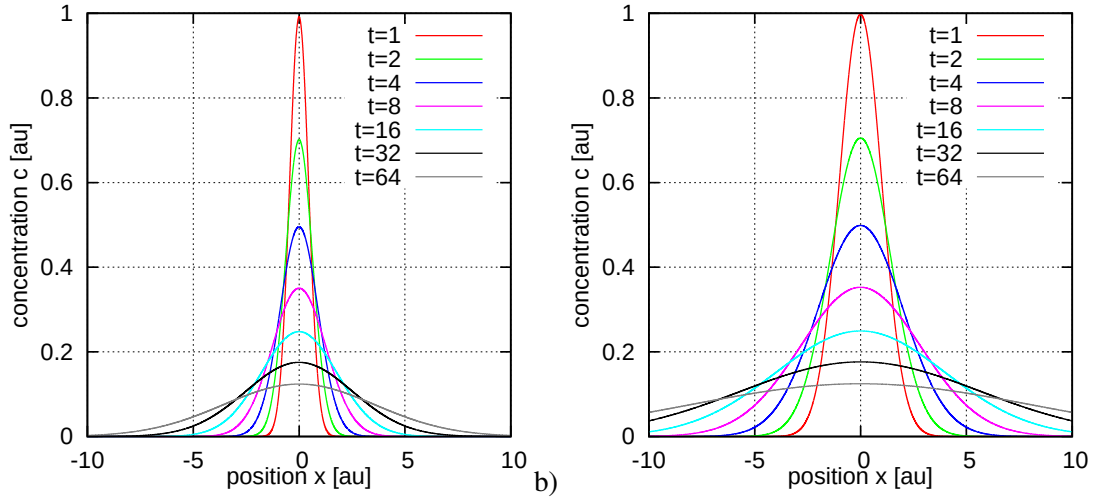

Figure 2.1.: Temporal development of a delta peak distribution of a substance with a diffusion coefficient of a) D=1 and b) D=5. To make both graphs better comparable, an integration constant C_0 was chosen such, that the curve at a time 1 has concentration 1 at the maximum. (All units arbitrary.)

To substantiate the findings gained from qualitatively analyzing figure 2.1, the standard deviation σ for the spatio-temporal change in concentration, equation 2.12, is found to be

$$\sigma = \sqrt{4\,D\,t}. \tag{2.13}$$

The standard deviation can be seen as measure for the spatial spread of the concentration and is indeed proportional to the time t and the diffusion coefficient D. The spread of the concentration is with $\sigma \propto \sqrt{t}$ slower than linear with time. This confirms that diffusion is a slow process at large distances.

The total differential on the left hand side in Fick's second law, equation 2.10, can be split up into a partial and a material derivative,

$$\frac{dc}{dt} = \frac{\partial c}{\partial t} + \vec{u}\nabla c, \tag{2.14}$$

modifying Fick's second law to the transport equation,

$$\frac{\partial c}{\partial t} = D\nabla^2 c - \vec{u}\nabla c, \tag{2.15}$$

or, expressed in words, the temporal change in concentration is due to the diffusion, as well as the transport of the concentration within the velocity field $\vec{u}$. However, the full knowledge of the velocity field at all times is necessary, which is experimentally hardly possible. In the form of turbulence, another approach can also be used to describe the transport, which eliminates the need for a fully known velocity field.

2.1.2. Turbulence

Movement within liquids and gases, when chaotic velocity changes are observed on almost all spatial scales, is called turbulent. The flow field itself is not of interest here. The main focus lies in the large scale transport effect turbulence imposes on admixtures. Generally, the concentration can be decomposed into an average $\overline{c}$ and a fluctuating component, c', in what is called Reynold's approach,

$$c = \overline{c} + c'. \tag{2.16}$$

By definition, the temporal mean of the fluctuating term vanishes,

$$\overline{c'} = \lim_{T\to\infty} \frac{1}{T} \int_0^T c' dt = 0. \tag{2.17}$$

In reality, integration and thus measurements to $T = \infty$ are hardly possible. Therefore, a limited integration time $\tau < \infty$ is introduced,

$$\overline{c'} = \frac{1}{\tau} \int_0^\tau c' dt. \tag{2.18}$$

This, however, has some unintended consequences. While a large scale convection eddy might be attributed to the mean $\overline{c}$ when the averaging time τ is relatively short, it will be seen as a fluctuation c' when the time scale τ is longer. Or more generally, a process may appear as fluctuation on long time scales, or as directional transport on shorter time scales. To counter this, the integration time scale τ must be longer than the characteristic time scale of the system. A useful concept in determining τ is autocorrelation. The normalized autocorrelation is defined as the correlation of a value at time t with the same value at time $t + \tilde{t}$,

$$r(\tilde{t}) = \frac{\overline{c(t)c(t+\tilde{t})}}{\overline{c^2}} \tag{2.19}$$

Obviously, $r(0) = 1$. Usually, as $\tilde{t} \to \infty$, $r(\tilde{t})$ goes to 0, because most processes are uncorrelated with themselves. Using this, an integral time scale $\tilde{t}_i$ can be defined as

$$\tilde{t}_i = \int_0^\infty r(\tilde{t}) d\tilde{t}. \tag{2.20}$$

The integral time scale $\tilde{t}_i$ is the time, at which the process is highly correlated with itself. That means, that the time scale τ in equation 2.18 needs to be chosen longer than this integral time scale, $\tau \gg \tilde{t}_i$. Similarly to temporal autocorrelation, a spatial autocorrelation can be defined to gain insights into the typical spatial scale of a turbulent process, see for instance Kundu [2008].

For the limit towards smaller scales, the kinematic viscosity ν of water plays an important role. The smallest spatial scale η and the smallest temporal scale τ_η in turbulent flows were postulated by Kolmogorov [1941],

$$\eta = \left(\frac{\nu^3}{\varepsilon}\right)^{\frac{1}{4}} \tag{2.21}$$

$$\tau_\eta = \left(\frac{\nu}{\varepsilon}\right)^{\frac{1}{2}}. \tag{2.22}$$

The parameter ε is called the turbulent kinetic energy (TKE) and is defined as the mean kinetic energy per mass unit present in turbulent eddies. TKE is typically produced by shear, buoyancy or other external forcing on relatively large scales. Large scale eddies tend to produce smaller scale

eddies, and thus hand down their energy to smaller and smaller scales. At the Kolmogorov scales, the energy is then dissipated due to friction, creating heat. This graduation of eddies is called the turbulent energy cascade. More about TKE as well as the governing equations can be found, for instance, in Pope [2009].

Another useful concept is covariance. The flux density $\vec{j}$ is a product of the flow velocity $\vec{u}$ and the concentration,

$$\vec{j} = \vec{u}c. \tag{2.23}$$

Using Reynolds decomposition, see equation 2.16, of the flow velocity and the concentration, yields

$$\bar{\vec{j}} = \overline{(\bar{c} + c') \cdot (\bar{\vec{u}} + \vec{u}')} = \bar{c} \cdot \bar{\vec{u}} + \overline{c' \cdot \vec{u}'} \tag{2.24}$$

under the assumption that the average of the fluctuations is zero, see equation 2.17. The first term, $\bar{c} \cdot \bar{\vec{u}}$, quantifies the mean transport due to convection. The covariance term $\overline{c' \cdot \vec{u}'}$, which is the temporal mean of the product of the fluctuations vanishes, if both functions $\vec{u'}(t)$ and $c'(t)$ are totally uncorrelated. Conversely, this poses a way of measuring turbulent transport by correlating fluctuations in velocity and concentration. This experimental technique, described in detail for instance in Aubinet et al. [2012], is commonly called eddy covariance. The larger the covariance, the larger the turbulent transport.

Applying the findings from the last paragraphs to the motion law derived from Fick's second law, equation 2.15, yields

$$-\frac{\partial \bar{c}}{\partial t} - \bar{\vec{u}} \nabla \bar{c} = \nabla \bar{\vec{j}} = \nabla \left(\overline{c' \vec{u}'} - D \nabla \bar{c} \right). \tag{2.25}$$

As an analogy between diffusion and turbulence, a turbulent diffusion coefficient $\mathbf{K_t}$ which is mathematically represented as a tensor, can be defined as

$$\overline{c' \vec{u}'} := -\mathbf{K_t} \nabla \bar{c}, \tag{2.26}$$

which modifies equation 2.25 to

$$\bar{\vec{j}} = -\left(\mathbf{K_t} \nabla \bar{c} + D \nabla \bar{c} \right). \tag{2.27}$$

2.2. Air-Sea Gas Transfer

The insights gained from the general consideration of the transport mechanisms in the previous section will be modified and transferred to gas transfer first. Then, some models will be presented which can be used to describe gas transfer. In the following contemplations, the flux density $\vec{j}$ is assumed to be constant across the air-water interface.

2.2.1. The Boundary Layer

To simplify further steps and to relate the equations, which were derived in the previous section to gas transfer, some simplifications are made. The water surface is assumed to be in the x-y-plane, the main flow is in x-direction and that the concentration gradient is one dimensional and oriented along the z axis, or

$$u_y = u_z = 0 \qquad \text{and} \tag{2.28}$$

$$\frac{\partial c}{\partial x} = \frac{\partial c}{\partial y} = 0 \tag{2.29}$$

Using these simplification, equation 2.27 changes to

$$j = -(K_t(z) + D)\frac{\partial \overline{c}(z)}{\partial z} \tag{2.30}$$

The turbulent diffusion coefficient K_t is now no longer a tensor, but a depth dependent property. Similarly, the argumentations can be made for the transport of momentum instead of the concentration, yielding

$$j_m = -\rho(K_m(z) + \nu)\frac{\partial \overline{u}(z)}{\partial z}, \tag{2.31}$$

with the turbulent transport coefficient K_m for momentum, the density ρ of the medium and the kinematic viscosity ν. By definition, the momentum flux is equal to the shear stress at the surface, $\tau := j_m$. To describe the turbulent momentum transport, a characteristic value is defined, that is a measure for momentum transfer from the air to the water or vice versa,

$$u_* := \sqrt{\frac{|\tau|}{\rho}}. \tag{2.32}$$

This value has the unit of a velocity and is commonly referred to as friction velocity u_*. The friction velocity can be defined for the air and for the water side, with the relationship between the two,

$$u_{*,w} = u_{*,a}\sqrt{\frac{\rho_a}{\rho_w}}. \tag{2.33}$$

being determined by the air and water densities ρ_a and ρ_w, respectively. In this thesis, with friction velocity the water sided one is meant, $u_* = u_{*,w}$, if nothing to the contrary is stated.

Directly at the water surface, turbulent transport of concentration and therefore the turbulent diffusion coefficient vanishes and equation 2.27 can be modified to

$$j = -D\left.\frac{\partial \overline{c}}{\partial z}\right|_{z=0}, \tag{2.34}$$

meaning, that the derivative of the concentration profile directly at the water surface is directly proportional to the flux density j. This can be used to define some convenient parameters describing typical spatial and temporal scales. Using the definition of the transfer velocity k, see equation 2.3 the boundary layer thickness, z_* is then defined as

$$z_* = \frac{\Delta c}{\frac{\partial \overline{c}}{\partial z}|_{z=0}} = \frac{D\Delta c}{j} = \frac{D}{k}. \tag{2.35}$$

The graphical interpretation of this equation can be seen in figure 2.2, where an example of a concentration profile is shown, along with the gradient of the concentration at the water surface. The intersection between this gradient and the z-axis defines the boundary layer depth. Or, more general, the intersection between the gradient at the surface and the concentration in the water bulk, which was chosen to be 0 in the graphical example, see also Münsterer [1996]. This kind of boundary layer can be defined in the air and water. For admixtures of substances, these boundary layers are called molecular boundary layers, as the limiting factor is molecular diffusion. They are characterized by the transport due to diffusion being faster than the transport due to the turbulence. For the momentum, a similar boundary layer exists, this is called the viscous boundary layer, as the kinematic viscosity is the limiting factor for momentum transport.

Similarly to the boundary layer thickness, a characteristic time scale t_* for the exchange process can be defined as

$$t_* = \frac{z_*}{k} = \frac{D}{k^2} \tag{2.36}$$

The characteristic time scale t_* can be seen as the time, a molecule needs to traverse the boundary layer with the thickness z_* with the velocity k.

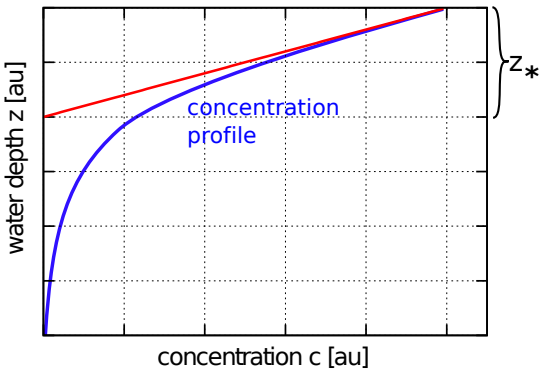

Figure 2.2.: Concentration profile of a substance with a concentration that's higher in the air than in the water. Also shown is the gradient at the surface, see equation 2.34 as well as the graphical interpretation of the boundary layer thickness z_*. (modified after Münsterer [1996]).

2.2.2. The Logarithmic Wind Profile

Using equation 2.31 something about the vertical wind profile can be deduced. Far from the interface, turbulent transport of momentum is larger than diffusive transport by some orders of magnitude. Then, the momentum transport does no longer depend on the viscosity ν, but can only depend on the shear stress τ, and the distance from the interface. A dimensional analysis shows, that the velocity gradient can be expressed by

$$\frac{du_x}{dz} = C\frac{u_*}{z} \tag{2.37}$$

Integration yields a logarithmic profile,

$$u_x(z) = C\, u_* \ln \frac{z}{z_0} \tag{2.38}$$

with the roughness length z_0 which corrects for effects of surface roughness on the flow. It is typically in the order of $1/10$ to $1/30$ of the dominant vertical structures on the surface. Experimentally, the yet undiscussed constant C is found to be the inverse of κ, the Von Kármán constant which has a value of $\kappa = 0.41$.

The momentum transport does not depend on the viscosity in the turbulent regime. Neglecting the viscosity ν in equation 2.31, inserting the definitions for the friction velocity $u_* = \sqrt{\tau/\rho}$ as well as equation 2.38, yields an estimate for the turbulent diffusion constant for momentum,

$$K_m(z) = \kappa'\, u_*\, z. \tag{2.39}$$

2.2.3. Concentration and Velocity Profiles

To be able to understand the concentration profile across the air-sea boundary layer, the solubility must be introduced.

A small amount of an admixture in a system with a water phase and an air phase will distribute between air and water. In Equilibrium, concentrations of the substance in the air and water phase are described by Henry's Law,

$$c_w^{eq} = \alpha c_a^{eq} \tag{2.40}$$

where α denotes the tracer's solubility and c_a^{eq} and c_w^{eq} are the tracer's air and water side concentration. The equilibrium is reached when there is no flux across the surface, $\vec{j} = 0$.

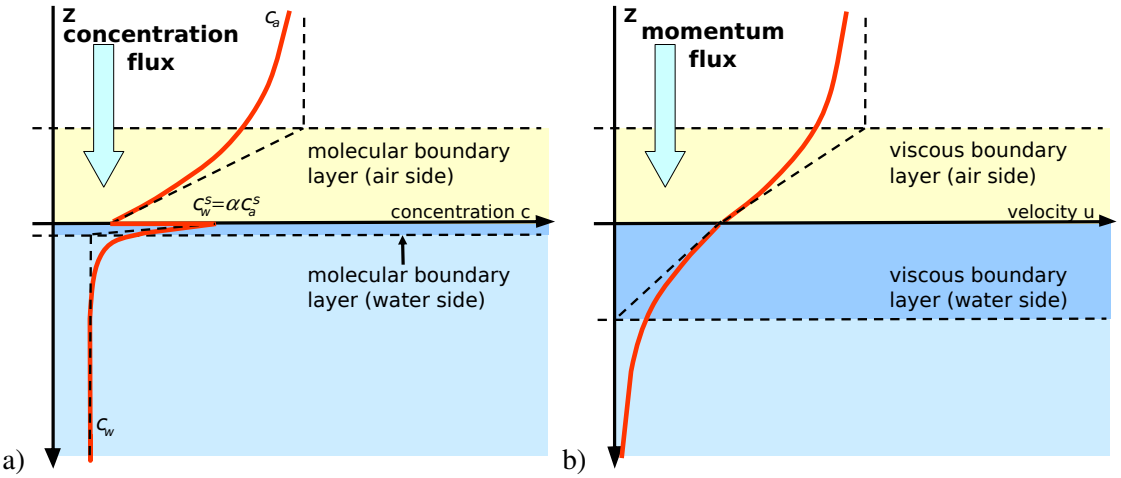

Figure 2.3.: a) Example of a concentration profile of a tracer with a solubility of $\alpha > 1$ for invasion ($\alpha c_a > c_w$) The molecular boundary layers are marked. b) Example of a velocity profile at the water surface with the wind being faster than the flow of the water bulk. Viscous boundary layers are marked. (Modified after Degreif [2006].)

Even for non-equilibrium concentrations in the air and water phase far from the interface, the water surface is always in equilibrium with the air directly above resulting in a concentration jump at the interface. Using this concentration jump at the water surface, a full concentration profile can be drawn, see figure 2.3a. For the momentum, an equivalent concept of solubility can be defined. Here, the difference in densities between water and air yields the solubility,

$$\rho_w = \alpha_m \rho_a, \tag{2.41}$$

with a value of around 1000 under normal conditions. Assuming a no-slip boundary condition at the interface is reasonable, because of adhesion between the lowest layer of the air molecules and the uppermost layer of the water molecules. Therefore, the velocity gradient must be smooth, see 2.3b.

2.2.4. The Schmidt Number

To compare transport of momentum to transport of an admixture of a substance, the Schmidt number is a useful concept. In accordance to equations 2.31 and 2.31, the Schmidt number Sc defined as

$$Sc := \frac{\nu}{D} \tag{2.42}$$

as the ratio of kinematic viscosity and diffusivity. Similarly, a turbulent Schmidt number can be defined as

$$Sc_t := \frac{K_m}{K_t}. \tag{2.43}$$

Along with the solubility, the Schmidt number is a tracer specific property. Figure 2.4 shows some environmentally important tracers in a Schmidt number-solubility diagram. Also shown is the concept of air and water side control, which will be discussed in the following section.

2.2.5. Transfer Resistances

To gain insight into the concentration profile, the turbulent diffusion coefficient K_t needs to be studied further. Solving the one dimensional transport equation, 2.30, for the concentration profile

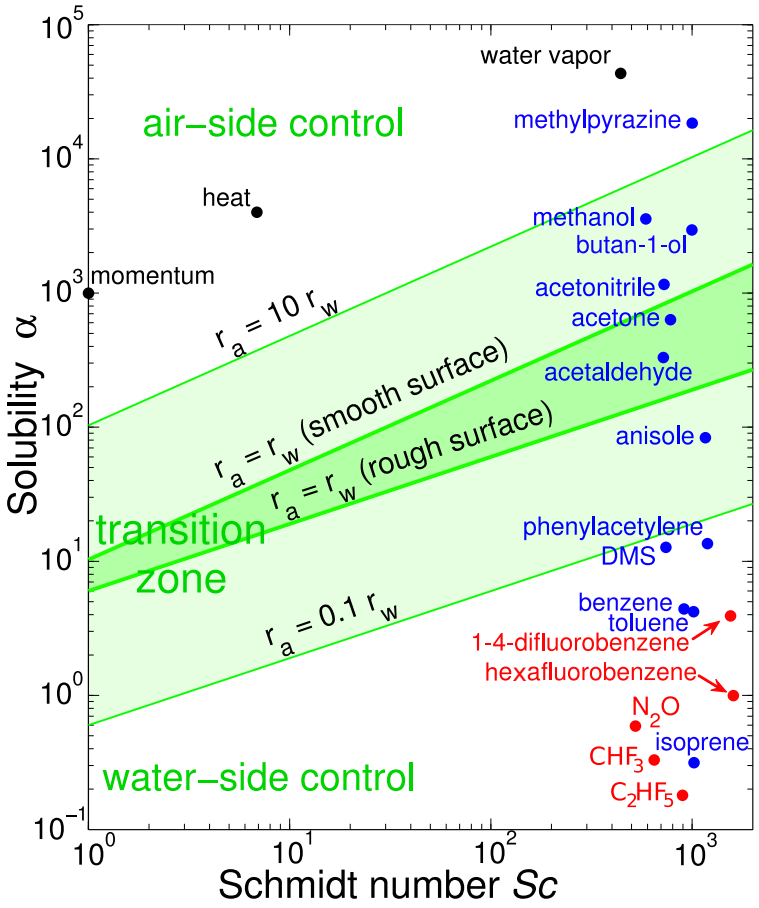

Figure 2.4.: Solubility-diffusivity diagram for some gaseous tracers. The ones used in this work are marked in red. The temperature is 20 ^{o}C. (modified after Jähne and Haußecker [1998] and Kräuter [2011]).

yields

$$\frac{\partial c(z)}{\partial z} = -\frac{j}{K_t(z) + D}, \tag{2.44}$$

which can be integrated between depths z_1 and z_2,

$$\frac{c(z_2) - c(z_1)}{-j} = \int_{z_1}^{z_2} \frac{1}{K_t(z) + D} dz. \tag{2.45}$$

Equation 2.45 is written in a way, that an analogy to electric resistances becomes clear. A difference in electric potential between two points (here: difference in concentration between two depths) results in an electric current (here: a flux of tracer particles). To take the analogy one step further, a specific transfer resistance can be defined,

$$R_{1,2} := \frac{c(z_1) - c(z_2)}{j} = \frac{1}{k_{1,2}} \tag{2.46}$$

Using equation 2.45 it can be shown, that the analogy holds even when additions of transfer resistances are considered,

$$R_{1,2} + R_{2,3} = \frac{c(z_1) - c(z_2)}{j} + \frac{c(z_2) - c(z_3)}{j} = \frac{c(z_1) - c(z_3)}{j} = R_{1,3}. \tag{2.47}$$

This leads to an inverse addition law for transfer velocities,

$$\frac{1}{k_{1,3}} = \frac{1}{k_{1,2}} + \frac{1}{k_{2,3}}. \tag{2.48}$$

Taking this line of thought one step further, many different phenomena can be split up and studied separately. For instance, turbulent transport and diffusive transport may be studied separately. However, it proved to be useful to split up the transfer directly at the water surface as proposed by Liss and Slater [1974]. This leads to a purely air side controlled part of the transfer, k_a and a purely water side controlled, k_w. The addition law needs to be modified further due to the concentration jump at the water surface due to the solubility, yielding

$$\frac{1}{k_t} = \frac{1}{k_w} + \alpha\frac{1}{k_a}. \tag{2.49}$$

Depending on the solubility of the tracer, the water-side resistance $1/k_w$ or the air-side resistance $\alpha\,1/k_a$ is the dominant one or both are roughly equal. For which solubilities the resistances are equal is shown in figure 2.4. This also depends on whether the water surface is smooth or wavy. Reasons for this as well as a detailed calculation of the curves can be found in Kräuter [2011].

In this work, only tracers with very low solubility are studied. Therefore, all of the transfer resistance is assumed to be in the water side.

2.2.6. Gas Transfer Models

In the following paragraphs, the theoretical foundations of three different models will be discussed, and a general description of the Schmidt number dependency of the gas transfer velocity will be given. In addition, a model that accounts for a changing water surface, from smooth to flat as the wind increases, will be shown.

The Thin Film Model

In the simplest of all models, a purely diffusive transport in the boundary layer is assumed. Outside of the boundary layer, turbulence is assumed to be fully developed, see figure 2.5. Within the boundary layer only diffusive transport in z direction is possible, leading to a linear concentration profile.

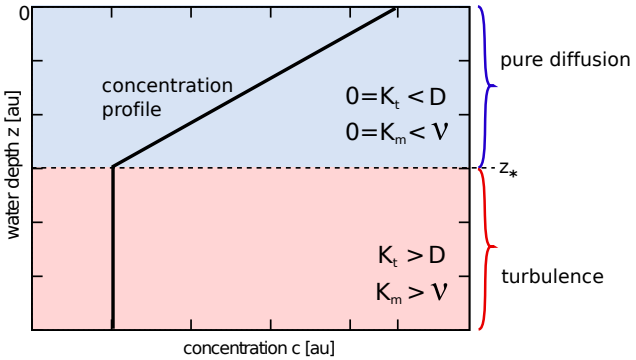

Figure 2.5.: Expected concentration profile for the thin film model. In the diffusive region, the concentration decreases linearly, while in the turbulent region the concentration is constant with depth due to turbulent mixing.

To simplify the mathematical description, a dimensionless velocity u_+, a dimensionless boundary layer thickness z_+ and a dimensionless transfer velocity k_+ are introduced,

$$u_+ := \frac{u}{u_*} \tag{2.50}$$

$$z_+ := \frac{u_* z}{\nu} \tag{2.51}$$

$$k_+ := \frac{k}{u_*}. \tag{2.52}$$

Experimentally it was shown, that $u_+(z_+)$ yields an universal shape for a flow near a smooth wall, see for instance Monin and Yaglom [2007] or Jähne [1980].

Equation 2.35 can be used to calculate the transfer velocity,

$$k = \frac{D}{z_*} \tag{2.53}$$

using the definition of the Schmidt number defined in equation 2.42 as well as the dimensionless boundary layer, the Schmidt number dependency can be seen,

$$k = \frac{u_*}{z_{+,*}} Sc^{-1} \tag{2.54}$$

with the dimensionless boundary layer thickness z_{+*}. This Schmidt number exponent of -1 is too small, as many experiments have shown. A reason for this is, that the assumed abruptly vanishing turbulence at the boundary layer depth is unphysical. However, this model can be seen as the lower boundary for transfer velocities.

The Diffusion Model

In the diffusion model, three different layers can be defined. In the uppermost layer directly under the water surface, diffusive transport is more efficient than turbulent transport for both momentum and concentration. In the middle layer, the turbulent momentum transport is larger than the diffusive momentum transport. For concentration, however, diffusion is still the dominant process. In the lowest layer, turbulent transport outweighs diffusive transport both for momentum and concentration. A depiction of this three layers can be seen in figure 2.6.

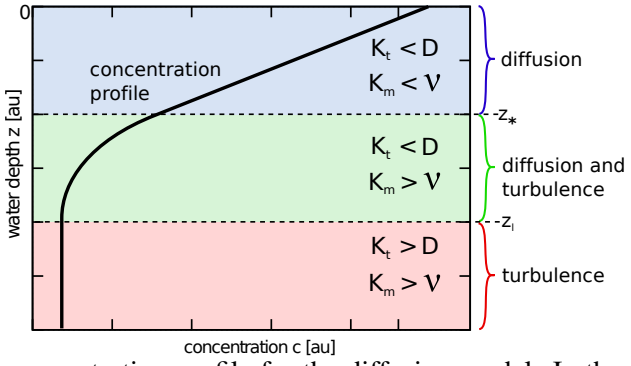

Figure 2.6.: Expected concentration profile for the diffusion model. In the uppermost layer, concentration and momentum are transported by diffusion only. In the middle layer, turbulent transport is dominant for momentum, diffusive transport is dominant for concentrations. In the lowest layer, turbulence is responsible for the transport of both. The viscous boundary layer depth z_* as well as the mass boundary layer z_l are marked.

To calculate the transfer velocity, the integral in equation 2.45 needs to be solved for the whole concentration profile. To do this, the turbulent diffusion coefficient needs to be studied. Deacon [1977] proposed a dependence of the turbulent diffusion coefficient on the dimensionless thickness z_+ for a smooth wall,

$$K_t(z_+) = \kappa\nu z_l \cdot \left(\frac{z_+}{z_l} - \tanh\left(\frac{z_+}{z_l}\right)\right) \tag{2.55}$$

using the dimensionless velocity profile by Reichardt [1951]. The depth z_l is defined as the dimensionless depth, below which pure turbulent transport is dominant. Deacon [1977] calculated this to be $z_l = 11.7$. Finally, for tracers with Schmidt numbers above 10, which all trace gases have, Deacon gives a dimensionless transfer velocity,

$$\frac{1}{k_+} = 12.1 \cdot Sc^{\frac{2}{3}} + 2.7 \cdot \log_{10}(Sc) + 2.9. \tag{2.56}$$

The tracer with the lowest Schmidt number used in this work is nitrous oxide with $Sc = 600$ at 20 ^{o}C. For this tracer, the last two terms are in the order of 1.2 % of the total inverse transfer velocity, and can therefore be neglected safely. The transfer velocity can then be calculated,

$$k = \frac{u_*}{12.1} Sc^{-\frac{2}{3}}. \tag{2.57}$$

Another common way of describing the turbulent diffusion coefficient is an exponential depth dependency with either z^3 or z^2, or more generally,

$$K_t(z) = a_m \cdot z^m \tag{2.58}$$

with $m = 2$ or $m = 3$. Here, $m = 2$ corresponds to a rough and wavy water surface, while $m = 3$ corresponds to a smooth one. Coantic [1986] integrated the equation 2.45 for a smooth water surface, $m = 3$, with this assumed turbulent transfer velocities, and yielded

$$k = \frac{1}{12.5}\, u_*\, Sc^{-\frac{2}{3}}. \tag{2.59}$$

For a rough water surface with $m = 2$, published by Yaglom and Kader [1974], the solution is

$$k = \text{const.} \cdot\ u_*\, Sc^{-\frac{1}{2}}. \tag{2.60}$$

These formulations for smooth and wavy water surfaces are very similar to Deacon's formula, equation 2.57. For low wind speeds or for surfactant covered water, where the condition of a smooth water surface is met, the Schmidt number exponent is expected to be $2/3$, while for a wavy surface, at higher wind speeds, the Schmidt number exponent is $1/2$. At the same time, the turbulent diffusion coefficient changes it's depth dependence from a cubic to a quadratic one. It is to be expected that this transition is not sudden, but gradual.

The Surface Renewal Model

In this model, postulated by Higbie [1935], concentration is transported by turbulent eddies which may reach into the boundary layer, making this model a statistical model. The characteristic time scale for this model is the surface renewal time τ, the mean time between two eddies which exchange water at the surface for water from the bulk. This is equal to the mean time that a volume element of water stays in the boundary layer. On top of the statistical renewal due to turbulence, diffusion also transports concentration.

Danckwerts [1951] gives the depth dependent renewal time τ as

$$\tau = \frac{1}{\gamma_p z^p}. \tag{2.61}$$

For the case of $p = 0$, the classic, depth independent case is covered. Directly at the water surface, the surface renewal $\tau \to \infty$, meaning that the renewal rate, $\lambda = 1/\tau$ vanishes, which is expected, because eddies can only approach the water surface infinitesimally.

Fick's second law, equation 2.9, can now be written in one dimension as

$$0 = \frac{\partial c}{\partial t} = D \cdot \frac{\partial^2 c}{\partial x^2} - \frac{c}{\tau} \tag{2.62}$$

assuming a steady state. The turbulence term was modified to account for statistical renewal. Solving this equation yields insights into the nature of the statistical renewal processes. According to Nielsen [2004] this can be solved by a an exponential approach, yielding

$$k = \sqrt{\frac{D}{\tau}}. \tag{2.63}$$

A dimensional analysis shows, that the renewal time scale τ depends on the friction velocity u_* and the kinematic viscosity ν,

$$\tau = \beta^2 \frac{\nu}{u_*^2} \tag{2.64}$$

with a dimensionless scaling factor β. The inverse relationship with the friction velocity is evident, as the turbulence is created by shear stress. Combining this finding with the formulation of the transfer velocity k in equation 2.63 yields the Schmidt number dependency for the transfer velocity

$$k = \frac{1}{\beta} \cdot u_* \cdot Sc^{-\frac{1}{2}}. \tag{2.65}$$

A more general formulation is given by Jähne et al. [1989] and Csanady [1990] for $p > 0$,

$$k = \frac{1}{\beta_p} \cdot u_* \cdot Sc^{-1+\frac{1}{p+2}}, \tag{2.66}$$

which, again, yields Schmidt number dependencies of $k \propto Sc^{-2/3}$ for a smooth water surface, and $k \propto Sc^{-1/2}$ for a wavy water surface.

Interim Summary: Models

Figure 2.7 shows the physical mechanisms at play for the three different models introduced in the previous sections.

To mathematically summarize the models shown, a general form of gas transfer can be written as

$$k(u_*, bc) = u_* \frac{1}{\beta(bc)} Sc^{-n(bc)} \tag{2.67}$$

with the dimensionless scaling factor β and the Schmidt number exponent n being subject to the **b**oundary **c**onditions, bc. To compare two tracers under the same boundary conditions, i. e. at conditions with the same β and n, Schmidt number scaling is used.

$$\frac{k_A}{k_B} = \left(\frac{Sc_A}{Sc_B}\right)^{-n}. \tag{2.68}$$

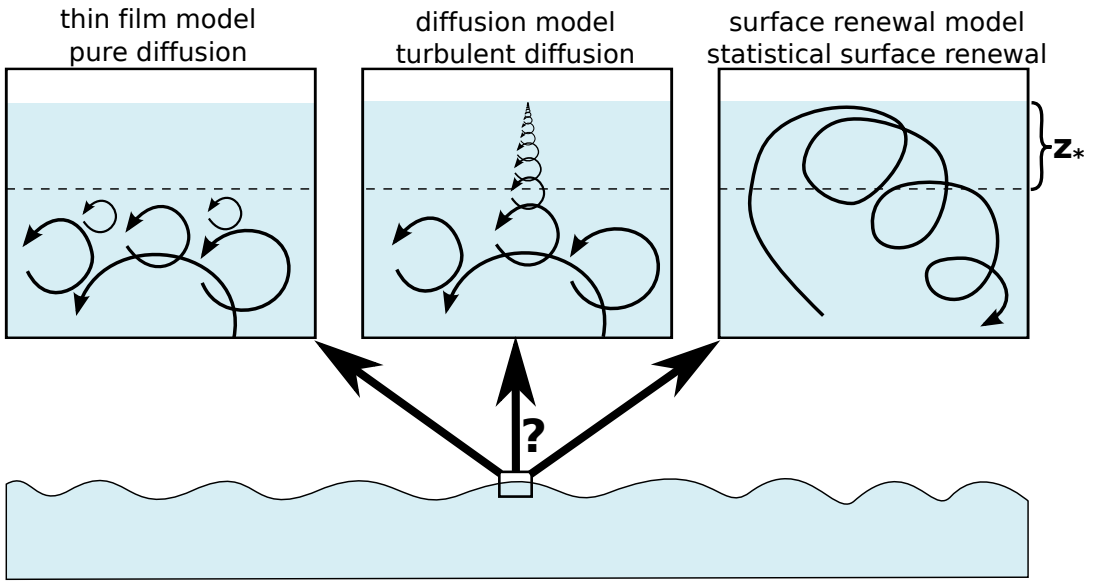

Figure 2.7.: Overview of the three models discussed so far. The viscous boundary layer is marked with a z_*. (modified after Schimpf [2000])

with the tracer's transfer velocities k_A and k_B as well as their Schmidt numbers Sc_A and Sc_B.

As all models yield the same general form of Schmidt number dependency, a closer look at the underlying mechanisms is not possible with measurements of the transfer velocity alone. However, all models predict different concentration profiles within the boundary layer, see for instance Münsterer [1996]. So looking at the concentration profile, the models can be distinguished.

But measurements of the transfer velocities, even without a closer look at the concentration profiles allow to study the transition of the Schmidt number exponent from smooth, $n = 2/3$, to wavy conditions, $n = 1/2$. A model to describe the changing boundary conditions is discussed in the next section.

The Facet Model

The capillary waves that are important for gas transfer as they are believed to enhance turbulence in the near surface layer, are not distributed uniformly across the whole water surface. With increasing wind speed, more and more of these important waves can be seen covering larger and larger parts of the water surface. It can be concluded from this everyday observation, that not all parts of the water surface are smooth (wavy) all the time. Gas transfer can be seen as a statistical process, with some portion of the total water surface behaving like a smooth surface, and the rest behaving like a wavy water surface. Mathematically, this presumption is described by the facet model, developed by Jähne and Bock [2001].

This model of a gradually changing water surface from smooth to wavy conditions is supported by experimental data, for example in Jähne et al. [1987], Nielsen [2004] and Zappa et al. [2004].

In the facet model, the total area is parted into a wavy fraction, a_w and a smooth fraction, a_s. Both fractions add up to the total water surface, i. e. $a_w + a_s = 1$. The transfer velocity is seen as an addition of transfer across both fractions of the surface,

$$k = \underbrace{a_s k_s}_{\text{smooth}} + \underbrace{a_w k_w}_{\text{wavy}} = \underbrace{(1 - a_w)\,\frac{u_*}{\beta_s} Sc^{-n_s}}_{\text{smooth}} + \underbrace{a_w \frac{u_*}{\beta_w} Sc^{-n_w}}_{\text{wavy}}. \tag{2.69}$$

Jähne [1985] suggested to use the mean square slope σ_s^2 of the water surface as a parameter to describe the boundary conditions. The fractional area a_w with a wavy boundary condition is then parameterized using the mean square slope as

$$a_w(\sigma_s^2) = \frac{(\sigma_s^2)^\gamma}{\delta^\gamma + (\sigma_s^2)^\gamma} \tag{2.70}$$

with the steepness parameter γ and the midpoint parameter δ. Figures 2.8a and 2.8c show the predicted wavy fractional area for several combinations of δ and γ.

A rather lengthy calculation involving the combination of equations 2.68 and 2.69 and derivation with respect to Sc reveals the relationship between the Schmidt number exponent n and the mean square slope σ_s^2,

$$n(\sigma_s^2) = \frac{\frac{2}{3}\left(1 - a_w(\sigma_s^2)\right)\frac{1}{\beta_s}Sc^{-n_s} + \frac{1}{2}a_w(\sigma_s^2)\frac{1}{\beta_w}Sc^{-n_w}}{\left(1 - a_w(\sigma_s^2)\right)\frac{1}{\beta_s}Sc^{-n_s} + a_w(\sigma_s^2)\frac{1}{\beta_w}Sc^{-n_w}}. \tag{2.71}$$

Using this equation, the change of n can be studied with respect to the steepness parameter γ and the midpoint parameter δ. Figures 2.8b and 2.8d show how different γ and δ values affect the shape of the transition of the Schmidt number exponent.

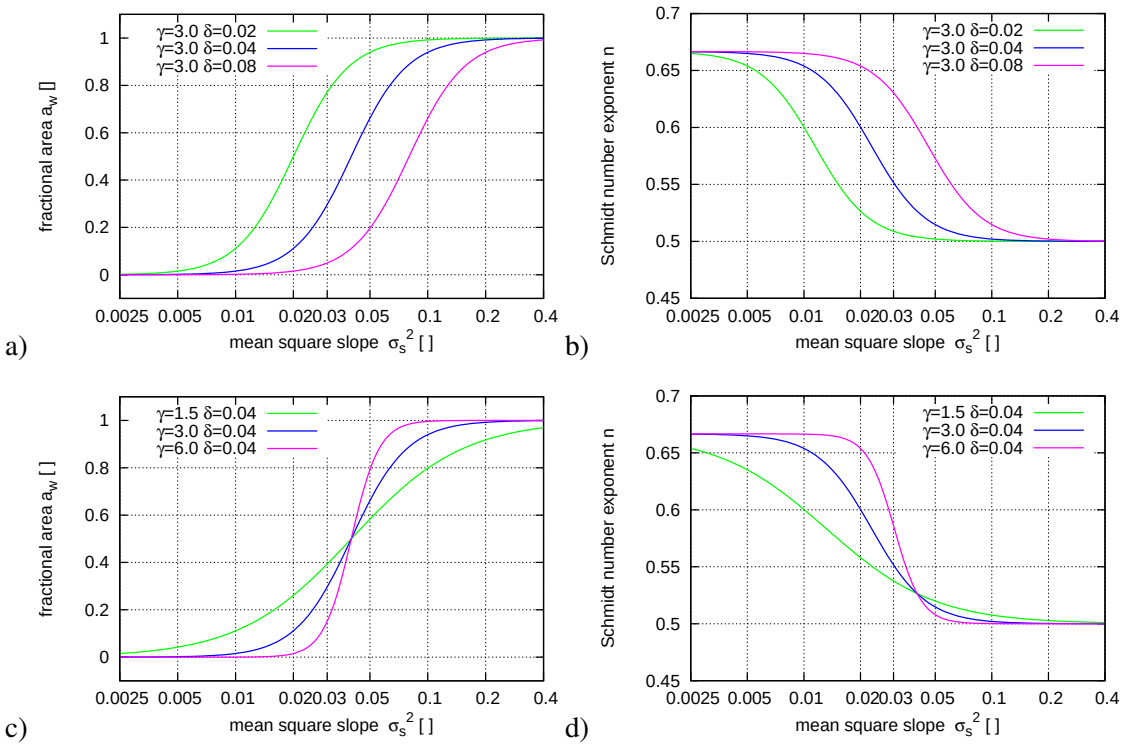

Figure 2.8.: Prediction of the Schmidt number exponent of the Facet Model. a) Fraction of the area a with wave induced gas transfer. The midpoint parameter δ is varied. b) Change of the Schmidt number exponent from smooth to wavy conditions for different midpoint parameters δ in relation to the mean square slope of the water surface σ_s^2. c) Fractional area with wave induced gas transfer for three different steepness parameters γ. d) relationship between the Schmidt number exponent n and the mean square slope for three steepness parameters δ. Further parameters chosen for this plots: $\beta_w = 6.7$, $\beta_s = 12.2$ and $Sc = 600$.

The facet model can be used to calculate an expected value for β. Combining equation 2.69 with the theoretical value for the transfer velocity equation 2.67 yields

$$k = \frac{1}{\beta} u_* Sc^{-n} = (1 - a_w(\sigma_s^2)) u_* \frac{1}{\beta_s} Sc^{-2/3} + a_w(\sigma_s^2) u_* \frac{1}{\beta_w} Sc^{-1/2} \tag{2.72}$$

Assuming that the measured Schmidt number exponent n can be replaced by the modeled one in equation 2.71, $n = n(\sigma_s^2)$, equation 2.72 can be solved for β,

$$\beta(\sigma_s^2) = \frac{Sc^{-n(\sigma_s^2)}}{(1 - a_w(\sigma_s^2)) \frac{1}{\beta_s} Sc^{-2/3} + a_w(\sigma_s^2) \frac{1}{\beta_w} Sc^{-1/2}} \tag{2.73}$$

This equation predicts a functional dependency of β from the mean square slope. Figure 2.9 shows the prediction of the facet model for the parameter β for different steepness parameters γ and different midpoints δ. Using this representation of β, an alternative representation of the facet model equation, 2.69 can be written as

$$k(\sigma_s^2, u_*) = u_* \frac{1}{\beta(\sigma_s^2)} Sc^{-n(\sigma_s^2)}, \tag{2.74}$$

with the modeled $\beta(\sigma_s^2)$, equation 2.73 and Schmidt number exponent $n(\sigma_s^2)$, equation 2.71.

Inserting the equation predicting β, eq. 2.73, into the alternative model equation, eq. 2.74, confirms the equality with the original model equation 2.69.

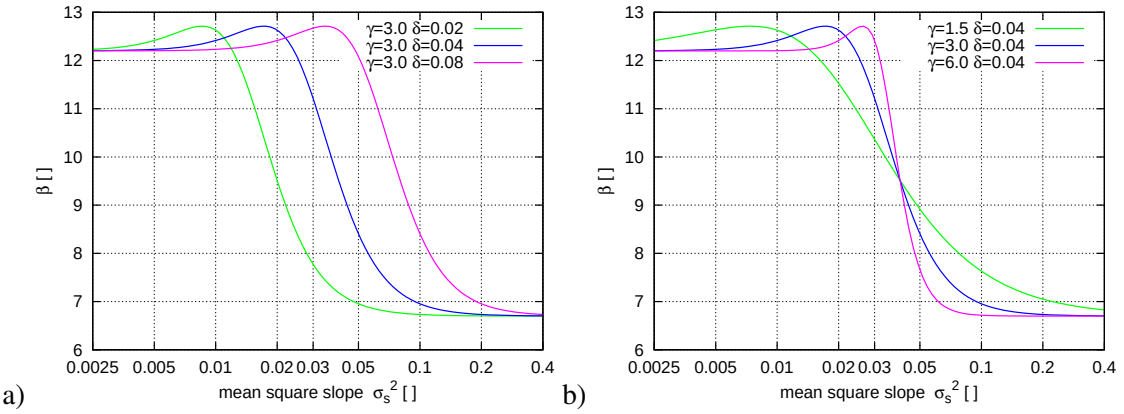

Figure 2.9.: Prediction of the scaling factor β of the Facet Model. a) The midpoint parameter δ is varied. b) The steepness parameters γ is varied. Further parameters chosen: $\beta_w = 6.7$, $\beta_s = 12.2$ and $Sc = 600$.

The Schmidt number exponent n and scaling factor β predicted by facet model depend on the Schmidt number, see figure 2.10. While the dependence of n on the Schmidt number is minimal, the scaling factor β shows some differences in values in the transition region. The amount of increase above the value of β at low slopes, β_s, seems to be depending on the Schmidt number itself.

A model similar to the facet model is developed in Zappa et al. [2004]. But the authors use a slightly different definition of the fractional area, which is determined by passive thermography, see also Schimpf [2000].

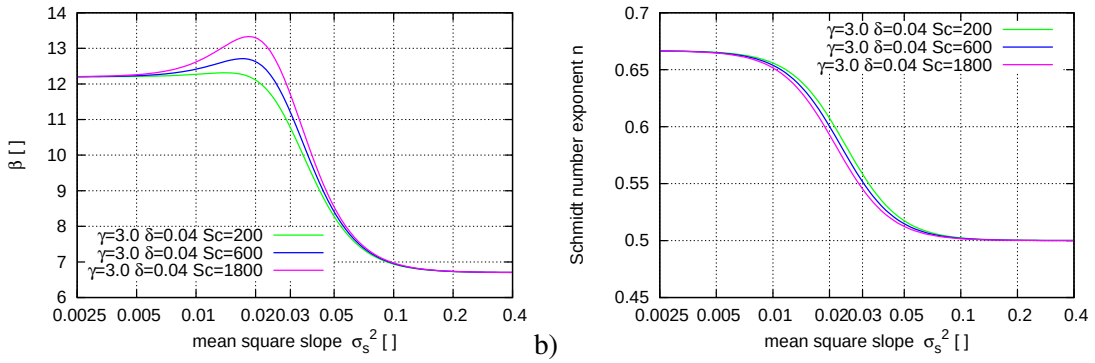

a) b)

Figure 2.10.: a) Prediction of the scaling factor β by the facet model. The Schmidt number Sc is varied. b) Prediction of the Schmidt number exponent. The Schmidt number Sc is varied in both plots. Further parameters chosen: $\beta_w = 6.7$, $\beta_s = 12.2$.

2.2.7. Surfactants

Chemicals, that lower the water's surface tension, when they are spread on water or mixed into water, are called **surf**ace **act**ive **a**ge**nt**, or surfactant.

A significant reduction in gas transfer rates by surface active materials has been shown experimentally, see for instance Asher and Pankow [1986]. Frew et al. [1990] showed, that the main factor that lowers gas exchange is not the formation of a mono molecular barrier at the interface limiting the diffusion of tracers, but hydrodynamic effects changing the flow field and turbulence structures near the boundary layer. A quantitative calculation of the changes in the capillary wave generation can be found in Ceniceros [2003].

Generally, surfactant molecules are made up of a hydrophilic part, called the head and a hydrophobic part called the tail. They accumulate on the water surface, typically in a mono molecular layer, with the hydrophobic part sticking out of the water, see figure 2.11. Surfactants can also form clusters in the water bulk which are called micelles, when they are mixed down into the water body, or when there are more surfactant molecules available than needed to cover the water surface.

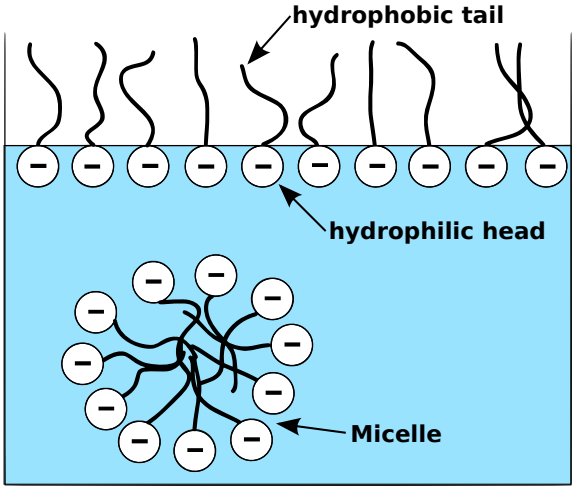

Figure 2.11.: Schematic view of typical positions of surfactant molecules in water. Most will accumulate on the water surface with the hydrophobic part sticking out of the water. If the surfactant concentration is high enough, micelles will form. Image modified after Stapf [2010].

2.2.8. Gas Transfer at Extreme Wind Speeds

The character of the sea surface changes visibly, as wind speeds increase. This is well known to seafarers, and the basis of the Beaufort wind scale, see for example Harding [1885]. At severe wind speeds, the sea surface becomes covered in a layer of foam and spray. During these extreme conditions, there is no clear water surface. The transition between air and water is rather a gradual transition from spray filled air to bubble filled water. A graphical depiction as well as a photo of this can be seen in figure 2.12.

a) 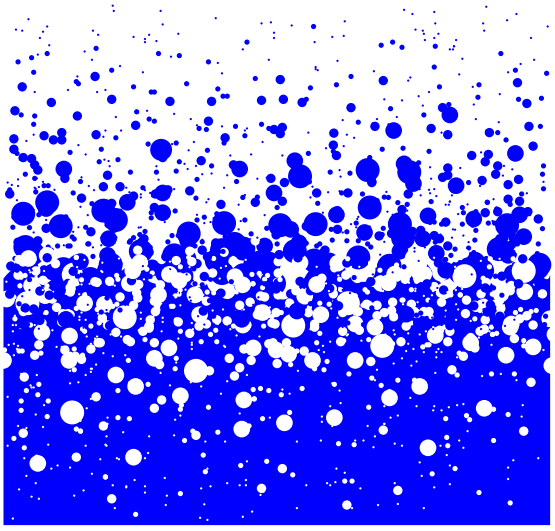 b) 

Figure 2.12.: a) Schematic representation of the water 'surface' at extreme wind speeds depicting a gradual transition from spray filled air to bubble filled water. b) Actual photo of the water surface at hurricane conditions, taken through the side window of a hurricane speed wind-wave tank at Kyoto University, Japan. While towards the right of the image, something resembling a water surface can be spotted, no such thing can be seen in the left part. The spray is smeared due to a water film on the inside of the window. Picture dimensions are roughly 30 x 40 cm, wind direction is left to right. The largest bubbles are in the order of 6-9 mm in diameter.

Two new phenomena need to be discussed here, spray and bubbles.

Bubbles increase the surface, and are therefore expected to increase gas transfer. However, the surface and the enclosed air volume is special in some regards. First, the size of bubbles changes, due to the surface tension, increased pressure at larger water depths and also due to bubbles taking up gas from the water, or dissolving gas into the water. The latter leading to the effect of supersaturation. Second, the life time of bubbles is limited due to bubbles dissolving or bursting through the water surface. This in turn, creates more turbulence in the boundary layer. Gas transfer due to single bubbles is well studied experimentally, see for instance Mori et al. [2002] and Vasconcelos et al. [2002], as well as theoretically, see Memery and Merlivat [1985].

Several time scales are involved in bubble induced gas transfer, a summary of which can be found in Mischler [2010]. The time scales depend on the radius of the bubbles. For instance, the equilibrium time scale describes the time that is needed for a bubble to be in solubility equilibrium with the surrounding water. The equilibrium time scale is also depending on the solubility of the gases looked at, and it is typically much shorter than the dissolution time scale of the bubble itself. Another time scale is the rise time, which is shorter for larger bubbles, so that these are more likely

to not come into saturation equilibrium with the surrounding water.

The effect of spray on air-sea gas transfer has not been studied as intensely as bubbles yet. Because most commonly used tracers have a very low solubility, the net dissolved gas capacity of a droplet detached from the water surface can be expected to be relatively small. Following this argumentation, the effect on the gas transfer velocity of spray should therefore be smaller than that of the same amount of bubbles. However, spray droplets still produce turbulence when they impact the water, which is enhancing gas transfer. Similar typical time scales as with bubbles can be envisioned. Smaller droplets are falling back to the water surface slower due to larger friction forces with the surrounding air, having a longer falling time. Depending on the size, they may even evaporate (evaporation time scale), leaving behind an aerosol particle, see for instance Wu [1992]. Also, droplets can come into solution equilibrium with the surrounding air (equilibrium time scale).

To describe both phenomena, an empirical parameter called whitecap coverage is commonly used. This parameter encompasses all effects provoked by large scale waves breaking: transfer due to bubble clouds and spray as well as enhanced turbulence due to bubbles and spray moving through water and air, and turbulence generated by breaking waves themselves. Whitecap coverage is defined as the fraction of the total area, that is covered by white caps and easily measured using cameras, see for instance Callaghan and White [2009].

Several empirical models exist which parameterize gas transfer velocities with respect to the whitecap coverage parameter as well as the solubility and the Schmidt number. The solubility dependence comes from the following qualitative line of thought. Assuming evasion, meaning that the net transport of a tracer is from water to air, the maximum gas concentration $c_{\mathrm{b,max}}$ inside a bubble is given by Henry's law,

$$c_{\mathrm{b,max}} = \frac{c_w}{\alpha}. \tag{2.75}$$

A bubble's capacity N_b to take up gas is limited by it's volume V_b,

$$N_b = c_{\mathrm{b,max}} * V_b = \frac{c_w}{\alpha} V_b, \tag{2.76}$$

or, in words, the smaller the solubility, the larger the bubble's capacity. To take into account, that not all bubbles reach solubility equilibrium, the dependence is usually generalized in the form α^{-m}. The argument for the Schmidt number dependence is similar to the arguments given for the free water surface. Around a bubble, a viscous boundary layer is found, which limits gas transport with an inverse Schmidt number dependency Sc^{-n_b}. Introducing the whitecap coverage parameter W_c, most models are a variation of

$$k_b = W_c \left(\frac{a}{\alpha} + b\, \alpha^{-m}\, Sc^{-n_b} \right), \tag{2.77}$$

with the empirical parameters a, b, m and n_b see for example Keeling [1993], Asher et al. [1995] and Asher et al. [1996]. More complex, but still empirical models are being worked on, for instance Woolf et al. [2007].

2.3. Absorption Spectroscopy

The absorption of light by an absorber along a light path of length l is described by Beer's Law,

$$I(\lambda) = I_0(\lambda) \exp\left(-l\, c\, \epsilon(\lambda)\right) \tag{2.78}$$

with the incident light intensity $I_0(\lambda)$, the extinction coefficient $\epsilon(\lambda)$ and the absorber's concentration c. The exponent is also called absorbance,

$$abs = l\, c\, \epsilon(\lambda) \tag{2.79}$$

In case of more than one absorber, their absorbances can be added linearly, modifying Beer's law into

$$I(\lambda) = I_0(\lambda) \exp\left(-l \cdot \sum_i (c_i\, \epsilon_i(\lambda))\right) \tag{2.80}$$

and the absorbance to

$$abs = l \sum_i (c_i\, \epsilon_i(\lambda))\,. \tag{2.81}$$

The light's wavelength λ is linked to the frequency of the light f and the energy E by

$$E = hf = \frac{hc}{\lambda} \tag{2.82}$$

with Planck's constant h and the speed of light c.

Different molecules absorb light at different wavelengths, depending on their chemical composition. Depending on the energy E of the incident light, different physical mechanisms are responsible for absorption. For example, light in the ultraviolet range of the spectrum ($\lambda = 10 - 380\,\text{nm}$) the distribution of electrons in most molecules is changed in the sense, that electrons are lifted into molecular orbits with higher energy levels. In the infrared range (λ between 2.5 μm and 16.5 μm) vibrational and rotational energy states are excited by the light. Both, UV spectroscopy and Fourier Transform Infrared spectroscopy which were used in this work will be discussed in the following two sections.

2.3.1. FT-IR Spectroscopy

Infrared light is capable of exciting vibrational energy states in many molecules. According to Griffiths [2007], vibrational energy states E_i can be described by

$$E_i = h\nu_0(i + \frac{1}{2}) + h\nu_0 x_i(i + \frac{1}{2}) \tag{2.83}$$

with Planck's constant h, the fundamental frequency of the vibrational mode ν_0 the dimensionless, usually negative anharmonicity constant x_i and the mode number $i = 0, 1, 2, 3....$ This type of energy potential is also called a Morse-type potential. Fundamental transitions, where $\Delta i = 1$ are common, but transitions with $\Delta i > 1$ and transitions to modes with different fundamental frequencies are also allowed due to the anharmonicity. Every molecule has different vibrational modes i with fundamental frequencies ν_0 allowing the identification of the molecule due to the uniqueness of their spectra. A molecule consisting of N atoms has $3N - 6$ different vibrational modes ($3N - 5$ for linear molecules). Vibrational modes of small linear molecules like nitrous oxide are, for instance, stretching along the axis of the molecule while the molecule remains linear throughout the vibration or bending of the molecule.

For smaller molecules, transition between rotational energy states also occur. The rotational energy levels can be described by

$$E_J = BJ(J+1) - DJ^2(J+1)^2 \tag{2.84}$$

with the rotational quantum number J and the rotational constant $B = h(8\pi^2 Ic)^{-1}$, with the mass moment of inertia I of the molecule in question and the speed of light c. The factor D called the centrifugal distortion constant takes stretching of the molecule due to centrifugal forces into account. Allowed transitions between rotational energy states are characterized by $\Delta J = \pm 1$. Linear molecules have two equal moments of inertia I with perpendicular axes, while the third one with the axis parallel to the molecule being zero. Non-linear molecules have three non-zero

moments of inertia and changes between different rotational and vibrational energy states can occur at the same time, which leads to very complex vibration-rotation spectra. One example of such a complex spectrum is that of the water molecule $H - O - H$.

Fourier Transform Infrared spectroscopy, or FT-IR spectroscopy, is an advancement of classical spectroscopy in the infrared range of the electromagnetic spectrum. Its key component is a two-beam Michelson interferometer, see Michelson [1891]. Figure 2.13 shows a schematic view of a Fourier Transform Infrared Spectrometer. The Michelson interferometer is denoted by a dashed light blue box. The interferometer divides the beam of incident, multi chromatic light into two paths with different lengths. The light is then recombined, allowing interference of the two beams of light. Technically, this is accomplished by dividing the light with a beam splitter, and sending it to two perpendicular mirrors, one of which can be moved along the axis perpendicular to its surface, the other one is fixed. The difference in the optical path length of the light being reflected

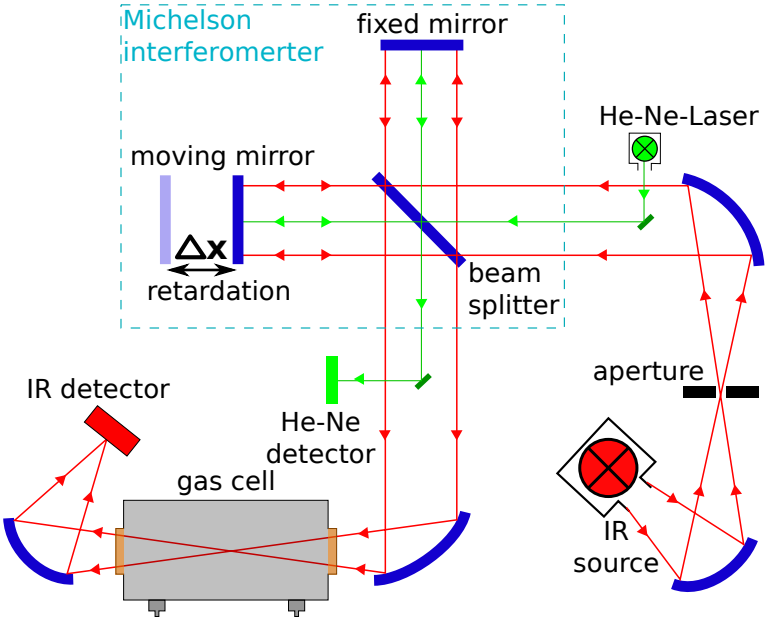

Figure 2.13.: Schematic view of a Fourier Transform Infrared Spectrometer.

by either mirror is called the retardation Δx. While the movable mirror is moving at a constant velocity of around 0.1 mm/s, the intensity $I'(\Delta x)$ is recorded with a detector. Intensity is largest at the point of zero retardation, meaning that both beams of light are in phase and interfere constructively. According to Griffiths [2007], the intensity record $I'(\Delta x)$ is composed of two parts, one constant one equal to half of the intensity of the IR source, and a modulated one. Only the modulated one, called the interferogram $I(\Delta x)$ is of interest in spectroscopic measurements. The interferogram can be linked to the light intensity $I_0(\nu)$ by

$$I(\Delta x) = 0.5 I_0(\nu) \cos(2\pi\nu\Delta x) \tag{2.85}$$

with the wavenumber $\nu = 1/\lambda$ being defined as the inverse wavelength of the light involved. Replacing $I_0(\nu)$ by the single beam spectral intensity, $B(\nu)$, and taking into account, that the source is a continuum of wavenumbers yields

$$I(\Delta x) = \int_{-\infty}^{+\infty} B(\nu) \cos(2\pi\nu\Delta x) d\nu. \tag{2.86}$$

Fourier transforming this, yields the beam intensity,

$$B(\nu) = \int_{-\infty}^{+\infty} I(\Delta x) \cos(2\pi\nu\Delta x) d\Delta x. \tag{2.87}$$

Because $S(\Delta x)$ is an even function, equation 2.87 can be rewritten as

$$B(\nu) = 2 \int_0^{+\infty} I(\Delta x) \cos(2\pi\nu\Delta x) d\Delta x. \tag{2.88}$$

So, in theory, measurement of the complete spectrum between $\nu = 0$ and ∞ at infinitely high resolution would require a retardation between 0 and ∞, which is hardly possible in reality. It can be mathematically shown that truncating the retardation leads to loss of separation of different wavelengths. Conversely, this means that lowering the required resolution of the spectrum in wavenumber space leads to limiting of the needed retardation. The spectral resolution is typically equal to the inverse of the retardation, for example, a resolution of $0.5\,\mathrm{cm}^{-1}$ is achieved with 2 cm retardation. One further method of limiting the needed retardation and thus the time it takes to acquire one spectrum is measuring asymmetrically around the point of zero retardation. Such an interferogram is referred to as a single-sided.

One fact that also limits resolution is the accuracy at which the retardation can be measured. To measure retardation as exact as possible, a laser in the visible range (typically a HeNe-laser with a light wavenumber of $\nu \approx 15\,800\,\mathrm{cm}^{-1}$) is coupled into the interferometer. The laser beam follows the signal path through the interferometer and produces its own interferogram at a separate detector. Due to the monochrome nature of the laser, the interference signal has as sinusoidal shape. The frequency of the interference signal f_{HeNe} is compared to a sinus function with the known frequency f_{ref}. If the signal frequency is lower than the reference frequency, $f_{\mathrm{HeNe}} < f_{\mathrm{ref}}$, the moving mirror needs to move faster and vice versa. This leads to a very well known speed of the moving mirror, making the retardation known with high precision. This method is called fringe counting.

Figure 2.14 shows a single-sided interferogram and the corresponding wavenumber spectrum. In the interferogram, the retardation of $\Delta x = 0$ is characterized by a very strong peak called the centerburst. The shown spectrum in figure 2.14b shows the radiation produced by the IR lamp, as well as absorption due to optics and also some signatures of water vapor (between $1400\,\mathrm{cm}^{-1}$ and $2000\,\mathrm{cm}^{-1}$) and carbon dioxide (around $2400\,\mathrm{cm}^{-1}$).

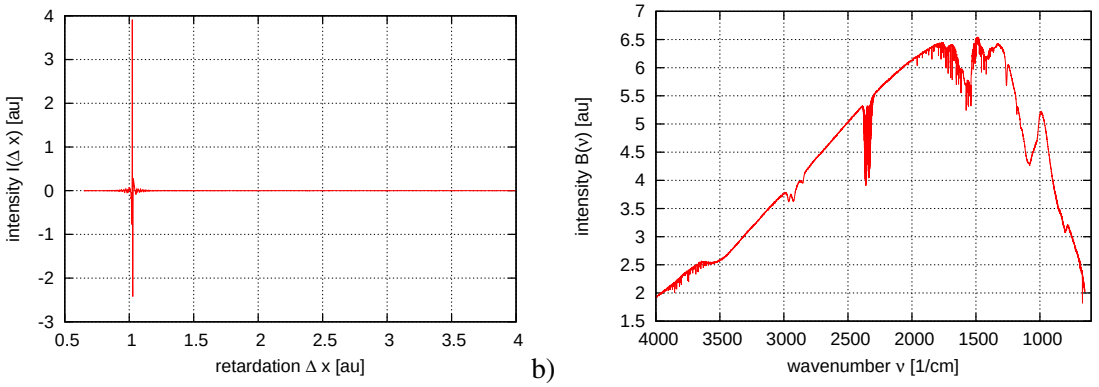

a) b)

Figure 2.14.: a) Interferogram measured with a Thermo iS10 FT-IR spectrometer. b) corresponding wavenumber spectrum measured with the same spectrometer. The wavenumber axis is inverted, which is common practice in IR spectroscopy.

A more thorough introduction to vibrational and rotational spectroscopy in the infrared range and FT-IR spectroscopy can also be found in Griffiths [2007].

2.3.2. UV Absorption Spectroscopy

UV light excites electrons within a molecule, so that they are lifted into a higher energy level, called a molecular orbital. An introduction to molecular orbital theory that describes the energy levels of electrons within molecules can be found in Atkins and de Paula [2009], for instance. Generally, electrons are easiest lifted from the highest occupied molecular orbit to the lowest unoccupied molecular orbit. Molecular electronic spectra are further complicated by molecular vibrations. As the exact position of the nuclei change due to molecular vibrations, so do the energy levels of the orbits. For each electronic state a multitude of vibrational states exist, leading to very complex spectra which typically do not have sharp peaks, but rather a smooth curve shaped peak.

Figure 2.15 shows a schematic view of a spectrometer setup used in the UV and visible range. A diffraction grating is typically used as a dispersive element to split up the light into different wavelengths. The surface of such a grating mirror is lined with parallel grooves. Incoming polychromatic is reflected in a way, that light of certain wavelengths interferes constructively at a particular angle. The main limiting factor of the spectral resolution of this spectrometer setup is the width of the slit, see Degreif [2006].

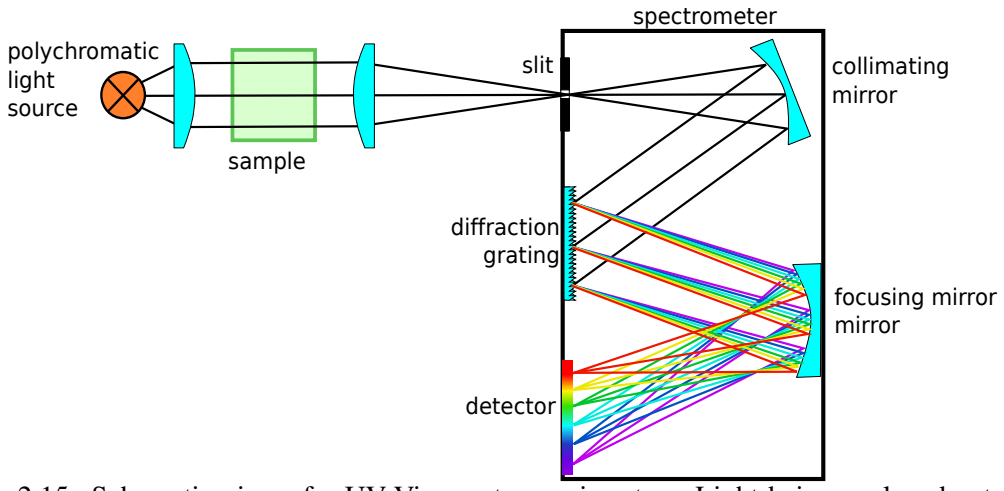

Figure 2.15.: Schematic view of a UV-Vis spectroscopic setup. Light being analyzed enters the spectrometer through the entrance slit, is collimated onto a grated diffracting element and focused on a detector.

3. Method

The experiments presented in this work were done in wind-wave tanks. In his chapter, a box model will be shown, that is used to simplify the mathematical description of the geometry of the wind wave tanks. Mass balance equations in the form of a coupled system of differential equations will be derived from this box model. Under certain conditions, these mass balance equations can be simplified allowing for a faster or easier way of obtaining gas transfer velocities. These simplifications and the derived equations will be detailed in the following sections.

3.1. The Box Model

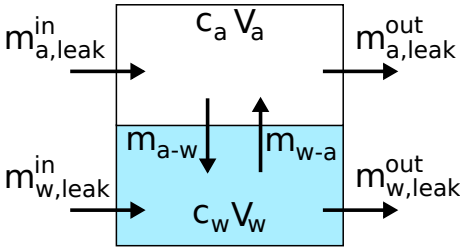

Figure 3.1.: General box model, comprising an air space V_a with an air side concentration c_a and a water space V_w with the water side concentration c_w. Both are connected through the water surface area A. Possible pathways of exchanging masses between the two boxes as well as with the outside are marked.

Figure 3.1 shows a schematic view of a wind-wave tank. Air and water space are depicted as two separate boxes with volumes V_a and V_w, respectively. Also shown are possible pathways of tracer entering or leaving the boxes. Under the assumptions, that both total air volume V_a and total water volume V_w do not change over time and that the temperature does not change, which ensures that the solubility is constant, the mass balances for small amounts of tracer in the air and water space can be found by summing up all possible pathways,

$$\text{air box}: \ \dot{m}_a = \dot{m}_{w-a} - \dot{m}_{a-w} + \dot{m}^{in}_{a,leak} - \dot{m}^{out}_{a,leak} \tag{3.1}$$

$$\text{water box}: \ \dot{m}_w = -\dot{m}_{w-a} + \dot{m}_{a-w} + \dot{m}^{in}_{w,leak} - \dot{m}^{out}_{w,leak}. \tag{3.2}$$

Symbols in the air space equation mean:

change in mass over time $\dot{m}_a$
mass per time unit that's coming from the water: $\dot{m}_{w-a} = kAc_w$
mass per time unit that's going into the water: $\dot{m}_{a-w} = kAc_a$
mass per time unit that's coming in through leaks: $\dot{m}^{in}_{a,leak} = \dot{V}_a c^{in}_a$
mass per time unit that's leaving through leaks: $\dot{m}^{out}_{a,leak} = \dot{V}_a c_a$

Symbols in the water space equation mean:

change in mass over time $\dot{m}_m$

mass per time unit that's coming from the air: $\dot{m}_{a-w} = kAc_a$
mass per time unit that's going into the air: $\dot{m}_{w-a} = kAc_w$
mass per time unit that's coming in through leaks: $\dot{m}^{in}_{w,leak} = \dot{V}_w c^{in}_w$
mass per time unit that's leaving through leaks: $\dot{m}m^{out}_{w,leak} = \dot{V}_w c_w$

Concentrations were used to substitute the masses, as they are much easier to measure. It should be noted that the first two terms on the right hand side of both equations match each other with opposite signs. This is understandable in the light of conservation of mass, that was assumed in deriving these equations. Mass leaving the air for the water, $\dot{m}_{a-w}$ (negative sign in the air side equation) must turn up in the water (positive sign in the water side equation). The values c^{in}_a and c^{in}_w denote the concentration of the tracer in the air or water, which is leaking into the respective compartments. Because in a system like a wind-wave tank, mass fluxes are hard to impossible to measure, concentrations are used instead. Using concentrations to substitute the exchanged masses, equations 3.1 and 3.2 can be modified to

$$V_a \dot{c}_a = Ak_w(c_w - \alpha c_a) + \dot{V}_a(c^{in}_a - c_a) \tag{3.3}$$
$$V_w \dot{c}_w = -Ak_w(c_w - \alpha c_a) + \dot{V}_w(c^{in}_w - c_w). \tag{3.4}$$

Figure 3.2 shows the modified box models with concentrations instead of masses.

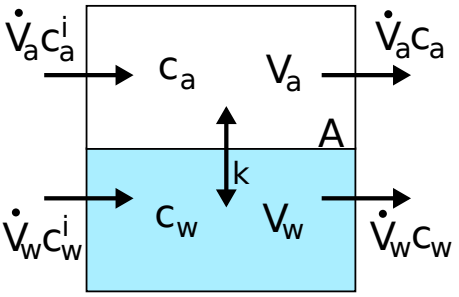

Figure 3.2.: General box model, comprising an air space V_a with an air side concentration c_a and a water space V_w with the water side concentration c_w. Both are connected through the water surface area A. Exchanged masses are expressed in the form of concentrations and volumes.

The tracers that are used in this work are neither present in the ambient air, nor in normal tap water. Therefore, when leaks are present, the input concentration is always 0, i.e. $c^{in}_a = 0$ and $c^{in}_w = 0$. This simplifies the box model equations to

$$V_a \dot{c}_a = Ak_w(c_w - \alpha c_a) - \dot{V}_a c_a \tag{3.5}$$
$$V_w \dot{c}_w = -Ak_w(c_w - \alpha c_a) - \dot{V}_w c_w. \tag{3.6}$$

A comprehensive solution of this system of equations can be found in the appendix of Nielsen [2004]. Here, only some special cases will be discussed in detail, yielding different schemes for measuring the gas transfer velocity k_w. One important parameter of the system that has to be known for most methods, is the size of the leaks. This will be addressed first.

3.2. Measuring the Leak Rate

The air side leak rate λ_a can be defined as the amount of air replaced in a given time, $\dot{V}_a$, divided by the total volume, V_a,

$$\lambda_a := \frac{\dot{V}_a}{V_a}. \tag{3.7}$$

There are two ways of measuring this leak rate, depending on the size of the leaks, which will be described in the following sections. The air side leaks are used to derive the applicable equations. The derivation for the water side is equivalent and therefore omitted here. Both methods of measuring the leak rate rely on a tracer, called leak test gas, that is insoluble in water.

3.2.1. Small Leaks: Closed System

For some of the methods that will be described in the following sections, a fully closed air space would be ideal, thus $\lambda_a = 0$. However, in reality this can hardly be accomplished, especially in larger, more complex wind-wave tanks. Therefore, the leak rate must be measured. When only small leaks are present, that are inherent to the system and can not be closed, the system is called a closed system from here on.

To measure the leak rate in a closed system, a small amount of an insoluble tracer is put into the air space at the beginning of the experiment. As the tracer is not soluble, the gas exchange terms in equation 3.5 vanish,

$$V_a \dot{c}_a = -\dot{V}_a c_a. \tag{3.8}$$

Using the definition of the leak rate 3.7 yields

$$\dot{c}_a = -\lambda_a c_a. \tag{3.9}$$

which can be solved easily,

$$c_a(t) = c_a(0) * \exp(-\lambda_a t) \tag{3.10}$$

with the starting concentration $c_a(0)$. So monitoring the concentration of the leak test gas over time and fitting an exponentially decaying function to the concentration yields the leak rate λ_a. This works best if the initial concentration decreases to a factor of about $1/e$, which can be many hours to days if the leaks are small.

Another option is to numerically derive the concentration time series with respect to time,

$$\dot{c}_a(t) = \lambda_a c_a(0) * \exp(-\lambda_a t) = \lambda_a c_a(t) \tag{3.11}$$

yielding a time resolved leak rate

$$\lambda_a(t) = \frac{\dot{c}_a(t)}{c_a(t)}. \tag{3.12}$$

However, due to the nature of numerical derivatives, the measurement of the concentration of the leak test gas must not contain too much noise.

Typical leak rates for closed systems are in the order of 0.05 h^{-1} to 0.5 h^{-1}.

3.2.2. Large Leaks: Open System

A system where an artificially produced, large leak exists is called an open system. By default, linear wind-wave tanks without an air recirculation are open systems.

It would be feasible to measure the leak rate of an open system in the same way as in a closed system. However, there are some disadvantages. Depending on the size of the leak rate, the time spent on mixing a leak test gas into the air might be in the same order of magnitude as the leak rate itself. This leads to the effect that the increase in concentration due to input is overlaid on the decrease due to leaks, thus skewing the measured leak rate towards smaller values. The leak rate can also not be monitored over the whole course of the experiment, because the leak test gas is gone too fast.

Therefore a different method of quantifying the leak for open systems is used. This method consists of a small, but well known rate of input $\dot{V}_l^i$ of pure leak test gas c_l^i=100 % = 1 000 000 ppm.

Using equation 3.5, neglecting the gas exchange terms because of the insolubility of the leak test gas and adding the input term $\dot{V}_l^i c_l^i$ yields

$$V_a \dot{c}_{a,l} = -\dot{V}_a c_{a,l} + \dot{V}_l^i c_l^i. \tag{3.13}$$

with the leak test gas concentration $c_{a,l}$ in the air space. In steady state, $\dot{c}_{a,l} = 0$, the leak rate can be calculated when the leak test gas concentration is measured,

$$\lambda_a = \frac{\dot{V}_l^i}{V_a} \frac{c_l^i}{c_{a,l}}. \tag{3.14}$$

Typical leak rates for open systems are above 20 1/h. This corresponds to an exchange of the air volume every 3 minutes or faster. Thus, a steady state is usually reached within at most 10 minutes.

3.3. Measuring Gas Transfer Velocities

In this section, two methods will be presented that were used to measure gas transfer velocities. One of the methods, the $\dot{c}_a$ method, which relies on the temporal derivative of the air side concentration, can be used in two variants, either with large leaks, or with a closed air space with technically unavoidable small leaks. While a full data set of time resolved air and water side concentration measurements are necessary for this method, the evasion method described in section 3.3.2 can be done with a measured water side concentration time series only. However, it is much slower than the $\dot{c}_a$ method described first. To derive both methods, the coupled system of differential equations, 3.5 and 3.6, will be modified.

3.3.1. The $\dot{\mathbf{c}}_\mathbf{a}$ Method

Solving the air side mass balance equation 3.5 for k_w yields

$$k_w = \frac{V_a}{A} \cdot \frac{\lambda_a c_a}{c_w} \cdot \frac{\lambda_a + \dot{c}_a/c_a}{\lambda_a} \cdot \frac{1}{1 - \alpha c_a/c_w} \tag{3.15}$$

with the leak rate $\lambda_a = \dot{V}_a/V_a$. Two variants of using this equation to calculate k_w, one with low leak rates and one with high leak rates, which is then called the controlled leakage method which will be detailed in the following sections.

The $\dot{\mathbf{c}}_\mathbf{a}$ Method with Small Leaks

For this method, the air space of the wind wave tank is closed. The small, technically unavoidable leak rate is measured by the exponentially decaying leak test gas method, described in section 3.2.1.

Figure 3.3 shows some expected air- and water-side concentration time series for a tracer with solubility $\alpha = 1$. The leak rate was chosen to be $\lambda_a = 0.2\,\mathrm{h}^{-1}$. The air side concentration at $t = 0$ was set to 0. The parameter that is varied between the three curves shown is the transfer velocity. The geometrical parameters air volume, water volume and water surface area were chosen to match those of the Aeolotron.

As expected, the air side concentration starts to increase once the experiment is started. The slope is the higher, the higher the gas transfer rate is. The increase is not linear. This is due to the fact, that tracer particles can go from the air back into the water. The more tracer particles are in

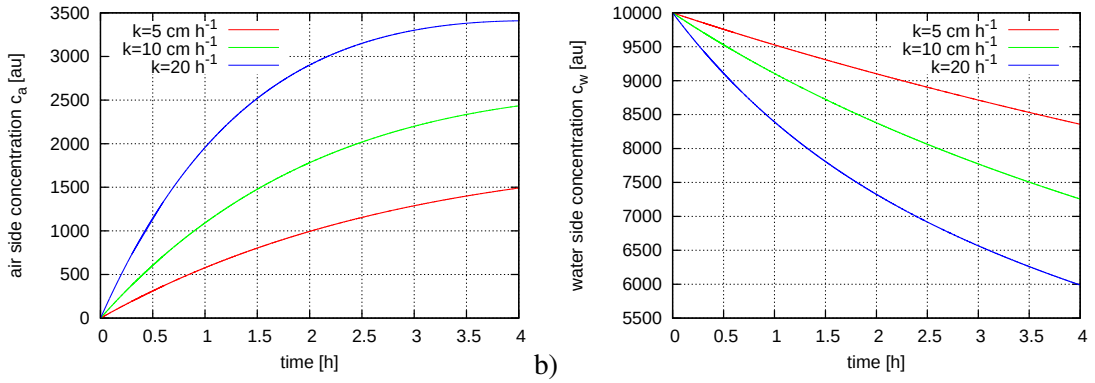

a) b)

Figure 3.3.: Exemplary concentration time series for three different transfer velocities for a closed system. a) air side concentration and b) water side concentration.

the air, the more are transfered back into the water, therefore the slope of the air side concentration flattens.

Besides applying equation 3.15 to the data, there is another option of evaluating the concentration time series to obtain the transfer velocity. Looking at the initial increase, where the air side concentration is negligible, yields

$$k_w = \frac{V_a}{A} \cdot \frac{\dot{c}_a}{c_w}. \tag{3.16}$$

To obtain this equation, small leak rate λ_a was assumed, yielding $\dot{c}_a/c_a \gg \lambda_a$. So, only measuring the slope of the air side concentration at the beginning of the experiment as well as the water side concentration yields one transfer velocity. However, this is an idealized case, because a start at an air side concentration of $c_a = 0$ can not always be experimentally achieved. For one, in the annular wind wave tank Aeolotron, the wind needs around 15 to 20 minutes to come into equilibrium with the water. Therefore, turning the wind on right at the start of an experiment is not an option. And second, the flushing of the air space to get rid of the tracer particles has a limited strength, so that with running wind generators, not all of the tracer particles can be removed from the air space, as they are fed back into the air from the water as they are removed. Also, with this method only one transfer velocity value is measured per wind speed.

Figure 3.4 shows, that the leak rate does not influence the initial increase of the concentration.

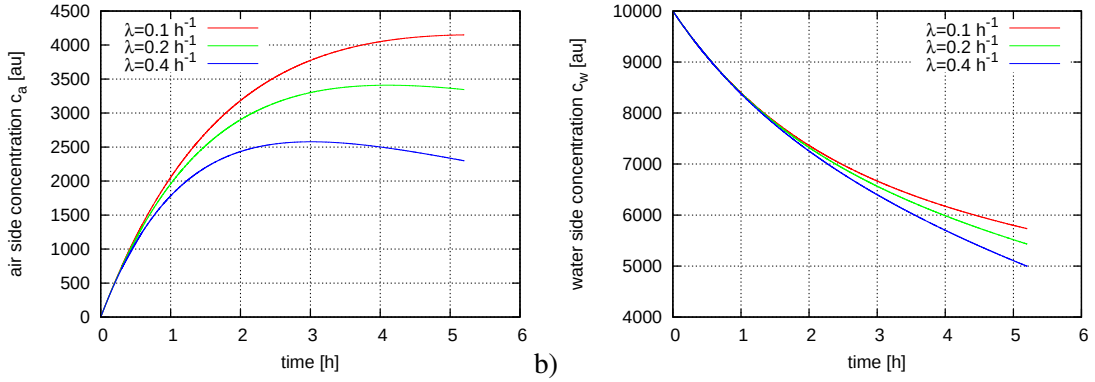

a) b)

Figure 3.4.: Exemplary concentration time series for transfer velocity $k = 20$ cm/h for a closed system for three different small leak rates. a) air side concentration and b) water side concentration.

If the concentration sampling rate is high enough, the method can be modified to yield better

statistics. This also eliminates the need for a zero air side concentration at each new wind speed setting. The idea for an increased statistics is, to calculate the numerical derivative of the air side concentration with respect to time, and insert all measured values into equation 3.15 to obtain a time resolved transfer velocity. This also eliminates the need for a negligible leak rate.

Advantages of the $\dot{c}_a$ method with small leaks are:

- speed: with a high enough sampling rate (one concentration measurement every 30 seconds is sufficient), known leak rate and when $\dot{c}_a$ is not too small, a value of k_w can be measured within a few minutes.
- statistics: if a high rate of gas concentration measurements can be achieved, many single measurements of the gas transfer velocity under the same conditions are possible within a short time, improving statistical errors
- homogeneity: As there is no or very little fresh air input, the concentration can be assumed to be well mixed in the air space.

Disadvantages are:

- calibration: An absolute calibration of the concentration measurements is necessary.
- transient conditions: it is not feasible to measure with slowly changing wind speed.
- leak rate: the leak rate has to be known or preferably measured. Depending on the time constant, measuring the leak rate takes up to a few hours.

The Controlled Leakage Method

Another version of this method is the so called controlled leakage method that was used by [Degreif, 2006]. An artificially large leak in air space is opened and the air space is continuously flushed with fresh air. The leak rate is monitored with a continuous input of a leak test gas as described in section 3.2.2.

Figure 3.5 shows exemplary concentration time series with the same parameters as in section 3.3.1, with the exception of the leak rate which was set to a higher value of $\lambda_a = 30\,\mathrm{h}^{-1}$.

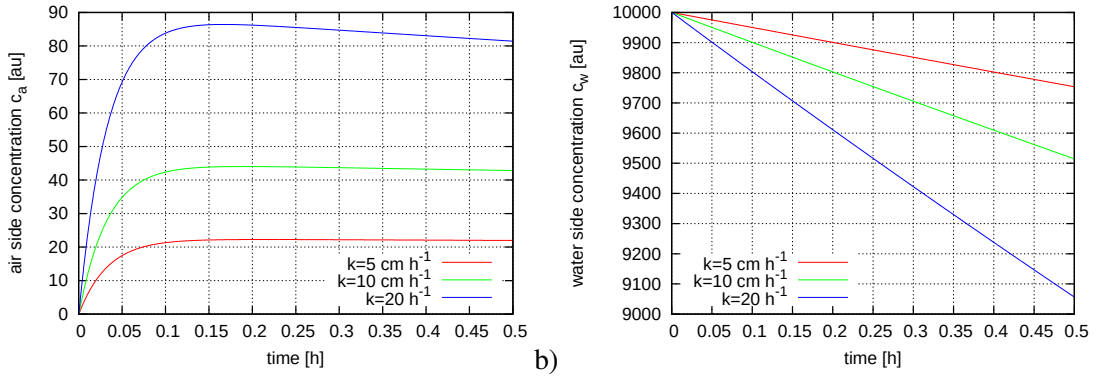

a) b)

Figure 3.5.: The same as figure 3.3, but for an open system. Note that the time axis is much shorter than in figure 3.3.

Here, a pseudo-equilibrium is reached quite fast, to be more precise, in the time scale given by the leak rate. The pseudo-equilibrium develops between the amount of tracer coming out of the water and the amount leaving through leaks, with the air side concentration being almost constant. It is not constant on longer time scales, because the water side concentration decreases over time,

but in the time scale given by the leak rate it can be seen as constant, therefore $\dot{c}_a = 0$. Using this, equation 3.15 simplifies to

$$k_w = \frac{V_a}{A} \cdot \frac{\lambda_a c_a}{c_w} \cdot \frac{1}{1 - \alpha c_a / c_w}. \tag{3.17}$$

In most cases, the air side concentration is also much smaller than the water side concentration, $c_w \gg c_a$, and if, in addition, the solubility is small $\alpha < 1$, the last term can be neglected yielding

$$k_w = \frac{V_a}{A} \cdot \frac{\lambda_a c_a}{c_w}. \tag{3.18}$$

This means, that just from the ratio of concentrations in air and water, as well as the leak rate, the transfer velocity can be calculated.

Advantages of the controlled leakage method are:

- speed: with a high enough sampling rate (one concentration measurement every 30 seconds is sufficient), known leak rate and when $\dot{c}_a$ is not too small, a value of k_w can be measured within a few minutes
- statistics: if a high rate of gas concentration measurements can be achieved, many single measurements of the gas transfer velocity under the same conditions are possible within a short time, improving statistical errors
- transient conditions: it is feasible to measure with slowly changing wind speed
- calibration: no absolute calibration is necessary, as only ratios of concentrations are needed
- leak rate: in an open system the leak rate can be measured relatively fast

The disadvantage is:

- homogeneity: the concentration must be distributed very homogeneously in the air and water space. Because all concentration measurements are point measurements in this work, inhomogeneities lead to wrong measured c_a/c_w ratios and therefore wrong transfer velocities

The major advantage of the method becomes obvious when slowly changing wind speed conditions are studied. To show the application of the method in a case of changing wind speeds, a numerical model was used to calculate expected concentration time series. The model is mathematically described in the appendix in section A.1. Under the assumption of a slowly changing wind speed in the Aeolotron, the true transfer velocity might behave like shown in figure 3.6. The wind was first increased, kept constant for approximately 20 minutes and was then decreased again, yielding the same shape for the transfer velocity. This time series of the transfer velocity is used as the ground truth for a further study of the controlled leakage method in this section.

Figure 3.7 shows the corresponding air side and water side concentration time series for three different large leak rates. With increasing transfer velocity, the air side concentration also increases. It increases faster, the lower the leak rate is. This is expected, as with a lower leak rate more tracer can accumulate in the air space.

The air and water side concentrations as well as the leak rates can then be used in equation 3.15 to calculate transfer velocities. Figure 3.8 shows the calculated transfer velocities for the three different leak rates, as well as the true value that was used to calculate the expected concentrations. A slight lag of the measured values can be seen, leading to a hysteresis like shape, when the measured transfer velocities are plotted against the true transfer velocities. However, on average the true transfer velocities are reproduced well. The hysteresis effect can be reduced by ensuring only slow changes in wind speed compared to the time scale given by the leak rate as well as a high leak rate.

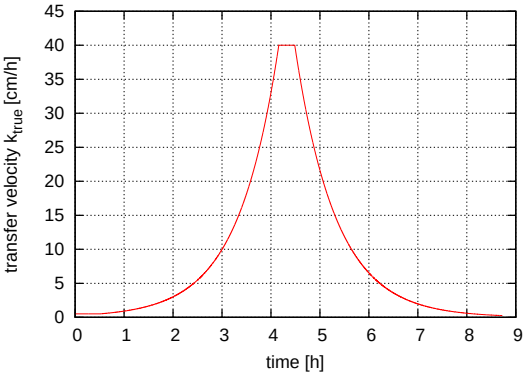

Figure 3.6.: Hypothetical, exponentially increasing and then decreasing transfer velocity used as the ground truth for the considerations in this section.

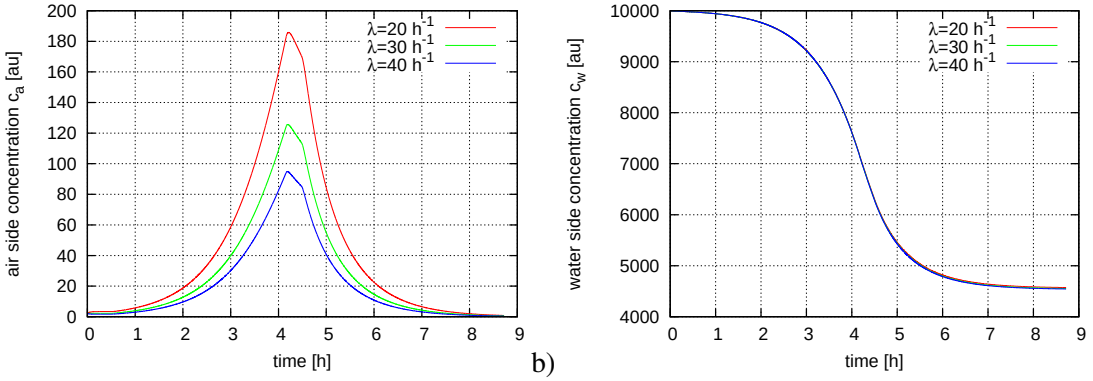

Figure 3.7.: Time series of a) the air side and b) the water side concentration, when the transfer velocity in figure 3.6 is used as the true velocity. The parameter varied was the leak rate.

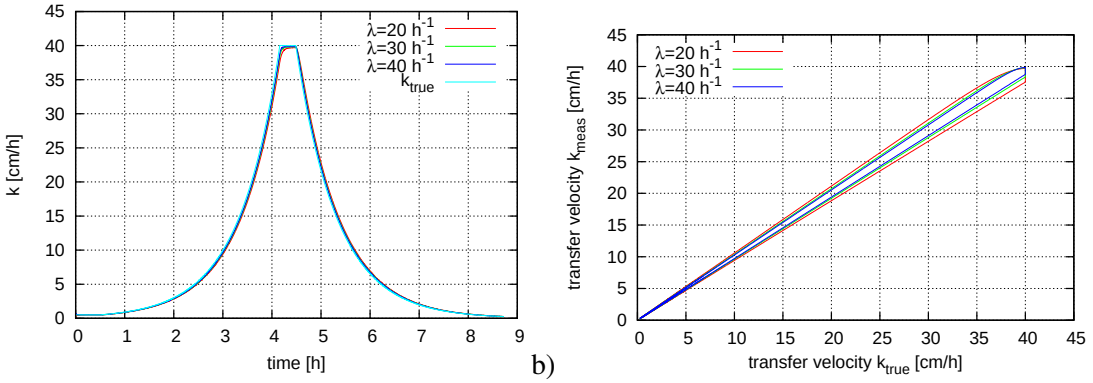

Figure 3.8.: Calculated transfer velocities from the concentration time series in figure 3.7 as well as the true transfer velocities from figure 3.6, plotted against a) time and b) the true transfer velocity. A hysteresis effect is visible, that reduces with increasing leak rate.

3.3.2. The Classic Evasion Method

Under the condition of a negligible air side concentration c_a and small solubility α, i. e. $\alpha c_a \approx 0$, the system of differential equations, 3.5 and 3.6, decouples. The water side equation simplifies to

$$V_w \dot{c}_w = -A k_w c_w - \dot{V}_w c_w. \tag{3.19}$$

The solution of this differential equation yields, that the water concentration decreases exponentially, when an initial concentration of $c_w(0)$ has been present in the water at the beginning of the experiment,

$$c_w(t) = c_w(0) * e^{\left(-(k_w * \frac{A}{V_w} + \frac{\dot{V}_w}{V_w}) * t\right)}. \tag{3.20}$$

The time constant τ of this equation is defined as

$$\frac{1}{\tau} := \lambda = k_w * \frac{A}{V_w} + \frac{\dot{V}_w}{V_w}, \tag{3.21}$$

with λ being the response rate of the system.

Except the gas transfer velocity k_w, all other variables in equation 3.21 are known or can be measured during the experiment. Therefore, first dissolving some tracer in the water and then monitoring the water side concentration during an evasion experiment allows the measurement of k_w.

Advantages of this method are:

- calibration: no absolute calibration of water side concentration measurement is necessary, relative concentration measurements are sufficient
- setup: no air side concentration measurement is needed
- homogeneity: because only temporal changes in concentrations are needed, spatial inhomogeneities in the concentration are unproblematic, as long as the position and relative size of the inhomogeneities do not change over time.

Disadvantages are:

- speed: the method is very slow. Ideally, the initial water side concentration has to decrease to a factor of $1/e$, which can take many hours.
- statistics: due to the slow measurement of the transfer velocity, only very few repetitions of the same conditions are feasible within the course of a measuring campaign.
- transient conditions: wind speed must remain constant throughout the experiment, transfer velocities during changing wind speed conditions can not be measured.

3.4. Measuring the Solubility

For many tracers, the solubility α is usually not known with sufficient precision under given experimental conditions. To measure the solubility, a small change must be made to the measuring scheme. When the water concentration c_w is not measured directly, but the concentration in a parcel of air, that is in solubility equilibrium with the water, see Henry's law equation 2.40,

$$c'_w = \frac{c_w}{\alpha} \tag{3.22}$$

is measured, the system of equations, 3.5 and 3.6 can be used to calculate α by eliminating k_w,

$$\alpha = -\frac{V_a}{V_w} \frac{\dot{c}_a + \lambda_a c_a}{\dot{c}'_w} \tag{3.23}$$

That means, that in any experiment when

- the tracer's concentration in the air bulk, c_a is measured,
- the temporal development of the air side concentration, $\dot{c}_a$ is measured,
- the temporal development of the tracer's concentration in a parcel of air that is in equilibrium with the water bulk, $\dot{c}'_w$ is measured,
- the air side leak rate, λ_a is measured, and
- the wind-wave tank's air and water volumes V_a and V_w, respectively, are known,

the solubility α can be measured alongside k_w.

Under the assumption, that the leak rate λ_a, as well as the air side concentration c_a is small, i. e. $\lambda_a c_a \ll 1$, equation 3.23 can be simplified,

$$\alpha = -\frac{V_a}{V_w}\frac{\dot{c}_a}{\dot{c}'_w} \tag{3.24}$$

No absolute concentration measurements are necessary, only the temporal changes in the ratio of air and water side concentrations are needed.

4. Experiments

The Experiments performed in this work were done in two different wind-wave tanks, which will be described first. The reasons for the choice of tracers and their physical properties, as well as the experimental conditions, will be discussed in sections 4.2 and 4.3.

It was chosen not to measure concentrations in the water directly, but rather in a small volume of air, that is equilibrated to the water by using an artificial lung. The reasons for this choice as well as an argument for the feasibility of this method are shown in section 4.5.

4.1. The Wind-Wave Tanks

Two distinctly different wind-wave tanks were used in this study. One, the Heidelberg Aeolotron, has an annular shape, the other one, the Kyoto high speed wind-wave tank is linear. Both will be discussed in this section.

4.1.1. The Heidelberg Aeolotron

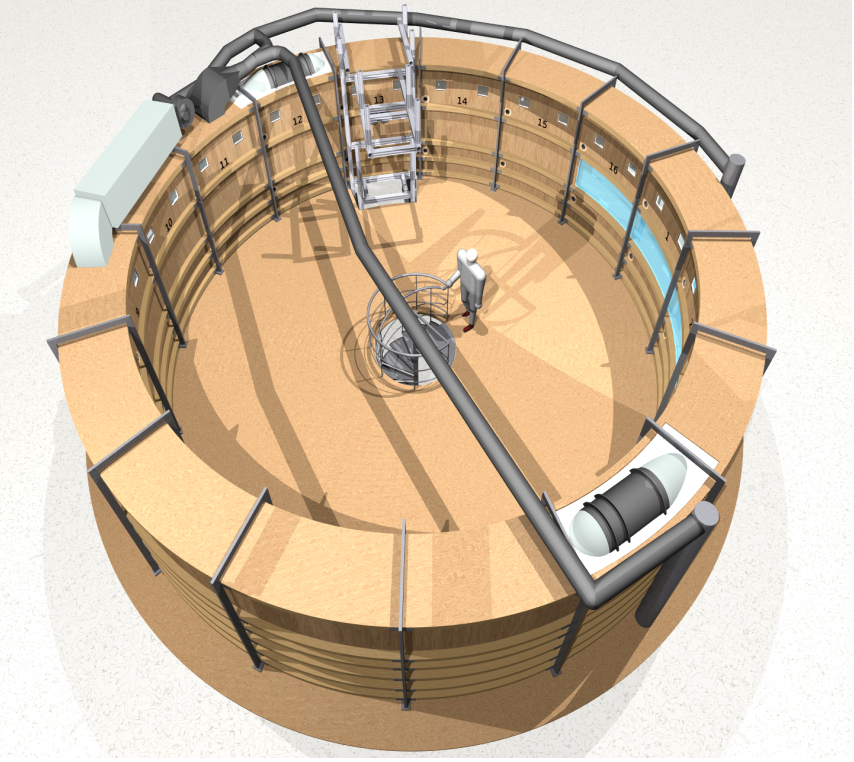

Figure 4.1.: Rendered view of the Aeolotron.

The Heidelberg Aeolotron (see fig. 4.1) has a ring shaped water flume of approximately 60 cm width, 2.41 m height and a circumference of 27.3 m at the inner wall. The water depth during experiments is usually close to 1.0 m with a volume of about 18.0 m^3. In the air space, encompassing a volume of about 24.4 m^3, wind is generated by two axial fans mounted into the ceiling of the

tank with 180 degrees separation between the fans. The highest possible wind speed with a filling of 1.0 m of water is approximately $u_{\mathrm{ref}} = 10.5$ m/s. The Aeolotron is thermally insulated, allowing heat exchange measurements. Pure water is used for the experiments. It can be operated with opened or closed air space, meaning that either fresh air is pushed through (open) or not (closed). In closed mode, there are some residual air leaks which depend on the wind speed. For higher wind speeds up to 30 % of the air is exchanged with the surrounding room within one hour. For lower wind speeds this leak rate is smaller.

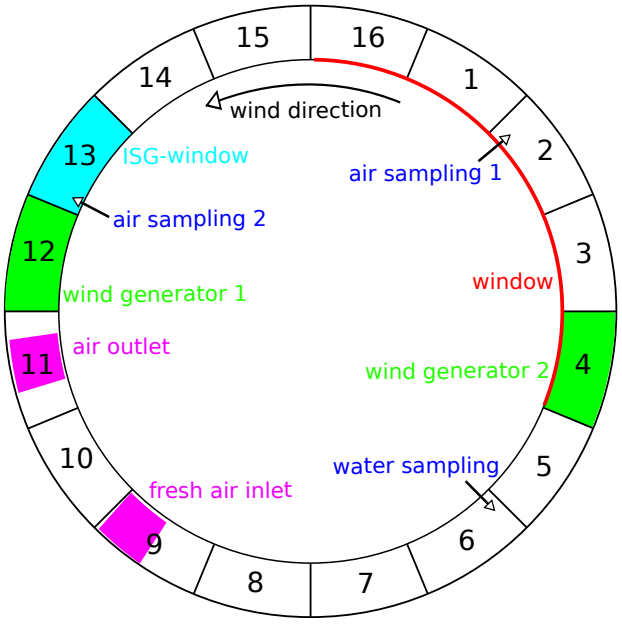

Figure 4.2.: Schematic top view of the Aeolotron showing the segment numbering scheme used throughout this work, as well as positions of the wind generator fans, sampling locations as well as the fresh air in- and outlets. The ISG-Window is a large window in the bottom of the water flume.

To orient oneself in the annular geometry, the Aeolotron can be parted into 16 radial segments, see figure 4.2. They are numbered from 1 to 16 in clockwise direction when seen from above, with the wind blows in counterclockwise direction. Each segment has one sampling location in the air space and one in the water space. A detailed description of all sensors mounted in the Aeolotron as well as the technical data of the wind generator and the fresh air supply can be found in [Richter, 2009].

4.1.2. The Kyoto High Speed Wind-Wave Tank

The Kyoto high speed wind-wave tank has a linear flume shape, see fig 4.3. The water flume is 80 cm wide, has a total length of 15.7 m with 12.9 m being exposed to the wind. The total height is 1.6 m, with roughly the lower, i. e. up to 0.8 m being usually filled with water. The wind is generated by a radial fan. The maximum wind speed, that can be reached, is $u_{10} = 67$ m/s, corresponding to a strong category 4 hurricane. Before the wind enters the air side of the tank, it is pushed through a honeycomb structure to minimize large eddies. The air is taken from the room surrounding the wind-wave tank and pushed out of the building after it was blown over the water. There is no option for a closed air circulation.

There is a large water tank available, which is connected to the wind-wave flume by two pipes. One such pipe attaches to the downwind end of the wind-wave flume, the other one to the upwind end. In each pipe a pump is mounted, such that one pump draws the water out at the downwind

end of the flume and into the water tank, the other pump draws the water out of the tank and into the upwind end of the wind-wave flume. The volume of the tank, which is mounted 36 cm lower than the wind-wave flume can be calculated as

$$V_t = 2.4\,\mathrm{m} * 1.5\,\mathrm{m} * (h_w + 0.36\,\mathrm{m}) \tag{4.1}$$

with the water height measured in the wind-wave flume, h_w.

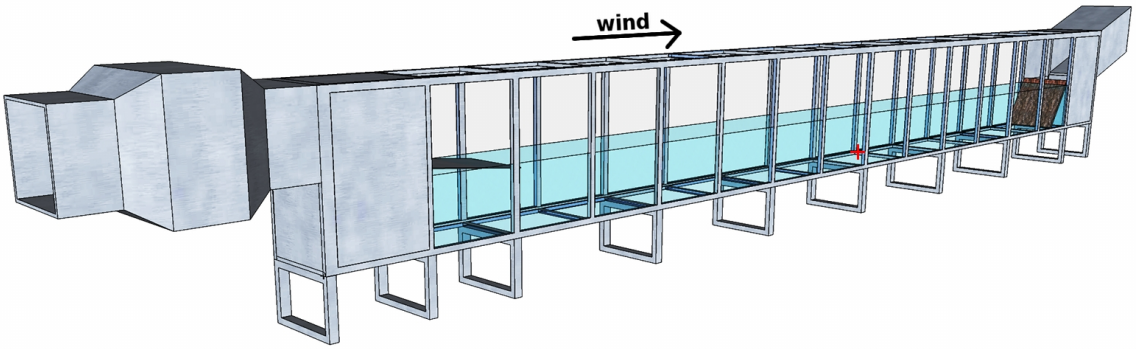

Figure 4.3.: Rendered view of the Kyoto high speed wind-wave tank. Not shown is the large radial blower (to the left) as well as piping and the external tank. The red cross marks the approximate water sampling location.

During experiments, water that is lost due to spray at the air outlet, can be replaced by water coming straight from a tap. The maximum amount that can be replaced lies in the order of 160 l/min. As up to 190 l/min are lost at the highest wind speed, the water tank acts as a buffer, providing the missing amount of water between the water lost and the maximum replacement capacity of the tap.

4.1.3. Comparison of the Wind-Wave Tanks

Table 4.1 lists the geometric and physical properties of both wind-wave tanks.

	Kyoto	Aeolotron
maximum wind speed u_{10} [m/s]	67	21
water depth [m]	0.8	1.0
total height [m]	1.6	2.4
water volume [m^3]	10.0	17.9
air volume [m^3]	10.0	24.4
water surface area [m^2]	10.3	17.9

Table 4.1.: Comparison of the properties of the Kyoto high speed wind-wave tank and the Heidelberg Aeolotron.

An advantage of the rather unusual annular shape of the Aeolotron is the virtually unlimited fetch (the length that wind can interact with the water). Wind and waves can interact long enough to reach a steady state. Also, the wave field looks identical on all of the water surface. On the water surface of a linear wind-wave tank, at the position where the wind enters, there are no waves. Further along in wind direction there are small capillary ripples, which may grow in height and wavelength into the capillary-gravity and gravity regime until they encounter the wave absorber at the end of the tank. Usually, at least at higher wind speeds, the length of linear tanks is not

sufficient for the waves to reach a steady state. Also, mass balance methods integrate the transfer of gases over the whole water surface, which has different conditions along the fetch of linear wind-wave tanks. With the conditions being the same at all of the water surface for the annular tank geometry, this is not a problem there. The main disadvantage of the annular shape of the Aeolotron are centrifugal forces which prevent the formation of a logarithmic wind profile which is present over the ocean. The wind profile in the Aeolotron is constant with height, but varies from slower wind speed near the inner wall to larger wind speed at the outer wall, see [Nielsen, 2004]. Also, helix-like secondary currents develop in the air and water space. A very illustrative explanation of this effect can be found in Weißer [1980].

In a linear wind-wave tank, a logarithmic wind profile, see section 2.2.2, can develop near the water surface.

4.2. Chemicals

In this section, the tracers used in the Aeolotron and the Kyoto high speed wind-wave tank are characterized. Reasons for the choice of the tracers are given, and the surfactant used in the Aeolotron is described.

4.2.1. Tracers Used in the Aeolotron

The tracers that were used were chosen by the following criteria:

- low solubility (for the leak test gas: insolubility)
- differing diffusivity
- high extinction coefficient in IR range
- distinctly different IR spectra
- not present in air
- non-toxic in concentrations used in the experiments

The chemical group of fluorinated hydrocarbons matches these criteria. Chosen tracers were: trifluoromethane, pentafluoroethane, and as the leak test gas, tetrafluoromethane. As a well studied reference, nitrous oxide was also chosen. The physical properties diffusion constant D in water, dimensionless solubility α, wavenumber at which the maximum absorption takes place $k_{\epsilon,\max}$, molar mass M and kinematic viscosity η of the tracers are given in table 4.2.

Tracer	Formula	D @ 25^{o}C 10^{-5}cm^2/s	α @ 20^{o}C	$k_{\epsilon,\max}$ cm^{-1}	M g/mol	η @ 25^{o}C 10^{-6}Ns/m^2
Nitrous Oxide	N_2O	1.91[1]	0.59[2]	2235[6]	44.01	14.98[7]
Trifluoromethane	CHF_3	1.53[1]	0.33[3]	1152[6]	70.01	14.77[7]
Pentafluoroethane	C_2HF_5	1.12[1]	0.184[4]	1208[6]	120.00	12.97[7]
Tetrafluoromethane	CF_4	1.42[1]	0.0052[5]	1283[6]	88.0	17.41[7]

Table 4.2.: Chemical and physical data of the tracers used in the Aeolotron. 1: Yaws [1995]. 2: Young [1981]. 3: Wilhelm et al. [1977]. 4: Yaws [1999]. 5: Jähne [2012] 6: own measurements. 7: material safety data sheet by manufacturer.

4.2.2. Surfactant used in the Aeolotron

Triton X-100, $C_{14}H_{22}O(C_2H_4O)_n$, is the nonionic, soluble surfactant, which was used in the Heidelberg Aeolotron. Figure 4.4 shows the structural formula of the Triton molecule. The molecule

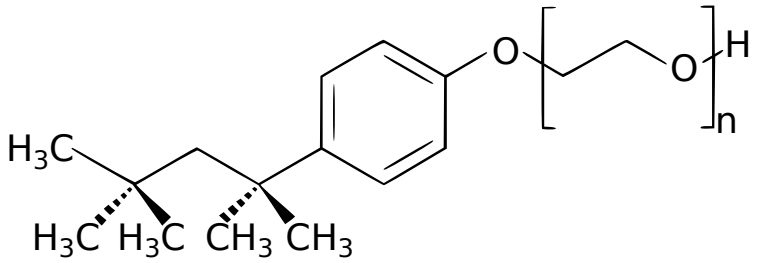

Figure 4.4.: Structural formula of the surfactant Triton X-100 used in the Heidelberg Aeolotron.

is composed of a polyethylene oxide chain with an average of $n = 9.5$ ethylene oxide units and an aromatic hydrocarbon group. The hydrocarbon group, identifiable by the characteristic benzene ring in the structural formula, is the hydrophobic part, while the polyethylene oxide chain is the hydrophilic part.

The manufacturer Dow Chemicals lists the molar weight as $m_M = 647$ g/mol. For the light surfactant case, 0.6 g of Triton X-100 was mixed into the water, for the heavy surfactant cases the amount was 3 g.

4.2.3. Tracers used in the Kyoto High Speed Tank

Unfortunately, transporting the large and heavy FT-IR spectrometers, adsorption dryer and pressurized air generator to Japan to conduct measurements in the Kyoto high speed wind-wave tank was not feasible. Therefore, the lighter, much more compact UV-absorption setup was chosen. Also, the aim of the experiments was different. Therefore, different tracers were used. They were chosen by the following criteria:

- low solubility
- similar diffusivity
- high extinction coefficient in UV range
- distinctly different UV spectra
- not present in air
- non-toxic in concentrations used in the experiments

Table 4.3 shows the molecular mass M, solubility α (own measurements), diffusivity in water D_w and the light frequency at which the extinction coefficient has a maximum, $\nu_{\epsilon,\max}$ of the two tracers that were used in this experiment, hexafluorobenzene and 1,4-difluorobenzene. Also shown is CO_2 for comparison.

Figure 4.5 shows the absorption spectra of the tracers used in this study in the UV range in air. The main peak above a wavelength of 210 nm is scaled to an absorbance of 1. Because of the strong overlap and similarity of both spectra in the region below 210 nm, as well as low intensity of the incident light into the absorption cell, this spectral region is disregarded in the analysis.

Name	M	α at 20^{o}C	D_w at 25^{o}C	$\nu_{\epsilon,\max}$
	g/Mol		10^{-5} cm^2/s	nm
Hexafluorobenzene	186.1	1.0 [1]	0.85[4]	230[5]
1,4-Difluorobenzene	114.1	3.08[2]	0.94[4]	267[5]
Carbon Dioxide	44.01	0.83[3]	1.89[4]	n.a.

Table 4.3.: Molar mass, solubility, diffusivity and wavelength at the maximum of the extinction coefficient of tracers hexafluorobenzene and 1,4-difluorobenzene. Also shown is CO_2 for comparison. 1: mole fraction solubility from Freire et al. [2005], vapor pressure from Ambrose et al. [1990]. 2: [Yaws and Yang, 1992] 3: [Degreif, 2006]. 4: [Yaws, 1995]. 5: own measurements

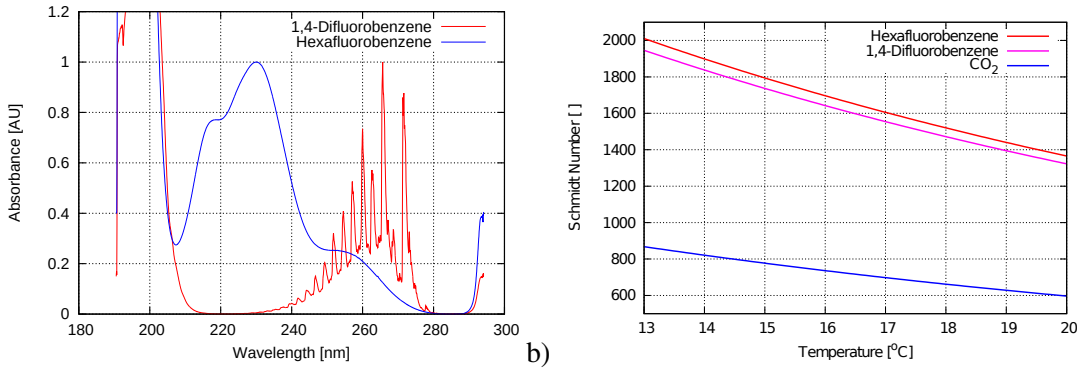

a) b)

Figure 4.5.: a) Absorption spectra of hexafluorobenzene and 1,4-difluorobenzene in the UV range in air. b) Schmidt numbers of the tracers used as well as the Schmidt number of CO_2 for comparison.

The temperature dependency of the diffusion coefficients of the tracers can be calculated by the empirical equations

$$\log_{10} D(T) = -1.5124 + \frac{-1061.426}{T[K]} \qquad \text{(hexaflurorbenzene)} \tag{4.2}$$

and

$$\log_{10} D(T) = -1.4817 + \frac{-1057.362}{T[K]} \qquad (1,4-\text{diflurorbenzene}), \tag{4.3}$$

with temperature measured in Kelvin and D in cm^2/s, see [Yaws, 1995].

The Schmidt number was calculated by $Sc = \nu/D$, the ratio between kinematic viscosity of water taken from [Kestin et al., 1978] and the diffusion coefficient. The temperature dependency of the Schmidt number of both tracers is shown in figure 4.5b.

4.3. Experimental Conditions

In the following sections, the conditions are listed, at which the experiments were performed in the Heidelberg Aeolotron and the Kyoto high speed wind-wave tank. Conditions at the Aeolotron included the addition of various amounts of a surfactant, which is described in section 4.2.2. The conditions set at the Kyoto high speed tank will follow in section 4.3.2.

4.3.1. Aeolotron

Table 4.4 lists the conditions used during measurements in the Heidelberg Aeolotron. The frequency that was set at the frequency converter which is driving the wind generators is denoted by f_{wind} which was the primary parameter that was varied from experiment to experiment. Conditions marked with an 'x' were measured. Also given are typical reference wind speeds u_{ref}, wind speed at 10 m height u_{10} and friction velocity u_*. The amount of surfactant mixed into the roughly 18.000 l of water is labeled m_s. This was the second parameter of interest that was varied. Also given is the mean bulk water temperature T_{mean} as well as the water height h_w measured in a transparent pipe that is connected to the water space.

Date	f_{wind} [Hz]									m_{s}	T_{mean}	h_w
Y M D	3	5	7	9	12	16	22	26	29	g	°C	cm
11 02 18	x	x	x	x	x	x	x		x	0	19.45	100.0
11 02 22	x	x	x	x	x	x	x		x	0	18.81	100.2
11 02 24	x	x	x	x	x	x	x	x		0	19.56	99.6
11 03 01	x	x	x	x	x	x	x		x	0	19.58	100.0
11 03 03	x	x	x	x	x	x	x		x	0.6	19.88	100.3
11 03 08		x	x	x	x	x	x		x	3.0	19.81	100.2
11 03 08		x	x	x	x	x	x		x	3.0	20.00	99.9
cond. #	1	2	3	4	5	6	7	8a	8			
u_{ref} [m/s]	0.74	1.41	2.05	2.66	3.61	4.80	6.45	7.51	8.26			
u_{10} [m/s]	1.15	1.71	2.43	3.27	4.81	7.05	10.6	13.2	15.0			
$u_{*\mathrm{w}}$ [cm/s]	0.108	0.165	0.241	0.336	0.523	0.825	1.37	1.80	2.14			

Table 4.4.: Experimental conditions used in the Aeolotron.

On the third measuring day, the wind speed at the last condition was erroneously set to a wrong value. For the conditions with the larger surfactant amount of 3 g the first condition was omitted. The surfactant concentration for the lighter surface film cases was 0.052 μmol/l, which corresponds to 0.6 g in 18.000 l and 0.26 μmol/l for the heavy surfactant cases labeled with an absolute amount of 3 g.

Figure 4.6 shows schematic time series of a typical experiment. On the evening before the experiments took place, the tracers were mixed into the water using a total of 4 oxygenators. Water was pumped through each of the oxygenators at a rate of approximately 1000 l/h. The gas outlet of the oxygenators was closed to ensure that all the gas entering the oxygenator was mixed into the water. The gas flux was set as high as possible, but so low that no gas bubbles were seen forming in the piping behind the oxygenators. The flow rates of the gases were not measured. Three of the oxygenators were used exclusively for the tracer nitrous oxide, the remaining one was used first for trifluoromethane, and afterwards for pentafluoroethane. During the gas input that took around 1.5 h, the Aeolotron's counter current generator was used to mix the water. While the gases were mixed into the water, the wind was turned off, and the air space was continuously flushed with fresh air to prevent any gas buildup. For the experiments with surfactants, these were also mixed into the water during gas input.

Over night, the water, that was moved in a circular fashion in upwind direction during the mixing, was allowed to settle down. As the last step in the preparation phase before the clean case experiment was started, the water surface was skimmed to clean off surface films. To do this, a small barrier with a channel is mounted between the walls perpendicularly to the wind direction, and the wind is turned on at a low wind speed (around 3 m/s). The wind pushes the water surface including any surfactants over the barrier into the channel. A pump continuously empties the channel and drains the water contaminated with surface films. For the experiments

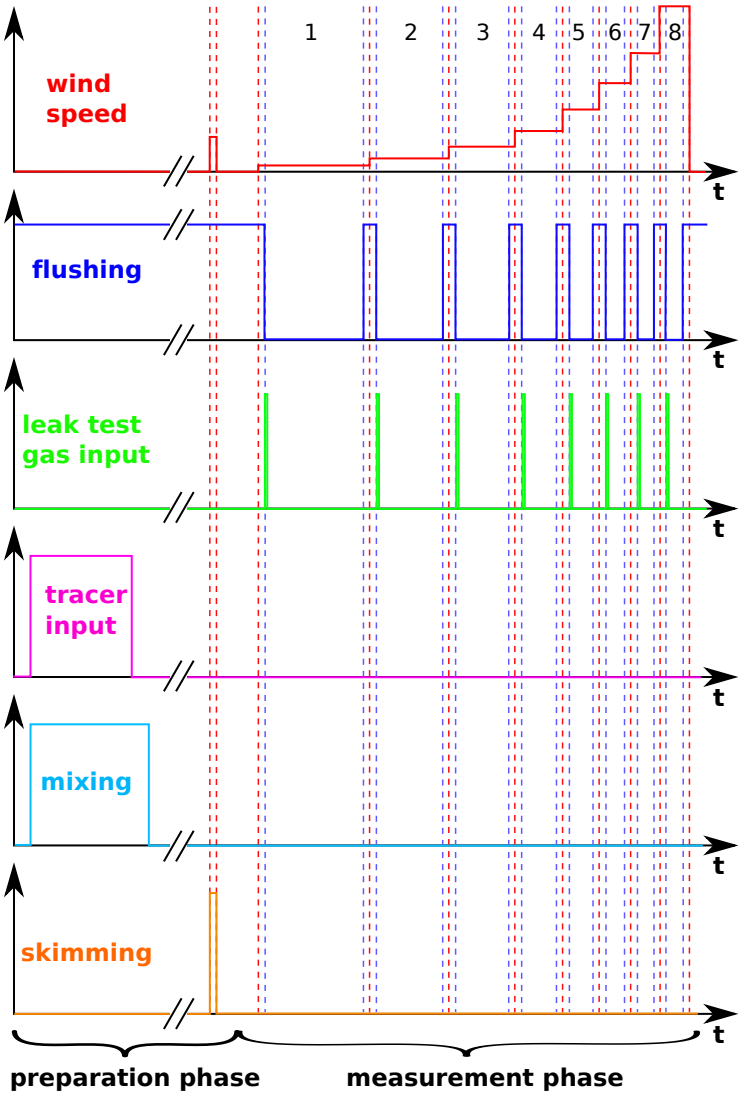

Figure 4.6.: Schematic time series of the experimental conditions. See text for description.

with surfactants, the water surface was not skimmed.

After the water settled down again after skimming, the actual experiment was started. At this point all data acquisition was started. The wind was set to the first (lowest) wind speed condition marked with 1 in figure 4.6. The flushing of the air space was turned off and the air space was closed. Immediately after turning off the flushing, a few ten milliliters of the leak test gas was pumped into the air space. After approximately 4.5 hours the flushing was turned on again, flushing all accumulated gases out of the air space for about 15 minutes. Then, the next condition # 2 was started by increasing the wind speed. After waiting 15 more minutes to let the wind build up the wave field for the new condition, the flushing was turned off again, followed by the input of the leak test gas. This scheme was repeated for all of the higher wind speed conditions, with decreasing waiting times in the closed phases.

After the last condition, the water was drained from the Aeolotron into tanks. Two tank fillings of water were available during the campaign, they were used in alternation. While an experiment was taking place with one filling of water being in the Aeolotron, the other filling of water was cleaned by repeatedly pumping it through carbon filters.

4.3.2. Kyoto High Speed Wind-Wave Tank

During 14 days, a total of 21 experiments at 9 different wind speeds were conducted. Table 4.5 lists the conditions that were used during the measurement campaign at the Kyoto high speed wind-wave facility, sorted by date.

The wind generator's rotational number f_{fan} was set and kept constant for each condition. The free stream wind speed u_{inf}, the air sided friction velocity u_* as well as the wind speed at a height of 10 m u_{10} that is commonly used as a reference was not measured directly but taken from a table kindly provided by the Japanese colleagues. Water height h_w was measured at the wind inlet before and after each experiment with no wind and no waves. The mean value is given here. For the highest wind speed conditions, $f_{\mathrm{fan}} = 800$ rpm, the external tank was used as a buffer to keep the water level constant inside the wind-wave tank. This was necessary, because the rate of the inflow of fresh water λ_w that was used to replace the water lost from the system due to spray was not high enough. Therefore, the total volume of the water decreased, while the water height within the wind-wave tank was stable. The average water temperature T_{mean} was measured using a PT-1000 sensor with a hand held device (*GMH-3710* manufactured by *Greisinger*) read out by a computer every 3 seconds in the gas extraction bypass, see section 4.5. The flow rate of the water replacing the water lost due to spray λ_w is also listed. This number was read from a flow sensor mounted into the water supply pipe.

Date	f_{fan}	$u_{*,a}$	u_{inf}	u_{10}	h_w	λ_w	T_{mean}	notes
Y M D	rpm	m/s	m/s	m/s	cm	l/min	^oC	
11 10 27	600	2.69	34.75	56.4	73.6	14.5	17.5	
11 10 28	400	2.08	22.17	40.7	73.55	0	17.1	
11 10 28	600	2.69	34.75	56.4	73.4	14	17.1	
11 10 31	200	0.67	10.29	16.7	73.3	0	18.3	
11 10 31	500	2.36	28.47	48.0	73.3	3.5	17.5	
11 11 02	300	1.49	16.26	29.8	75.8	0	19.9	
11 11 02	500	2.36	28.47	48.0	74.8	0	18.5	
11 11 04	100	0.24	4.72	7.0	74.0	0	19.5	
11 11 04	600	2.69	34.75	56.4	74.0	14.4	19.2	
11 11 08	300	1.49	16.26	29.8	71.5	0	17	
11 11 10	800	3.31	43.29	67.1	79.8	192	17.25	V_w decreased, external tank used
11 11 11	600	2.69	34.75	56.4	77.3	14.8	17.25	
11 11 14	100	0.24	4.72	7.0	71.7	0	17.0	
11 11 15	400	2.08	22.17	40.7	72.5	0	16	
11 11 16	200	0.67	10.29	16.7	71.5	0	14.5	
11 11 16	400	2.08	22.17	40.7	71	0	13.25	
11 11 17	150	0.43	10.36	12.1	71	0	14.1	
11 11 17	250	0.89	n.m.	23.75	71	0	13.3	
11 11 18	100	0.24	4.72	7.0	71.7	0	14.15	
11 11 19	300	1.49	16.26	29.8	72.5	0	15.2	
11 11 19	800	3.31	43.29	67.1	78.5	192	17.25	V_w decreased, external tank used

Table 4.5.: Experimental conditions used at the Kyoto high speed wind-wave tank. One free stream velocity u_{inf} was not measured, this is labeled with n.m.

Mixing the Tracers into the Water Body

Before the start of an experiment, the tracers were mixed into the water body. Two different methods were used.

The first method, used from the beginning of the campaign until the 15th of October, consisted of extracting 100 liters of water into two separate 50 liter tanks from the wind wave flume. Then, into each tank a few milliliters of one of the liquid tracers was given and the tanks were stirred using a pump. A blue-black dye, *Sudan Black*, that is soluble in the tracer, but not in water was used to make the otherwise colorless tracer visible. The amount of tracer was chosen such that some of the liquid tracer was still present after stirring. That means, that after stirring the water was saturated with the tracer. Then, only the saturated water was fed back into the wind-wave flume. With the addition of the dye it was visually ensured, that none of the pure tracer entered the wind wave flume. Then, for the tank containing the hexafluorobenzene, this was repeated one more time, as one filling of the 50 liter tank was not yielding a high enough water concentration.

The second method was to mix a few milliliters of the tracer into approximately 50 ml of pure ethanol. Both tracers are soluble so well in this solvent that they are considered miscible. Ethanol, in turn is miscible with water. This mixture of ethanol and tracers was then put into the large external tank, see section 4.1.2. This method was used during the last days of the campaign, from the 16th of October to the end. Ethanol is not detected by the spectroscopic setup and only used as a carrier. As the tracer mixes well with the ethanol, and the ethanol in turn mixes well with the water, single molecules or tiny tracer droplets are deposited into the water when the ethanol-tracer solution is mixed into the water.

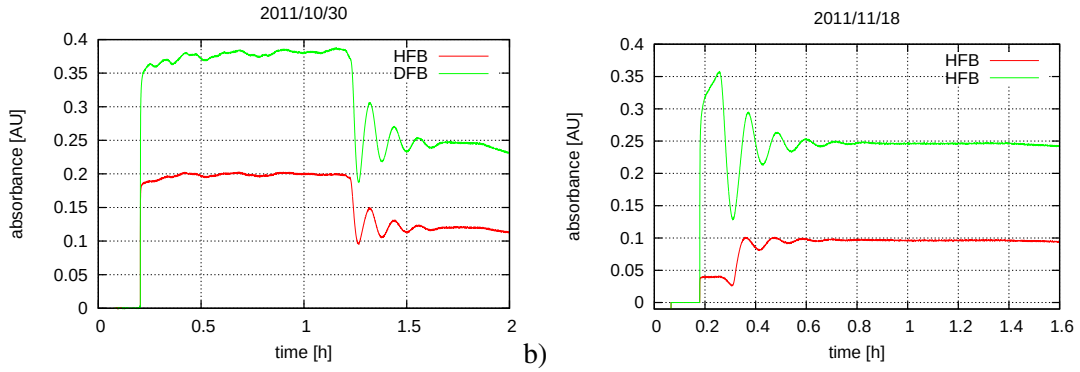

a) b)

Figure 4.7.: Time series of both tracers being mixed into the water, on a) 2011/10/30 with the first method and b) 2011/11/18 with the second. In a) the mixing was turned on about 1 h after the tracer solution was put into the wind wave tank near the water sampling pipe. In b) the mixing was turned on almost immediately after the start of the shown concentration measurement.

After putting the tracer into the wind wave tank or the external tank, respectively, the two pumps connecting the flume to the external tank were turned on to promote mixing. Examples of time series of both methods can be seen in figure 4.7. In each of the two graphs, the concentration measurement was started after the tracer was put into the water body of the flume, but before the mixing itself was started. In both cases, mixing took around 30 minutes and no systematic differences were found between the two methods. Method 2, however, was much faster than the first method during preparation and was therefore preferred once it was tried and tested to yield the same results as method one.

4.4. Experimental Setup

Two slightly different setups were used to measure the water side concentration in Kyoto and in Heidelberg. In Heidelberg, an additional air sampling setup was needed. All setups will be described in this section.

4.4.1. Setup at the Aeolotron

Concentrations during the campaign at the Aeolotron were measured using two FT-IR spectrometers (*iS10* manufactured by *Thermo*). One directly sampled the air side concentration, the second used an artificial lung to equilibrate the water space with a small volume of air and sampled this air's concentration.

Air Side Concentration Measurement

One directly sampled the air drawn with a pump (*Watson Marlow 313FD/50rpm* pump with 2 *313D* pump heads in parallel configuration using 6.4 mm bore *marprene* tubing) from the air space in segment 2 of the Aeolotron. A schematic view of the whole air side sampling setup at the Aeolotron can be seen in figure 4.8. The air side spectrometer was equipped with a temperature

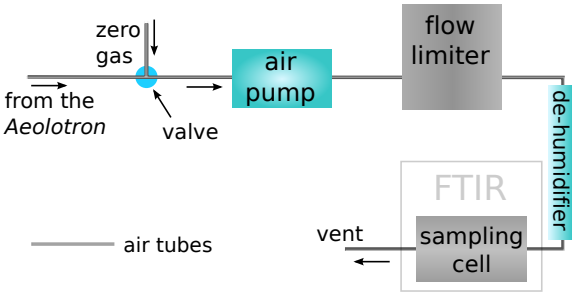

Figure 4.8.: Schematic view of the air sampling system used in the Heidelberg Aeolotron.

stabilized measuring cell with a length of 2 m. Before the air was pushed through the sampling cell, it was dried to remove water signatures from the spectrum. Drying was accomplished using a glass tube filled with granular phosphorous pentoxide. This is a potent dehydrator, forming phosphorous acid in its reaction with water vapor,

$$\mathrm{P_4O_{10}} + 6\,\mathrm{H_2O} \rightarrow 4\,\mathrm{H_3PO_4}. \tag{4.4}$$

This limited the flow rate that could be used to sample in the air space to 150 milliliters of air per minute which was set using a flow limiter. The reason is, that only a limited amount of phosphorous pentoxide could be integrated into the sampling loop. The chemical is used up and no longer drying once it reacted with water. Due to the high amount of water vapor present in the sampled air, the flow had to be limited so that one filling of phosphorous pentoxide granules guaranteed sufficient drying during one whole experimental day. The measuring cell itself has an internal volume of about 250 ml.

Due to the length of the pipes as well as unavoidable air volumes before the sampling cell, for instance in the pump and the dehumidifier, a time lag of about 30 seconds between sampling the air and analyzing the air occurred. This was measured using a small syringe filled with diluted tracer that was directly put into the sampling tube within one second. The time that it took this tracer to show a measuring signal in the spectrometer was measured and corrected for in data analysis.

Before each measuring day, background spectra, i. e. spectra that do not contain any tracer had to be taken. To achieve this, a valve was installed into the tubing. A clean air generator (*Zander*

KMT-3) that removes carbon dioxide and water vapor from normal pressurized air was connected to valves to feed the CO_2 and H_2O free air into the sampling loop.

The FT-IR spectrometer monitoring the air side concentration was set to a wavenumber resolution of 0.241 cm^{-2}. Six spectra were averaged by the FT-IR spectrometer before they were sent to a computer for storage, including a time stamp at which the spectra was taken. This lead to a data rate of about 1 stored spectrum every 30 seconds. The length of each of the spectra is 13898 data points. The spectra are stored in one image file per day with each line of the image containing a spectrum and the corresponding time stamp.

Water Side Concentration Measurement

Due to the sampling technique being spectroscopy in the infrared range, where water is not transparent, a way of extracting the water side concentration into an air volume was needed. The fastest and easiest way to equilibrate the concentration of the water with an air parcel was found to be a membrane oxygenator, a medical device normally used in surgical procedures to supply a patient's blood with oxygen and remove carbon dioxide. The used oxygenator (*Jostra Quadrox*) contains thin porous hollow polypropylene fibers that are oriented in a grid. Gas flows through the inside of the fibers, while water is pushed through perpendicular to the grid. The surface tension of the water keeps the water from entering the fibers through the micro slits in the walls of the fibers, but allows for a large contact area between gas and water. The *Jostra Quadrox* oxygenator has a surface that is actively taking part in gas exchange of about 1.8 m^2 in a compact 14x14x7 cm^3 box. The oxygenator that was used also had the option of cooling or heating the water, which was not used during the measurements. The performance of the used oxygenators is investigated in section 4.5.

Due to the gas exchanging fibers being oriented in a tight grid within the oxygenators, dust and debris in the water that is pumped through can block the water flow. The oxygenators are built such that they can not be cleaned of things blocking the water passage. Therefore, a filter with pores of 50 μm size (*Atlas Filtri* type *Edelstahl 316*) is installed into the water tubing before the water enters the oxygenator. A rotary pump (*Pan World Magnetic Pump HN-100PX*) draws the water from the middle of segment 6 of the Aeolotron at approximately 50 cm water depth and pushes it through the filter and then the oxygenator. The water that leaves the oxygenator is reinserted into the water bulk also at segment 6. In figure 4.9 the water tubing is shown in dark blue color.

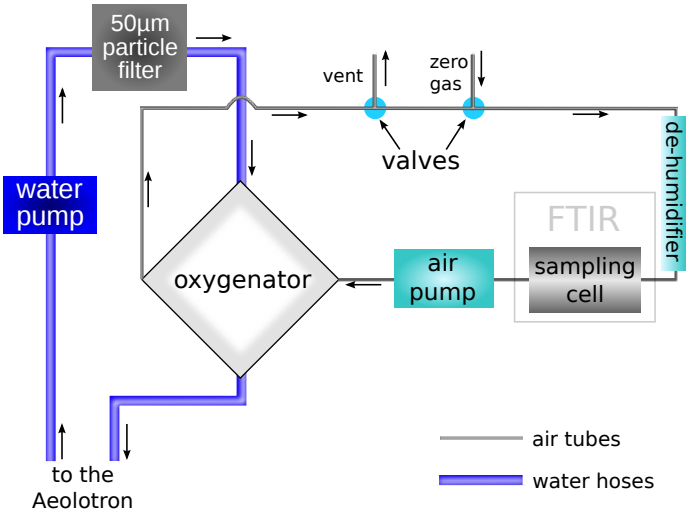

Figure 4.9.: Schematic view of the water sampling system used in the Heidelberg Aeolotron.

At the air side ports of the oxygenator, a closed air circulation was constructed, see figure 4.9.

A peristaltic pump (*Watson Marlow 313FD/50rpm* pump with one *313D* pump head using 6.4 mm bore *marprene* tubing) pushed air through the oxygenator, after which the air was dried, again using phosphorous pentoxide granules in a glass tube. After the drier the air entered the measuring cell of the FT-IR spectrometer with an optical length of 5 cm. The pump is connected to the outlet of the cell closing the air loop.

The time lag between sampling the water and measuring the concentration in the spectrometer was measured using two tanks of water, one with pure water, one with some tracer present in the water. The sampling location was switched from one tank to the other, measuring the time delay. It was found to be around 30 seconds, which is corrected for in later analysis.

The FT-IR spectrometer measuring the water side concentration was set to the same resolution of 0.241 cm^2 as the air side spectrometer with 6 averaged spectra, leading to a data rate of about 1 stored spectrum every 30 seconds and the length of the spectra of 13898 data points. The spectra are stored in one image file per day with each line of the image containing a spectrum and the corresponding time stamp.

Additional Measurement Devices

An anemometer (*Greisinger STS 020*) is installed in the center line (i.e. equidistant from inner and outer wall) of the Aeolotron at a distance of approximately 10 cm from the upper wall of segment 15 to measure the wind speed. Nielsen [2004] showed that the wind speed does not have a logarithmic profile in the Aeolotron. The wind is mostly constant with height above the water surface (except for a few centimeters directly above the water surface), but varies with radial position of the wind sensor. Therefore care was taken that it is installed in the center line to give the most representative wind values. The anemometer is connected to a hand held measurement device (Greisinger GMH 3330) which is read out by a computer once every 3 seconds. The wind speed, along with a time stamp when the measurement was done, is stored in a file for later processing.

A total of 10 PT-100 temperature sensors are placed at various locations at the Aeolotron. These are connected to hand held measurement devices (*Greisinger GMH 3710*) which are stored by a computer every 3 seconds. Measuring locations of interest in this work are the water bulk temperature taken at 50 cm water depth, 10 cm from the inner wall at segment 15 and the air bulk temperature measured right next to the anemometer in the roof of section 15.

Several devices measuring the water velocity are installed at the Aeolotron, though none of which was functional during the measurement campaign. The water velocity is needed to calculate the friction velocity, an important parameter in gas exchange models. However, it can be assumed that with the same setting of the wind generator and the same surfactant coverage of the water surface, the friction velocity is the same. Therefore, it was measured in separate experiments by Bopp [2011]. A description of the momentum balance method as well as the measurement devices used can also be found in Bopp [2011].

The surface roughness parameter mean square slope was measured using a color imaging slope gage (CISG) which is installed at segment 12. This device uses the refraction properties of light at the air-water boundary. A color coded light source is placed below the water and a camera watches the water surface from above. Using lenses to achieve a telecentric setup, a relationship between surface slope and the color the camera registers can be determined. A more thorough explanation of the CISG can be found in Rocholz [2008].

4.4.2. Setup at the Kyoto High Speed Wind-Wave Tank

At the Kyoto high speed wind-wave tank only the air sided concentration needed to be measured. The choice of UV spectroscopy would have permitted direct measurements in the water phase, but

it was decided against this. Advantages and disadvantages of measuring directly in the air space are listed in section 4.5.

A setup similar to the one used in the Heidelberg Aeolotron, see section 4.4.1 was used. As water vapor is transparent in the UV range in which the spectroscopy was performed, there was no need to dry the air. Also, no temperature measurement equipment was present at the Kyoto facility, therefore a temperature sensor was installed into the tubing directly before the water entered the pump. The water was sampled at a water depth of approximately 35 cm at a fetch of 6.5 m. A schematic view of the setup used in the Kyoto facility can be found in figure 4.10.

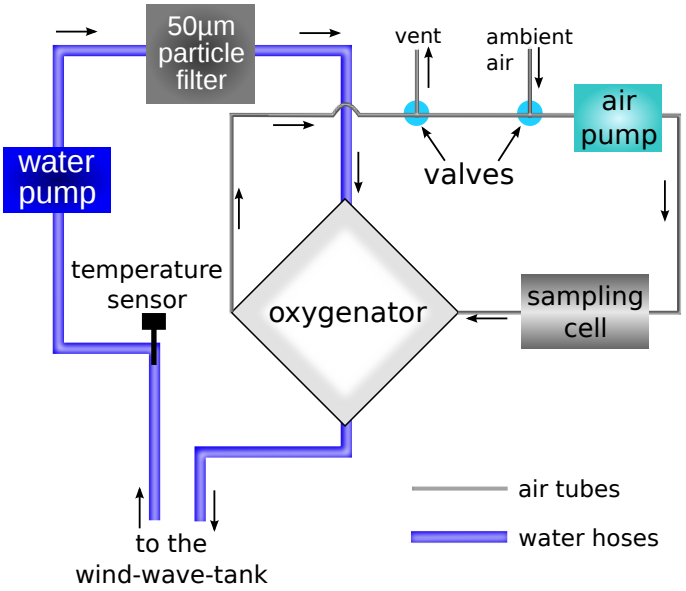

Figure 4.10.: Schematic view of the gas extraction setup used in the Kyoto high speed Wind Wave Tank showing the oxygenator, its water and air connections as well as the UV spectroscopy sampling cell.

To measure UV spectra without tracer, tracer free air was pushed through the sampling cell. As the tracers used are not present in the ambient air, this could be used to measure the lamp spectra by opening the valves shown in the air circulation in figure 4.10.

The sampling cell itself is constructed from a quartz glass tube with a length of 1 m and an outer diameter of 5 mm. Light produced by a deuterium lamp enters through a quartz glass lens with focal length of 5 cm and a quartz glass window. It leaves the measuring cell through another quartz glass window and lens to be focused on a glass fiber. This glass fiber leads the light into a UV spectrometer (*Ocean Optics Maya2000 Pro*). Before the light reaches the glass fiber, it can be blocked from entering the fiber using a shutter to acquire dark spectra. Due to the mounting mechanisms of the quartz glass tube and windows, the light path is 1.05 m long, which is about 5 cm longer than the tube itself. A schematic picture of the setup can be found in figure 4.11. The *Ocean Optics Maya2000 Pro* spectrometer used to collect the spectra can resolve wavelengths from 190.5 nm to 294.1 nm. Spectra are discretized into 2068 pixels. The relationship between wavelength and pixel number was slightly non linear, see figure 4.12. Several spectra were averaged before storage. The number of averages as well as the integration time for each spectrum is listed in table 4.6.

The *Ocean Optics Maya2000 Pro* spectrometer used to collect the spectra can resolve wavelengths from 190.5 nm to 294.1 nm. Spectra are discretized into 2068 pixels. The relationship between wavelength and pixel number was slightly non linear, see figure 4.12. Several spectra were averaged before storage. The number of averages as well as the integration time for each spectrum is listed in table 4.6.

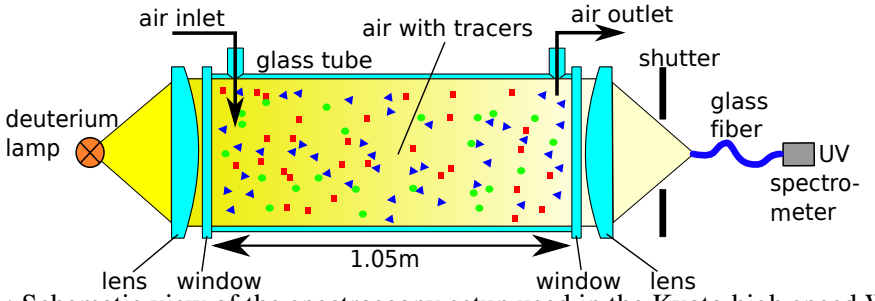

Figure 4.11.: Schematic view of the spectroscopy setup used in the Kyoto high speed Wind Wave Tank. All glass elements are made from quartz glass to permit UV transmission. The outer diameter of the quartz glass tube is 5 mm, the inner diameter is 3 mm.

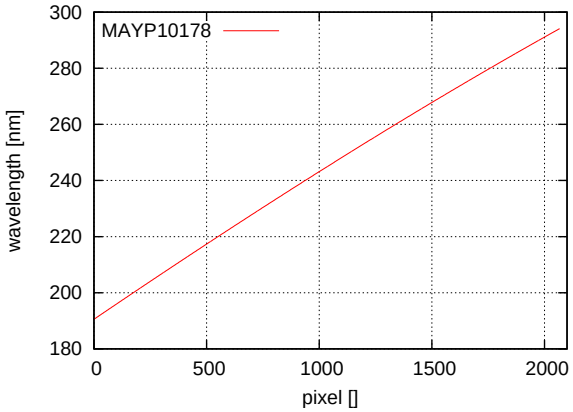

Figure 4.12.: Relationship between pixel number and wavelength of the spectrometer used in the Kyoto experiments.

date [Y M D]	t_{int} [ms]	# of averages
11 10 27	35	20
11 10 28	35	20
11 10 31	35	20
11 11 02	35	20
11 11 04	35	20
11 11 08	35	20
11 11 10	35	20
11 11 11	45	20
11 11 14	45	20
11 11 15	45	20
11 11 16	50	20
11 11 17	55	15
11 11 18	55	15
11 11 19	60	15

Table 4.6.: Integration times t_{int} and number of averaged spectra used during the Kyoto campaign.

Integration times and number of averages where chosen so that about 1 spectrum per second could be stored, as well as the incident light intensity I_0 is maximized. On each day, before the start of the measurement, the ideal integration time yielding a maximum of light intensity in the spectrometer without saturating single pixels was determined. The integration time had to be increased because dust was slowly settling down on the inner wall of the sampling cell, inhibiting total reflection and scattering light out of the system. Dust could unfortunately enter the system because in order to obtain spectra without any tracer, ambient air had to be sampled and the otherwise closed circuit had to be opened. No other source of clean, tracer free air was available.

The spectra are stored in one image file per day with one line representing one spectrum. One more column is added where a time stamp belonging to the spectrum in the same line is written. The first 200 lines are used for background spectra, the next 200 for lamp spectra. All following lines contain measured data. Further data analysis is detailed in chapter 5.

4.5. Oxygenator Performance

An artificial lung (*Maquet Jostra Quadrox* oxygenator) was used to equilibrate a small volume of air with the water, and this air was then analyzed with respect to gas concentration.

Ideally, assuming a 100 % efficiency of the oxygenator, the water concentration c_w can be calculated from the measured concentration c_{oxy} in the oxygenator's air phase using Henry's Law,

$$c_w = \alpha c_{\mathrm{oxy}}. \tag{4.5}$$

To achieve best efficiency in the equilibration, the air volume is circled through the oxygenator repeatedly at a rate of about 180 ml/min for the Aeolotron measurements and 550 ml/min for the Kyoto measurements due to the differing configuration of the peristaltic pump.

Advantages of sampling air that has been equilibrated to the water by an oygenator are:

- Water is opaque in the IR wavelength range, making direct measurements impossible
- In the UV range of 190 nm to 290 nm water is not fully transparent, see figure 4.13.
- In the transparent regions of the UV wavelength range the absorption peaks of tracers are broadened in water making separation of different tracers more difficult and decreasing the sensitivity.
- For tracers with low solubility $\alpha < 1$ the sensitivity is enhanced due to higher concentrations in the equilibrated air than in the water
- Air bubbles within the water generated by breaking waves are not a problem in air phase measurements. If these were in water pumped through the sampling cell they could block the UV light by scattering it out of the sampling cell making evaluation of the data difficult or impossible.

Disadvantages of air phase measurements are:

- For tracers with solubility $\alpha > 1$ the water concentration needs to be larger because of lower equilibrated air side concentrations.
- The lower the solubility of the tracer, the longer the time until the equilibration is reached, therefore fast changes in the water concentrations might not be resolved
- Volatile organic tracers might contaminate the plastic surfaces of the oxygenator leading to faulty concentration measurements

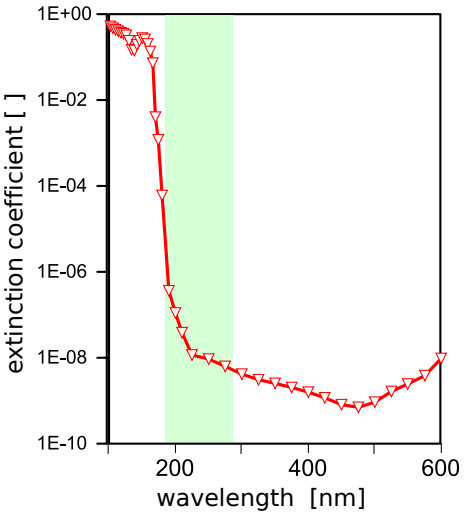

Figure 4.13.: Extinction coefficient of water, taken from Palik [1991]. The spectral region used for the UV spectroscopy is marked.

For the measurements in the Aeolotron, the only option was to measure in the equilibrated air phase. The choice of the tracers was such that FT-IR spectroscopy was used as an analysis method, which is not possible directly in water because of the opaqueness of water in the IR range. For the measurements in Kyoto UV spectroscopy was used. Air bubbles generated by breaking waves at high wind speeds trapped in the UV measurement cell would have made measurements directly in water very hard or even impossible. Therefore, in both tanks the equilibration method was chosen.

4.5.1. Estimating the Time Constant of the Equilibration

To show the applicability of the gas equilibration method, some theoretical considerations can be made.

The box model that describes the concentrations in the air and water side of the oxygenator is similar to the model described in 3.1. Assuming no leaks in tubing, air pump, oxygenator and the spectroscopy cell, the air side mass balance equation is

$$V_{\mathrm{oxy}}\dot{c}_{\mathrm{oxy}} = A_{\mathrm{oxy}}k_{\mathrm{oxy}}(c_w - \alpha c_{\mathrm{oxy}}) \tag{4.6}$$

with the oxygenator's surface area A_{oxy}, the total air volume V_{oxy} and the gas exchange rate k_{oxy} across the oxygenator's membrane. Assuming good mixing of the air volume and a rather slow changing water concentration, $c_w \approx \mathrm{const.}$, a solution of equation 4.6 can be found,

$$c_{\mathrm{oxy}}(t) = \frac{c_w}{\alpha} + \left(c_{\mathrm{oxy},0} - \frac{c_w}{\alpha}\right) e^{-\frac{k_{\mathrm{oxy}}*\alpha*A_{\mathrm{oxy}}}{V_{\mathrm{oxy}}}t} \tag{4.7}$$

with $c_{\mathrm{oxy},0}$ being the initial concentration in the air side. The time constant of this equilibration process τ_{oxy} is

$$\tau_{\mathrm{oxy}} = \frac{V_{\mathrm{oxy}}}{k_{\mathrm{oxy}} * \alpha * A_{\mathrm{oxy}}}. \tag{4.8}$$

This indicates, that the time constant scales with the inverse of the solubility α of the tracer.

According to the manufacturer of the oxygenator the gas exchange surface area is $A_{\mathrm{oxy}} = 1.8\,\mathrm{m}^2$. The total air volume V_{oxy}, including piping and the measuring cell was determined to be less than 300 ml. As the change in the water side concentration is expected to be fastest in the Kyoto high-speed wind wave tank, the setup and tracers of the Kyoto campaign are used

for the study of the performance of the oxygenator. Hexafluorobenzene is the tracer with the lowest solubility of $\alpha = 1.0$ which was used in Kyoto. Pore size (meaning maximum width of spaces filled with water between the semi permeable membrane used for gas exchange) inside the oxygenator can be roughly estimated to be below $1\ \mathrm{mm}$. Using half of this pore size as the maximum distance $z_* = 0.5\ \mathrm{mm}$ that the gas molecules have to traverse with diffusive movement only, the gas transfer velocity k_{oxy} within the oxygenator can be calculated as

$$k_{\mathrm{oxy}} = \frac{D}{z_*} \tag{4.9}$$

using equation 2.36 with the tracer's diffusivity D, which is in the order of 10^{-5}. This yields a transfer velocity of about $k_{\mathrm{oxy}} \approx 0.72\,\mathrm{cm/h}$. Conservatively assuming an even lower gas exchange rate of $k_{\mathrm{oxy}} = 0.5\,\mathrm{cm/h}$, a time constant for the oxygenator's performance can be estimated using 4.8 to be around $\tau_{\mathrm{oxy}} = 2\,\mathrm{min}$.

A rough estimation of the expected time constant of gas exchange in the Kyoto high speed wind-wave tank can be made using empirical relationships between wind speed and gas transfer velocity. Depending on the relationship between gas transfer velocities and wind speed used, different estimates for the gas transfer velocity at the highest wind speed of $v_w = 67\,m/s$ and the time constants of the gas exchange process in the wind wave tank can be found. The expected transfer velocities range from $k_{600} = 3500\,cm/h$ [Wanninkhof et al., 2009], to $k_{600} = 1050\,\mathrm{cm/h}$ [Nightingale et al., 2000] to as low as $k_{600} = 350\,\mathrm{cm/h}$ [Liss and Merlivat, 1986]. Using Schmidt Number scaling 2.68, the wind-wave tank's volume $V_w = 13.5\,\mathrm{m}^3$ and surface area $A = 10.0\,\mathrm{m}^2$ used for the highest wind speed yields time constants ranging from 30 minutes for the Liss-Merlivat relationship, 13 minutes for the Nightingale relationship down to 3 minutes for the Wanninkhof relationship. This is lower than the expected time constant of 2 min expected from geometrical considerations of the extraction setup. To confirm this, the performance of the oxygenator was tested experimentally.

Experimental Validation.

An experimental validation of the estimation above was performed. The setup used was the same as in Kyoto described in section 4.4.2.

A small amount of tracer with the lowest solubility and therefore the highest expected time constant, hexaflurobenzene, was dissolved in a water tank of approximately 8 l that was connected to the gas extraction setup. During the tracer input the pump of the extraction unit was switched off, meaning that only the concentration of the (stagnant) pure water was sampled. Care was taken that the tracer was mixed well into the water in the tank. When the pump was turned on, water containing the tracer was immediately pumped through the oxygenator, simulating a jump in concentration. After reaching an equilibrium, the water was cleaned of the tracer and the process was started again. To eliminate a possible bias due to always starting at a concentration of 0, two more concentration jumps from non-zero start values where done. Figure 4.14a shows the time series of the concentration of hexafluorobenzene obtained in this way.

Combining equations 4.7 and 4.8 yields

$$c_{\mathrm{oxy}}(t) = c'_w + \left(c_{\mathrm{oxy},0} - c'_w \right) e^{-\lambda_{\mathrm{oxy}} t} \tag{4.10}$$

with $c'_w := c_w/\alpha$ and $\lambda_{\mathrm{oxy}} = \tau_{\mathrm{oxy}}^{-1}$.

This equation was fitted to each concentration jump, see figures 4.14 b) through f). c'_w, $c_{\mathrm{oxy},0}$ and λ_{oxy} were treated as free parameters. Obtained time constants were 1.23 min, 1.30 min and

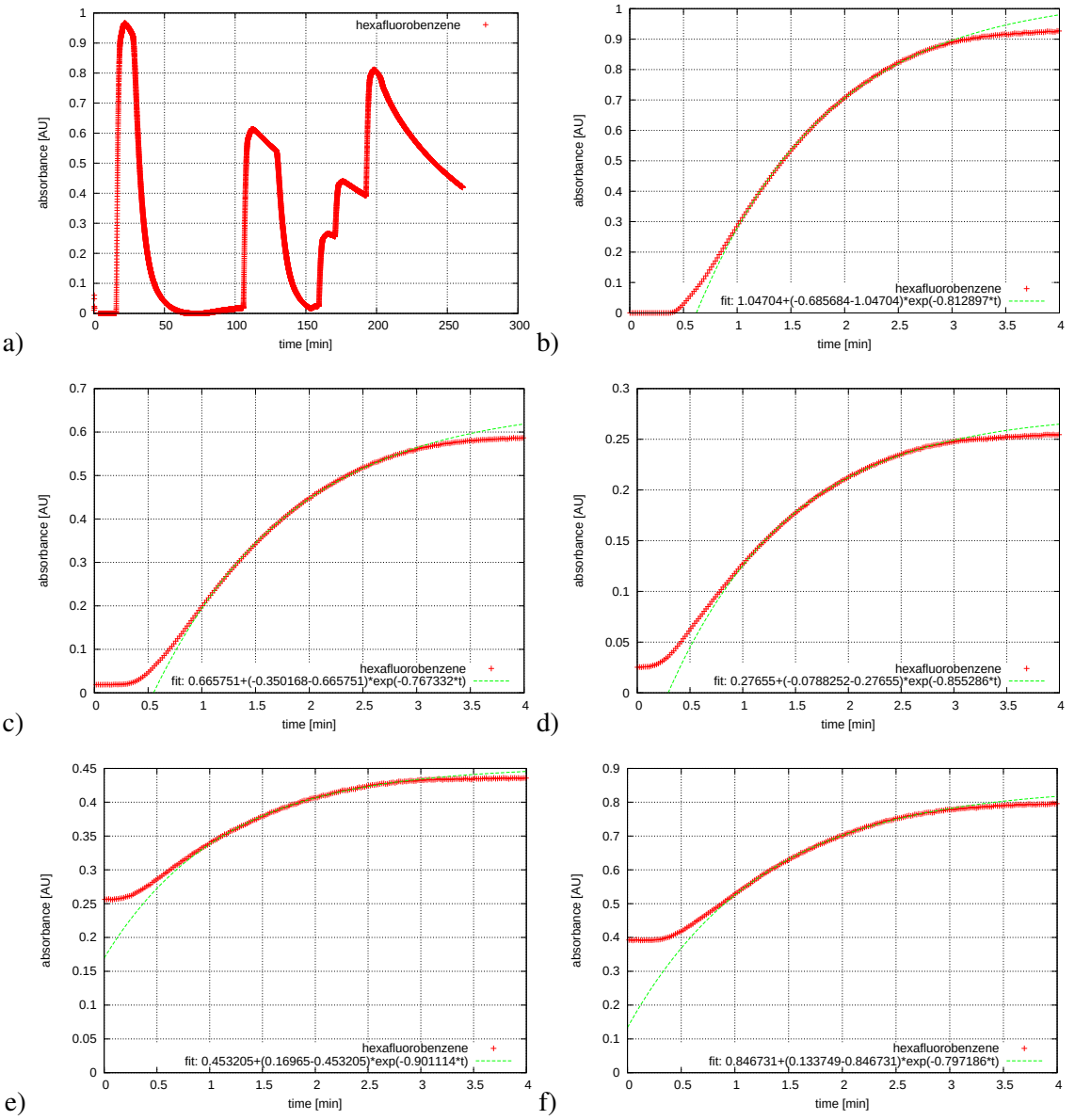

Figure 4.14.: Concentration time series that was used to measure the performance of the oxygenator. a) complete series of experiments b) through f) single concentration jumps with fitted exponential increase. The time axis was shifted in some figures to make the fit more stable.

1.17 min for the start from zero concentration, and 1.11 min and 1.25 min for the start from a nonzero concentration. These values lie below the estimate from geometrical considerations, and also below the lowest time constant expected from the empirical gas transfer - wind speed relations.

Therefore, with the extraction system the proposed gas exchange measurements are possible.

5. Data Processing

In this chapter, the data processing process is presented. The raw data in the form of IR and UV spectra was stored in gray scale images. Each line of the images corresponds to one spectrum and each column to the intensity or absorbance at one fixed wavelength. In the last column of the image, i. e. in the last position of every spectrum, a time stamp identifying the time at which the respective spectrum was measured is stored. However, for both measuring techniques, UV- and FT-IR spectroscopy, the raw data format is slightly different, leading to some differences in the data processing.

UV spectroscopic data needs to be preprocessed which is described in section 5.1. The actual fitting algorithm that yields the measured absorbances is described in section 5.2. The final part of this chapter deals with how to calculate gas transfer velocities in section 5.3.

5.1. Preprocessing

As the FT-IR data read from the FT-IR spectrometers are already in the absorbance format, only very little preprocessing is needed. The UV setup, to the contrary, yields intensity spectra which have to be transformed into the absorbance format.

5.1.1. Preprocessing the UV Spectroscopic Data

An example of one raw data image can be seen in image 5.1.

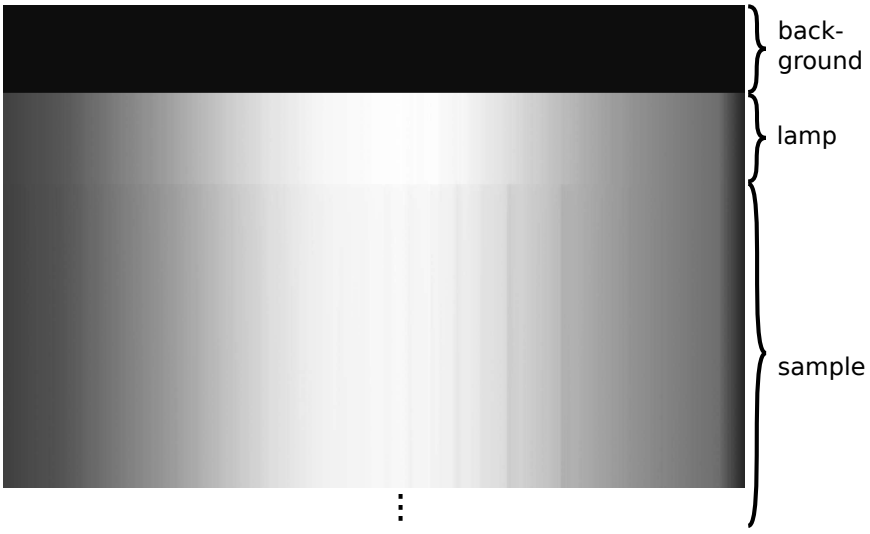

Figure 5.1.: Example of a UV spectroscopy raw data image. Each line contains 1 spectrum. For better illustration, the image is cropped considerably at the bottom as well as slightly cropped on the left and right side. The first 200 spectra correspond to dark spectra, followed by 200 lines of lamp spectra without any tracers.

To obtain absorbance spectra from intensity spectra, three different measurements are necessary. First, the spectrometer response $I_{\mathrm{dark}}(\lambda)$ without any illumination, the so called dark spectrum,

needs to be known. Second, the pure spectrum of the lamp without any absorber in the lights path, $I'_0(\lambda)$, has to be measured, and third, the actual absorption spectrum $I'(\lambda)$ is needed.

There are also three different regions visible in 5.1 image. The first 200 lines are dark spectra. During dark spectra acquisition, a shutter is placed between the UV lamp and the spectrometer blocking all light from entering the spectrometer. To prevent measured negative intensity values, a small artificial offset is produced by the electronics of the spectrometer. Also, different pixels on the detector show different thermal noise signatures. Both are sources of non zero dark values and have to be corrected for in the measured spectra. Therefore, the dark spectrum needs to be known. To obtain a representative dark spectrum, lines 10 to 190 in 5.1 were averaged. This mean dark spectrum $I_{\mathrm{dark}}(\lambda)$ is shown in figure 5.2a.

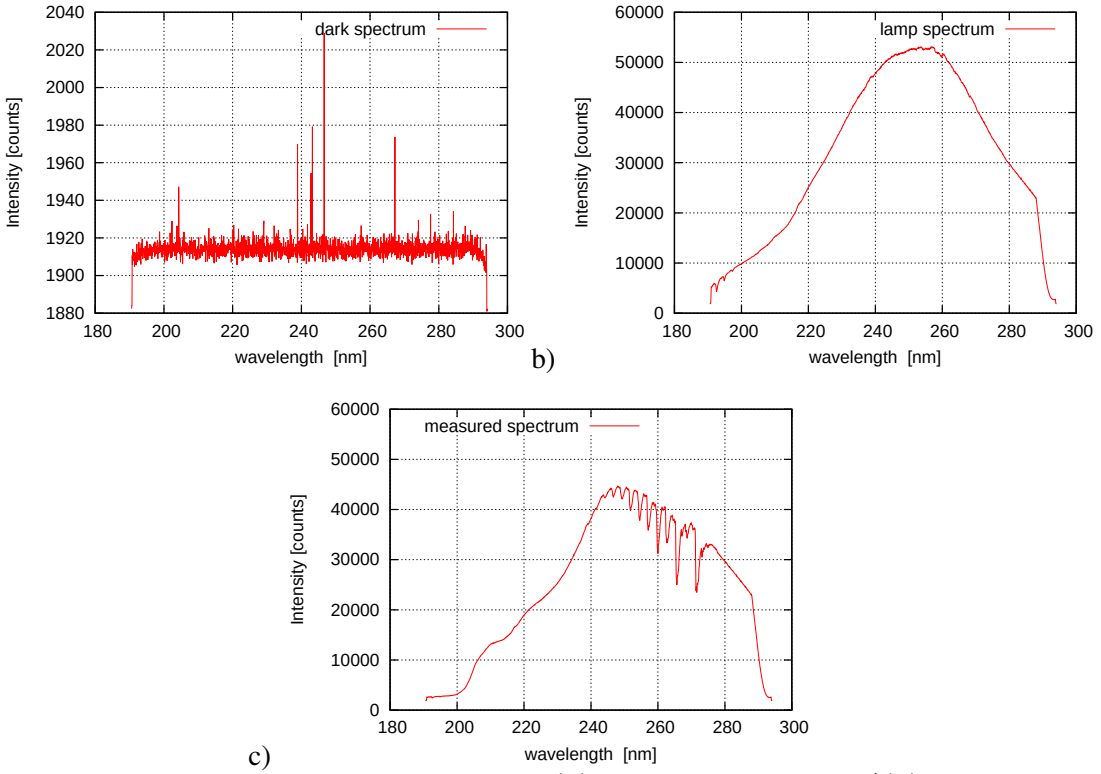

Figure 5.2.: Example of a) a dark spectrum $I_{\mathrm{dark}}(\lambda)$, b) a lamp spectrum $I'_0(\lambda)$ and c) a measured spectrum $I'(\lambda)$. Not shown in all three graphs is the last pixel of the spectrum containing the time stamp.

The next 200 lines in 5.1 are so called lamp spectra. That means, the shutter blocking the light during acquisition of the dark spectra was removed, so that light enters the spectrometer. To obtain a pure lamp spectrum, no tracer must be present in the sampling cell. Again, a mean spectrum of lines 210 to 390 is calculated as a representative lamp spectrum $I'_0(\lambda)$, see figure 5.2b. All following lines in 5.1 are the actual measured spectra with tracer present in the measuring cell. One example of a measured spectrum $I'(\lambda)$ can be seen in 5.2c.

To calculate the absorbance spectra, several steps are necessary. First, the lamp spectrum has to be corrected for the dark spectrum,

$$I_0(\lambda) = I'_0(\lambda) - I_{\mathrm{dark}}(\lambda). \tag{5.1}$$

Next, each line n in image 5.1 that contains a measured spectrum $I'(\lambda)$ has to be corrected for the dark spectrum, too,

$$I(\lambda, n) = I'(\lambda, n) - I_{\mathrm{dark}}(\lambda). \tag{5.2}$$

As the next step, Beer's law, 2.78 can be applied to each line in the form

$$abs(\lambda, n) = -\ln\left(\frac{I(\lambda, n)}{I_0(\lambda)}\right) = -\ln T(\lambda, n) \tag{5.3}$$

to calculate absorbance spectra $abs(\lambda, n)$ with the intermediate step of transmittance spectra $T(\lambda, n)$. Figure 5.3 summarizes the preprocessing in a flow chart. As a last final step in preprocessing, outliers with unrealistic absorbances larger than 6 or lower than 0 are set to 0.

During the preprocessing steps, the time stamp in the last column is not changed. After preprocessing, the image contains 200 lines of dark spectra, 200 lines of lamp spectra, and absorbance spectra, each with a time stamp.

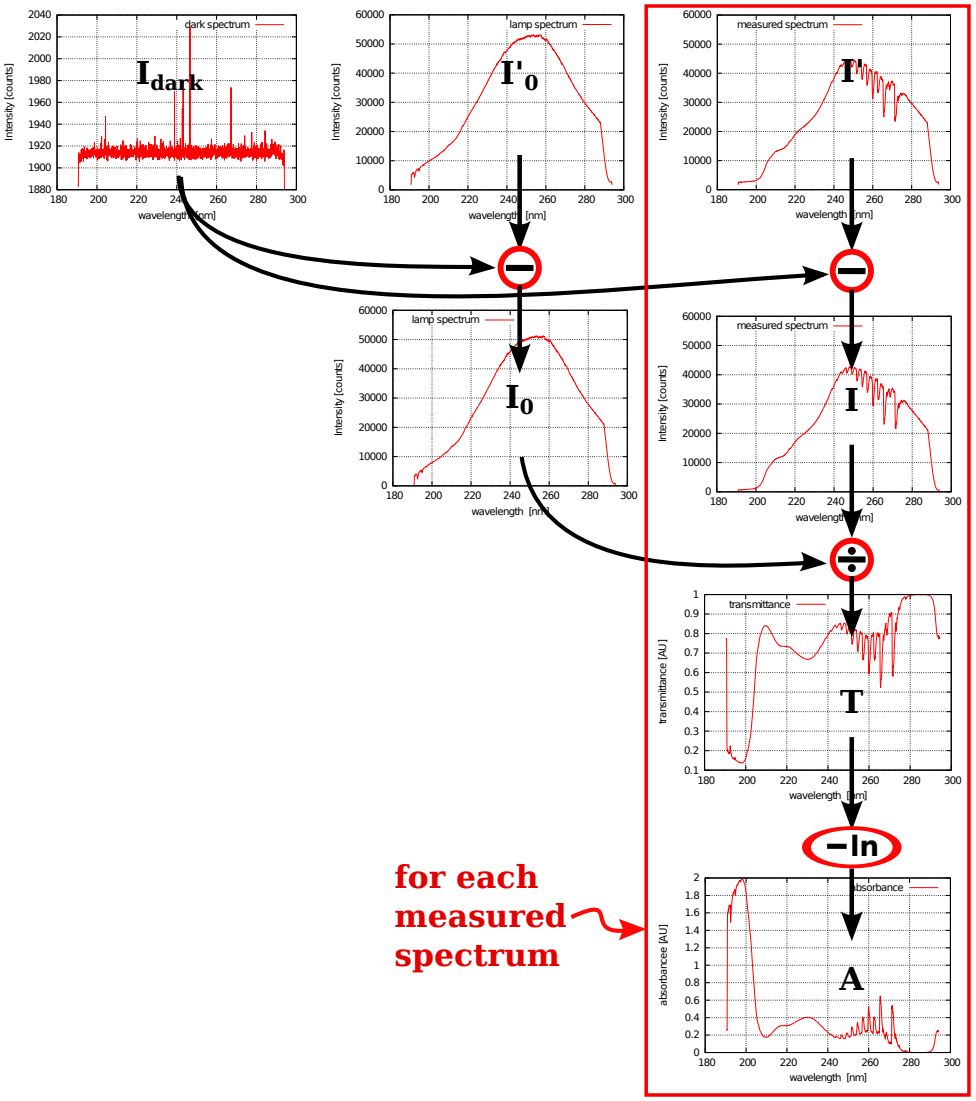

Figure 5.3.: A flow chart of reprocessing steps done for the UV spectroscopy data. Processing steps include removal of dark spectra, calculation of transmittance spectra labeled T and absorbance spectra labeled A. The red circles mark the performed operations.

5.1.2. Preprocessing the FT-IR Spectroscopic Data

As the FT-IR spectrometers' output already consists of absorbance spectra, only one small preprocessing step is necessary. Carbon dioxide, which is present in the wind wave tanks' air and

water in varying concentrations, has an absorption band between wavenumber 2265.080 cm^{-1} and 2397.427 cm^{-1}. To make further processing easier and more reliable, the carbon dioxide signature is removed from all spectra by setting all measured values to 0 in the mentioned wavenumber region.

5.2. Calculating Absorbances

To calculate gas transfer rates, a single value for the absorbance for each tracer at each time step is preferred over absorbance spectra. Therefore, the absorbance spectra measured (FT-IR spectroscopy) or calculated (UV spectroscopy) have to be transformed into a concentration measurement. This is done by a fitting approach.

As a preparation for further analysis of the measured spectra, for each single tracer an absorbance spectrum is produced, that has a maximum absorbance of 1. This is achieved by systematically varying the concentration of the tracer in the measuring cell to yield a maximum absorbance of nearly 1. Then, the maximum absorbance $abs_{\max}$ of this spectrum is determined, and then the whole spectrum is scaled with $1/abs_{\max}$,

$$abs_{\mathrm{ref}}(\lambda) = abs(\lambda)\frac{1}{abs_{\max}}. \tag{5.4}$$

These spectra are called reference spectra. The reference spectra of the UV and FT-IR spectroscopy are shown in figure 5.4. The spectra measured with the air sided FT-IR spectrometer are plotted against the wavenumber on an inverted axis, which is common practice in FT-IR spectroscopy. For the UV reference spectra, the region below $\lambda = 205\,\mathrm{nm}$ is not shown because it will be disregarded in a later step in analysis.

When more than one tracer is present in an air sample their absorbances add,

$$abs_{\mathrm{tot}}(\lambda) = \sum_i abs_i(\lambda) \tag{5.5}$$

to give the total absorbance $abs_{\mathrm{tot}}(\lambda)$ as discussed in section 2.3. In other words, the absorbance spectrum is a linear combination of the single tracer spectra. An example, that emphasizes this is shown in figure 5.5.

The fact that the absorbance of a mixture of tracers is a linear combination of the absorbances of each single tracer is used in further analysis. When $abs_{\mathrm{ref,A}}$, $abs_{\mathrm{ref,B}}$, $abs_{\mathrm{ref,C}}$ ... denote the reference spectra of tracers A, B, C..., the measured spectrum can be approximated as

$$abs_{\mathrm{meas}}(\lambda) = a \cdot abs_{\mathrm{ref,A}} + b \cdot abs_{\mathrm{ref,B}} + c \cdot abs_{\mathrm{ref,C}} + ... \tag{5.6}$$

with a, b, c ... being scaling factors.

The exact algorithm used deviates slightly between UV and FT-IR spectroscopy. It will be described separately for both spectroscopic techniques in the following sections.

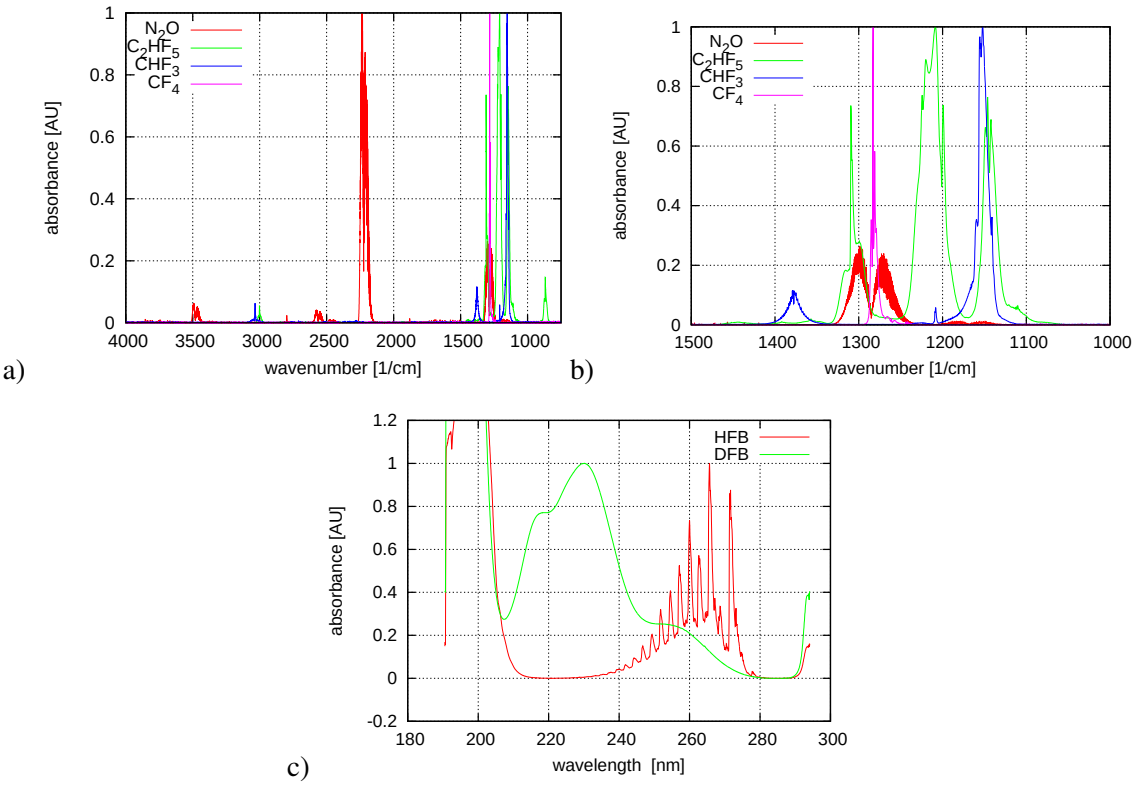

Figure 5.4.: a) reference spectra measured with the air sided FT-IR spectrometer. b) enlargement of the wavenumber region between 1500 and 1000 cm^{-1} c) reference spectra measured with the UV spectrometer. DFB: 1,4-difluorobenzene and HFB: hexafluorobenzene. Not shown: The spectra measured with the water sided FT-IR spectra. They are virtually identical to the air sided ones and can be found in appendix A.2.

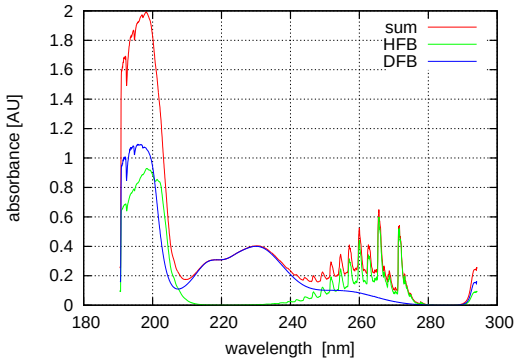

Figure 5.5.: Example of addition of two pure tracer spectra labeled HFB and DFB.

5.2.1. UV Spectroscopy

To compensate for changes in the lamp or dark spectra, three more artificial absorbance spectra are generated. One, $A_0(\lambda)$, is a simple offset, independent on wavelength. The second, $A_1(\lambda)$, is a linear function of wavelength and the third $A_2(\lambda)$, a quadratic function. The three artificial spectra as well as the reference spectra are shown in figure 5.6. The reference spectra of the tracers are limited in the wavelength region between $\lambda = 206.65\,\mathrm{nm}$ and $\lambda = 291.6\,\mathrm{nm}$ because, one, outside of this region both spectra are very similar there, adding nothing to the separability and two, because the incident light that the UV lamp produces has a very low intensity outside of

this region leading to a higher noise. Taking the three artificial spectra into account, function 5.6

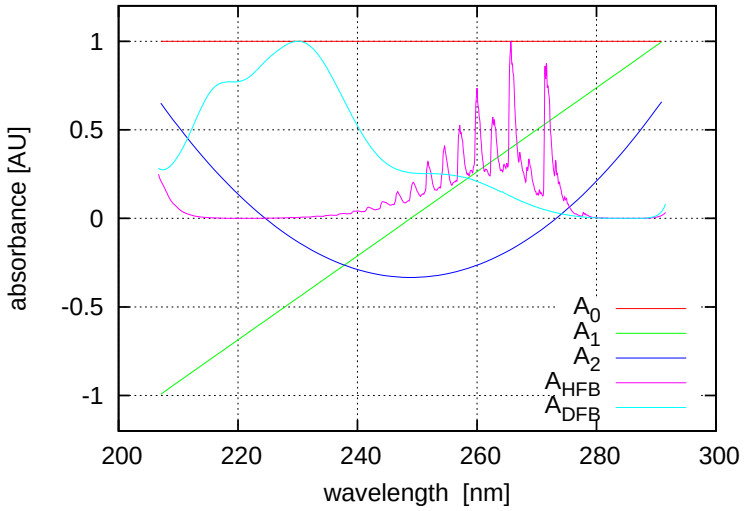

Figure 5.6.: All UV reference spectra fitted to the data. A_0, A_1 and A_2 denote computer generated spectra that compensate for variations in the lamp or dark spectra. A_{DFB} and A_{HFB} are the two tracers that are analyzed.

can be modified to

$$abs_{\mathrm{meas}}(\lambda) = a_0 \cdot A_0(\lambda) + a_1 \cdot A_1(\lambda) + a_2 \cdot A_2(\lambda) + f_1 \cdot A_{\mathrm{HFB}}(\lambda) + f_2 \cdot A_{\mathrm{DFB}}(\lambda) \quad (5.7)$$

for the UV spectroscopy. The free parameters a_0, a_1, a_2, f_1 and f_2 are determined by a least squares fit. Parameters f_1 and f_2 are the desired single absorbance values that characterize the whole measured spectrum.

The widely used differential optical absorption spectroscopy approach (DOAS), see Platt et al. [1979], is not applicable here. It relies on a broad band incident spectrum, and very narrow banded absorption spectra of the tracers that are to be analyzed. With hexafluorobenzene, one tracer is present that has a broad absorption band, which would not be treated correctly by the DOAS method.

5.2.2. FT-IR Spectroscopy

Two slightly different methods were studied to calculate single absorbance values from the absorbance spectra of the FT-IR spectroscopy. The first is identical to the method used for UV spectroscopy. The second is a modified version that eliminates systematic errors. Both will be detailed in the next sections.

The air side measurements are chosen for the explanations. The water side was treated identically with the only differences being the reference spectra, which were measured using the water side spectrometer and the absence of the tracer tetrafluoromethane.

The Straight Forward Method

In the most straight forward approach, the FT-IR spectra are treated just like the UV spectra. The fitted spectra for this approach is shown in figure 5.7 and the fitted function is

$$\begin{aligned} abs_{\mathrm{meas}}(\lambda) =& a_0 \cdot A_0(\lambda) + a_1 \cdot A_1(\lambda) + a_2 \cdot A_2(\lambda) + \\ &+ f_1 \cdot A_{\mathrm{N_2O}}(\lambda) + f_2 \cdot A_{\mathrm{CHF_3}}(\lambda) + f_3 \cdot A_{\mathrm{C_2HF_5}}(\lambda) + f_4 \cdot A_{\mathrm{CF_4}}(\lambda). \end{aligned} \quad (5.8)$$

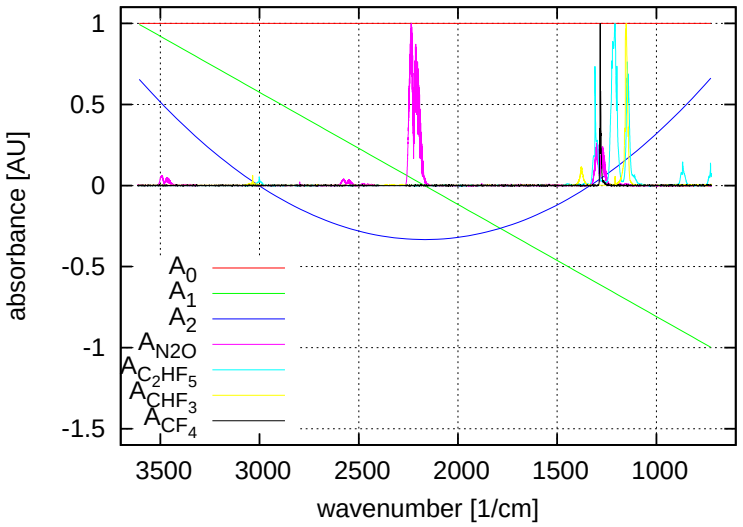

Figure 5.7.: All FT-IR reference spectra fitted to the data. A_0, A_1 and A_2 denote computer generated spectra that compensate for changes in the lamp or dark spectra. $A_{\mathrm{N_2O}}$, $A_{\mathrm{CHF_3}}$, $A_{\mathrm{CF_4}}$ and $A_{\mathrm{C_2HF_5}}$ are the four tracers that are analyzed.

This straight forward method proved to be problematic in the case of the FT-IR spectra. The spectra of both, nitrous oxide as well as tetrafluoromethane are non-linear meaning, that doubling the concentration leads to less than a doubling in measured absorbance. These effects are accompanied by a change in the shape of the spectra, meaning that simple scaling of the spectra by a factor does not accurately represent measured spectra, see for example figure 6.8. A further description of this can be found in section 6.4.2.

The non-linearity is by itself not a problem, as it can be compensated for by a calibration curve that is also non-linear. However, a problem arises under some circumstances in the fit itself. A different shape of the measured spectrum compared to the scaled reference spectrum yields a non-zero residuum. A residuum is the residual spectrum after the scaled reference spectrum is subtracted from the measured spectrum. If two tracers have extinction coefficients larger than zero in the same wavelength regions with one of them behaving non-linearly, the residuum of the non-linear one could be misinterpreted as non-zero absorbance of the second tracer.

The only absorption peak of the tracer tetrafluoromethane (which is slightly non-linear) lies right within the side band of the tracers nitrous oxide (which behaves strongly non-linear) and pentafluoroethane (which is linear) in the wavenumber region $1330\,\mathrm{cm}^{-1} > \omega > 1230\,\mathrm{cm}^{-1}$, see figure 5.8.

Therefore, a different approach is used to eliminate the nitrous oxide from the measured spectrum before the other tracers are fitted.

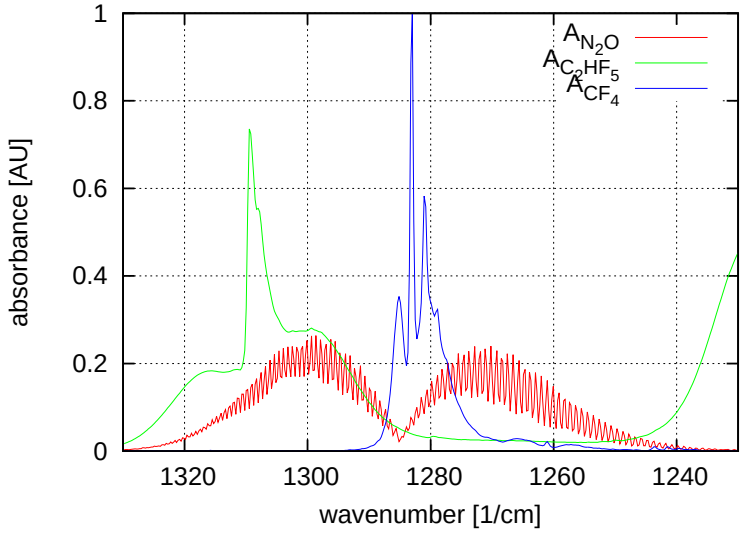

Figure 5.8.: Overlapping reference spectra of nitrous oxide and tetrafluoromethane in the wavenumber region between 1230 cm^{-1} and 1330 cm^{-1}. Also shown is pentafluoroethane, which has some absorptivity in this wavenumber region.

The Nitrous Oxide Removal Method

As a preparation, a total of 1424 reference test spectra A_{test} of nitrous oxide, ranging in maximum absorbance from 0 to 2.0 were generated by slowly increasing the concentration in the measuring cell of the FT-IR spectrometer while spectra were stored continuously.

In the wavenumber region between 2168.65 and 2264.84 cm^{-1}, of all the tracers only nitrous oxide absorbs light. Therefore a first fit is constricted to the mentioned region. Also, only a reference spectrum of nitrous oxide along with the three synthetic spectra A_0, A_1 and A_2 is fitted using the function

$$abs_{\text{meas}}(\lambda) = a_0 \cdot A_0(\lambda) + a_1 \cdot A_1(\lambda) + a_2 \cdot A_2(\lambda) + f_1 \cdot A_{\text{N}_2\text{O}}(\lambda) \tag{5.9}$$

yielding only absorbance values f_1 for nitrous oxide. The fitted spectra A_0, A_1 and A_2 as well as $A_{\text{N}_2\text{O}}$ can be seen in figure 5.9a. Up to this point, the measured spectrum remains unchanged.

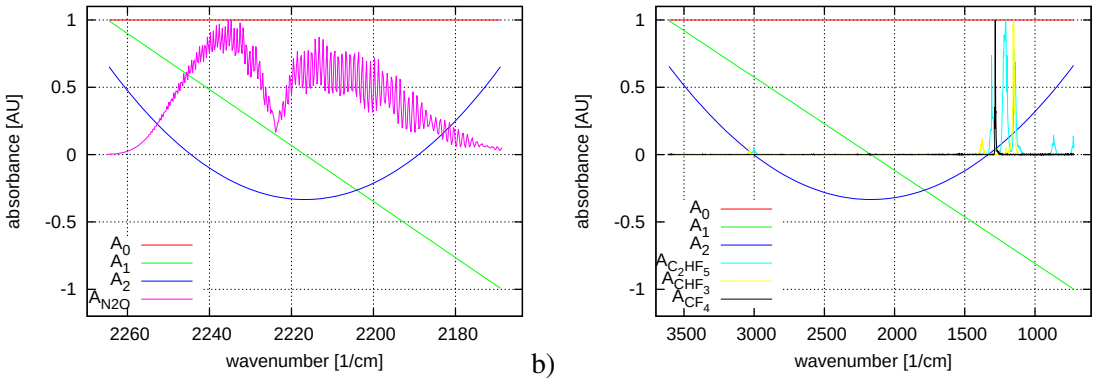

a) b)

Figure 5.9.: Fitted spectra used in the nitrous oxide removal method. a) only Nitrous oxide is fitted in the first step and then removed from the measured spectrum. b) all the other tracers are fitted next.

As a next step, nitrous oxide is removed from the measured spectrum. To do this, the best fitting reference test spectrum A^b_{test} is searched for. In the wavenumber region between 2168.653 and

2264.839 cm $^{-1}$, for all reference test spectra a residual value R_i is calculated after the reference test spectrum is subtracted from the measured spectrum,

$$R_i = \sum_{\lambda} \left| abs(\lambda) - A^i_{\text{test}}(\lambda) \right| . \tag{5.10}$$

The best fitting reference test spectrum A^b_{test} is the one spectrum, that has the lowest R_i value. This is subtracted from the whole measured spectrum, which is now free of absorbance signal of nitrous oxide.

As the last step, the other tracers are fitted using the function

$$abs_{\text{meas}}(\lambda) = a_0 \cdot A_0(\lambda) + a_1 \cdot A_1(\lambda) + a_2 \cdot A_2(\lambda) + f_2 \cdot A_{\text{CHF}_3}(\lambda) + f_3 \cdot A_{\text{C}_2\text{HF}_5}(\lambda) + f_4 \cdot A_{\text{CF}_4}(\lambda) \tag{5.11}$$

yielding absorbance values f_2 through f_4 for all other tracers. The reference spectra used in this fit can be seen in figure 5.9b.

Comparison of Both Methods

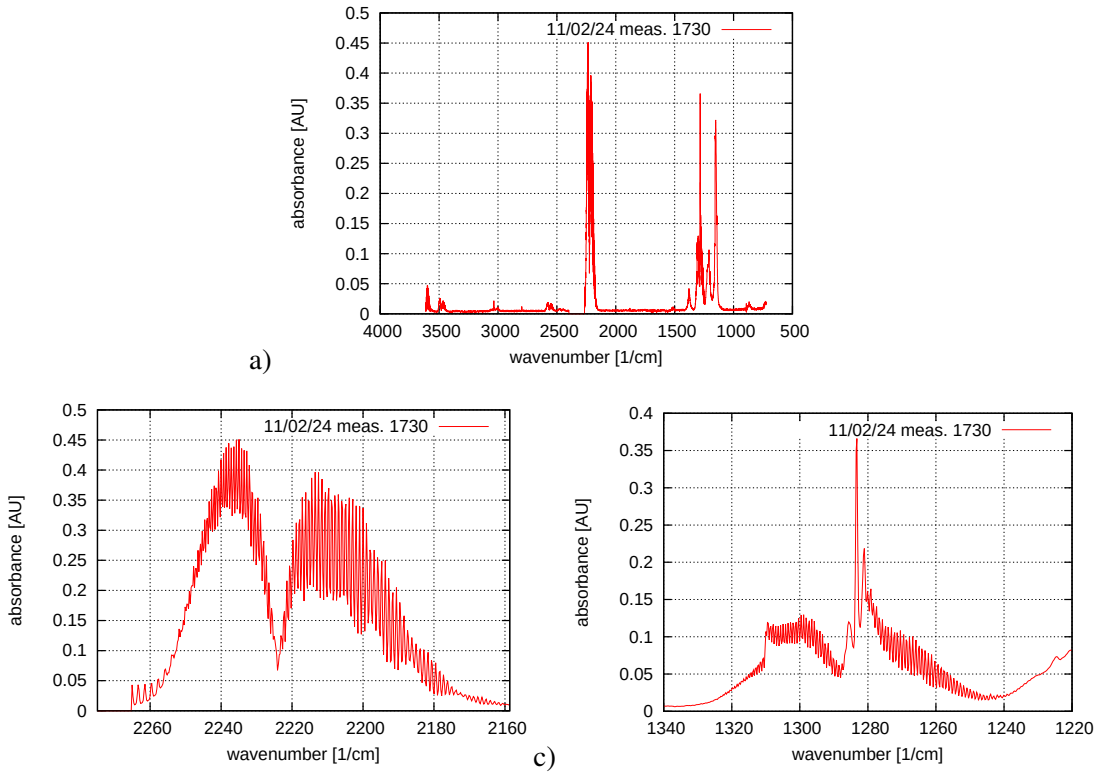

Figure 5.10.: a) One arbitrarily chosen measured spectrum from measuring day 12/02/24. b) Region of the measured spectrum where nitrous oxide has the maximum absorbance. c) Region of the spectrum, where nitrous oxide, tetrafluoromethane and Pentafluoroethane overlap, see also figure 5.8.

Both methods can be compared most easily in an example. Figure 5.10 shows an arbitrarily chosen measured spectrum as an example. A closer view of the region where nitrous oxide has its maximum absorbance and the region where multiple tracers' absorbances overlap is also shown. This spectrum was evaluated with the straightforward method as well as the method where nitrous oxide is removed from the spectrum before all other tracers are fitted. It should be noted that the

absorbance of carbon dioxide has been mostly removed from the spectrum. In figure 5.10b, at a wavenumber of around 2260 cm^{-1} in the rising flank of the absorbance of Nitrous oxide, some remnants of carbon dioxide are still visible as small peaks with the frequency of roughly one peak every 2 wavenumbers with an absorbance of less than 0.04.

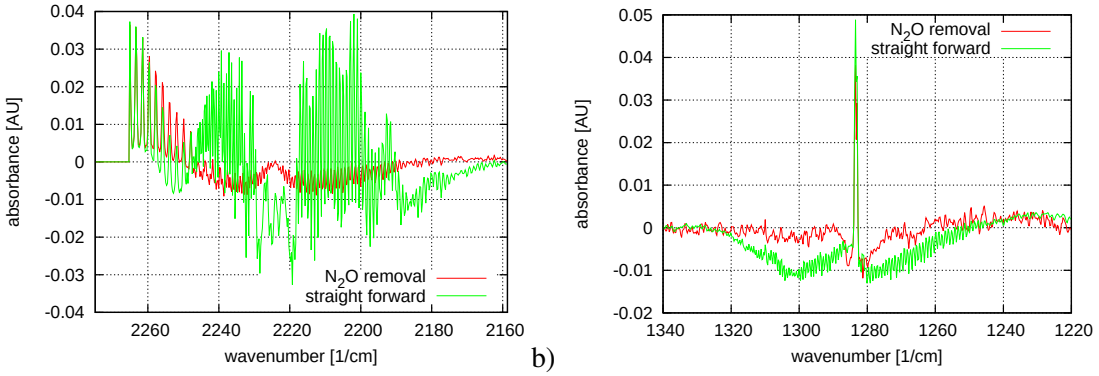

a) b)

Figure 5.11.: Comparison of residuals after two different analysis methods were applied to the spectrum shown in figure 5.10 a) in the region of the measured spectrum where nitrous oxide has the maximum absorbance; and b) in the region of the spectrum, where nitrous oxide, tetrafluoromethane and Pentafluoroethane overlap, see also figure 5.8.

Figure 5.11 shows a comparison of the residuals of the fit of both methods. In this context, a residual means all absorbance information as well as noise that was not accounted for by the fit. In figure 5.11a, the remnants of the carbon dioxide absorption signal are clearly visible at a wavenumber around 2260 cm^{-1}.

In the maximum absorbance region of nitrous oxide, see figure 5.11a, the residual of the straight forward method lies between 0.04 and -0.032 while the residual of the removal method lies between 0.002 and -0.008, when the CO_2 remnants are disregarded. This corresponds to a reduction of the residual by more than 80 % in the shown case. Also in the wavenumber region with the overlapping reference spectra, see figure 5.11b, the residuals changed considerably. With the removal method, only a large peak caused by an insufficient match between the scaled reference spectra of the tracer tetrafluoromethane and the measured spectrum is left. No traces of Nitrous oxide remain visible. That, in turn, means that no residual left over from the fit of nitrous oxide can be attributed to the absorbance of tetrafluoromethane and thus yield a wrong absorbance value for tetrafluoromethane as it happens in the straight forward method. Therefore, the N_2O removal method was chosen to evaluate the data.

Treatment of the Time Stamp

The time stamp that was stored during data acquisition with the gathered spectra is always kept with the absorbances. More than one spectrum needs to be evaluated for most measurements. Each of the single spectra is processed sequentially, one after another. The time stamp, that accompanies each spectrum is first read and then removed from the last position in the spectrum. Then the fit, either by the straight forward method or the removal method is performed, and the fit results, i.e. the absorbances of the tracers at that time, along with the time stamp is written sequentially into a file for further processing.

As the next step, the absorbance values need to be translated into actual concentrations for the FT-IR spectroscopy. This calibration procedure will be described in chapter 6.

For the UV spectroscopy, no absolute concentrations are needed. Looking at Beer's Law, equation 2.78, it can be seen that the Absorbance abs is proportional to the concentration, $abs \propto c$.

As only the temporal development of the concentration is of interest, no absolute concentrations have to be calculated. For UV spectroscopy, the term concentration will be used as a synonym of absorbance.

5.3. Calculating Transfer Velocities and Schmidt Number Exponents

Up to this section, data processing yielded time series of absorbance or concentration values. Further data processing is needed to arrive at the sought for transfer velocities.

5.3.1. FT-IR Spectroscopy in the Heidelberg Aeolotron

The calculation of two results, the transfer velocity as well as the Schmidt number exponent will be described here.

5.3.2. Transfer Velocities

Chapter 6 clarifies how to translate absorbances into concentrations for the FT-IR spectroscopy. Once the concentrations in each time step are known, transfer velocities can be calculated.

To evaluate the experiments, the $\dot{c}_a$ Method with a small leak rate, see section 3.3.1, was used. To apply this method, the air side concentration time series needs to be derived with respect to time. First, the concentration time series was smoothed using a filter with a mask size of 16 data points (operator *Bin16()* in the image processing software *Heurisko*). Then the actual derivation was made by calculating differences between the preceding and following data point and multiplying by 0.5 (operator *D1_3S()* in *Heurisko*).

For each time step in which the Aeolotron is closed, a transfer velocity was calculated using equation 3.15. Because the water side concentration c_w was not measured directly, see section 4.4.1, this equation needs to be modified. The concentration in air, that was equilibrated with water, c'_w was measured. The water side concentration and the equilibrated concentration are linked by the solubility α of the tracer, $c_w = \alpha\, c'_w$. Therefore, equation 3.15 is modified to

$$k_w = \frac{V_a}{A} \cdot \frac{\lambda c_a}{\alpha\, c'_w} \cdot \frac{\lambda + \dot{c}_a/c_a}{\lambda} \cdot \frac{1}{1 - c_a/c'_w}. \tag{5.12}$$

All measured values are inserted into this equation, yielding a time resolved transfer velocity.

As an example figure 5.12a and 5.12b show air and water side concentration of the tracer nitrous oxide on measuring day 2011/02/18. Gaps in the in the shown data are due to the removal of data taken during the flushing phases of the experiment. Time resolved transfer velocities were calculated in this fashion for all tracers and all days.

As a final step, the arithmetic mean of the gas transfer rates for each wind speed condition was calculated. These average transfer velocities will be discussed in detail in the results chapter, see section 7.4.2.

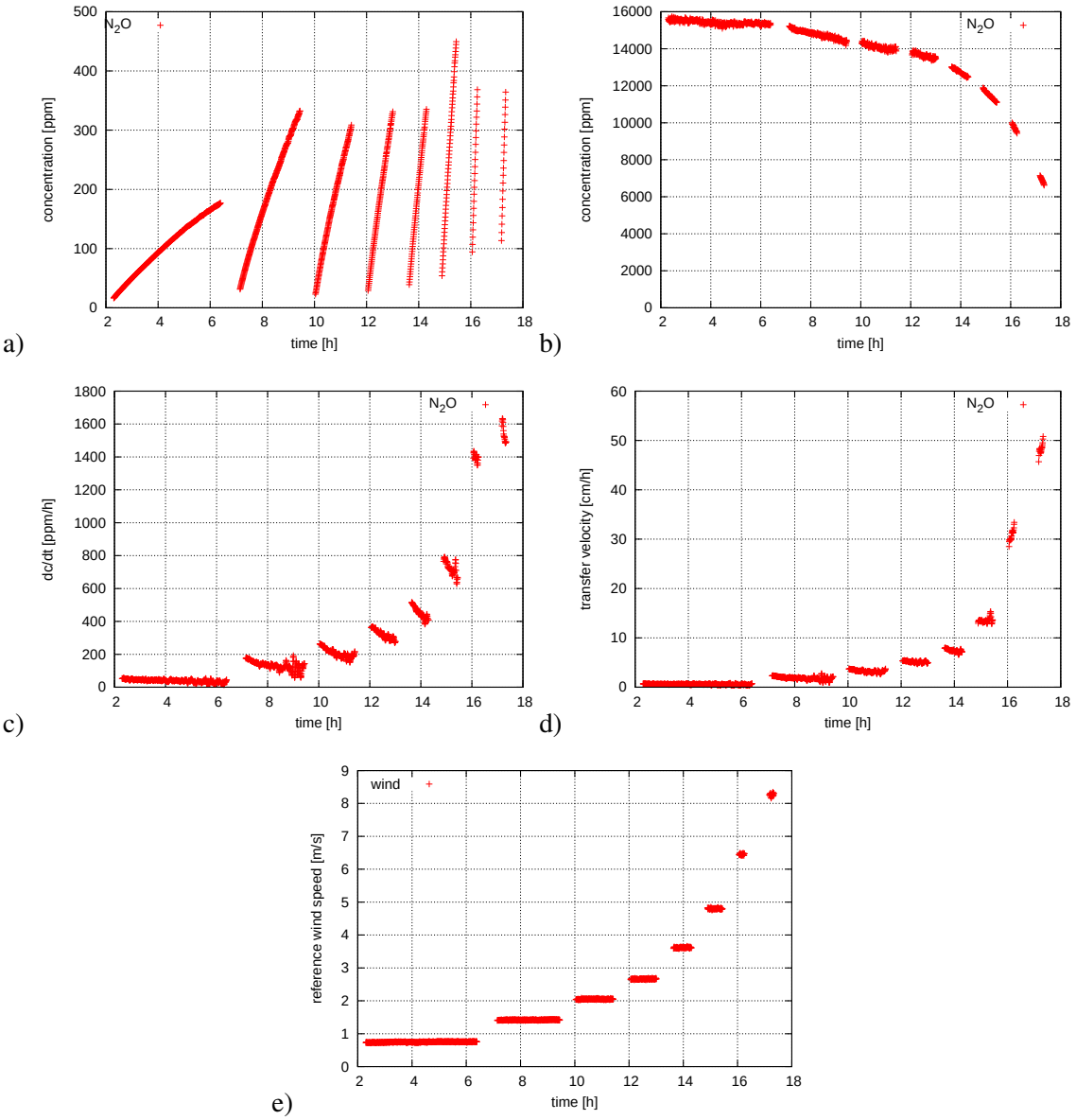

Figure 5.12.: a) measured air side concentration b) measured water side concentration c) calculated derivative of the air side concentration d) calculated transfer velocities of tracer N_2O as well as e) the reference wind speed on measuring day 2011/02/18.

5.3.3. Schmidt Number Exponents

The concentration time series of two tracers A and B are also used to calculate the Schmidt number exponents. Equation 2.68 is transformed to

$$n = \frac{\log\left(k_A/k_B\right)}{\log\left(D_B/D_A\right)}. \tag{5.13}$$

Using equation 5.12, the ratio of the two transfer velocities can be expressed as

$$\frac{k_A}{k_B} = \frac{\alpha^A}{\alpha^B} \cdot \frac{c_w'^B}{c_w'^A} \cdot \frac{c_a^A\lambda + \dot{c}_a^A}{c_a^B\lambda + \dot{c}_a^B} \cdot \frac{1 - c_a^B/c_w^B}{1 - c_a^A/c_w^A}. \tag{5.14}$$

This Schmidt number exponent depends only on ratios of measured concentrations and solubilities and is no longer depending on geometric properties of the wind-wave tank. Figure 5.13 shows the

measured, time resolved Schmidt number exponents for all three tracer combinations for measuring day 2011/02/22.

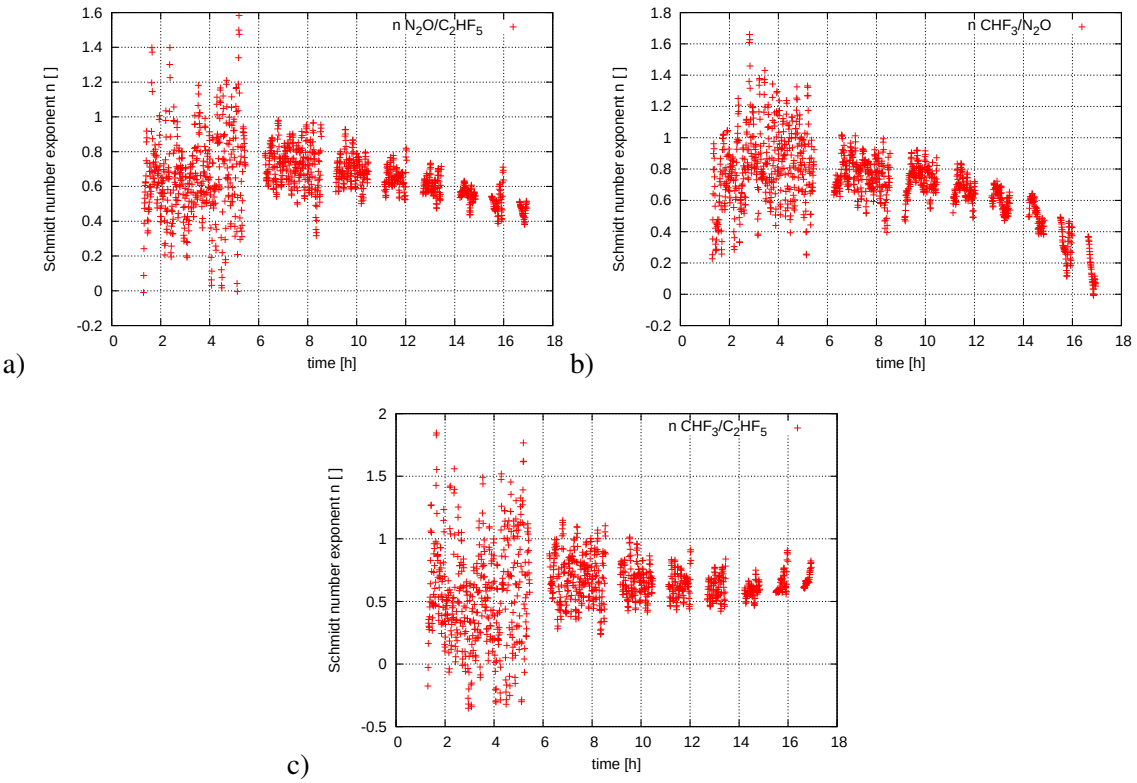

Figure 5.13.: Measured time resolved Schmidt number exponents for measuring day 2011/02/22 a) tracer combination N_2O and C_2HF_5. b) tracer combination N_2O and CHF_3. c) tracer combination CHF_3 and C_2HF_5.

As a last step, for each wind speed condition the arithmetic mean of the measured Schmidt number exponents is calculated. These will be discussed in detail in section 7.4.3.

5.3.4. Transfer Velocities in the Kyoto High-Speed Wind Wave Tank

The classic evasion method, see section 3.3.2, was used to measure the transfer velocities of two volatile organic hydrocarbons, hexafluorobenzene and 1,4-difluorobenzene.

Figure 5.14 show the absorbance time series of the tracers Hexafluorobenzene and 1,4-Difluorobenzene measured on day 2011/10/30. Two different wind speed conditions were covered on this day. In the first hour of the shown time series, the mixing of the tracer into the water body is visible in the form of damped oscillations of the absorbance.

The classic evasion method predicts an exponential decrease of the concentration, see equation 3.20. Once the wind is turned on to u_{10}=16.7 m/s, at a time of about 1.8 h, the concentration of both tracers starts to decrease as expected. At 4.7 h into the measurement, the wind is turned off, leading to a constant concentration. At t=5 h, the wind is turned on to the higher velocity of u_{10}=48.0 m/s, the concentrations of both tracers start to decrease again. At about t=6.05 h, the experiment is finished by turning the wind off and disconnecting the sampling loop from the gas extraction to sample lamp spectra yielding a concentration of 0 for both tracers.

The evaluation of this time series uses the exponential decay of the concentration. Due to Beer's law stating that absorbance is proportional to concentration, $abs \propto c$, the concentration in equation

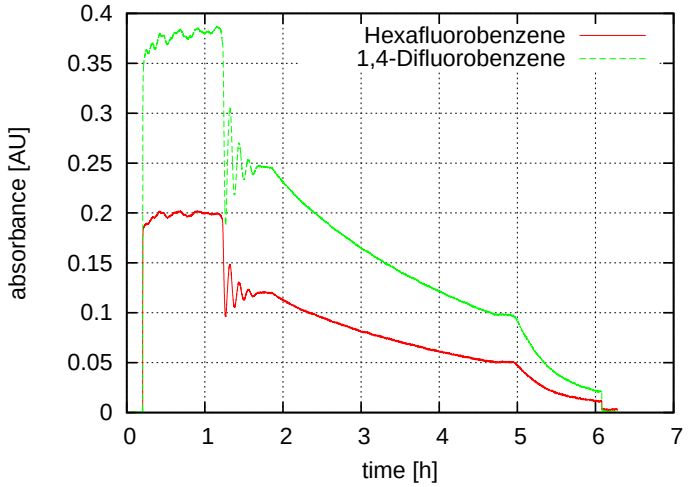

Figure 5.14.: Time series of the absorbances of the tracers Hexafluorobenzene and 1,4-Difluorobenzene on measuring day 2012/10/30.

3.20 can be substituted for the absorbance,

$$abs(t) = abs(0) * e^{(-\lambda * t)}. \tag{5.15}$$

with the time constant of the process

$$\lambda = k_w * \frac{F}{V_w} + \frac{\dot{V}_w}{V_w} \tag{5.16}$$

depending on the transfer velocity k_w, the water surface area F and the water volume V_w as well as the water lost to spray and replaced by fresh water, $\dot{V}_w$.

This equation could be fitted to the absorbance time series obtained in the previous steps of data processing. However, it turned out that the absorbances rarely decreased to exactly zero. Therefore, equation 5.15 is modified by introducing an offset abs_{off},

$$abs(t) = abs_{\text{off}} + abs(0) * e^{-\lambda * t}. \tag{5.17}$$

This equation was chosen to fit to the measured absorbance time series with the free parameters abs_{off}, $abs(0)$ and λ by a least squares fit using the data analysis tool *gnuplot*. Equation 5.16 was then used to calculate the transfer velocity k_w. Figure 5.15 shows the fits of equation 5.15 and 5.17 to the time series shown in figure 5.14.

It is clearly evident that the fit of the equation allowing for a linear offset of the absorbance yields a better approximation of the actual shape of the decrease of the concentration. Therefore, equation 5.17 was chosen to be fitted to all data sets. In about one third of all experiments, the offset abs_{off} was negative, in the other cases positive. There are some different possible causes for this non-zero offset. If the cause lay in an impure lamp spectrum, meaning that some tracer was in the measuring cell during the acquisition of the lamp spectrum the offset would always be negative. If tracer accumulated in the plastic tubing of the sampling loop or in the plastic mounting mechanism of the spectroscopy cell, then the offset would always be positive. Because the sign of the offset varies, both assumptions cannot account for the observed effects.

Most likely the lamp spectrum changed in shape during the experiment. Warming (the UV-lamp produces some waste heat) or cooling of the mounting mechanism of the optical components (*Linos microbank*) during one measurement day may have slightly changed the length of the light path. Due to the chromatic aberration of the lenses used in the setup, a change in optical length

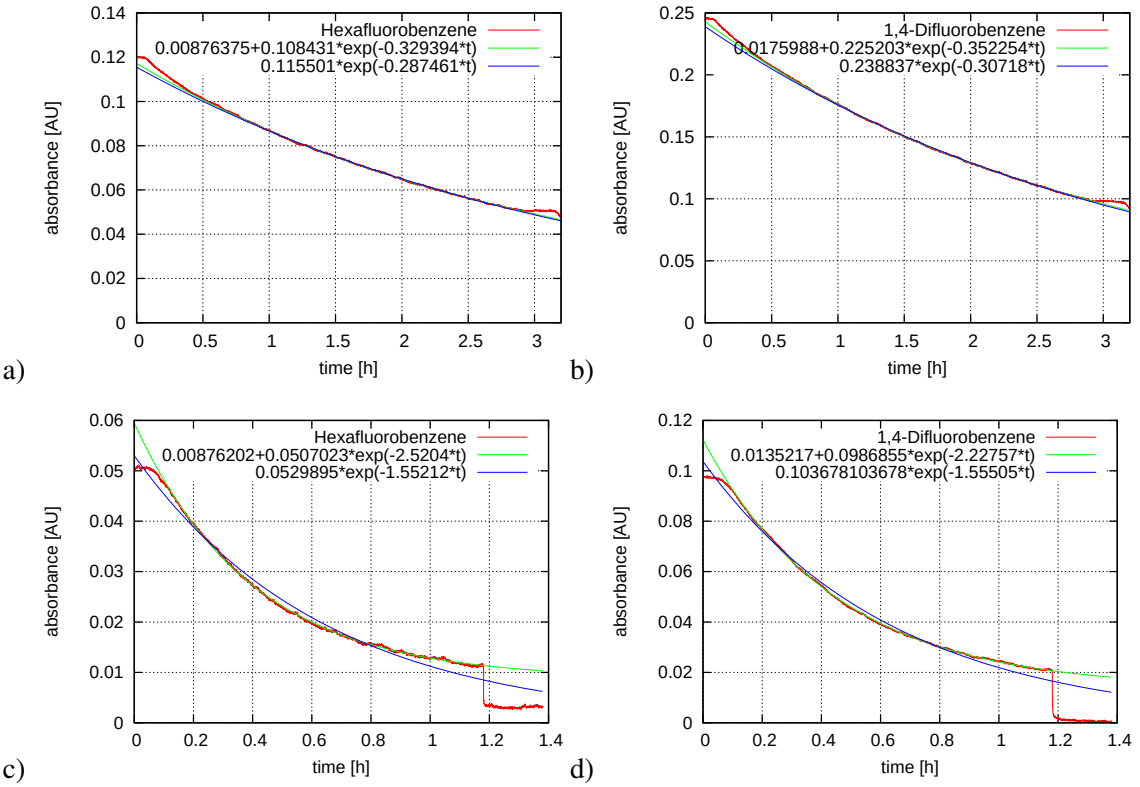

Figure 5.15.: Time series of the absorbances (red) of both tracers on measuring day 2011/10/30 including fits of equation 5.15 (blue) and 5.17 (green). a) u_{10}=16.7 m/s, tracer: hexafluorobenzene. b) u_{10}=16.7 m/s, tracer: 1,4-difluorobenzene. c) u_{10}=48.0 m/s, tracer: hexafluorobenzene. d) u_{10}=48.0 m/s, tracer: 1,4-difluorobenzene. The start of the time axis (t=0) was modified to allow for a more stable fit.

could have focused different wavelength regions onto the glass fiber that led the light into the spectrometer, thus changing the shape of the spectrum. This is not fully corrected by the fitting algorithm described in section 5.2. Only a uniform change in light intensity at all wavelengths (reference spectrum A_0) or changes that lead to linear (reference spectrum A_1) or quadratic (reference spectrum A_2) signature in the calculated absorbance are corrected.

Except for the offset that is not predicted by theoretical considerations, some more measurements were problematic in the analysis. They will be discussed in the next section. All time series as well as their fits can be found in [Krall, 2012].

Problematic cases

On two measuring days (**2011/10/28** and **2011/11/10**) the absorbance of hexafluorobenzene suddenly increases or decreases from one time step to the next, see figures 5.16a and 5.16c. However, an attempt to fit equation 5.17 to the data was made. In figure 5.16b, the fit was limited to the regions between 0.95 h and the upward jump of the absorbance at 1.15 h and the region between the downward jump at 1.52 h and 2.1 h. All data points between 1.15 h and 1.52 h were not included in the fit. The fit results can be seen in figure 5.16b. On 2011/11/10 in figure 5.16d, two different fits were made. The first fit, green in the figure, included the 'upper' parts of the concentration, meaning the regions between 0.15 h and the downward jump at 0.23 h as well as he time region between 0.67 h and 0.97 h. The second fit, blue in 5.16d, included the time region between 0.23 h and 0.67 h. The fit parameters $\lambda = 6.62\,h^{-1}$ for the green fit and $\lambda = 6.57\,h^{-1}$ for the blue fit

are identical within the error margins. This indicates, that there are indeed no sudden increases or decreases of the concentration itself, but rather some sort of intensity problem within the optical setup.

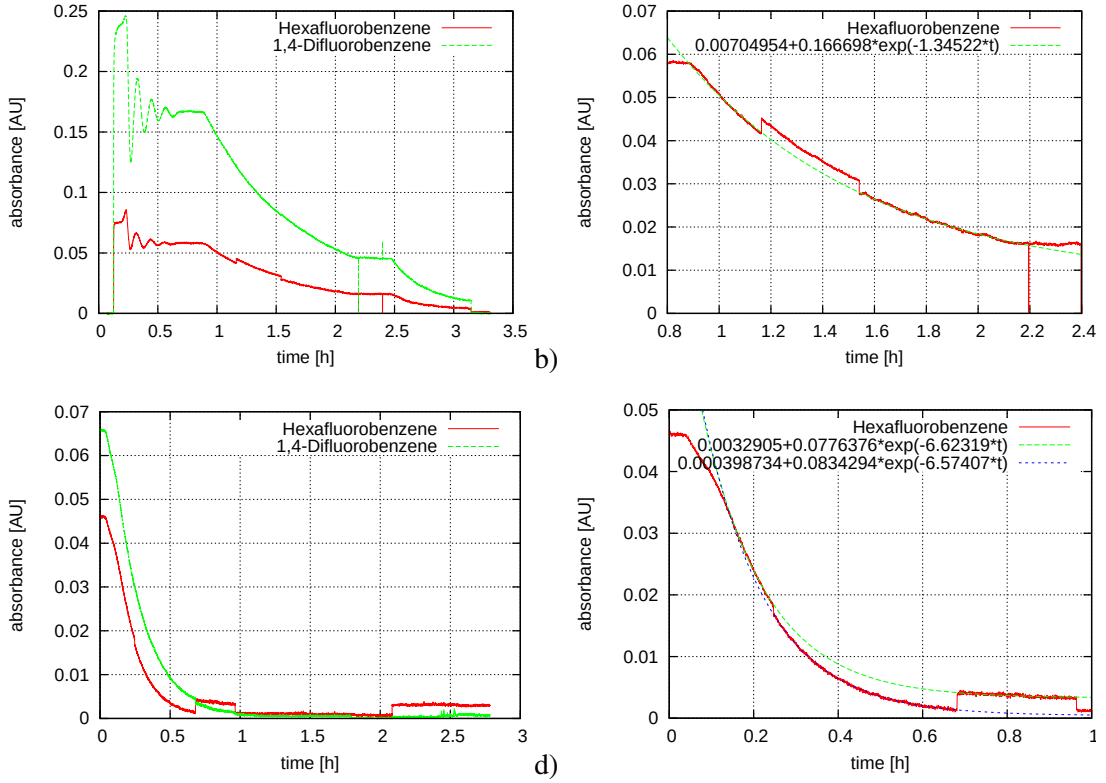

Figure 5.16.: a) Absorbance time series of both tracers on 2011/10/28. b) Hexafluorobenzene on 2011/10/28. Sudden increases and decreases at 1.15 h and 1.52 h, respectively, are clearly visible. c) Absorbance time series of both tracers on 2011/11/10. d) Hexafluorobenzene on 2011/11/10. At 0.23 h, 0.67 and 0.97 h the absorbance suddenly decreases or increases.

A further study was done with the data from 2011/11/10. Figure 5.17 shows in the upper part a section of the raw data from that measuring day. The light intensity, measured by the spectrometer is color coded. One vertical line of the image corresponds to one spectrum. The time runs horizontally. Below the image the measured absorbance of hexafluorobenzene is shown within the same time frame. The red arrows in the raw data mark the times, when the measured absorbance suddenly increases or decreases. In the raw data, across the whole spectrum, the light intensity visibly changes. It can only be guessed why this is happens. It may well be the case that some larger piece of dust settled down somewhere within the optical path and was loosened again some time later. But since the measured time constants λ are identical, the results are considered as valid. It is assumed, that the same cause led to the change of the spectrum on 2011/10/28. Therefore, the fit result from this day is also considered as valid.

On **2011/11/14**, **2011/11/15** and **2011/11/17** the concentrations measured do not show a smooth exponential decay as expected, but rather two different exponential segments with bend in the middle, see figure 5.18.

Both exponential sections were fitted separately and the fit result was compared. Figure 5.19 show the fits of the affected concentration time series. In all but one case (the 1,4-difluorobenzene on 11/11/14, fig. 5.19b) the exponents λ were found to be equal for both exponential sections

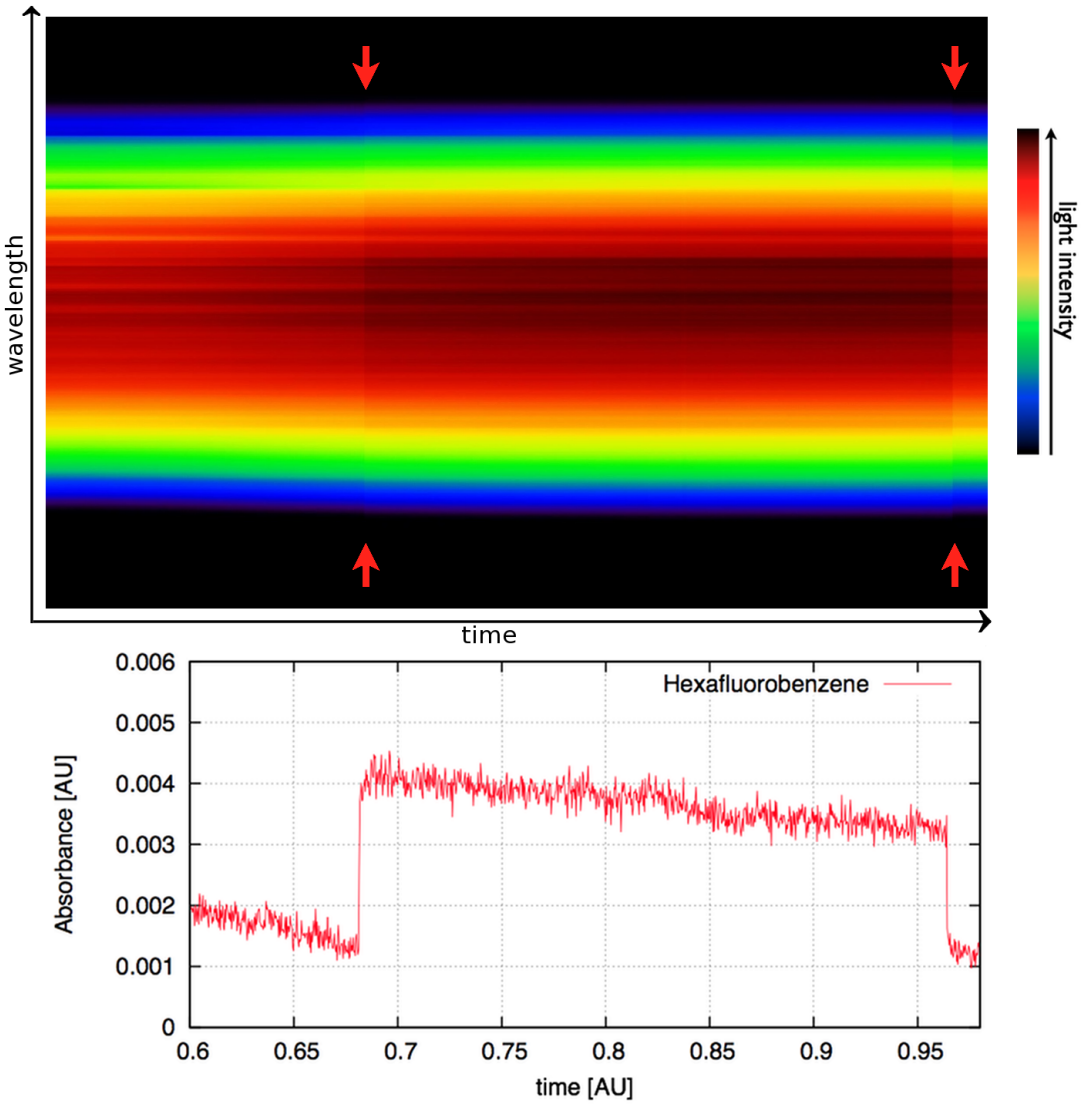

Figure 5.17.: Upper part: raw data taken on 2011/11/10, color coded. One vertical line corresponds to one spectrum. Calculated hexafluorobenzene absorbance during the same time frame as the raw data.

within the accuracy of the fit. However, large differences in the offset fit parameter abs_{off} can be seen. In one case (hexafluorobenzene on 11/11/14, fig.5.19a) the offset decreased from $abs_{\text{off}} =$ 0.0184 to -0.0316, in two other cases the offset increased (hexafluorobenzene on 11/11/15 and 11/11/17, fig.5.19c and 5.19d) from abs_{off} =-0.0216 to -0.00322 and abs_{off} =-0.0291 to -0.00611. What caused this bend in the concentration time series, or this shift in the offset, is not known. For the three cases in which the exponent parameter λ is identical, the mean of both values is used as the measured value. A comparison of the exponents λ with exponents measured under identical conditions, when the bend was not observed, showed that they are very plausible. Therefore, they are considered to be correct values. For the one measurement, where the exponents did not agree (1,4-difluorobenzene on 11/11/14), the more plausible value of $\lambda = 0.091\, h^{-1}$ is regarded as the correct value.

The concentration time series for hexafluorobenzene proved to be non-evaluable on **2011/11/11**. Figure 5.20a shows the hexafluorobenzene concentration time series during an experiment with stable, constant conditions. The corresponding 1,4-Difluorobenzene is shown in figure 5.20b. In

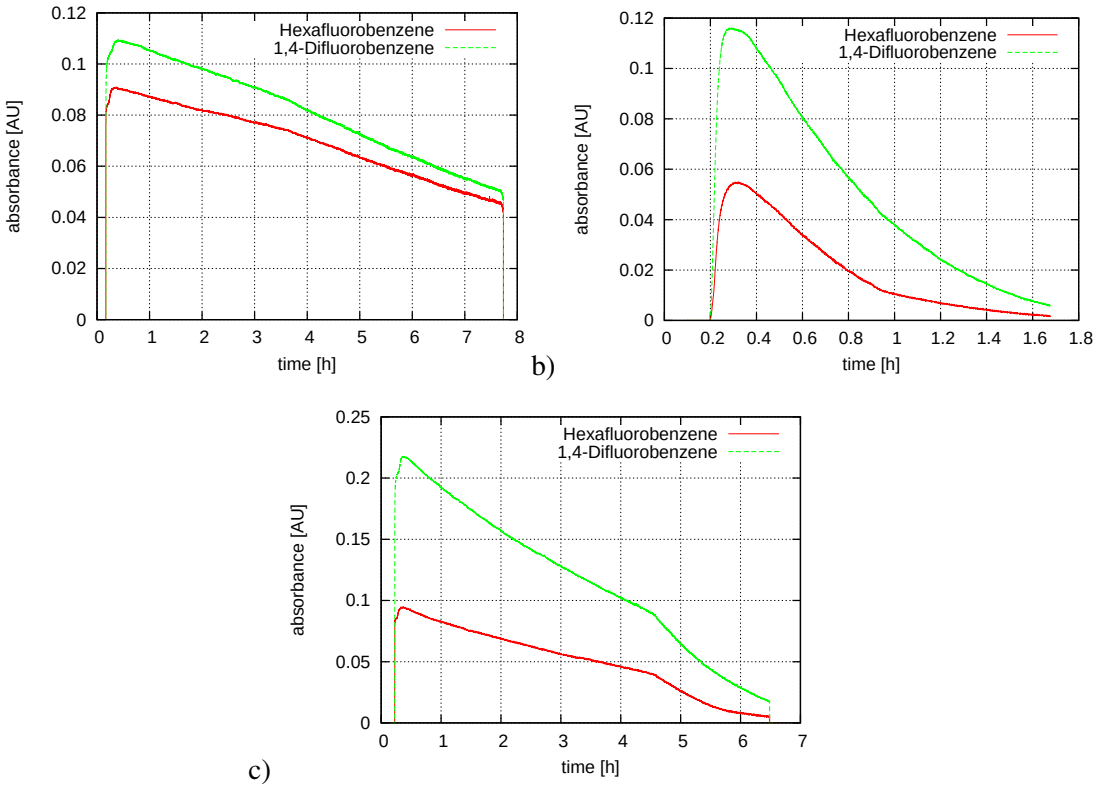

Figure 5.18.: a) absorbance time series from 2011/11/14, showing a bend in the exponential decrease at 3.6 h, although none of the experimental conditions were changed b) absorbance time series from 2011/11/15 with a bend in the hexafluorobenzene absorbance at 0.95 h and c) from 2011/11/17 with a bend in the hexafluorobenzene during the second condition at 5.6 h (hardly visible, see also figure 5.19d for a close up plot)

the Hexalfuorobenzene plot several different, yet possible exponential curves are fitted. Depending on the fitted time frame, many exponents λ can be determined, differing by as much as a factor of 2. To the contrary, the 1,4-difluorobenzene concentration behaves just like expected with a smooth exponential decrease.

The cause of this is unknown. One possible explanation is that a droplet of the pure liquid hexafluorobenzene may have entered the water volume during the input of the tracer as the other tracer 1,4-difluorobenzene does not show any unusual behavior. Due to the ambiguity of the resulting exponent λ, the time series of hexafluorobenzene is discarded totally.

On **2011/11/16** the hexafluorobenzene again showed an unexpected behaviour during the first of two different wind speed conditions, see figure 5.21a. The 1,4-Diffluorobenzene is, again, normal, see figure 5.21b. At about 0.97 h, a tiny drop in concentration can be seen in the hexafluorobenzene concentration time series. After that drop, the concentration does no longer show the expected exponential behavior. At about 2.7 h, the concentration time series turns exponential again. The fit was therefore limited to the region before 0.97 h and after 2.7 h.

The cause is also unknown. As the calculated λ has the expected size, the data is flagged valid.

On **2011/11/19** the concentration of hexafluorobenzene was not exponentially decreasing until roughly 30 minutes into the experiment, see figure 5.22a, while the 1,4-difluorobenzene behaved normally, see figure 5.22b. The fit was limited to the time region after 0.5 h. As the λ has the expected size, the data is considered valid. The cause is unknown, but might be related to the one

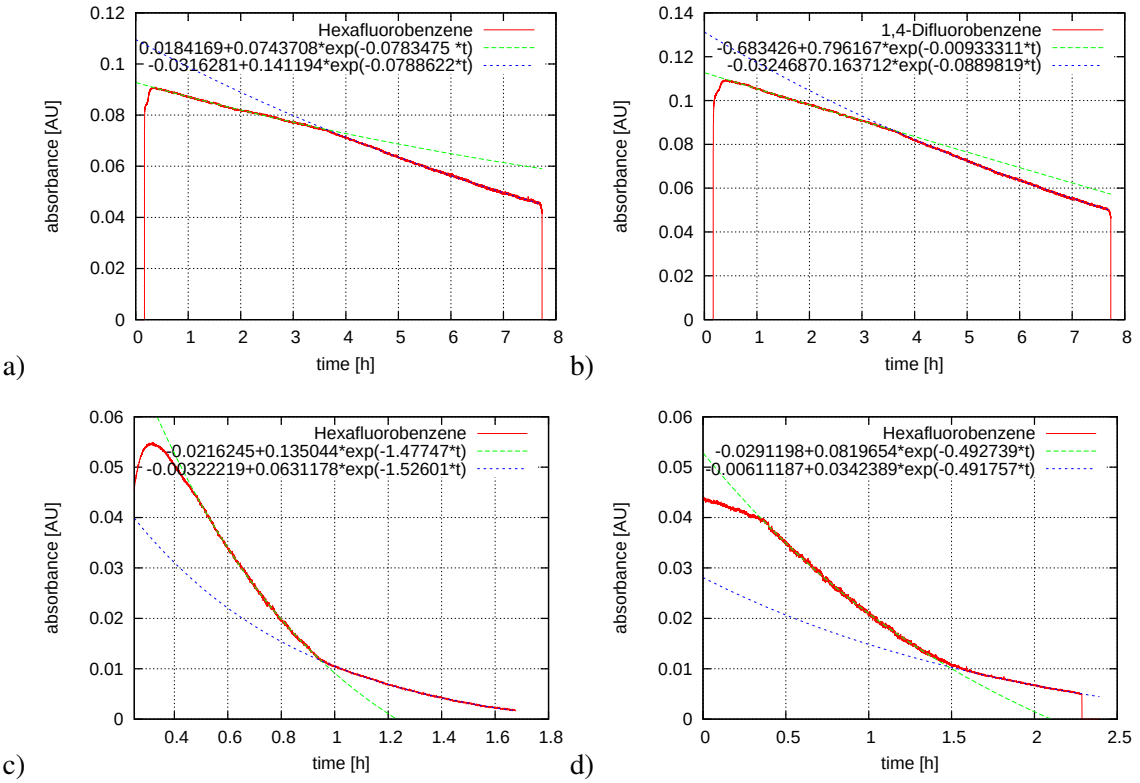

Figure 5.19.: Fits of the concentration time series shown in figure 5.18 that show a peculiar bend a) 2011/11/14 hexafluorobenzene b) 2011/11/14 1,4-difluorobenzene c) 2011/11/15 hexafluorobenzene d) 2011/11/17 hexafluorobenzene. For all but b) the exponent λ of the exponential curves is identical for the two exponential sections.

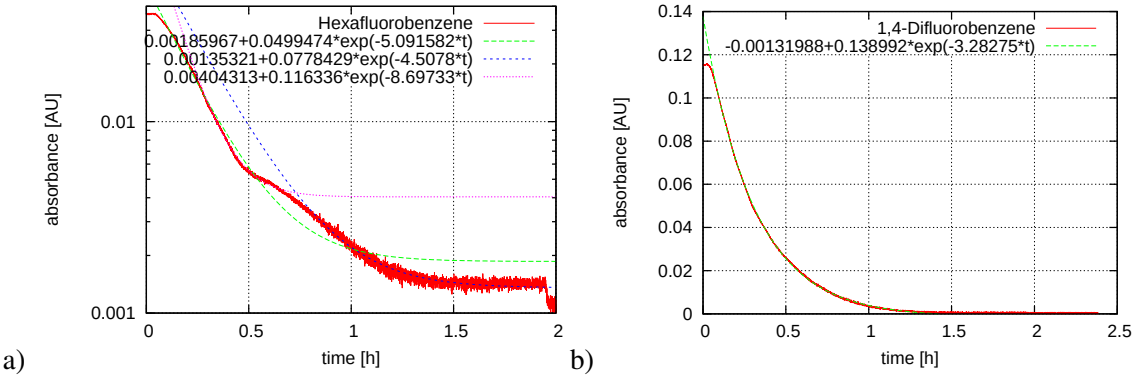

Figure 5.20.: a) Hexafluorobenzene and b) 1,4-Difluorobenzene on 2011/11/11. Shown in a) are three different fits with different fitting region.

that caused the bend in other time series shown before.

In table 5.1 a summary of the evaluability of the measurements is shown. In total, one fourth of the time series were slightly problematic, with only one out of 42 being not evaluable.

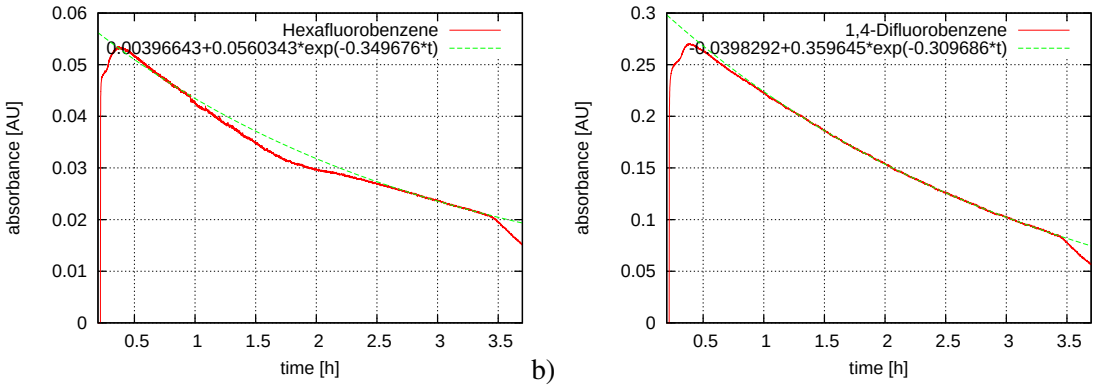

a) b)

Figure 5.21.: a) non-exponential behavior of the concentration of hexafluorobenzene on 2011/11/16. b) same experiment, but 1,4-difluorobenzene is shown.

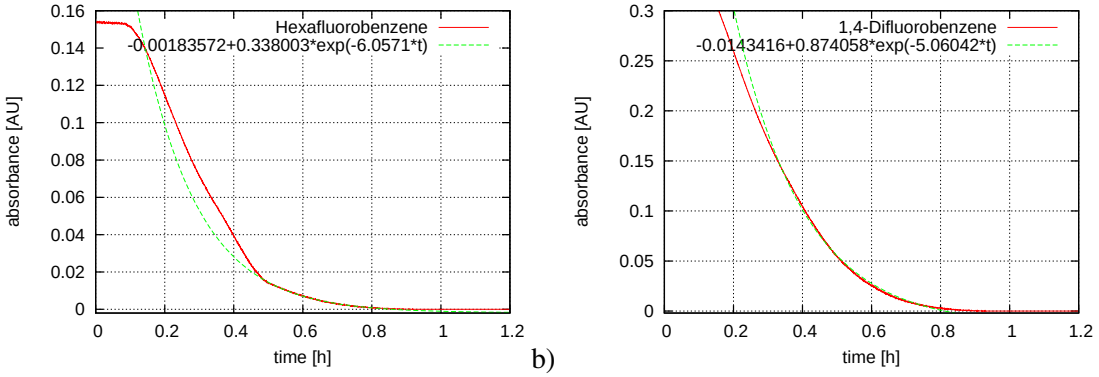

a) b)

Figure 5.22.: a) non-exponential behavior of the concentration of hexafluorobenzene on 2011/11/19. b) same experiment, but 1,4-difluorobenzene is shown.

tracer	Number of conditions with		
	no Problem	a problem, but evaluable	not evaluable
1,4-Difluorobenzene	18	3	0
Hexafluorobenzene	13	7	1
all	31	10	1

Table 5.1.: Evaluability of the UV spectroscopic time series.

6. Calibration of the FT-IR Spectrometers

The spectra taken by the Fourier Transform Infrared Spectrometers (FT-IR) have to be translated into gas concentrations. For this, a calibration is needed. Obtaining such a calibration is discussed in detail in this chapter.

6.1. General Principle

A continuous flow of pure gas is mixed into a stream of dried, CO_2-free air using a mixing cell, see figure 6.1. This mixture is then pumped through the measuring cell in the FT-IR spectrometers. Using precise mass flow controllers for the air as well as the gas to be calibrated, the mixing ratio can be adjusted. To obtain the whole relationship between tracer concentration and absorbance, the concentration of the pure gas was slowly varied in time between 0 and an absorbance of about 1, while the FT-IR spectrometer was continuously taking sample spectra.

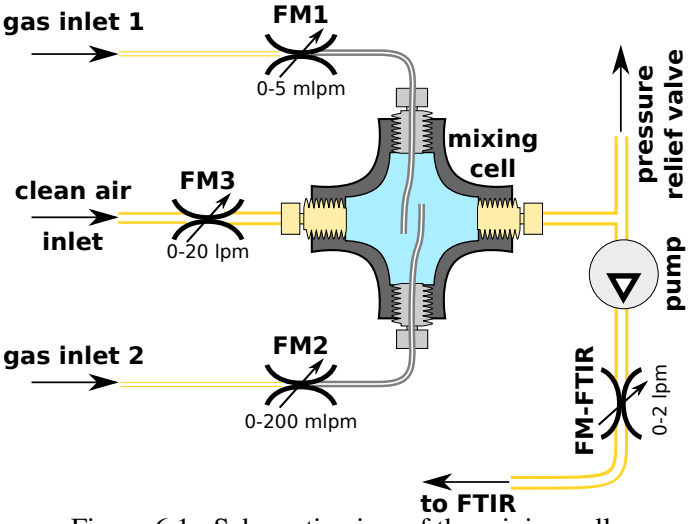

Figure 6.1.: Schematic view of the mixing cell.

The mixing cell was constructed such that a large range of output concentrations can be set. Therefore, at the gas inlet two different mass flow controllers where used. When very low concentrations where needed, mass flow controller FM1 (*MFC Series 358*, manufactured by *Analyt-MTC*) with a throughput of $0 - 5\,\mathrm{ml/min}$ was connected to the tracer supply. For higher concentrations, FM2 (*MFC Series 358*, manufactured by *Analyt-MTC*) with $0 - 200\,\mathrm{ml/min}$ was used. Air was supplied by FM3 (*MFC Series 358*, manufactured by *Analyt-MTC*) which is capable of providing a flux of $0 - 20000\,\mathrm{ml/min}$.

To enhance turbulent mixing within the cell, the two stainless steel tubes supplying the pure gas where inserted into the cell so that they ended right within the air flow.

6.2. Determining the Concentration

The mass flow controllers used in the mixing cell work by opening and closing a precise valve which limits the flux. The flux $\dot{V}$ is monitored by generating a laminar flow through a tube of length z and radius r and measuring the pressure difference Δp between the beginning and the end of that tube. Using Hagen-Poiseuille's law,

$$\dot{V} = \frac{\pi r^4}{8\eta}\frac{\Delta p}{l}, \tag{6.1}$$

the flux can be calculated. However, the flux also depends on the kinematic viscosity η_g of the tracer used. In their internal calculation, the mass flow controllers assume a viscosity of pure air at normal conditions, η_{air}. For all other gases the flux reading $\dot{V}_r$ of the mass flow controller has to be modified by

$$\dot{V}_g = \dot{V}_r \frac{\eta_g}{\eta_{air}}. \tag{6.2}$$

to get the actual gas flux, V_g.

The volume mixing ratio c of the gas in the output of the mixing cell can then be calculated as

$$c = \frac{\dot{V}_g}{\dot{V}_{tot}} = \frac{\dot{V}_g}{\dot{V}_{air} + \dot{V}_g} = \frac{\dot{V}_r \cdot \eta_g/\eta_{air}}{\dot{V}_{air} + \dot{V}_r \cdot \eta_g/\eta_{air}} \tag{6.3}$$

This air is then entering the FT-IT spectrometer measuring cell as input concentration c_{in}.

6.3. Calibration Factors

The absorbance spectra taken during the calibration measurements are first processed as described in chapter 5 to yield time series of absorbance numbers for the tracer that is to be calibrated.

Using the time stamps stored with each spectrum, the concentration c that was flowing through the measurement cell of the FT-IR while that spectrum was measured can be matched to the absorbances abs. A parameterization of the form

$$c[ppm] = A * \mathrm{abs} + B * \mathrm{abs}^2 \tag{6.4}$$

with the free parameters A and B is fitted to the concentration-absorbance pairs. This function can then be used to calculate the concentration from the measured absorbance in gas exchange measurements.

Shown here are concentration and absorbance time series as well as fit results of the tracers Nitrous Oxide, Trifluoromethane, Pentafluoroethane and Tetrafluoromethane.

6.3.1. CHF_3

Figure 6.2a shows the time series of the input concentration of Trifluoromethane into the air sided spectrometer during the calibration. Figure 6.2b, in turn, shows the time series of the measured absorbance during the same calibration run. The relationship between both as well as the calibration fit of equation 6.4 is shown in figure 6.3a.

All tracers were calibrated in this fashion. For the water sided spectrum of Trifluoromethane, $c(\mathrm{abs})$ as well as the fit is shown in 6.3b.

For clarity reasons, no error bars are shown. The calibrations including the errorbars are shown in Appendix A.3.

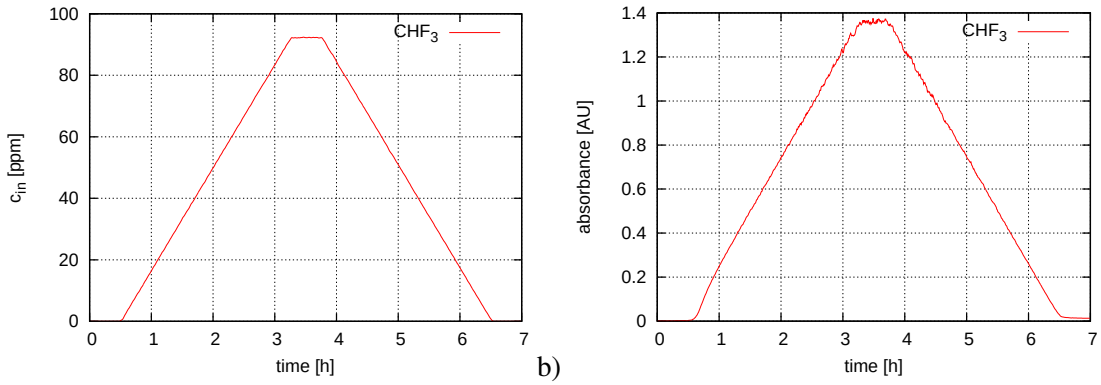

Figure 6.2.: a) Concentration time series of CHF_3 that was put through the measuring cell of the air sided spectrometer. b) Measured absorbance time series in the same calibration run.

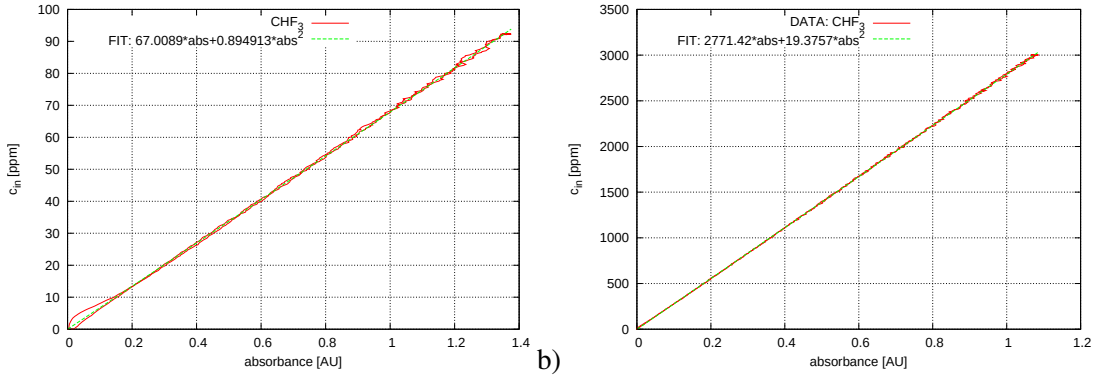

Figure 6.3.: Relationship between input concentration and measured absorbance of CHF_3 for a) the air-sided spectrometer and b) the water sided spectrometer. Also shown is a quadratic fit. In the air-sided (water-sided) fit the region between 0 and 0.2 (0 and 0.05) was omitted. For clarity reasons, the errorbars are not shown.

6.3.2. N_2O

The air- and water-side calibration of Nitrous Oxide is shown in figure 6.4. This tracer does not show a linear behavior like Trifluoromethane, meaning that a doubling of the concentration does not lead to a doubling in the measured absorbance. Reasons for this are discussed in section 6.4 about the uncertainties of the calibration.

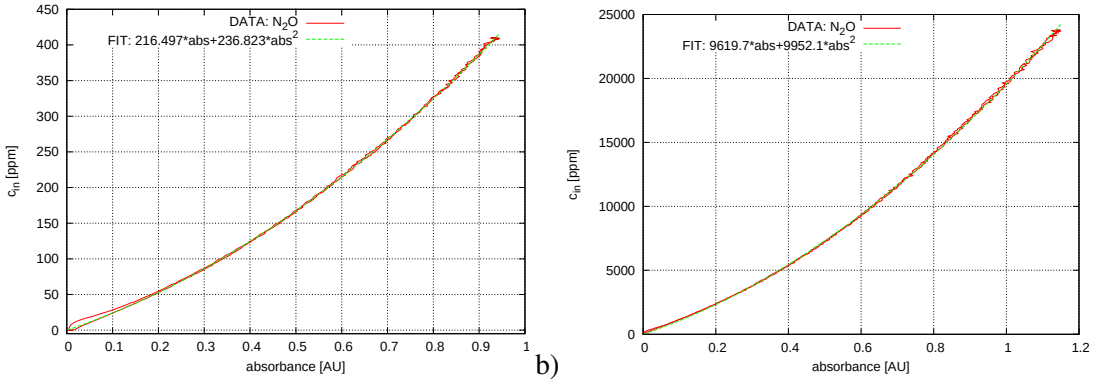

a) b)

Figure 6.4.: Relationship between input concentration and measured absorbance of N_2O for a) the air-sided spectrometer and b) the water sided spectrometer. Also shown is a quadratic fit. In the air-sided (water-sided) fit the absorbance region between 0 and 0.2 (0 and 0.05) was omitted. For clarity reasons, the errorbars are not shown.

6.3.3. C_2HF_5

Figure 6.5 shows the air- and water-side calibration of Pentafluoroethane.

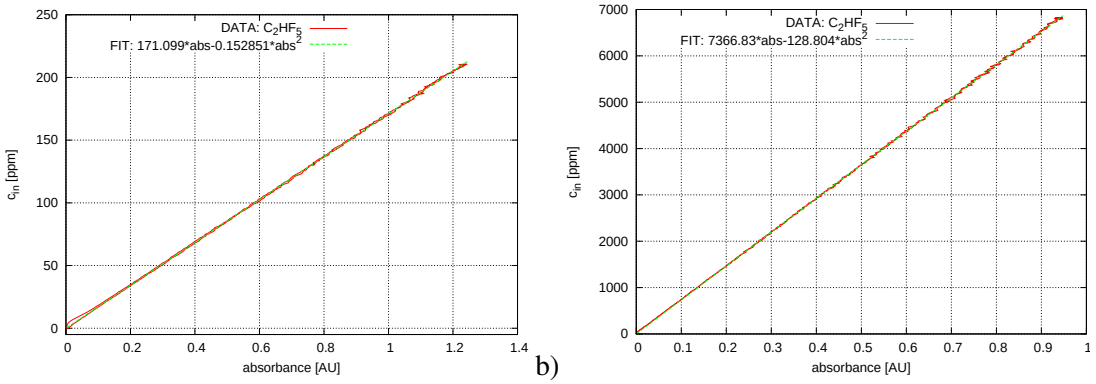

a) b)

Figure 6.5.: Relationship between input concentration and measured absorbance of C_2HF_5 for a) the air-sided spectrometer and b) the water sided spectrometer. Also shown is a quadratic fit. In the air-sided (water-sided) fit the absorbance region between 0 and 0.2 (0 and 0.05) was omitted. For clarity reasons, the errorbars are not shown.

6.3.4. CF_4

For Tetrafluoromethane, only an air-side calibration is needed, which is shown in figure 6.6. Again, this tracer does not show a linear relationship between concentration and absorbance. See section 6.4 for an explanation.

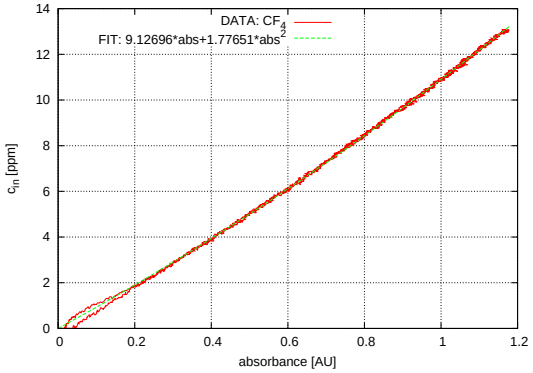

Figure 6.6.: Relationship between input concentration and measured absorbance of CF_4 for the air-sided spectrometer Also shown is a quadratic fit where the absorbance region between 0 and 0.2 was omitted. For clarity reasons, the errorbars are not shown.

6.3.5. Overview of Calibration Factors

Using the equation

$$c\,[ppm] = A \cdot abs + B \cdot abs^2, \tag{6.5}$$

concentrations of the tracers can be calculated using the calibration factors shown in table 6.1

		A	B	ΔA	ΔB
N_2O	air	216.50	236.82	0.37	0.54
	water	9619.7	9952.1	23.8	26.7
CHF_3	air	67.009	0.895	0.082	0.077
	water	2771.4	19.4	1.8	2.2
C_2HF_5	air	171.1	-0.15	0.15	0.15
	water	7366.3	-129	5.1	6.9
CF_4	air	9.1270	1.7765	0.0065	0.0070
	water	-	-	-	-

Table 6.1.: Overview of the calibration factors measured.

6.4. Uncertainties

6.4.1. Uncertainty of the Input Concentration

The manufacturer Analyt-MTC of the mass flow controllers lists the uncertainties in the volume flux at $\Delta\dot{V} = \pm 0.4\,\% \cdot \dot{V}_{set} \pm 0.2\,\% \cdot \dot{V}_{max}$ with $\dot{V}_{set}$ being the set value of the flux and the maximum value $\dot{V}_{max}$ that the controller can produce. To keep the relative errors in the input concentration as low as possible, care was taken that the smallest possible mass flow controller was used in each run.

In mixing the input concentration, 2 mass flow controllers are used. The combined error can then be calculated as a quadratic addition of the relative errors,

$$\Delta c_{\text{in}} = c_{in}\sqrt{\left(\frac{\Delta\dot{V}_1}{\dot{V}_1}\right)^2 + \left(\frac{\Delta\dot{V}_2}{\dot{V}_2}\right)^2} \tag{6.6}$$

where $\dot{V}_1$ ($\dot{V}_2$) denotes the flow of the first (second) mass flow controller.

The error of the input concentration c_{in} was parameterized using a simple interpolation of the form

$$\Delta c_{\mathrm{in}}(c_{\mathrm{in}})[\%] = A + \frac{B}{c_{\mathrm{in}}[ppm]} \tag{6.7}$$

with the free parameters A and B.

One example of this can be seen in figure 6.7. The relative error Δc_{in} of the concentration of N_2O in dependency of the input concentration c_{in} is shown as well as a parameterization using equation 6.7. For all tracers, the error was parameterized in this fashion. The parameters for the calculation of the errors for all tracers are detailed in section 6.4.5.

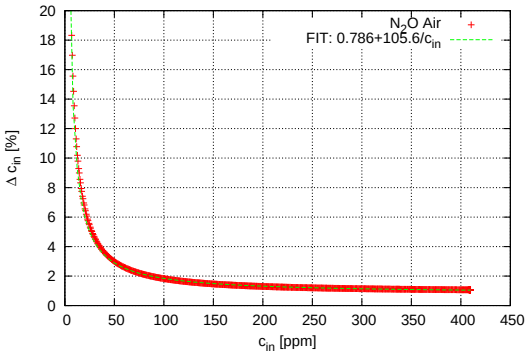

Figure 6.7.: Relative error Δc_{in} of the input concentration of N_2O in the air-side spectrometer depending on the input concentration

6.4.2. Choice of Reference Spectrum

During evaluation, see chapter 5, a reference spectrum is scaled in height to best represent the measured spectrum, with the scaling factor being the measured absorbance value. A spectrum can change its shape as well as the height when the concentration increases or decreases. This happens predominantly when a tracer has very sharp absorption lines. These absorption lines, along with the whole spectrum, are folded with the slit function of the spectroscopic setup and thus broadened with a decreased peak height. Due to this, an absorption line which is in saturation (i.e. all the light that can be absorbed is absorbed) may have a peak height which is well below the maximum detectable absorbance. Increasing concentration will not change this line of the measured absorption spectrum much, because it already is in saturation, which changes the shape of the absorption spectrum. An example of two different spectra of N_2O taken at a maximum absorbance of 1.0 and 0.2 (scaled to 1.0 for comparison) can be seen in 6.8. Here, deviations between the two spectra that should be identical lie in the order of up to 10 %. Because of this effect, the choice of the reference spectrum itself may pose a source of uncertainty.

To test whether this is an important effect or not, a second reference spectrum with a maximum absorbance of 0.2 was used. From this reference spectrum, a new calibration $c_{0.2}(\mathrm{abs})$ was obtained in the way described in section 6.1. From this new calibration, the concentrations of the calibration run were calculated. These can then be compared to the concentrations calculated when the standard calibration with a reference spectrum with a maximum absorbance of 1.0 is used. As an example, figure 6.8b shows the relative deviation of the concentrations $c(\mathrm{abs}$ from the standard calibration $c(abs)$. As the overall error that is caused by the choice of the reference spectrum, the maximum value of this deviation at typically seen concentrations during the experiments is used. In the case of the air sided calibration of N_2O, where typical concentrations lie above 120 ppm, the error is $\Delta c_{\mathrm{ref}} = 0.5\,\%$.

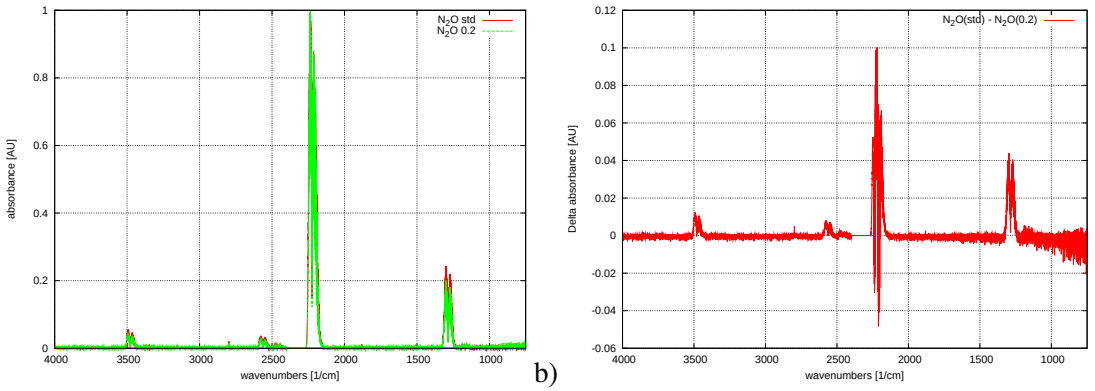

a) b)

Figure 6.8.: a) Two different reference spectra of N_2O. One with a maximum absorbance of 1.0, one with a maximum absorbance of 0.2, multiplied by 5 to make both spectra comparable. b) Difference between the two spectra.

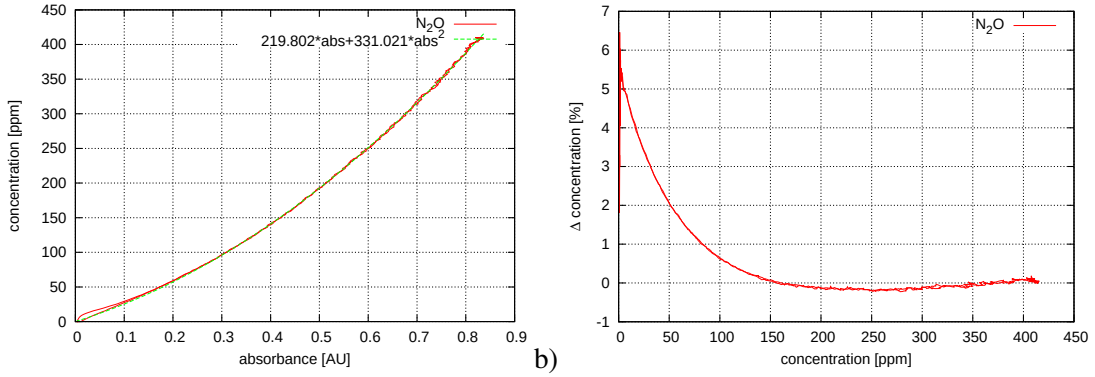

a) b)

Figure 6.9.: a) Alternative calibration of the air sided N_2O concentration using the scaled spectrum with a maximum absorbance of 0.2 seen in figure 6.8a b) Deviation of the concentration measured using the standard calibration from the calibration with the alternative reference spectrum.

The water sided calibration as well as the other tracers were treated in the same way. The deviations between the standard calibration and the calibration using a reference spectrum with a maximum absorbance of 0.2 are shown in appendix A.3.2. The errors obtained in this way are summarized in section 6.4.5.

6.4.3. Statistical Errors

To quantify the statistical errors, the deviation between the input concentration c_{in} and measured concentration c_{meas} was calculated,

$$\Delta c[\%] = \frac{c_{\mathrm{meas}} - c_{\mathrm{in}}}{c_{\mathrm{in}}} * 100. \tag{6.8}$$

Figure 6.10 shows Δc for N_2O for the air- as well a the water-side calibration run. Ideally, the input concentration equals the measured concentration, yielding a value of $\Delta c = 0$. Deviations from this value of 0 allow an estimation of the statistical error. Also shown is the mean value Δc of as well as the standard deviation. The mean was calculated using only the concentration region, that was not omitted in the calibration, see section 6.3.2. The standard deviation is used as a measure for the statistical errors. For the air side calibration of N_2O, the standard deviation was found to be 0.84 %, for the water side 0.93 %.

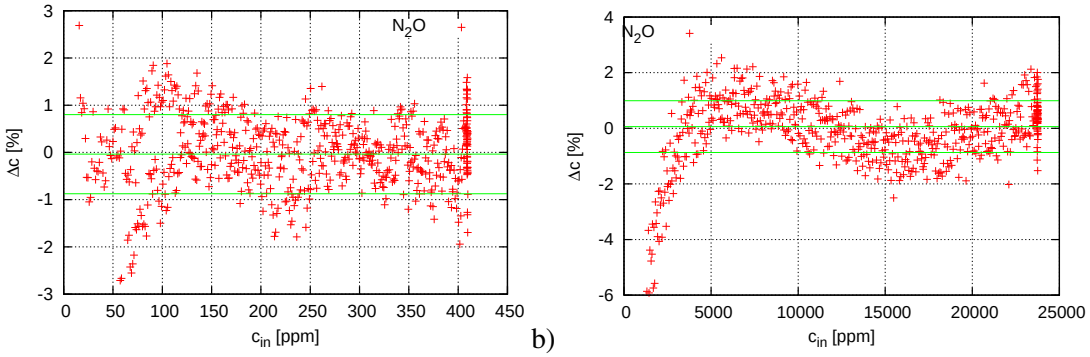

Figure 6.10.: Deviation between measured concentration and input concentration for N_2O in a) the air and b) the water side calibration. The Standard deviation is 0.84 % (air) and 0.93 %(water)

For the water side, there seems to be a slight dependence of the mean Δc on the input concentration. This is an indication, that the quadratic parameterization curve, equation 6.4, used in the calibration, does not fully describe the relationship between measured absorbance and concentration. This deviation, however, lies in the order of the standard deviation and is therefore neglected.

The statistical errors for the other tracers CF_4, CHF_3 and C_2HF_5 are listed in section 6.4.5 with the corresponding graphs in appendix A.3.3.

6.4.4. Uncertainty of the Calibration Factors

In table 6.1, the statistical errors of the fit parameters A and B of the calibration curve, equation 6.4, are shown. To estimate the error in the measured concentration, a worst case analysis is done. To do this, the lowest possible concentration $c_{\min}$ is calculated using the lowest possible calibration parameters, $A' = A - \Delta A$ and $B' = B - \Delta B$,

$$c_{\min}[ppm] = A' * \mathrm{abs} + B' * \mathrm{abs}^2. \tag{6.9}$$

Then, the relative deviation from the standard calibration is calculated,

$$\Delta c_{\mathrm{calfac}}(abs)[\%] = \frac{c(abs) - c_{\min}(abs)}{c(abs)} * 100. \tag{6.10}$$

As a typical absorbance, a value of 0.5 is chosen and the error $\Delta c_{\mathrm{calfac}}(0.5)$ is calculated. The errors obtained in this way are summarized in section 6.4.5

6.4.5. Summary of the Errors

Table 6.2 lists the errors described in the previous section.

		input concentration	reference spectrum	statistical	calibration factors
N_2O	air	$0.786 + 105.6/c_{\mathrm{in}}$	0.5	0.84	0.19
	water	$1.19 + 15681.6/c_{\mathrm{in}}$	0.5	0.93	0.25
CHF_3	air	$0.566 + 59.20/c_{\mathrm{in}}$	0.4	0.98	0.18
	water	$0.52 + 2433.4/c_{\mathrm{in}}$	0.3	0.58	0.10
C_2HF_5	air	$0.634 + 63.18/c_{\mathrm{in}}$	0.1	0.71	0.13
	water	$0.60 + 5483.4/c_{\mathrm{in}}$	0.2	0.82	0.12
CF_4	air	$0.44 + 52.13/c_{\mathrm{in}}$	0.2	1.23	0.10
	water	-	-	-	-

Table 6.2.: Overview of the errors in the calibration. Values are given in [%].

7. Results

As a first preparatory experiment, the homogeneity of the air side concentration in the Aeolotron was studied while it was flushed with large amounts of fresh air. Results of this homogeneity study are presented in section 7.1. Due to the significant inhomogeneities measured, the fast controlled leakage method, see section 3.3.1, was found to be not applicable in the Aeolotron.

In section 7.2 the measured leak rates during the campaign described in section 4.1.1 will be shown. Measurements of the solubility of two of the tracers used in the Aeolotron will be presented in section 7.3.

The presentation of the gas transfer velocities will be split up into those measured at low to medium wind speeds in the Aeolotron in section 7.4 and those measured in the Kyoto High Speed Wind Wave Tank in section 7.5. The discussion of gas transfer at low to medium wind speed will include the Schmidt number exponent in section 7.4.3 as well as the facet model in section 7.4.5. The effect of bubbles on gas transfer as well as the validation of three models for bubble mediated gas transfer can be found in sections 7.5.3 and 7.5.4.

7.1. Homogeneity of the Air Side Concentration in the Aeolotron

With the newly installed wind generator in the Aeolotron, measurements using the fast controlled leakage method, see section 3.3.1, in varying wind speeds are feasible. One prerequisite of this method is the homogeneity of the air side concentration, as only bulk concentrations enter into the equations to calculate the transfer velocity k, see equation 3.15. To test the homogeneity, a classic evasion experiment is performed, see section 3.3.2.

As the tracer for this test, trifluoromethane was chosen, because it can be mixed into the water faster than the other tracers and also only comparatively small amounts are needed. Prior to the start of the experiment, the tracer was mixed into the water. The wind was set to a fixed wind speed of $u_{\mathrm{ref}} = 5.45\,\mathrm{m/s}$ which was not changed during the experiment. Fresh air was pumped through the Aeolotron at a high flush rate of $\lambda = 29.3\,\mathrm{h}^{-1}$. Water and air side concentrations were monitored. Water was sampled at a depth of approximately 50 cm at the center of the water flume. Air was sampled from segments 2 and 13 at 8 different positions using different pipes located in a grid oriented in a plane perpendicular to the wind direction, see figure 7.1 as well as 4.2 for segment numbering.

First, air was sampled from the standard sampling position (labeled D) at segment 13 for roughly 1 hour. Then, for around 10 to 15 minutes each air was sampled from positions 1 (closest to the water surface) through 4 (highest above the water surface) in segment 2. This change in sampling positions from 1 through 4 was repeated two more times. After sampling from segment 2, air from the normal sampling position in segment 13 was analyzed again.

Figure 7.2a shows the measured air side concentration of trifluoromethane. Air that was sampled from segment 2, which is closer to the fresh air inlet than segment 13, has clearly a significantly lower concentration of the trace gas that is coming from the water. There is also a clear vertical profile with the concentration being highest closest to the water surface. Deviations of the concentration measured in segment 2 from the concentration measured in segment 13, approximated

by an exponential fit, are shown in figure 7.2b. The deviation is in the order of 5 % (position 1) to 15 % (position 4).

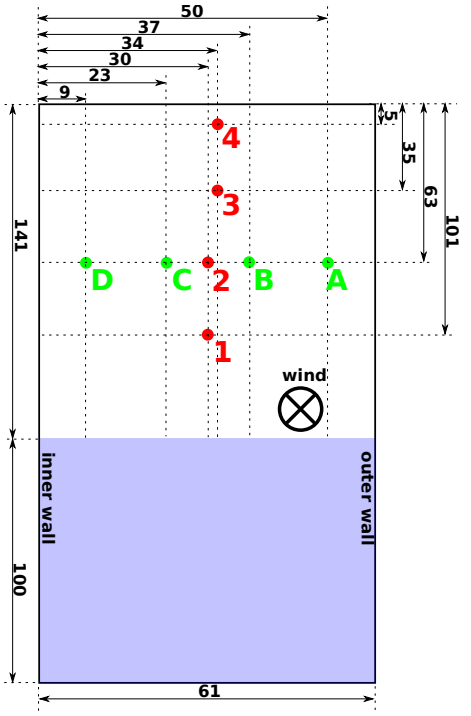

Figure 7.1.: Sampling positions and naming convention in the air side of the Aeolotron. Distances are given in [cm].

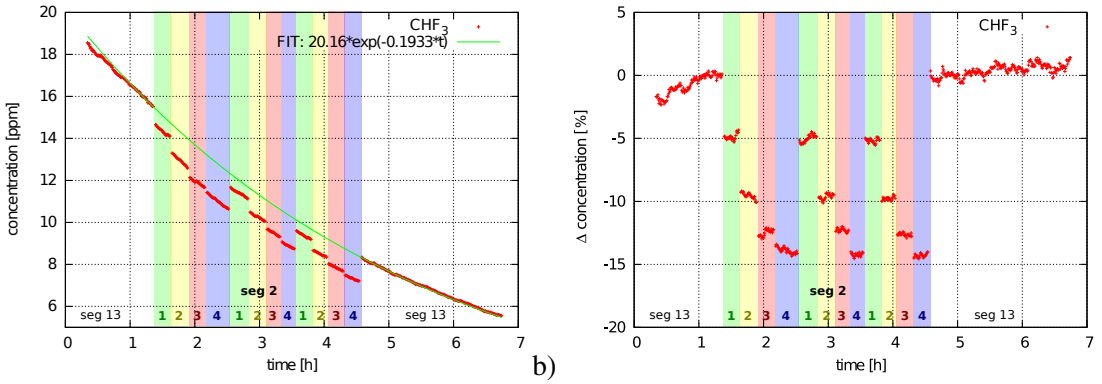

a) b)

Figure 7.2.: a) Air side concentration measured during an evasion experiment with constant wind speed. Sampling locations are color coded and follow the naming convention shown in figure 7.1. Also shown is a fit to the data taken at segment 13. b) Deviation of the data from the fit.

Next, the experiment was repeated, but the sampling location was varied radially in segment 2 along locations A trough D in figure 7.1. This change in sampling location was repeated a second time, then, to make the data comparable, another set of sampling the vertical positions was done. Figure 7.3 shows the concentrations measured and the deviation from the exponential fit, see section 3.3.2, which was performed only considering data from segment 13. Measured concentrations in segment 2 lie again much lower than in segment 13. There is again considerable variation in concentrations, with the highest concentration being measured near the inner wall, and

the lowest near the outer wall.

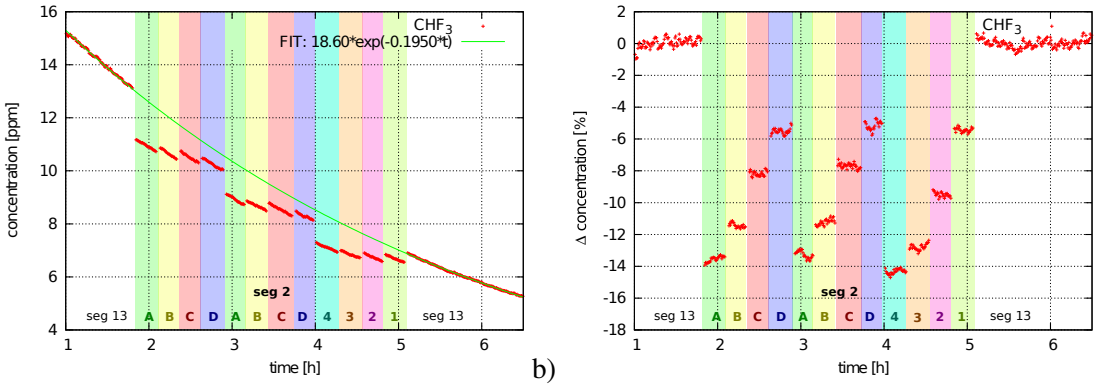

a) b)

Figure 7.3.: a) Air side concentration measured during an evasion experiment with constant wind speed. Sampling locations are color coded and follow the naming convention shown in figure 7.1. Numbered locations run vertically in the center line of segment 2, alphabetic locations radially in a medium height. Also shown is a fit to the data taken at segment 13. b) Deviation of the data from the fit.

These variations can be explained in the light of the secondary currents in the air space. Figure 7.4 shows a graphical depiction of the concentrations measured in segment 2. Also shown are pathways for transport of the tracer. The source for the tracer is the water surface from where it enters the air. Then the tracer is picked up by the secondary currents due to centrifugal forces mentioned in section 4.1, and is transported upwards along the inner wall. The air flushing system puts around 12 m^3 per minute of fresh air, devoid of any tracer, into the Aeolotron at segment 9. The same amount of air is removed through an opening in the ceiling of segment 11, after almost one full turn. The fresh air is entering the airspace straight downwards from an opening in the ceiling does not have any momentum in windward direction. Because it is so slow in windward direction, it should be first pushed towards the inner wall due to the lower centrifugal forces this air is subjected to. As it picks up speed, it enters the secondary currents while mixing into the surrounding air. The bulk of the fresh air seems to have reached the ceiling or the upper corner at the outside wall at segment 2, making the measured concentration lowest there.

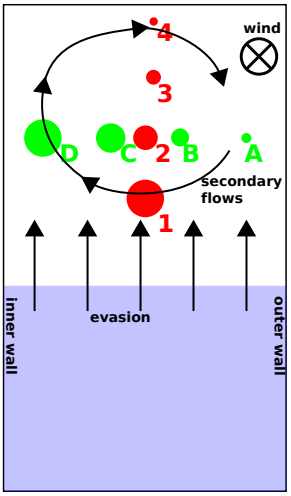

Figure 7.4.: Concentration observed in segment 2. The size of the dots is a measure for the concentration. The larger the dot, the higher the observed concentration. Differences in concentration are strongly exaggerated. The black arrows show transport mechanisms.

These findings are in agreement with those of Weißer [1980] and Ilmberger [1981], who measured humidity and velocity profiles in a smaller annular wind-wave tank.

An additional test was performed to rule out the possibility, that the measured concentration differences are only occurring in segment 2. The sampling grid that was used in segment 2, see figure 7.1, was moved to segment 13. Here, differences in concentration are also present, although not as strong as in segment 2. The variations between the sampling locations in segment 13 varied by up to 11 %.

With variations in this order of magnitude, the fast controlled leakage method can not be used to measure gas transfer velocities in the Aeolotron. Therefore, the $\dot{\mathbf{c}}_\mathbf{a}$ method, see section 3.3.1, with a closed facility (small leak rates) was chosen.

Due to no fresh air input and more than two orders of magnitude smaller leaks, there are no significant variations expected in the air side concentration. Therefore, the concentration in air sampled from any location under closed conditions is representative for all of the air space.

7.2. Leak Rates in the Aeolotron

To measure solubility, gas transfer rates and the Schmidt number exponent, the leak rates have to be known.

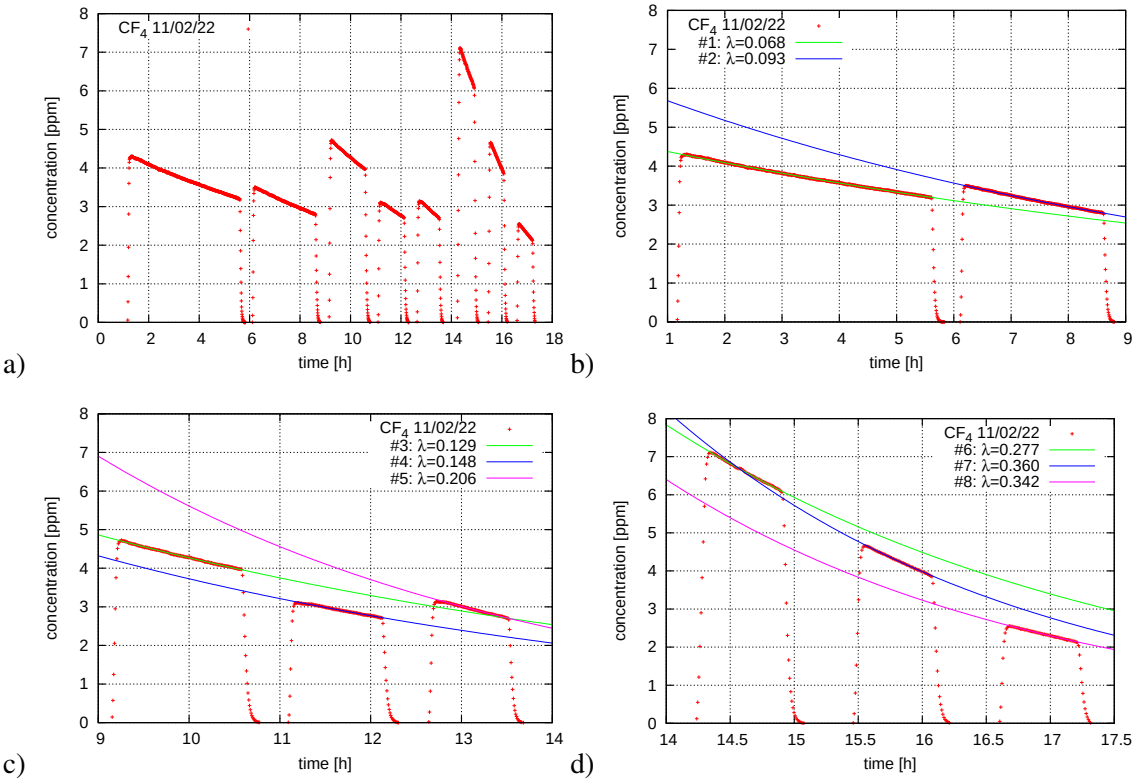

Figure 7.5.: Leak rate measurements on Feb. 22 2011. After closing the Aeolotron, a varying amount of the leak test gas tetrafluoromethane was put into the air space. a) concentration time series for the whole measuring day. b) Fits of equation 3.10 to the first two wind speed conditions. c) Fits of equation 3.10 to conditions number 3 to 4. d) Fits of equation 3.10 to conditions number 6 to 8.

Figure 7.5a shows the concentration time series of the leak test gas tetrafluoromethane on the measuring day Feb. 22 2011, during which an experiment of the form described in section 4.3.1

was performed. Right after closing the Aeolotron, the gas was put in manually. Therefore, the amount added was not always the same, leading to a variation in the maximum concentration for each condition. To obtain the leak rates, equation 3.10 was fitted using a least squares method to the measured concentration in each of the wind speed conditions where the Aeolotron was closed. As free parameters, the starting concentration $c_a(0)$ and the leak rate λ were used. Figures 7.5b through 7.5d show the fits to the 8 different wind speed conditions.

For all measuring days, the leak rates were obtained in this fashion. For conciseness reasons, no further plots are shown here, but the obtained leak rates are reported in table 7.1 and figure 7.6. A clear relationship between condition number and therefore wind speed and leak rate is apparent. There are a number of significantly lower values of the leak rate (marked with 2 in table 7.1). These are due to turning off the air conditioning in the room into which the Aeolotron is built. For all other conditions, the air conditioning was on. This surprising influence on the leak rates of the air conditioning was not known prior to the experiments. At condition 4 on the first measuring day, February 18 2011, no leak test gas was inserted, and therefore no leak rate was measured. For further analysis, the mean of the value measured at the same condition on the two following measuring days, $\lambda = 0.152\,\mathrm{h}^{-1}$, is used.

Day	condition number							
YMD	1	2	3	4	5	6	7	8
u_{ref} [m/s]	0.74	1.41	2.05	2.66	3.62	4.79	6.45	8.26
110218	0.062	0.025[2]	0.122	n.a.[1]	0.091[2]	0.149[2]	0.350	0.319[2]
110222	0.068	0.093	0.129	0.148	0.206	0.277	0.360	0.342[2]
110224	0.068	0.092	0.120	0.155	0.211	0.260	0.322	0.386
110301	0.048	0.076	0.102	0.124	0.181	0.120[2]	0.280	0.374
110303	0.048	0.073	0.099	0.049[2]	0.170	0.218	0.204[2]	0.392
110308	-	0.071	0.101	0.133	0.076[2]	0.210	0.281	0.280[2]
110310	-	0.074	0.106	0.131	0.168	0.208	0.282	0.384

Table 7.1.: Measured leak rates for all days in [1/h]. The approximate reference wind speed is labeled u_{ref} Legend: [1]) not measured, due to no leak test gas being inserted. [2]) air conditioning of the room into which the Aeolotron is built was turned off.

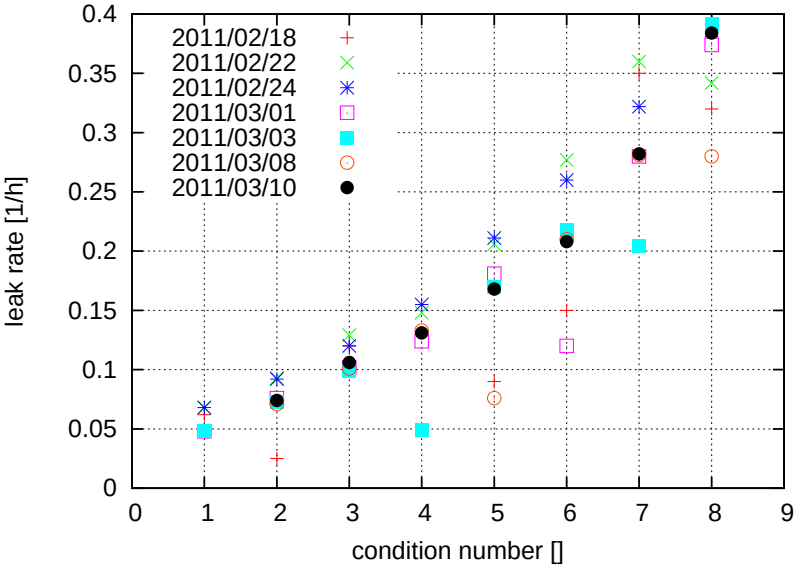

Figure 7.6.: Measured leak rates for all measuring days.

The standard deviation of the fit yields errors that are in the order of less than 1 %. Therefore, an error of $\Delta\lambda$ =1 % is used for all given values of λ as an upper boundary for the error.

7.3. Solubility

As described in section 3.4, equation 3.4 can be used to measure a tracer's solubility α.

Another method of calculating the solubility of a tracer is to use a temperature parameterization, in case this is known. Of the tracers used here, only N_2O, has a well known temperature dependency of the solubility, see Degreif [2006]. The solubility is given there in a polynomial form as

$$\alpha_{\text{param}} = 1.2661 - 0.043195 \cdot T + 0.00084316 \cdot T^2 - 8.560510^{-6} \cdot T^3 + 3.153310^{-8} \cdot T^4, \quad (7.1)$$

with the temperature T given in ^{o}C.

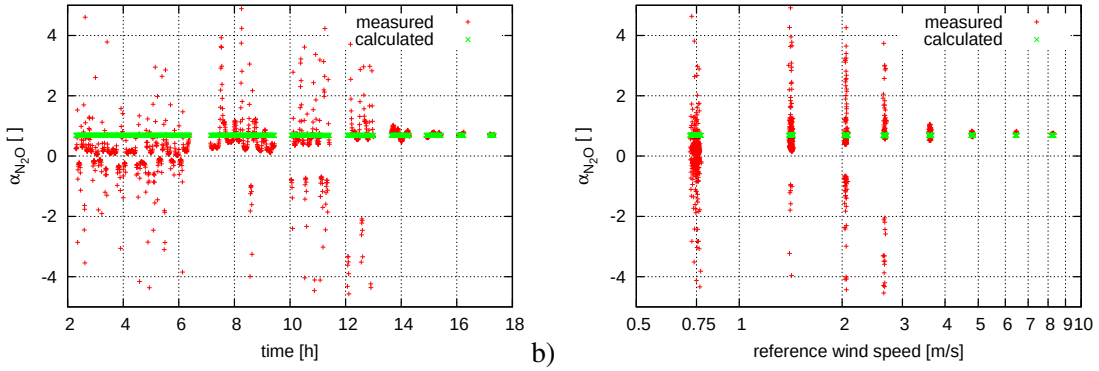

a) b)

Figure 7.7.: Example of the solubility of N_2O calculated from the concentration measurements, see equation 3.4 in red and the temperature using equation 7.1 in green for measuring day 11/02/18. The y-axis of this figures is limited to a range of -5 to 5. Higher and lower values than the ones shown were measured. Not shown are the phases where the Aeolotron was opened to flush the air space. a) versus time since the start of the measurement b) versus the reference wind speed.

Figure 7.7 shows the solubility of tracer N_2O for the measurements on 11/02/18 calculated from the parameterization 7.1 using the water temperature as well calculated from the gas concentration measurements as described in section 3.4. The solubility axis of this graphs is limited to show only values between $\alpha = -5$ and 5, while extreme values can be found as low as $\alpha = -170$ and as high as $\alpha = 460$. The scatter in the measured solubilities for the low wind speeds is large. The averaged solubility over the whole wind speed range is $\overline{\alpha_{\text{meas}}} = 0.706$ with a standard deviation of 15.0, while the calculated solubility from the parameterization has an average of $\overline{\alpha_{\text{param}}} = 0.6871$ with a standard deviation of 0.0012. The measured and the calculated solubilities agree only for the higher wind speeds. This is likely the case, because the temporal change in the water side concentration $\dot{c}'_w$ and the change in the air side concentration $\dot{c}_a$ are very close to zero for the low wind speeds. The measured solubility is proportional to

$$\frac{\dot{c}_a + \lambda c_a}{\dot{c}'_w} \quad (7.2)$$

with the leak rate λ also being small. The solubility is therefore heavily dependent on two numbers which are close to zero being divided, magnifying the systematic errors in the concentration measurement. For the higher wind speeds, to the contrary, the temporal derivatives of air and water side concentrations are larger, allowing for a more robust estimation of the solubility.

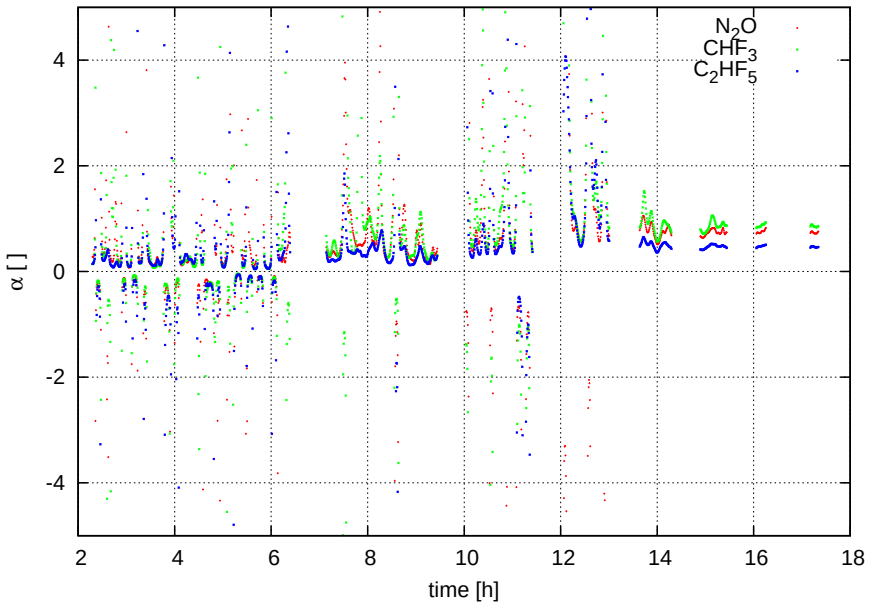

Figure 7.8.: Measured solubility for all the tracers, N_2O (red), CHF_3 (green) and C_2HF_5 (blue) for measuring day 11/02/18. The y-axis is limited to a range or -5 to 5. Not shown are the phases where the Aeolotron was opened to flush the air space.

Figure 7.8 shows the measured solubilities of all the tracers, N_2O, CHF_3 and C_2HF_5 for measuring day 11/02/18. All tracers show the same scatter in the solubility data for the lower wind speeds. Therefore, the solubility measured in each time step can not be used to calculate a transfer velocity k for this time step. As the temperature dependency of the solubility of CHF_3 and C_2HF_5 is not known, the following method was used to obtain solubilities for the tracers.

For tracer N_2O, the solubility is calculated from the parameterization equation 7.1 for each time step (equivalent to one measurement of concentration). For the other two tracers, the following scheme was used:

Step 1 chose a time region where the mean solubilities of tracer N_2O, obtained from the two methods are close to being equal, $\overline{\alpha_{\mathrm{meas}}} \approx \overline{\alpha_{\mathrm{param}}}$

Step 2 calculate the mean values of the solubilities of each of the other tracers in the same time region

Step 3 use this mean as an estimate for the most likely value for α for the whole measuring day.

Solubilities of CHF_3 and C_2HF_5 obtained in this way, as well as mean solubilities of N_2O calculated using the temperature parameterization, equation 7.1, are listed in table 7.2, as well as the mean temperature of each of the measuring days.

The measured solubilities of CHF_3 and C_2HF_5 differ significantly from the literature values of $\alpha_{\mathrm{CHF_3}} = 0.33$ [Wilhelm et al., 1977] and $\alpha_{\mathrm{C_2HF_5}} = 0.184$ [Yaws, 1999] respectively. There also seems to be a small effect of the surfactant, with the solubility being lower for surfactant covered water. This apparent dependency on the surfactant coverage is likely not significant, see the following section on the uncertainties of the measured solubilities.

Even though the measured solubilities differ significantly from the literature values, the measured solubilities are used to calculate transfer velocities, because they close the mass balance, which is the core of the method.

day	Temperature [^{o}C]	α N_2O	α CHF_3	α C_2HF_5	surfactant
11/02/18	19.45	0.6868	0.81	0.444	0
11/02/22	18.81	0.6990	0.82	0.455	0
11/02/24	19.55	0.6854	0.82	0.446	0
11/03/01	19.57	0.6825	0.82	0.450	0
11/03/03	19.88	0.6790	0.78	0.431	0.052 μmol/l
11/03/08	19.82	0.6800	0.78	0.434	0.26 μmol/l
11/03/10	20.00	0.6766	0.76	0.415	0.26 μmol/l

Table 7.2.: Measured solubilities for all used tracers. For N_2O the temperature parameterization was used, for the other two tracers the method described in the text.

7.3.1. Uncertainties of the Measured Solubilities

The scatter in the measured, time resolved solubilities of the tracers CHF_3 and C_2HF_5 is quite large with standard deviations of around 6 % in the chosen time region of the 3-step-method described in section 7.3. In addition it was observed that a variation in the time region also had an effect on the measured solubility value. Choosing only 10 more measured solubility values in the calculation of the mean values, yielded differences in the mean solubility values of up to $\pm$4 %. Therefore, the error of the solubility measurement method for CHF_3 and C_2HF_5 is at least 10 %, which is used for all further calculations. The errors in the concentration measurements, which are in the order of 1 %, see section 6.4 are neglected here as they are an order of magnitude smaller than the statistical errors.

For the tracer N_2O, Degreif [2006] does not give errors for the parameterization of the solubility. Only the error of the temperature measurement can be considered which is in the order of 0.003 ^{o}C according to the manufacturer of the temperature sensor. At common temperatures of 20 ^{o}C observed during the presented campaign, that amounts to an error of 0.015 %.

7.4. Gas Exchange at Low to Medium Wind Speeds

In this section, the calculated parameters friction velocity and u_{10}, wind speed at a height of 10 m will be shown first. These as well as another parameter, the mean square slope are presented in section 7.4.1. The measured transfer velocities will be shown next. In section 7.4.3, the measured Schmidt number exponents will follow. Using the transfer velocities and the Schmidt number exponent, the CO_2 equivalent transfer velocities k_{600} can be calculated. In section 2.2.6, a model that allows the description of the gas transfer process with varying boundary conditions was introduced. This will be applied to the data in section 7.4.5. Finally, the errors will be discussed.

7.4.1. Wind Speed, Friction Velocity and Mean Square Slope

The parameters friction velocity u_* and the wind speed at a height of 10 meters, u_{10} are commonly used to interpret the gas transfer data. The friction velocity u_* was not directly measured. According to Bopp [2011], the polynomial relationship,

$$u_* = 0.0271 * u_{ref}^2 + 0.0265 * u_{ref} + 0.0732, \tag{7.3}$$

between the measured reference wind speed u_{ref} and the friction velocity u_* found for a clean water surface by Nielsen [2004] can be used to calculate u_* even after the excessive remodeling of the Aeolotron in the years 2007 to 2009. Bopp [2011] also measured the friction velocity under

surfactant covered conditions. Within the margins of error, the friction velocity does not depend on surfactant concentration. Therefore, equation 7.3 is also used for the surfactant cases.

The wind speed at a height of 10 meters, u_{10} is calculated from its relationship with the air sided friction velocity $u_{*,a}$, using

$$C_d = \frac{u_{*,a}^2}{u_{10}^2} \tag{7.4}$$

with the drag coefficient C_d. The empirical relationship between the drag coefficient C_d and the wind speed u_{10} published by Smith and Banke [1975] was used,

$$10^3\, C_d = 0.63 + 0.066\, u_{10}. \tag{7.5}$$

The wind speed can then be calculated by

$$u_{10}^3 + \frac{105}{11} u_{10} - 158.730 u_{*,a} = 0. \tag{7.6}$$

The implicit form is given here, as the explicit solution of equation 7.6 is rather lengthy.

A parameter that describes the roughness of the wave field, aptly called mean square slope, σ_s^2, was measured using a Color Imaging Slope Gage (CISG) by R. Rocholz, see Rocholz [2008]. His results for the presented measurement campaign are given here. Unfortunately, some measurements could not be evaluated due to technical faults of the measurement device. Affected are the measurements on measuring day 2011/02/18 (clean water surface), as well as the last three conditions at measuring day 2011/03/08 (heavy surfactant coverage).

Figure 7.9 shows the dependency of friction velocity u_*, wind speed at a height of 10 meters u_{10} and mean square slope σ_s^2 on the reference wind speed.

Figure 7.9c shows the dependency of mean squared slope on the reference wind speed. The detection limit of the CISG lies in the order of 0.0025. Below this limit, the device picks up only noise leading to a non zero mean square slope value, even if the mean square slope is zero, i. e. a totally flat water surface. In this work, mean square slope values below 0.0025 are treated as flat water surface. In figure 7.9c the effect of the surfactant on the water surface can be nicely seen. While waves on the water surface are detectable under clean conditions at reference wind speeds of 1.5 m/s, with a small surfactant concentration the water surface stays smooth up to a wind speed of over 2 m/s, and with the highest surfactant concentration, the surface film starts to break up and allow waves at around 3 to 3.5 m/s. In medium wind speed ranges of 3.5 to 5 m/s, the waves are suppressed by a factor of 6 by a heavy surfactant. The dashed red line, that is labeled clean but which shows lower mean square slope values than the other clean cases in the medium wind speed range, belongs to measuring day 2011/02/22. An explanation for this behavior is, that the water surface was insufficiently cleaned (skimmed) before the experiment, or that surfactant material might have entered through the air conditioning in the flushing phases of the experiment. However, data measured on that day is still considered as measured under a clean water surface.

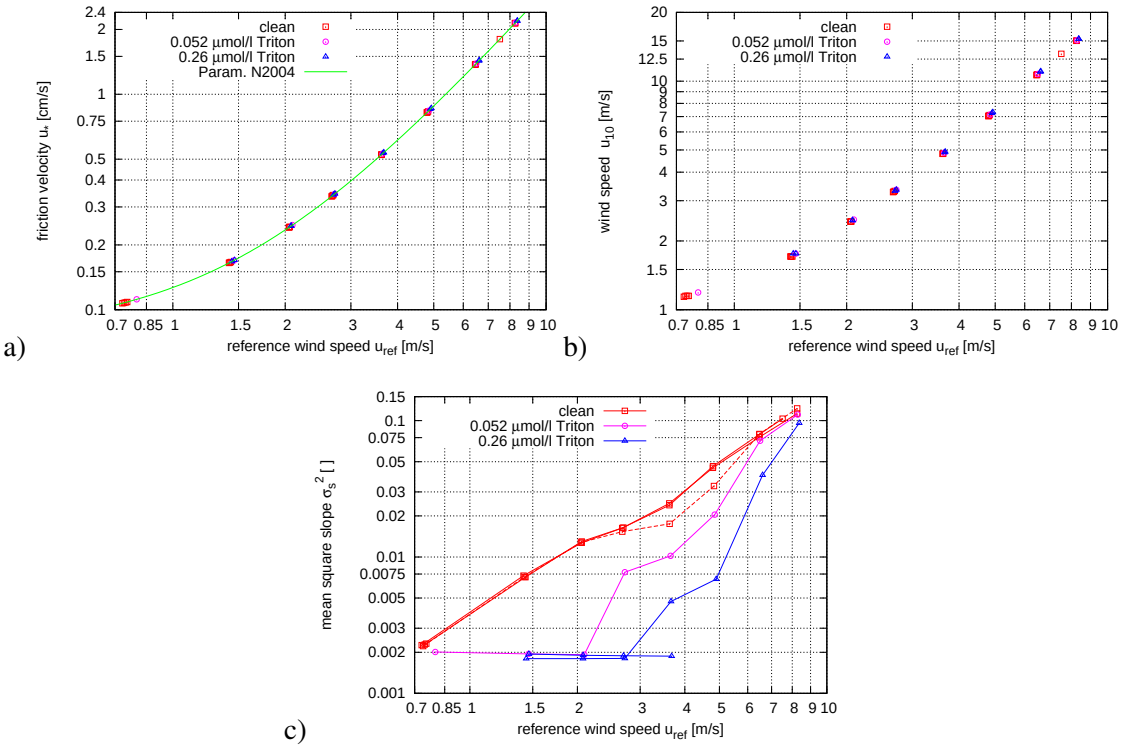

Figure 7.9.: a) Dependency of the friction velocity on the measured reference wind speed, together with the parameterization by Nielsen [2004] (labeled *N2004*). b) Dependency of the wind speed that would be measured at a height of 10 meters, u_{10} on the reference wind speed. c) Dependency of the mean square slope σ_s^2 on the reference wind speed (data kindly provided by R. Rocholz). The red dashed line marks an experiment, where a surface film seems to have developed over time.

7.4.2. Transfer Velocities

As described in section 4.3.1, 4 repetitions of 8 wind speed conditions were done with a clean water surface, 1 set of 8 wind speed conditions was done with the addition of 0.6 g of the surfactant Triton X-100 and 2 sets of 7 wind speed conditions were done with the addition of 3 g of Triton X-100 each. The wind speeds were chosen such that they are roughly equidistant in log-space.

Figure 7.10 shows the measured gas transfer velocities.

All three tracers show the same behavior. For a clean water surface, between friction velocities $u_* = 0.15$ cm/s and 1.5 cm/s, the transfer velocities are a factor of 3 larger than values measured with heavily surfactant covered water with the highest surfactant concentration. Even at the highest friction velocity, the surfactant covered water has a 30 % lower gas transfer rate. Nielsen [2004] measured gas transfer rates of N_2O with a clean surface in the Aeolotron. To check the plausibility of the data measured in this work, the piecewise parameterization Nielsen developed for a temperature of 20.2 ^{o}C, which is reasonably close to the 19 to 20 ^{o}C of the campaign presented here, is shown together with the transfer velocities of the clean cases in 7.11. Taking into consideration that Nielsen [2004] used a different model of wind sensor which was mounted at a position differing from the current wind sensor position, that the wind generator was replaced with a new one and that there are minor differences in the temperature, the agreement between the parameterization and the data presented here for a clean water surface is very good. There is only one exception, which is the lowest data point at $u_{ref} \approx 0.75$ m/s. For one, Nielsen [2004] did not measure below u_{ref} =1.6 m/s, so the applicability of his parameterization to a lower wind speed

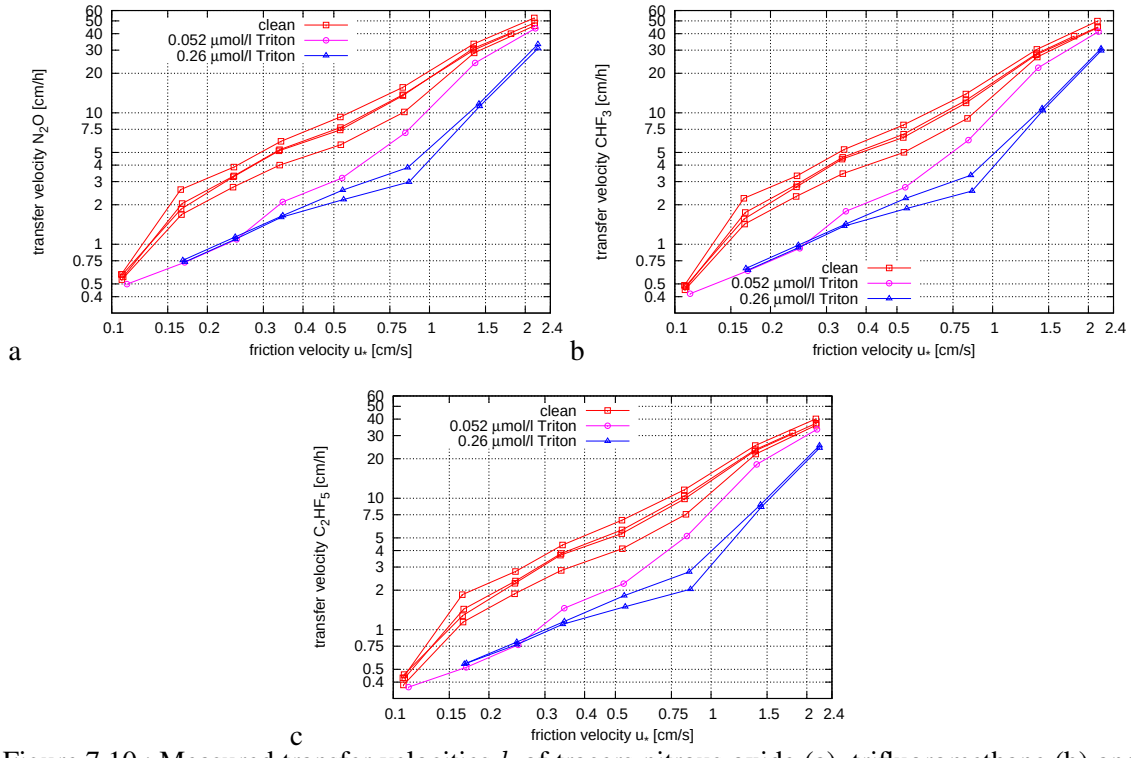

Figure 7.10.: Measured transfer velocities k of tracers nitrous oxide (a), trifluoromethane (b) and pentafluoroethane (c) against friction velocity u_*.

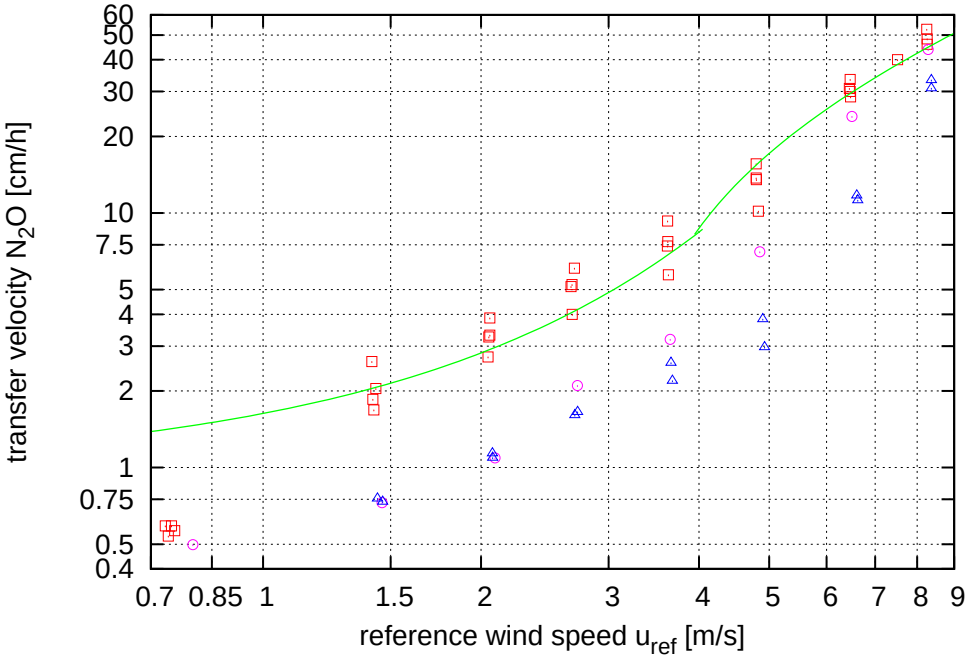

Figure 7.11.: Transfer velocities depending on the reference wind speed compared to a piecewise parameterization developed by Nielsen [2004].

range is disputable. On the other hand, also the Schmidt number exponents measured at the lowest wind speed presented in this work show unexpected values, see the following section 7.4.3. So the values measured at the lowest wind speeds need to be viewed with caution.

7.4.3. Schmidt Number Exponents

In section 5.3.3 the calculation of the Schmidt number exponents was described in detail.

With three tracers, three pairs of tracers can be formed. Therefore, three Schmidt number exponents can be calculated for each condition at each measuring day. Figure 7.12 shows the measured Schmidt number exponents for all three pairings.

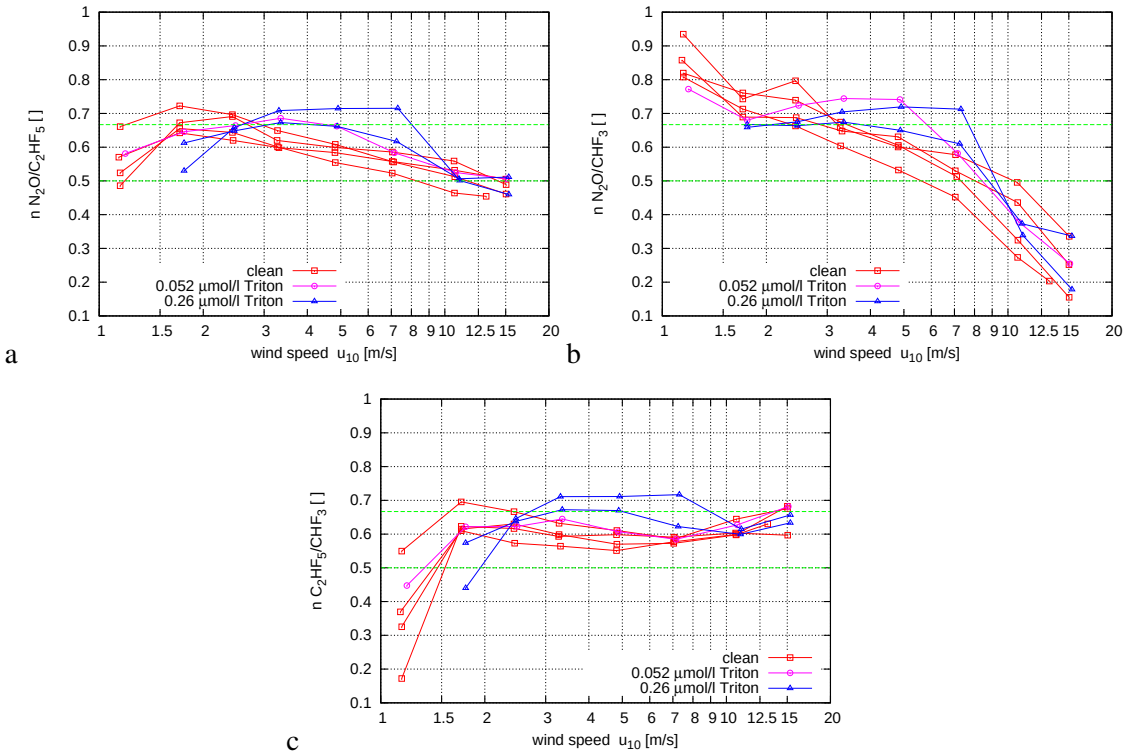

Figure 7.12.: Schmidt number exponents measured for the tracer pairings a) N_2O and C_2HF_5, b) N_2O and CHF_3, and c) C_2HF_5 and CHF_3 against wind speed u_{10}.

Of the three possible tracer pairs, only the combination N_2O and C_2HF_5, see figure 7.12a, shows the expected behavior of a Schmidt number exponent of $n = 2/3$ for a smooth water surface, i.e. at low wind speeds as well as under surfactant influence and $n = 1/2$ for a wavy surface at high wind speeds. However, the first data point of each measured series lies lower than the following points, which is unexpected. What causes this is unknown. A possibility might be insufficient mixing of the air or water space with a potential formation of layers in the air or water at very low wind speeds which leads to a wrong air or water side concentration measurement. Unexpected measured values were also observed in other tracers with high solubility not presented here that were measured during the same campaign, see Kräuter [2011].

Both combinations including the tracer CHF_3 behave not as expected. For the combination CHF_3 and N_2O, see figure 7.12b, the Schmidt number exponent is with values of up to 0.9 too high for the low wind speeds, and with values as small as 0.2 much too low for the high wind speeds. To the contrary, the Schmidt number exponent the combination CHF_3 and C_2HF_5 is almost constant for the whole wind speed range.

As a reminder, the Schmidt number exponent is calculated as

$$n = -\frac{\log\left(k_A/k_B\right)}{\log\left(D_A/D_B\right)}. \tag{7.7}$$

To figure out what causes the strange behavior of combinations including trifluoromethane, the

nominator and the denominator will be looked at separately. The Schmidt numbers, or the diffusion coefficients, respectively, can be ruled out as a cause for the strange behavior of the combinations including trifluoromethane. Figure 7.13a shows $ln(D_A/D_B)$ for all three tracer combinations for the four clean experiments. Because the temperature was relatively constant during the experiments, the diffusion constants did not change much, and $ln(D_A/D_B)$ is almost constant with wind speed.

Figure 7.13b, to the contrary, shows variations in the values of $ln(k_A/k_B)$ for all three tracer combinations for the clean cases. First of all, variations for the same tracer combination between the measuring days are seen, which stems from differences in the temperature between the measuring days as well as variations in the cleanliness of the water surface. The curves that are seen here are of the same shape as the Schmidt number exponent curves.

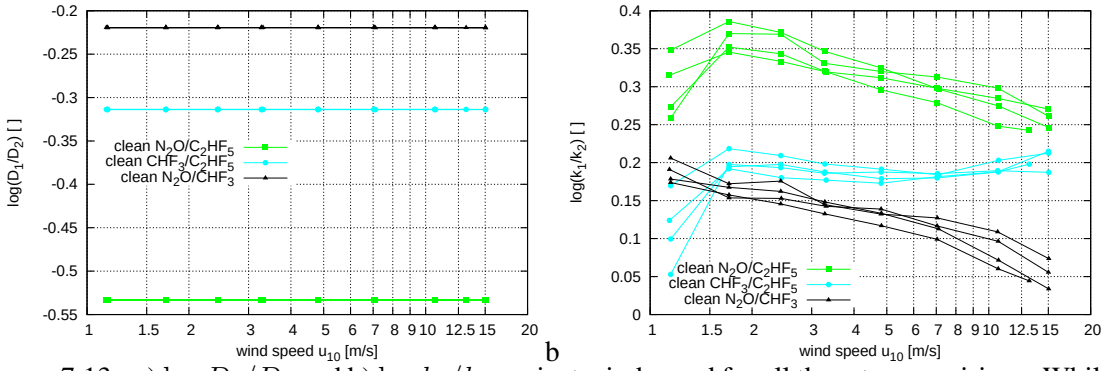

a b

Figure 7.13.: a) $\log D_1/D_2$ and b) $\log k_1/k_2$ against wind speed for all three tracer pairings. While the logarithm of the ratio of Schmidt numbers is only subject to minor changes due to slightly different temperatures during an exeriment, the logarithm of the ratio of transfer velocities shows the same relationship to the wind speed as the Schmidt number exponent.

Only concentration measurements, the leak rate and the solubility enter in the calculation of the ratio of transfer velocities, see section 5.3.2. The leak rate can be ruled out, because it is the same for all tracers. The temperature did not change much within the course of an experiment, therefore the solubility is also expected to change only very slightly. This leaves the concentration measurement of CHF_3 as an explanation for the wrong Schmidt number exponents. Reasons for erroneous concentration measurements could be that trifluoromethane has a further sink or source not covered in the mass balance, i.e. that it is accumulating on the walls of the Aeolotron, the tubing, or that it is reacting with the phosphorous pentoxide or phosphoric acid in the dryer unit in the sampling lines. Due to this, the transfer velocities of trifluoromethane are flagged as incorrect and disregarded in the further analysis. The Schmidt number exponent measured using the tracer combination N_2O and C_2HF_5 is regarded as the best estimate of the true Schmidt number exponent. Both tracer combinations with trifluoromethane are also flagged as incorrect and not used in further analysis.

When the Schmidt number exponents (from the tracer combination N_2O and C_2HF_5) are averaged using a simple arithmetic mean, their differences with respect to surfactant coverage become much clearer. Figure 7.14 shows mean Schmidt number exponents for the three surface conditions. Ignoring the data point at the lowest wind speed for each condition, the change from smooth, $n = 2/3$, to wavy, $n = 1/2$ surface is seen in all three cases. The stronger the surfactant, the steeper the change. For the clean surface, the change from 2/3 to 1/2 happens between wind speeds of 2.5 m/s and 11 m/s with the mid point at around 4.5 m/s. For the strongest surfactant coverage, the water surface behaves smooth until the wind reaches 7 m/s, and wavy at wind speeds

higher than 11 m/s. The mid point of the change is reached at $u_{10} = 9$ m/s for the highest surfactant coverage used.

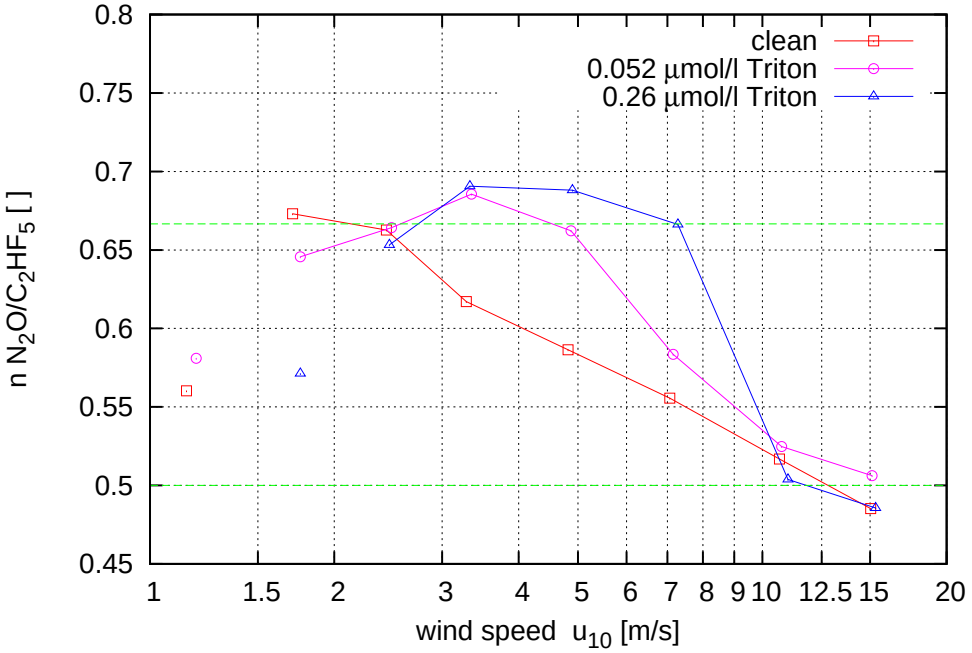

Figure 7.14.: Mean Schmidt number exponents for the three surface conditions. Also shown are the theoretical predictions for a smooth (n=2/3) and a wavy (n=1/2) water surfaces.

Surface active materials are also abundant in nature even at wind speeds higher than the global mean wind speed over the ocean of $u_{10} = 6.6$ m/s, see Wurl et al. [2009]. In studies at the open ocean, the standard temperature of exactly 20^{o}C is rarely measured. Also, tracers other than CO_2 are commonly used. Results obtained in those field studies are usually scaled to the Schmidt number of CO_2 at 20^{o}C, $Sc = 600$ to make them comparable using Schmidt number scaling, see equation 2.68. Schmidt number exponents are commonly not measured in the field. It is rather assumed, that the Schmidt number exponent has the value of 1/2 all the time. This poses a large source for errors. As an example, helium ($Sc = 150$ at 20^{o}C, see Degreif [2006]) is a commonly used tracer in field experiments. Using the wrong Schmidt number exponent (1/2 instead of 2/3) when scaling to a Schmidt number of 600, leads to an error of up to 20 %. The error gets even larger when the temperature is different from 20^{o}C, leading to a larger difference in Schmidt numbers.

7.4.4. Carbon Dioxide Equivalent Transfer Velocities

To compare the measured transfer velocities k_T with previously measured values, they can now be Schmidt number scaled to $Sc = 600$, which is the Schmidt number of carbon dioxide in fresh water at 20 ^{o}C,

$$k_{600} = k_T \left(\frac{600}{Sc_T} \right)^{-n}. \tag{7.8}$$

Because the Schmidt number exponent was measured using the tracer combination N_2O and C_2HF_5, see section 7.4.3, it makes mathematically no difference whether k_{N_2O} or $k_{C_2HF_5}$ is used for scaling. Here, the measured transfer velocities of N_2O shown in section 7.4.3 and Schmidt number exponents shown in section 7.4.3 were used.

Figure 7.15 shows the measured transfer velocities of N_2O which were scaled to $Sc = 600$. The tracer N_2O was chosen because the systematic error is expected to be much smaller than for C_2HF_5, see section 7.4.7.

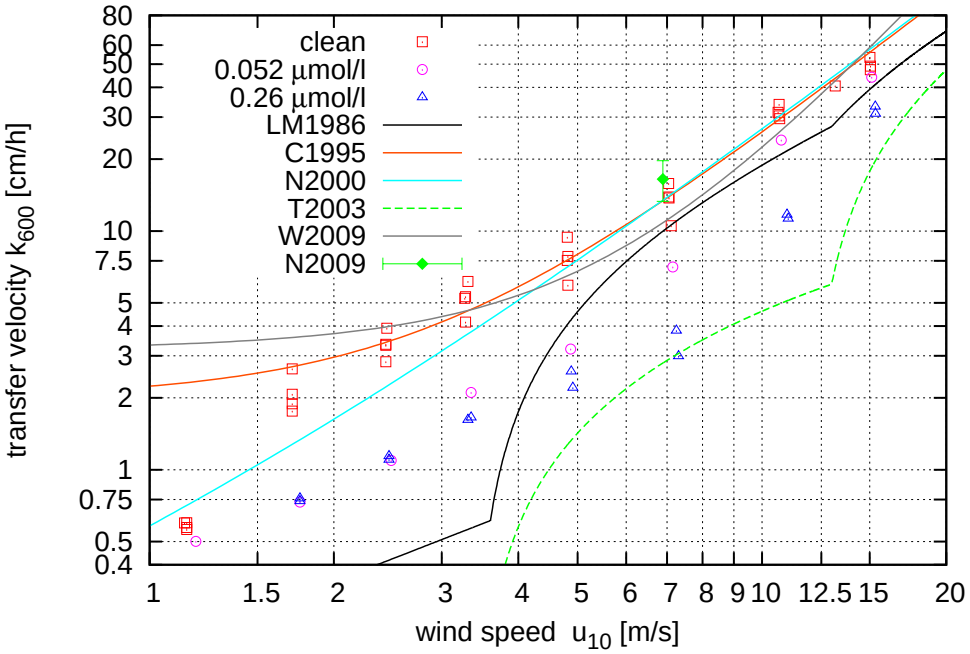

Figure 7.15.: Transfer velocity of N_2O scaled to a Schmidt number of 600. Also shown are some empirical parameterizations: LM1986: Liss and Merlivat [1986]; C1995: Clark et al. [1995]; N2000: Nightingale et al. [2000]; T2003: Tsai et al. [2003]; W2009: Wanninkhof et al. [2009]. Naegler [2009] (N2009) constrained the gas transfer velocity using atomic bomb ^{14}C.

Also shown in figure 7.15 are some commonly used empirical parameterizations. With the exception of the Tsai et al. [2003] parameterization, all are given for a clean water surface. The measured values for k_{600} lie right within the range of the empirical parameterizations, giving an indication, that results from the Aeolotron-lab can indeed be transferred to the open ocean. With the exception of the data point at the lowest wind speed, the Clark et al. [1995] parameterization seems to represent the data taken with a clean water surface slightly better than the other ones shown. However, the surfactant cases are not represented by any of the parameterizations. Also shown is the gas transfer velocity calculated by Naegler [2009], using the flux of ^{14}C produced by atomic bomb tests across the air-sea interface. His value, even though it is a global average, agrees well with the data measured with a clean water surface in this work.

With Tsai et al. [2003] one parameterization created for surfactant covered water is shown. This parameterization was developed from the clean surface Liss and Merlivat [1986] parameterization, using some data measured by Broecker et al. [1978] in a linear wind wave tank under the effect of a mono-molecular layer of oleyl alcohol. This is an insoluble surfactant, while in this work the soluble Triton X-100 was used. The parameterization by Tsai et al. [2003] does not agree with the data measured in this work. The reason for this could be the a different type of surfactant (soluble vs. insoluble) or the possibility, that also the underlying Liss and Merlivat [1986] parameterization also was unknowingly developed with partial surfactant coverage.

It becomes very clear here, why all attempts to parameterize gas transfer velocities with the wind speed as a parameter are bound to fail. The parameterizations for a clean water surface themselves predict differing transfer velocities at the same wind speed, varying by a factor of up to 10 at lower wind speeds and 1.5 for mid to high wind speeds. Also, the measured transfer velocities show a large difference between clean and surfactant covered water surface by a factor of 3 for low to medium wind speeds, and still a difference of 30 % at the highest wind speed measured. It might well be the case, that some of the shown parameterizations were unknowingly developed with

partially or even strongly surfactant covered water surface, which might also explain some of their variation. According to Wurl et al. [2011], surface active material can be found almost everywhere on the ocean, and is not mixed down into the water bulk even at wind speeds exceeding the mean global wind speed of 6.6 m/s, see Wurl et al. [2009]. So also the parameterizations developed from field measurements are likely to be influenced by naturally occurring surfactants.

As an interim summary can be concluded, that wind speed u_{10} is not a suitable single parameter to describe gas transfer rates, neither in the lab nor in the field.

Another parameter, that is commonly used, is the friction velocity u_*. As all transfer velocities for the individual tracers k were measured with slightly different temperatures, the Schmidt numbers of the tracers were also slightly different from measuring day to measuring day. Therefore, the Deacon model, $k \propto u_* \cdot Sc^{-n}$ with a fixed Schmidt number was not shown together with measured transfer velocities k. But for k_{600} the Schmidt number is one fixed value, so the measured values can be compared to the theoretical prediction.

Figure 7.16 shows the measured transfer velocities k_{600} plotted against the friction velocity. Also shown is the theoretical prediction

$$k(u_*) = \frac{1}{12.2} u_* Sc^{-2/3} \tag{7.9}$$

for a completely smooth water surface. The parameter $\beta_s = 12.2$ stems from Deacon's parameterization and was calculated by Jähne [1980]. This curve can be seen as a lower boundary for the wind induced gas transfer. The gas transfer velocities measured under the influence of a strong surfactant coverage (0.26 μmol/l Triton X-100) in the low to mid friction velocity range are well represented by equation 7.9. The transfer velocities measured under light surfactant coverage (0.052 μmol/l Triton X-100) agree with the theoretical prediction only for the lowest wind speeds.

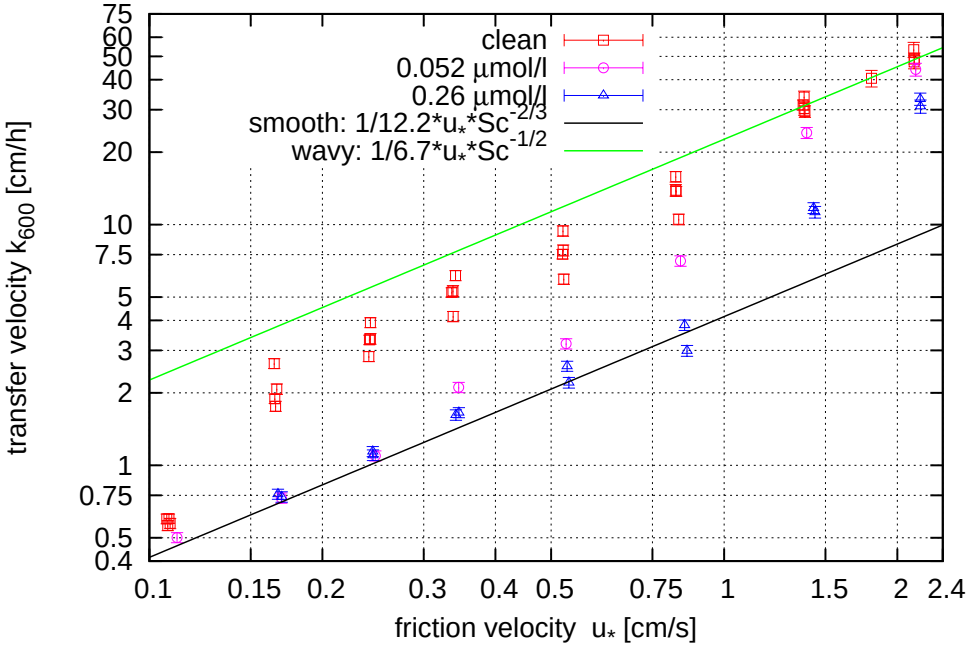

Figure 7.16.: Transfer velocity of N_2O scaled to a Schmidt number of 600 plotted against the friction velocity.

The case for the upper boundary is not so easy, as one parameter, β_w, is not predicted by theory. The curve shown in figure 7.16 for the completely wavy case was fitted to the data measured under clean conditions with friction velocities larger than 1 cm/s,

$$k(u_*) = \frac{1}{\beta_w} u_* Sc^{-1/2} \tag{7.10}$$

with the fitted $\beta_w = 6.7$. Degreif [2006] found $\beta_w = 4.5$ in a much smaller annular wind wave tank, and Nielsen [2004] $\beta_w = 7.5$ in the Aeolotron. The β_w measured here lies right between these two values. The theoretical predictions are well suited to explain the extreme cases of a completely smooth and a completely wavy water surface. However, they do not explain the change from smooth to wavy water surface.

Besides the wind speed and the friction velocity, a third parameter is occasionally used to describe the gas transfer, the mean square slope σ_s^2 of the water surface. Figure 7.17 shows the measured transfer velocities k_{600} plotted against the mean square slope.

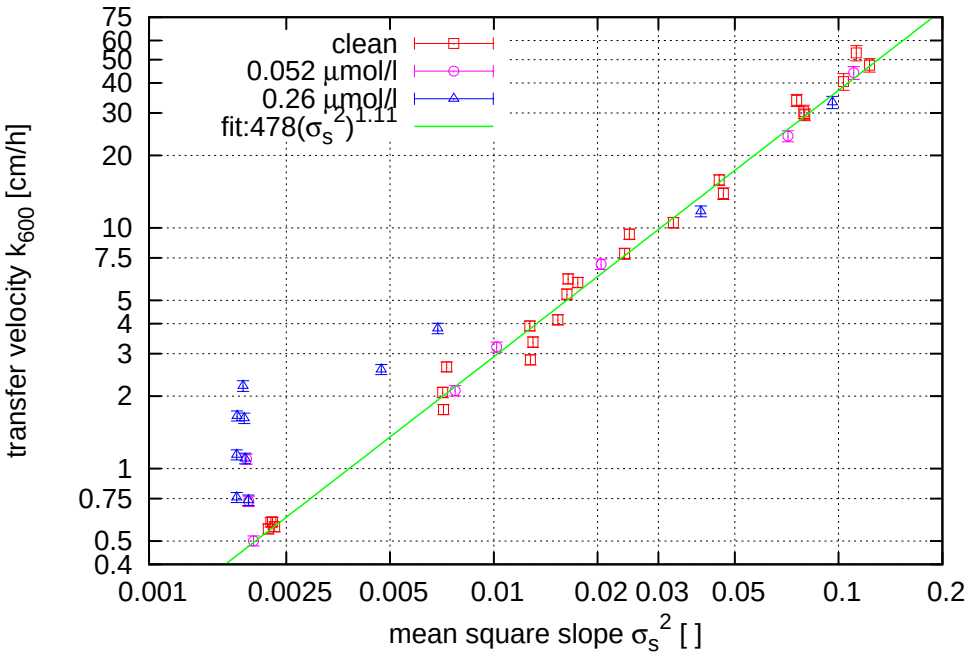

Figure 7.17.: Transfer velocity of N_2O scaled to a Schmidt number of 600 plotted against the mean square slope (mss data kindly provided by R. Rocholz.).

Slope values lower than 0.0025 correspond to a very smooth water surface. That this does not show as $\sigma_s^2 = 0$ is due to noise in the instrument measuring the mean square slope. For mean square slopes higher than 0.01 there is a very good correlation between mean square slope and the gas transfer velocity. To guide the eye, a curve of the shape

$$k(\sigma_s^2) = C \cdot \left(\sigma_s^2\right)^E \tag{7.11}$$

with the fitted parameters $C = 478$ and $E = 1.11$ is also shown.

However, for lower mean square slopes between 0.004 and 0.01 the correlation is not so good, with the transfer velocity measured for the strongly surfactant covered case being a factor of 2 higher than the one measured at a clean surface. For even lower mean square slopes, the variation between surfactant and clean cases are even larger, with the transfer velocities differing by a factor of more than 4.

7.4.5. Validation of the Facet Model

In section 2.2.6 the facet model was introduced. Here, it will be tested if it can be used to describe the gas transfer rates.

Figure 7.18 shows the measured Schmidt number exponents with a fit of the facet model's prediction of the change in the Schmidt number exponent from 2/3 for a smooth water surface to 1/2 for a wavy surface.

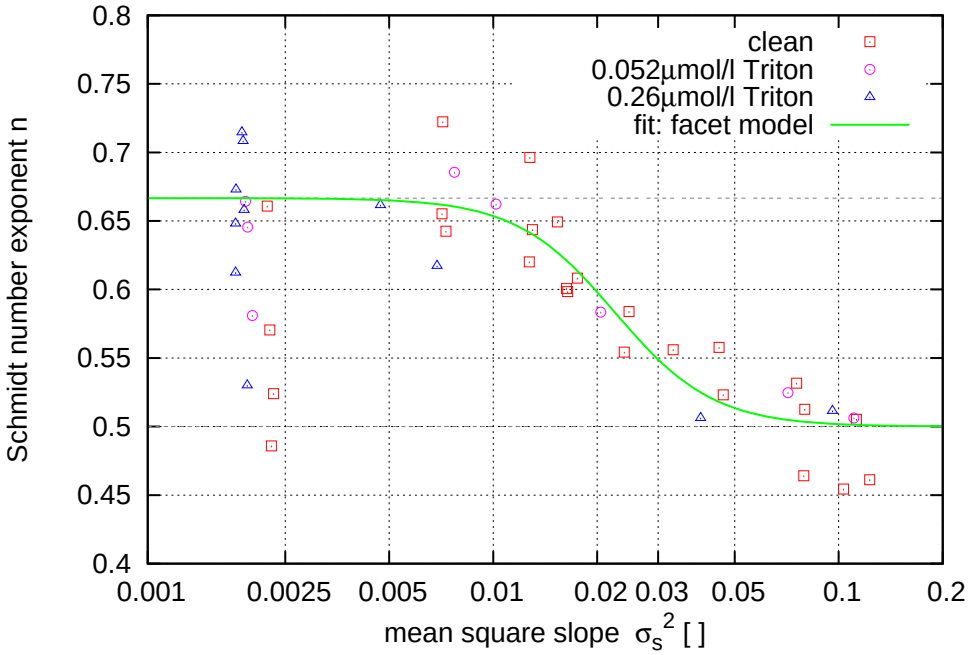

Figure 7.18.: All measured Schmidt number exponents, as well as the fit result of the facet model, see section 2.2.6. Values below a mean square slope of 0.0025 were omitted in the fit.

The fitted function, see also section 2.2.6, was

$$n(\sigma_s^2) = \frac{\frac{2}{3}(1-\frac{\sigma_s^{2\gamma}}{\delta^\gamma+\sigma_s^{2\gamma}})\frac{1}{\beta_s}Sc^{-\frac{2}{3}} + \frac{1}{2}\frac{\sigma_s^{2\gamma}}{\delta^\gamma+\sigma_s^{2\gamma}}\frac{1}{\beta_w}Sc^{-\frac{1}{2}}}{(1-\frac{\sigma_s^{2\gamma}}{\delta^\gamma+\sigma_s^{2\gamma}})\frac{1}{\beta_s}Sc^{-\frac{2}{3}} + \frac{\sigma_s^{2\gamma}}{\delta^\gamma+\sigma_s^{2\gamma}}\frac{1}{\beta_w}Sc^{-\frac{1}{2}}} \tag{7.12}$$

with the free parameters δ and γ. The midpoint parameter δ was found to be 0.0395±15 % and the steepness parameter $\gamma = 3.04$±20 %. Measured Schmidt number exponent values below a mean square slope of 0.025 were omitted in the fit due to the already mentioned problems with the mean square slope data.

Figure 7.19 shows the deviation between the measured values and the fit curve,

$$\Delta n = \frac{n_{meas} - n(\sigma_s^2)}{n(\sigma_s^2)} \tag{7.13}$$

with the facet model $n(\sigma_s^2)$ from equation 7.12.

The deviation is largest for the already mentioned values below $\sigma_s^2 = 0.0025$. For higher mean square slopes, the deviation is less than 10 %. This is in the order of the error of the measured Schmidt number exponent of 8 % to 12 % which will be discussed in section 7.4.7. An interim conclusion here is, that the mean square slope, together with equation 7.12 can be used to describe the transition of the Schmidt number exponent, and that the transition is independent of the surface coverage with surfactant.

Using equation 2.69, the modeled transfer velocities can be calculated. Figure 7.20a shows a comparison between the measured and modeled transfer velocities k_{600} for the Schmidt number of 600. Figure 7.20b shows the deviation between the model and the data in the form

$$\Delta k_{600} = \frac{k_{data} - k_{model}}{k_{model}}. \tag{7.14}$$

Correlation is very poor, with deviations of almost 300 %. The model underestimates most values.

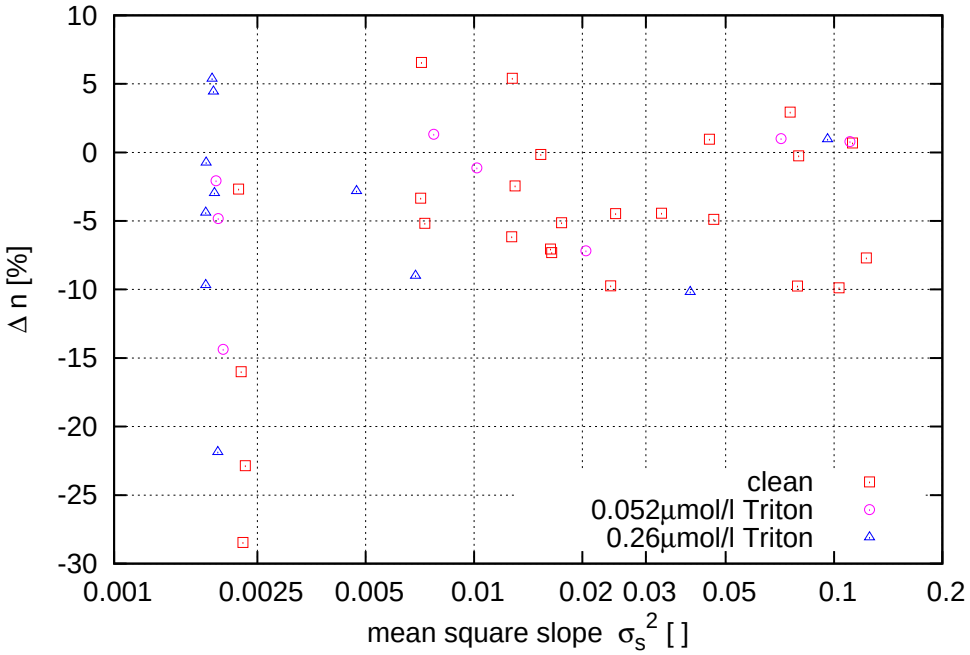

Figure 7.19.: Deviation between the facet model and the measured Schmidt number exponents.

Some transfer velocities are well represented by the model, for instance the surfactant cases at very low wind speeds, corresponding to low transfer velocities up to 4 cm/h. Also, at high wind speeds (with high transfer velocities), the clean case is modeled adequately. Surprisingly, for the data points where the Schmidt number exponent is modeled poorly, the deviation of the modeled transfer velocities from the measured ones is comparatively small.

No graph showing the facet model's prediction of the transfer velocity k depending on the mean square slope can be shown here, because k is not only depending on σ_s^2 bu also on the friction velocity u_*. The functional dependency of $u_*(\sigma_s^2)$ would need to be parameterized. The dependency $u_*(\sigma_s^2)$ is also not unique, because there are large differences in the different surfactant cases, see images 7.9c and 7.9a.

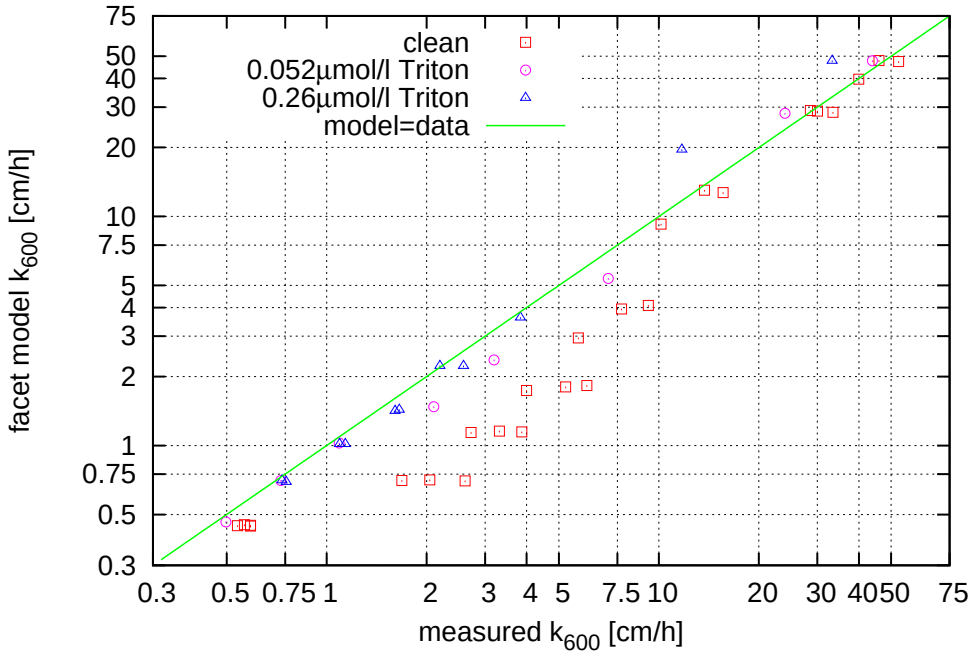

a)

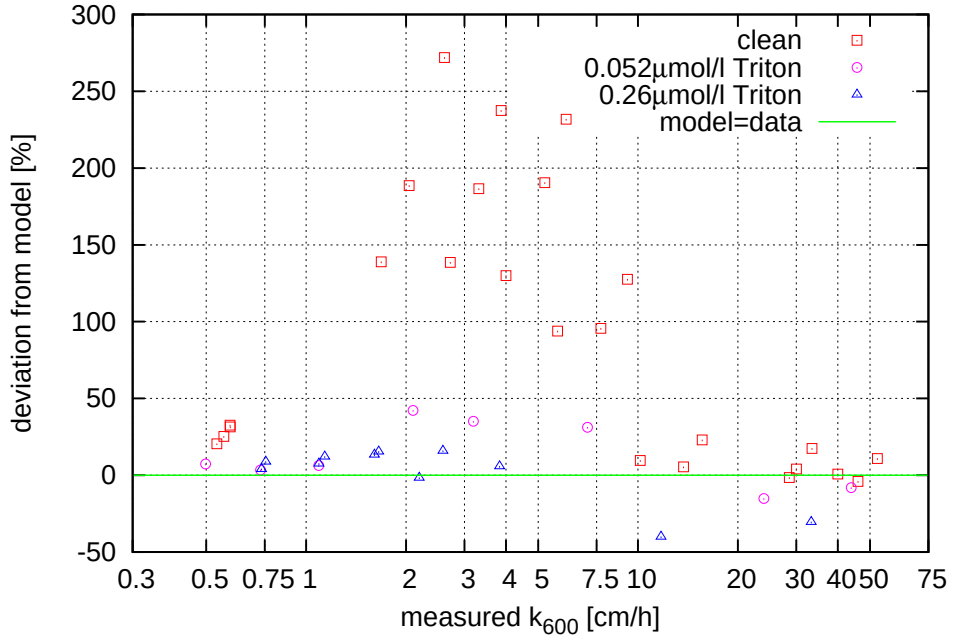

b)

Figure 7.20.: Deviation between the modeled transfer velocities calculated using the facet model and the measured transfer velocities.

The dimensionless constant β

One parameter that has not been looked at yet is the dimensionless constant β. It can be calculated using equation 2.67 solved for β,

$$\beta = \frac{k}{u_*} Sc^{-n}, \tag{7.15}$$

with the measured values transfer velocity k_{600}, friction velocity u_* and Schmidt number exponent n.

Figure 7.21a shows β in dependency of the inverse of the friction velocity, $1/u_*$, as equation

7.15 predicts an inverse dependency of beta on the friction velocity. For high inverse friction velocities above 5 s/cm (which corresponds to low wind speeds and low mean square slopes), the Schmidt number exponent used was likely erroneous, see sections 7.4.2 and 7.4.3. Due to this, β in this region is also likely wrong. Therefore, the theoretical prediction of $\beta_s = 12.2$ for a smooth water surface is not well reproduced. Figure 7.21b shows the same, with the exception, that the affected Schmidt number exponents were set to the theoretically expected value of $n = 2/3$ (smooth water surface, see section 2.2.6) for inverse friction velocities above 5 s/cm. Here, for the strong and partial surfactant case, the theoretical expectation of $\beta_s = 12.2$ is well reproduced. This is a further indication, that the measured Schmidt number exponents for low friction velocities are indeed wrong.

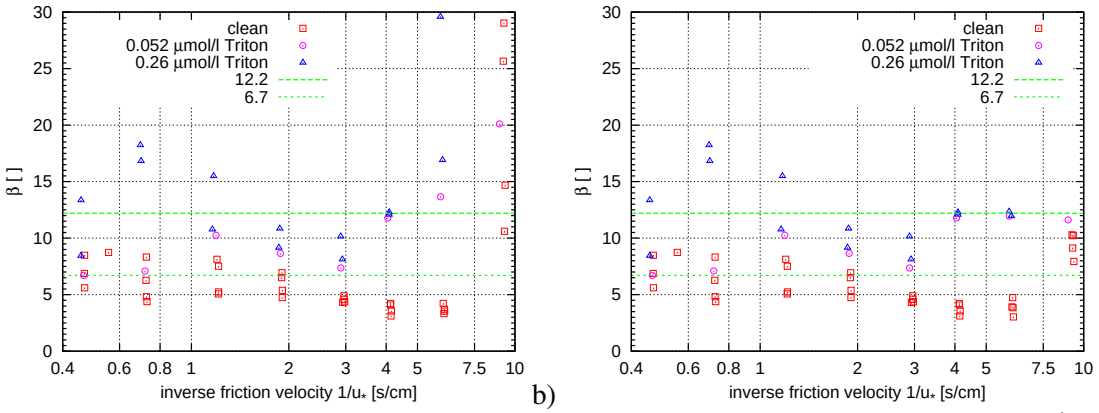

Figure 7.21.: Measured dependency of the measured β values on the inverse friction velocity $1/u_*$. Also shown are the theoretical prediction β_s=12.2 (dashed green line) for a smooth water surface and the fitted value β_w=6.7 (dotted green line) for a wavy surface, see section 7.4.4. a) calculated values from equation 7.15 using measured data. b) calculated values from equation 7.15 using a Schmidt number exponent of $n = 2/3$ for friction velocities of below 0.2 cm/s (inverse friction velocities above 5 s/cm), and measured data otherwise.

The facet model predicts a dependency of the scaling parameter β on the mean square slope, see equation 2.73. Figure 7.22 shows the measured β values in dependency of the mean square slope. Due to the arguments regarding the Schmidt number exponent at low friction velocities, which correspond to low mean square slopes, all values of β with a mean square slope below 0.0025 were calculated with a fixed Schmidt number exponent of $n = 2/3$. Again, the correlation between data and model, especially in the transition region, is very poor. As a reminder, the transition region of the Schmidt number exponent lies in the mean square slope region of 0.01 to 0.05, so no statement can be made wit respect to the constancy of the parameter β at constant surface conditions, as only very few data points are available at mean square slopes higher than 0.05.

It can be concluded here, that the facet model is very capable of modeling the transition of the Schmidt number exponent. However, it fails in predicting the correct transfer velocities, and the scaling parameter β is also not correctly modeled.

The parameter β is neither proportional to the inverse friction velocity u_*^{-1} nor to the mean square slope σ_s^2. Therefore, a modification of the model, that relates the parameter β to either a combination of the friction velocity u_* and the mean square slope σ_s^2 or to one or more different parameters, is needed. Such parameters could be the turbulent kinetic energy, see section 2.1.2, or different wave field parameters such as the wave age, see for instance Zülicke [2005], neither of which were measured in the presented experiments.

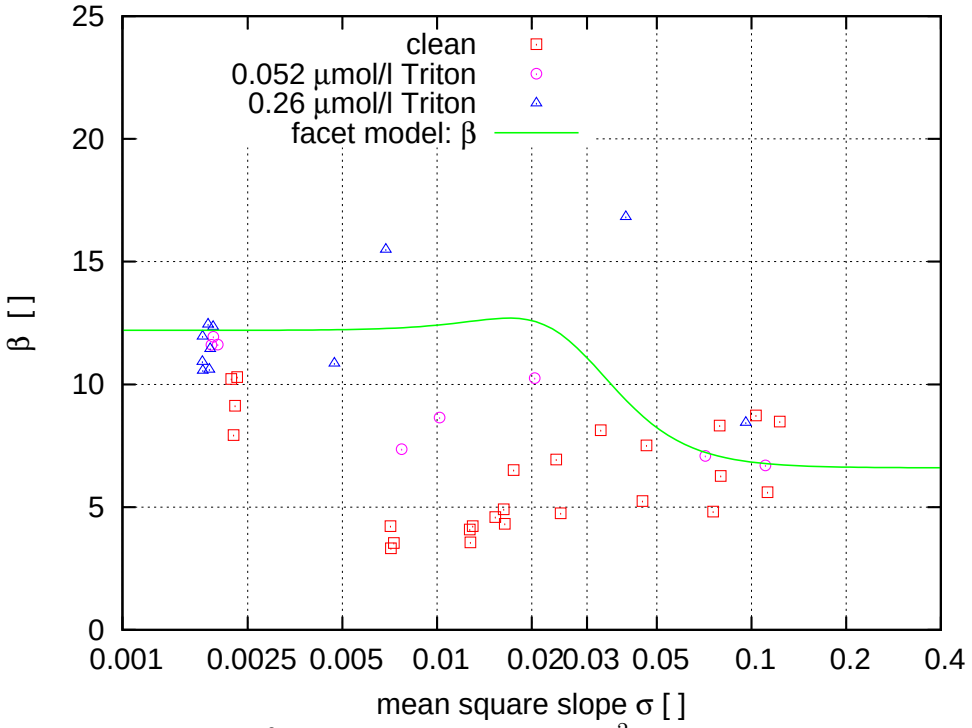

Figure 7.22.: Dependency of β on the mean square slope σ_s^2. Also shown are the facet model's prediction β_s=12.2, see equation 2.73. A Schmidt number exponent of $n = 2/3$ was used for the calculation of β for mean square slopes below 0.0025, and measured Schmidt number exponents were used for higher mean square slopes.

7.4.6. Comparison with Previously Measured Values

In this section, the data will be put into context of previously measured values. Combined measurements of gas transfer rate, the Schmidt number exponent, friction velocity and the mean square slope have been made in annular wind wave tanks by Jähne et al. [1987], Nielsen [2004] and Degreif [2006]. Table 7.3 lists the geometrical properties of the wind wave tanks used.

Data referenced as Jähne et al. [1987] is mostly a summary of the data measured by Jähne [1980], Huber [1984], Dutzi [1985], Bösinger [1986], and Libner [1987]. Fuß [2004] contributed the wave slope measurements to the gas exchange measurements made by Nielsen [2004]. Degreif [2006] made both the gas transfer as well as the wave slope measurements.

Figure 7.23 shows a comparison of the relationships between the mean square slope of the water surface σ_s^2 and the friction velocity u_*. All measurements with the exception of the presented work, were made without the addition of surfactants.

Mean square slopes for the clean water surface in this work are among the highest ones measured. For high friction velocities, they are comparable in size to those of Jähne et al. [1987], for lower friction velocities to those of Nielsen [2004]. For medium friction velocities between 0.5 and 1 cm/s, Nielsen's data is almost reproduced for the slightly surfactant covered case. This is an indication, that the water surface was not perfectly clean during his measurements in that friction velocity regime. However, there is a distinct bend visible in Nielsen's data at a friction velocity of $u_* = 0.5$ cm/s, which corresponds to a mean square slope of $\sigma_s^2 = 0.01$. Nielsen does not give an explanation for this. It is likely, that his mean square slope values below 0.01 are erroneous, see also Fuß [2004]. As a brief reminder, mean square slopes measured in this work below approximately 0.0025 are likely not correct, as the noise in the instrument used to measure the slopes was of the same order of magnitude.

	HD1	HD2	WH	Aeolotron
circumference [m]	1.57	11.6	3.14	29.2
flume width [m]	0.10	0.20	0.20	0.63
outer diameter [m]	0.60	4.0	1.2	9.93
inner diameter [m]	0.40	3.4	0.8	8.67
total height [m]	0.50	0.70	0.41	2.41
max water depth [m]	0.08	0.25	0.20	1.0
water surface area [m^2]	0.16	3.5	0.63	17.9
water volume [m^3]	0.01	0.87	0.13	17.9

Table 7.3.: Technical data of the annular wind wave flumes. HD1: used by Jähne et al. [1987]. HD2: used by Jähne et al. [1987], no longer operational. WH: used by Degreif [2006], formerly at Woods Hole Oceanographic Institution, now at University of Hamburg. Aeolotron: used by Nielsen [2004] and in this work.

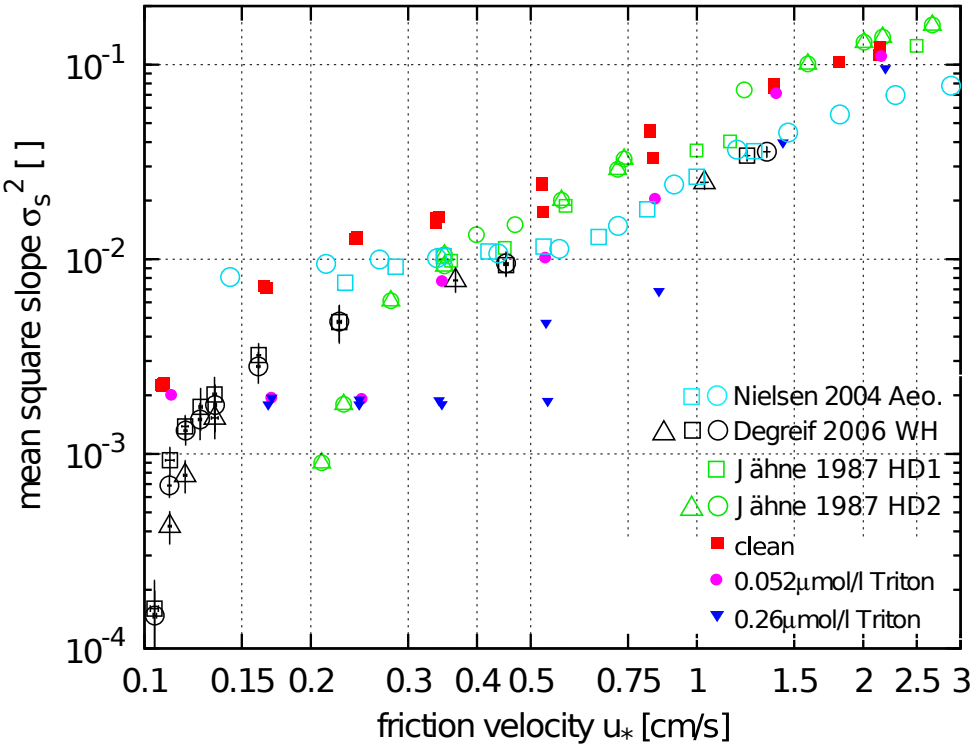

Figure 7.23.: Comparison of the relationship between the friction velocity u_* and the mean square slope σ_s^2 between Degreif [2006], Nielsen [2004], Jähne et al. [1987] and this work.

Figure 7.24 shows the measured transfer velocities k_{600} in dependence of the mean square slope σ_s^2. Again, the data presented in this work correspond best to the data from Jähne et al. [1987]. However, transfer velocities measured here are slightly larger than those of Jähne et al. [1987] for the high mean square slopes and slightly smaller for the lower mean square slopes around 0.01. Transfer velocities measured by Degreif [2006] are a factor of 4 to 5 larger than the ones in this work. An explanation for this could be, that secondary currents, which develop due to the annular shape of the wind wave tanks, are a lot more pronounced in the much smaller WH tank. Stronger secondary currents enhance the near surface turbulence and thus increase the gas transfer velocity, especially in the surfacing region near the inner wall of the wind wave flume. However, some

of the Jähne et al. [1987] data was measured in an equally small tank, and does not show this enlarged transfer velocities. Also, looking at the relationship between the transfer velocity k_{600} and the friction velocity u_*, these large differences become smaller, see figure 7.25.

When the dependency of the gas transfer rate on the friction velocity is studied, see image 7.25, there is good agreement between the Nielsen [2004] data, the Jähne et al. [1987] data set measured in HD2 and the data for the clean case presented in this thesis. Jähne's HD1 data lies slightly below the clean case, indicating the possibility of a slight surfactant in their measurements. This

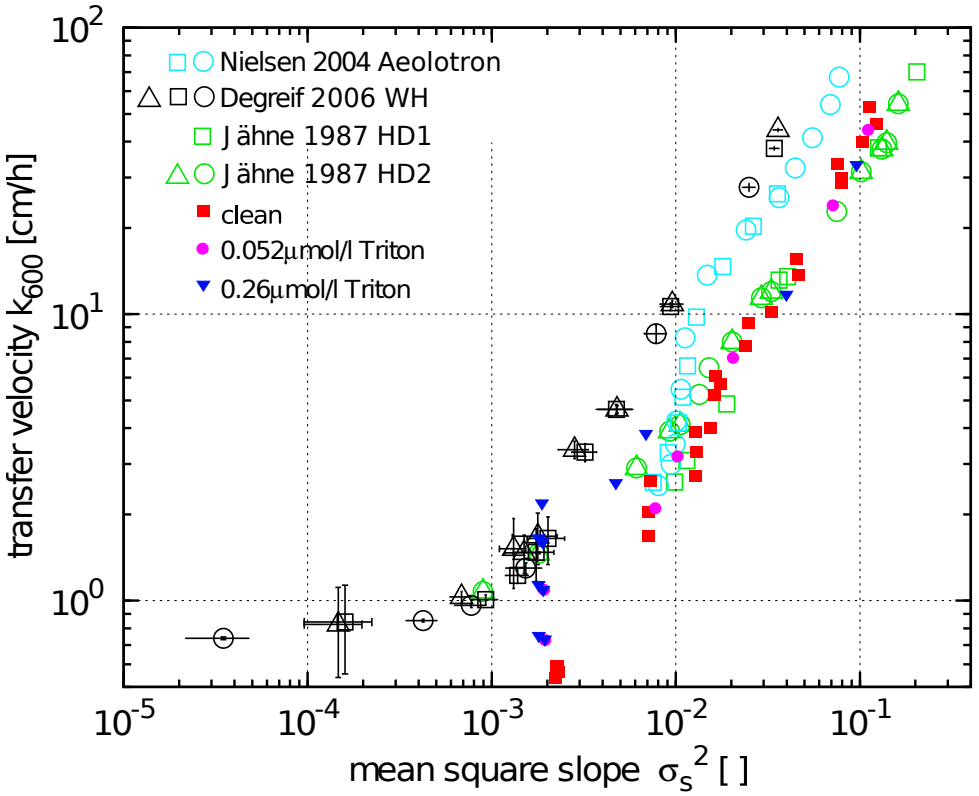

Figure 7.24.: Comparison of the transfer velocity k_{600} in relation to the mean square slope measured by Degreif [2006], Nielsen [2004], Jähne et al. [1987] and this work.

is an indication, that the mean square slope measurement might have an offset towards too small values in the Degreif [2006] data set. Degreif [2006] measured only the along wind component of the mean square slope and extrapolated this using a parameterization by Wu [1990]. This might have led to an underestimation of mean square slopes.

Figure 7.26 shows the comparison of measured Schmidt number exponents, as well as the fit result of the facet model. Again, data measured in this work is most compatible with the Jähne et al. [1987] data. However, they did not fit the facet model to their data. For the Degreif [2006] data set, the change in the Schmidt number exponent starts at much lower mean square slopes than for the other data sets. This is again an indication, that the Degreif data set is biased towards too small mean square slopes. Data from Nielsen [2004] could not reproduce the flat case with $n = 2/3$ and has a systematic deviation towards too small Schmidt number exponents for higher mean square slopes The deviation of the measured values from the fitted curves of the facet model presented here is around 10 %, making this largest deviation between fit and data for all data sets. However, no systematic deviation can be seen. Deviation is in the order of 5 % for the Degreif [2006] values, and Nielsen [2004] up to 16 % for the lowest measured value.

Table 7.4 summarizes the fit parameters of the facet model found by Nielsen [2004], Degreif [2006] and in this work. While this work lies right between the two others for the steepness

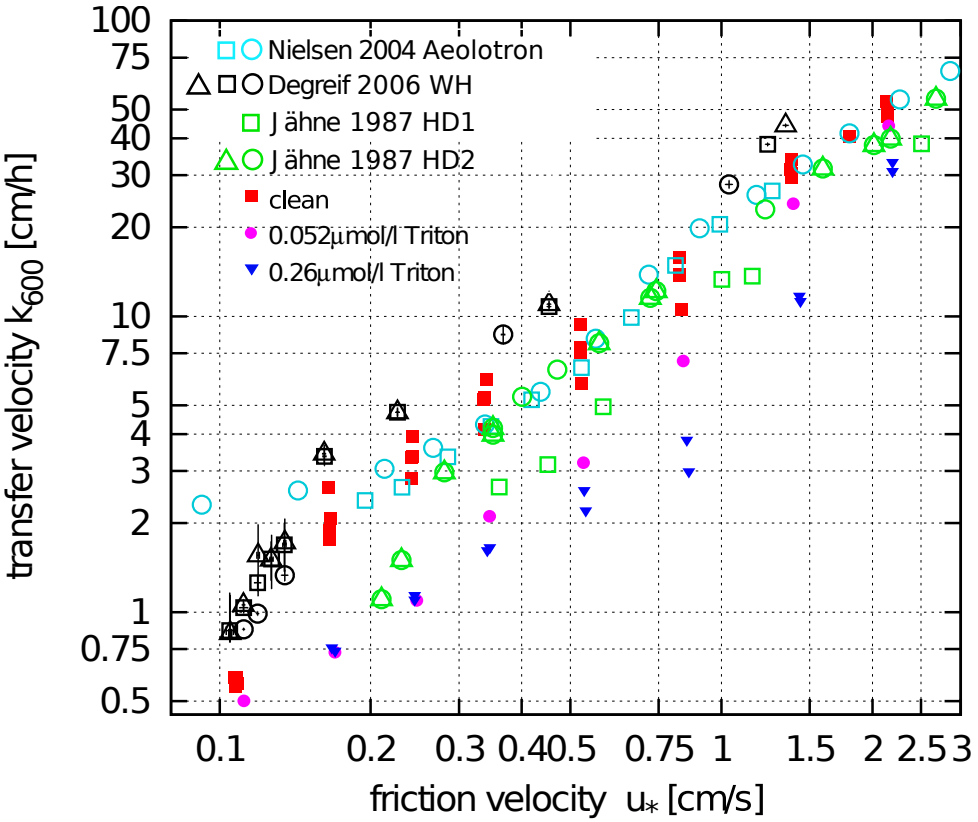

Figure 7.25.: Comparison of the transfer velocity k_{600} in dependence of the friction velocity measured by Degreif [2006], Nielsen [2004], Jähne et al. [1987] and this work.

parameter γ, the midpoint parameter δ is the largest of all three. No clear dependency on the geometrical parameters of the wind-wave tanks can be seen.

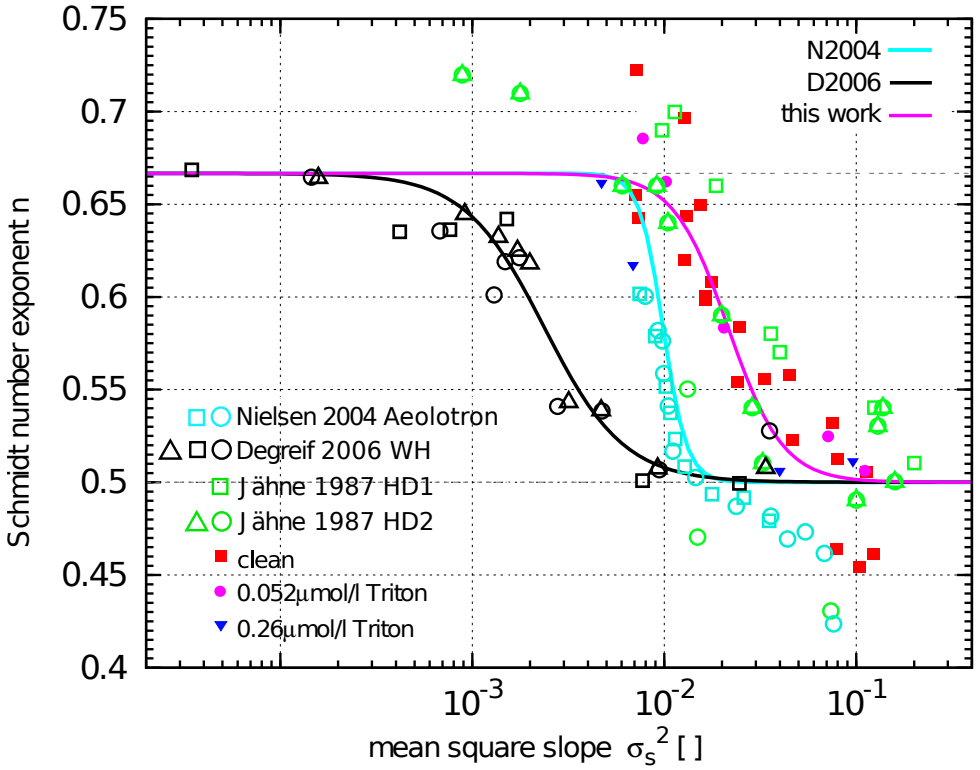

Figure 7.26.: Comparison of the transfer velocity k_{600} between Degreif [2006], Nielsen [2004], Jähne et al. [1987] and this work. Data measured in this work with mean square slopes smaller than 0.002 are not shown.

	β_s	β_w	δ	γ
N2004	2	7.5	0.0095	7
D2006	12.2	4.5	0.00638	2.09
this work	12.2	6.7	0.0395	3.04

Table 7.4.: Comparison of the parameters measured for the facet model by: N2004: Nielsen [2004], D2006: Degreif [2006] and this work.

7.4.7. Uncertainties of Gas Exchange at Low to Medium Wind Speeds

Gas transfer velocities and Schmidt number exponents were mostly shown without error bars, where it did not contribute to understanding the mechanisms. In the following sections calculation of the errors is shown.

Uncertainty in the Reference Wind Speed

The manufacturer of the anemometer that was used to measure the reference wind speed u_{ref} lists an error of 3.1 % of the measured value plus an additional absolute uncertainty of 0.2 m/s. As the friction velocity u_* and the wind speed at a height of 10 m, u_{10} was calculated from the reference wind speed, the same relative error is assumed for both:

$$\frac{\Delta u_{\mathrm{ref}}}{u_{\mathrm{ref}}} = \frac{\Delta u_*}{u_*} = \frac{\Delta u_{10}}{u_{10}} \tag{7.16}$$

This likely underestimates the error, as errors in the parameterizations used to calculate u_* and u_{10} are not considered. However, neither of the authors who provided said parameterizations listed an error estimate.

Uncertainties in Gas Exchange Velocities

The transfer velocities are calculated by

$$k = \underbrace{\frac{V_a}{A}}_{T_1} \cdot \underbrace{\frac{1}{\alpha}}_{T_2} \cdot \underbrace{\frac{c_a}{c'_w} \cdot \left(\lambda + \frac{\dot{c}_a}{c_a}\right)}_{T_3} \cdot \underbrace{\frac{1}{1 - c_a/c'_w}}_{T_4}, \tag{7.17}$$

the different terms T_x will be looked at separately.

The first term T_1 contains geometric values. The volume is considered as known with an uncertainty of ΔV_a =3 %, and the surface area with ΔA =2 %.

The uncertainty of the solubility in the second the second term T_2 is discussed in detail in 7.3.1. Here, the uncertainty is $\Delta\alpha$ =0.15 % for N_2O, 10 % for CHF_3 and C_2HF_5.

In the term T_3, λ is one to two orders of magnitude smaller than the term $\dot{c}_a/c_a$. For the estimation of the uncertainties, λ can therefore be neglected. The term T_3 simplifies to

$$T_3 = \frac{\dot{c}_a}{c'_w}. \tag{7.18}$$

The sources of uncertainty of the water side concentration c'_w are described in detail in section 6.4. The derivatives of the air side concentration $\dot{c}_a$ are calculated by first smoothing, and then numerically deriving the concentration time series. Smoothing eliminates the statistical error of the concentration measurement described in 6.4.3. Further, the derivative does not show additive

offsets in concentrations, which the uncertainty in the input concentration, described in 6.4.1, likely is. Therefore, this source of uncertainty can also be neglected. This leaves the error due to the choice of the reference spectrum, see section 6.4.2 and the fit error 6.4.4 as sources for uncertainty. The derivation process itself, however, poses another source for uncertainties. As the derivative in time step i is calculated by $(c_a(i+1) - c_a(i-1))/2$, i.e. comprising two separate concentration measurements, the errors given in section 6.4.5 need to be doubled.

Because the water side concentration is very large compared to the air side concentration, the expression c_a/c'_w in the fourth term T_4 is close to zero, the fourth term, T_4 can be neglected altogether as it is very close to 1.

All the mentioned error sources are treated as independent, therefore, the uncertainty of the transfer velocities k can be estimated from the relative errors mentioned above,

$$\Delta k = k\sqrt{(\Delta V_a)^2 + (\Delta A)^2 + (\Delta\alpha)^2 + (\Delta\dot{c}_a)^2 + (\Delta c'_w)^2}. \tag{7.19}$$

Figure 7.27 shows the measured gas transfer velocities. Due to the smaller error in the solubility, the uncertainties in the gas transfer rates of nitrous oxide are smaller than those of the other gases. Numerical values of the measured gas transfer velocities and their uncertainties are also listed in appendix A.4.1.

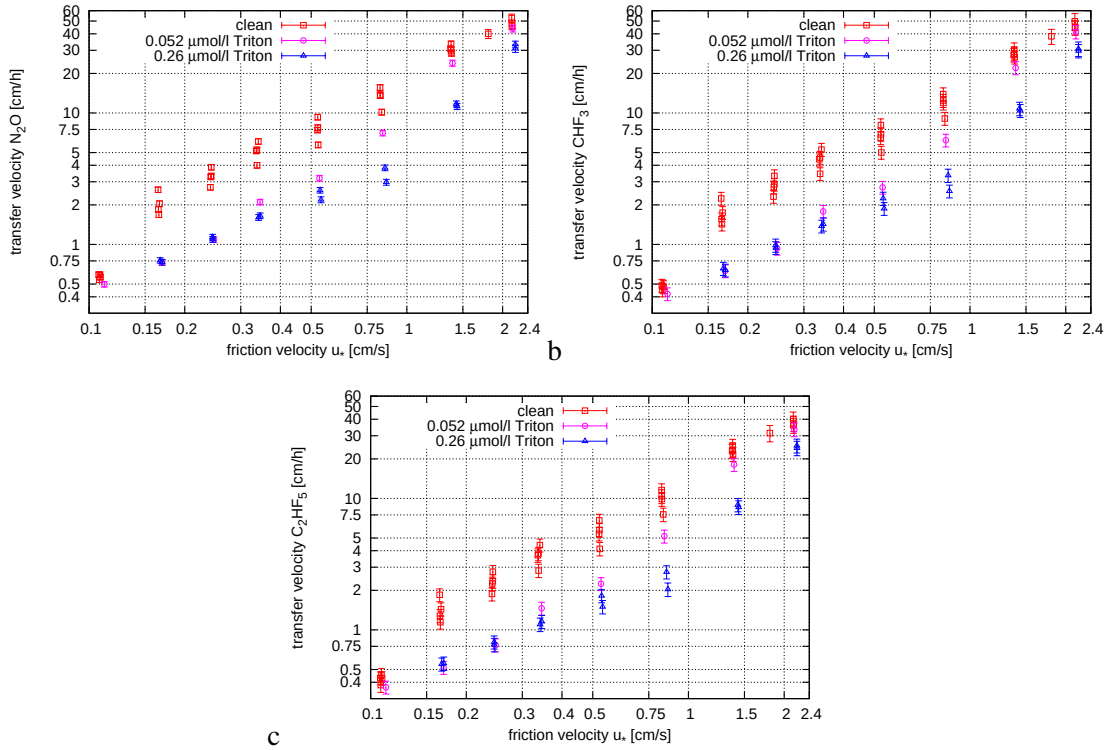

Figure 7.27.: Measured transfer velocities k of tracers nitrous oxide (a), trifluoromethane (b) and pentafluoroethane (c) depending on friction velocity u_* including systematic errors.

Uncertainties in the Schmidt number exponent

The Schmidt number exponent is calculated by

$$n = \frac{\log(k_A/k_B)}{\log(D_B/D_A)} = \frac{\log(R)}{\log(D_B/D_A)} \tag{7.20}$$

with the ratio $R = k_A/k_B$ of two gas transfer velocities, which can be written as

$$R = \underbrace{\frac{\alpha^A}{\alpha^B}}_{T_1} \cdot \underbrace{\frac{c_w^{\mathrm{meas},B}}{c_w^{\mathrm{meas},A}}}_{T_1} \cdot \underbrace{\frac{c_a^A\lambda + \dot{c}_a^A}{c_a^B\lambda + \dot{c}_a^B}}_{T_3} \cdot \underbrace{\frac{1 - c_a^B/c_w^B}{1 - c_a^A/c_w^A}}_{T_3}. \tag{7.21}$$

Each term in equation 7.21 will be looked at separately.

Uncertainties in the solubilities were discussed in section 7.3.1. In tracer combinations that involve nitrous oxide, the uncertainty of the solubility of this tracer can be neglected, as it is much smaller than the uncertainty in the solubility of the other tracers. In that case, the uncertainty amounts to ΔT_1 =10 %, which equals the uncertainty of the solubility measurement of one of the other tracers, otherwise an error of ΔT_1 =20 % is assumed.

The second term T_2 in equation 7.21 is the ratio of water side concentrations, $c_w^{\mathrm{meas},B}/c_w^{\mathrm{meas},A}$. In section 6.4 the sources of uncertainties of the water side concentration measurement are discussed. As the error of the input concentration, see section 6.4.1 is likely an offset, and ratios of concentrations are looked at here, this error can be neglected. This leaves uncertainties of around Δc_w =1 % for each concentration measurement. The combined uncertainty can be calculated by $\Delta T_2 = \left((2\Delta c_w^{\mathrm{meas},A})^2 + (2\Delta c_w^{\mathrm{meas},B})^2\right)^{0.5}$ for the ratio of water side concentrations with the uncertainties of the concentration measurement being regarded as independent.

The third term T_3 in equation 7.21 depends on measured air side concentrations c_a, the derivative of the air side concentration $\dot{c}_a$ and the leak rate λ. The product of leak rates and air side concentrations $c_a\lambda$ is at least one order of magnitude smaller than the derivative of the air side concentration $\dot{c}_a$. Therefore, $c_a\lambda$ can be neglected and the third term reduces to $\dot{c}_a^A/\dot{c}_a^B$. The derivatives of the air side concentrations are calculated by first smoothing, and then numerically deriving the concentration time series. Smoothing eliminates the statistical error of the concentration measurement described in 6.4.3. The derivative does not show additive offsets in concentrations, which the uncertainty in the input concentration likely is, see section 6.4.1. Therefore, this uncertainty can also be neglected. The derivation process itself, however, poses another source for uncertainties. As the derivative in time step i is calculated by $(c_a(i+1) - c_a(i-1))/2$, i.e. comprising two separate concentration measurements, the errors given in section 6.4.5 need to be doubled. The error of the third term can then be calculated by $\Delta T_3 = \left((2\Delta c_a^A)^2 + (2\Delta c_a^B)^2\right)^{0.5}$ when the errors of the concentration measurements of both tracers are seen as independent.

The last term, $T_4 = (1 - c_a^B/c_w^B)/(1 - c_a^A/c_w^A)$, yields values very close to 1.0 due to the measured water concentrations being two to three orders of magnitude larger than the air side concentrations. The factor T_4 deviates from 1.0 by no more than 3 %. Therefore, relatively small uncertainties in air and water side concentrations, that are in percent range, see section 6.4, do not have an influence on the measured Schmidt number exponent. So the uncertainty of the last term is negligible, $\Delta T_4 \approx 0$.

The relative uncertainty ratio of the two transfer velocities R was then estimated as

$$\Delta R = R\sqrt{(\Delta T_1)^2 + (\Delta T_2)^2 + (\Delta T_3)^2} \tag{7.22}$$

with the relative errors ΔT_x.

Using this, the error of the Schmidt number exponent can be calculated using error propagation,

$$\Delta n = \sqrt{\left(\frac{\partial n}{\partial R}\Delta R\right)^2 + \left(\frac{\partial n}{\partial D_1}\Delta D_1\right)^2 + \left(\frac{\partial n}{\partial D_2}\Delta D_2\right)^2}. \tag{7.23}$$

The error of the diffusion coefficients D are assumed to be no larger than 1 %.

The largest part of the uncertainty of the Schmidt number exponent n stems from the uncertainties in the solubilities, contributing up to 20 % to the uncertainty. This stems from the fact, that only very limited data on the solubility of fluorinated hydrocarbons that were used in this work is available. The available data is considered unreliable, as it does not close the mass balances used for evaluating the data, see section 7.3. Also the temperature dependency of the solubility of the used chemicals is not known.

Due to clarity reasons, the errors were not shown in section 7.4.3 where the Schmidt number exponents were presented first. Figure 7.28 shows the Schmidt number exponents measured from the combination N_2O and C_2HF_5 with their respective systematic errors. Numerical values of Schmidt number exponents and their errors are given in appendix A.4.1.

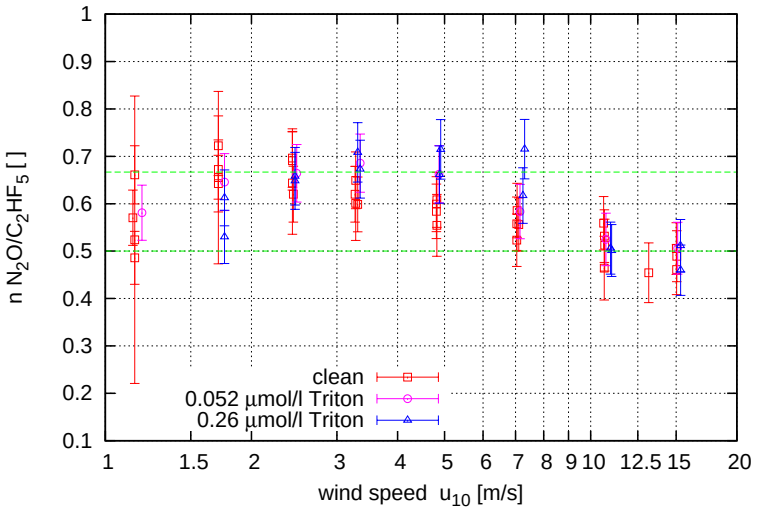

Figure 7.28.: Measured Schmidt number exponents for the tracer combination N_2O and C_2HF_5, with the systematical errors.

Uncertainties in the Carbon Dioxide Equivalent Transfer Velocities

The transfer velocity scaled to $Sc = 600$ was calculated from the transfer velocity of nitrous oxide by

$$k_{600} = k_{N_2O} \left(\frac{600}{Sc_{N_2O}} \right)^{-n} \tag{7.24}$$

The Schmidt number of nitrous oxide under the conditions observed in the Aeolotron deviated from 600 by no more than 6 %. Therefore, the factor $600/Sc_{N_2O}$ is very close to one, making $(600/Sc_{N_2O})^{-n}$ also very close to one. Consequently, uncertainties in the Schmidt number and especially the Schmidt number exponent do not have much influence on the calculated k_{600} and can be ignored. This leaves the uncertainty of k_{N_2O} as the only source for errors in k_{600}, which is then calculated from the absolute error Δk_{N_2O} by:

$$\Delta k_{600} = k_{600} \frac{\Delta k_{N_2O}}{k_{N_2O}}. \tag{7.25}$$

7.5. Gas Exchange Velocities at High Wind Speeds

In this section, the measured transfer velocities will be presented first. Interpretation in the light of bubble mediated gas transfer will follow. A model, that is developed from an empirical parameterization will be proposed that can be used to calculate the transfer velocity of any water side controlled tracer.

7.5.1. Measured Transfer Velocities

Figure 7.29 shows the measured gas transfer velocities. The first notable thing is that the transfer

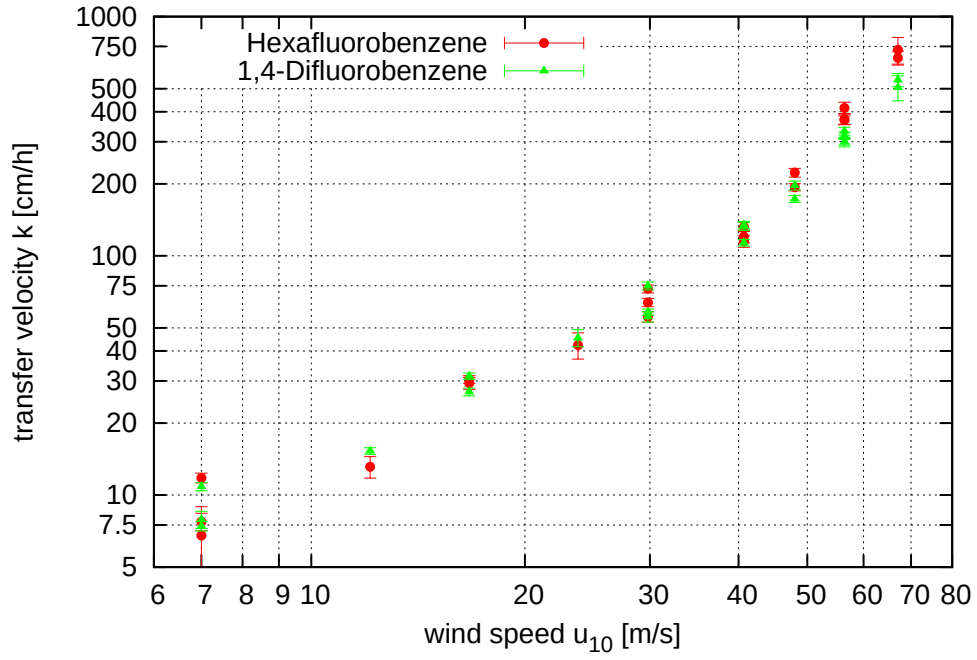

a)

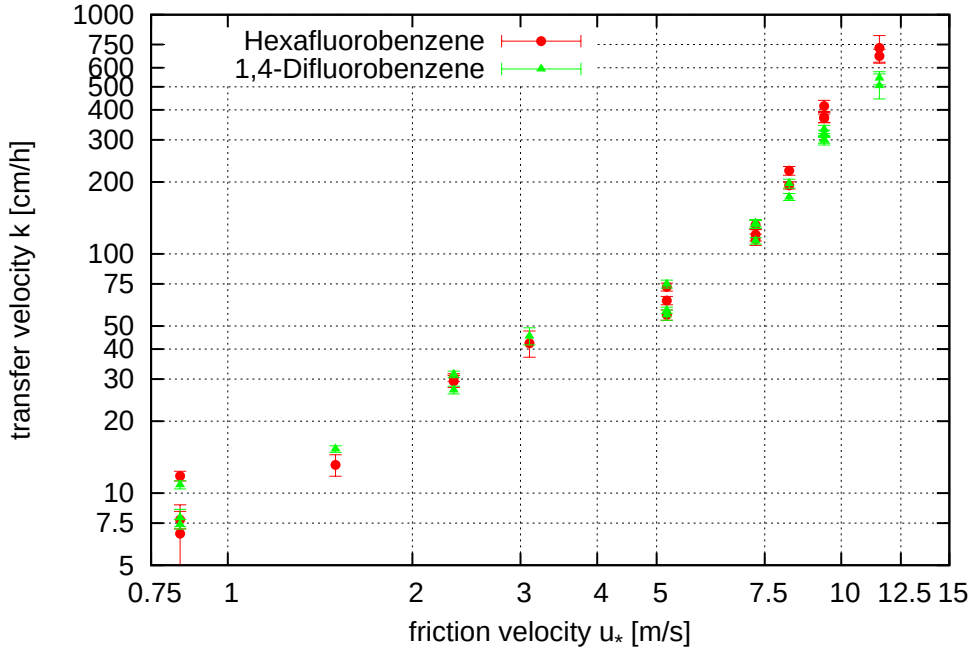

b)

Figure 7.29.: Measured transfer velocities k of tracers hexafluorobenzene and 1,4-difluorobenzene a) against wind speed u_{10} and b) against water side friction velocity u_*.

velocity continues to increase with wind speed and shows no sign of saturation, as proposed by Soloviev and Lukas [2010]. At a wind speed of $u_{10} = 35$ m/s (friction velocity $u_* = 6$ cm/s) the rate of increase of the gas transfer velocity becomes steeper.

The temperature varied slightly from measuring day to measuring day, see section 4.3.2. This in turn modified the chemical and physical parameters such as Schmidt number, solubility and kine-

matic viscosity of the water. Therefore comparing transfer velocities measured at the same conditions must be done with caution. One way of making transfer velocities comparable is Schmidt number scaling, see equation 2.68, to a Schmidt number of 600, which corresponds to CO_2 at 20 ^{o}C in fresh water. In section 7.5.4, an argument will be made that this is not fully applicable in the case of bubble mediated gas transfer and a new modified scaling will be proposed. However, as Schmidt number scaling is common practice, it will be shown here.

Figure 7.30 shows gas transfer velocities that were scaled to k_{600} by Schmidt number scaling,

$$k_{600} = k_{\mathrm{xFB}} \left(\frac{600}{Sc_{\mathrm{xFB}}(T)} \right)^{-n} \tag{7.26}$$

with xFB being either hexafluorobenzene or 1,4-difluorobenzene. The Schmidt number was calculated from the diffusion coefficient and the kinematic viscosity of water as described in section 4.2.3. As the Schmidt number exponent n, 0.55 was chosen for the two lowest wind speeds to account for the area near the wind inlet (low fetch) where no waves were observed. The value of n=0.55 was measured at a wind speed of $u_{10} = 7$ m/s in the Aeolotron. For the higher wind speeds 0.5 was used as Schmidt number exponent, indicating wavy conditions.

To check the plausibility of the measured k_{600} transfer velocities, in figure 7.30a some commonly used empirical parameterizations are shown with the data. The measured data are within the range of these parameterizations. In figure 7.30b, the theoretical prediction, equation 2.67, with parameters $\beta = 6.7$ and $n = 0.5$,

$$k_{\mathrm{theo}}(u_*) = u_* \cdot \frac{1}{6.7} Sc^{-0.5}. \tag{7.27}$$

is also shown. For low friction velocities, the data matches the theoretical prediction. For higher friction velocities, the data lies higher than the theoretical curve. The reason for this will be discussed in section 7.5.3.

The transfer velocities of each tracer, scaled to a Schmidt number of 600, k_{600}, can be averaged per wind speed condition. Contrary to the measured transfer velocities k, they correspond to the same temperature, while each k was measured at slightly different temperature and therefore Schmidt number. To account for the different accuracy Δk_{600} at which the single transfer velocities k_{600} were measured, weighted mean transfer velocities $\overline{k_{600}}$ were calculated from the n repeated measurements of the transfer velocities at the same condition,

$$\overline{k_{600}} = \frac{\sum_{i=1}^{n} k_{600\,i} * w_i}{\sum_{i=1}^{n} w_i} \tag{7.28}$$

with the weights being defined as the inverse of the error of each value i, $w_i = 1/\Delta k_{600\,i}$. Figure 7.31 shows the calculated mean transfer velocities.

Now, an enhancement factor E_f can be defined that describes the enhancement of the transfer velocity of hexafluorobenzene (HFB) over the transfer velocity of 1,4-difluorobenzene (DFB) by

$$E_f := \frac{k_{600,HFB} - k_{600,DFB}}{k_{600,DFB}} * 100\,\% \tag{7.29}$$

with the average transfer velocity of hexafluorobenzene $k_{600,HFB}$ and of 1,4-difluorobenzene $k_{600,DFB}$. Figure 7.32 shows the enhancement factor E_f. Up to a wind speed of around $u_{10} = 40$ m/s both tracers have the same transfer velocities, but for higher wind speeds, hexafluorobenzene is transferred faster across the air-sea surface than 1,4-difluorobenzene. This is likely due to the effects of bubbles, which are more efficient for lower soluble gases like hexafluorobenzene.

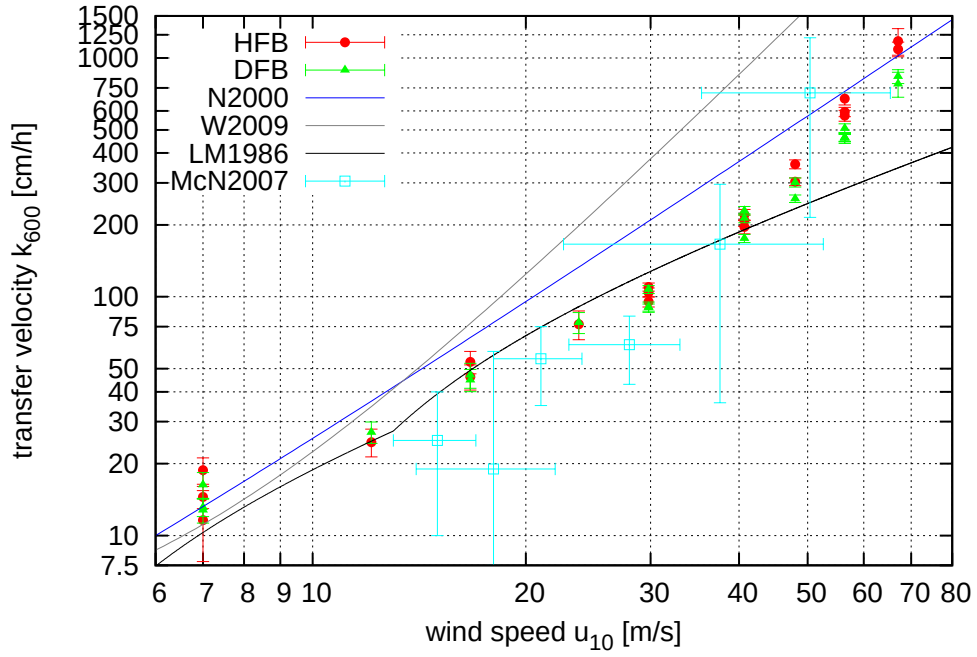

a)

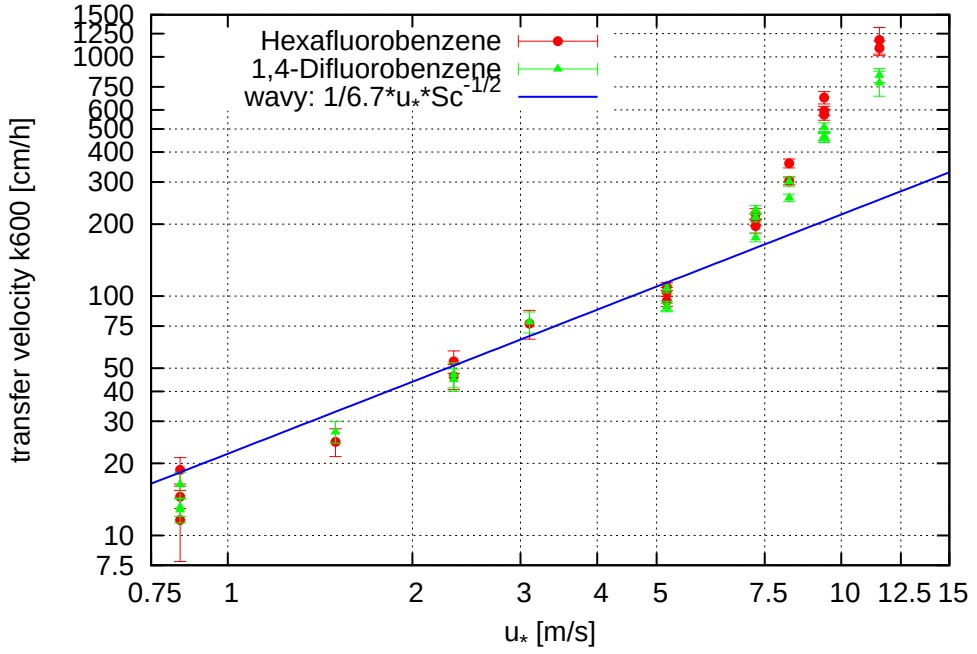

b)

Figure 7.30.: All measured transfer velocities k_{600} of tracers hexafluorobenzene and 1,4-difluorobenzene a) against wind speed u_{10} along with some empirical parameterizations (N2000: Nightingale et al. [2000], W2009: Wanninkhof et al. [2009], LM1986: Liss and Merlivat [1986]) and the only measured data at hurricane wind speeds (McN2007: McNeil and D'Asaro [2007]) and b) against friction velocity u_* with the theoretical prediciton.

A different enhancement factor will be defined and discussed in section 7.5.3, where empirical gas transfer models related to breaking waves entraining bubbles into the water are discussed in depth.

Measured, as well as averaged transfer velocities are also listed numerically in appendix A.4.2.

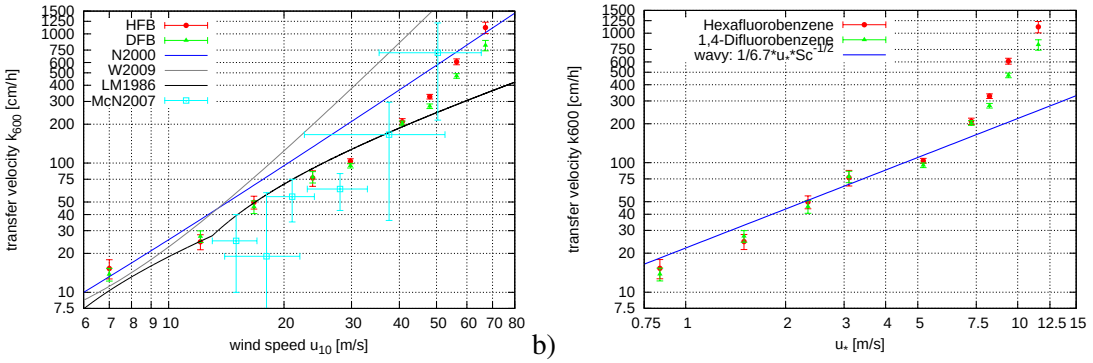

a) b)

Figure 7.31.: Measured mean transfer velocities k_{600} of tracers hexafluorobenzene and 1,4-difuorobenzene a) against wind speed u_{10} along with some empirical parameterizations (N2000: Nightingale et al. [2000], W2009: Wanninkhof et al. [2009], LM1986: Liss and Merlivat [1986]) and the only measured data at hurricane wind speeds (McN2007: McNeil and D'Asaro [2007]) and b) against friciton velocity u_* with the theoretical prediciton.

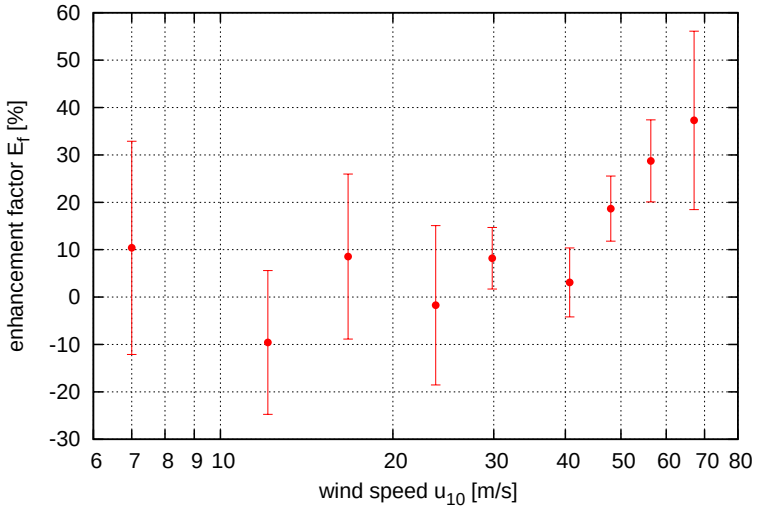

Figure 7.32.: Enhancement factor E_f describing the enhancement of the gas transfer of hexafluorobenzene over the transfer of 1,4-difluorobenzene.

7.5.2. Comparison between Heidelberg and Kyoto Gas Transfer Velocities

To further validate the measured gas transfer velocities, a comparison between the measurements in the Kyoto High-Speed Wind Wave Tank and in the Heidelberg Aeolotron, see section 7.4.2, is made, see figure 7.33. In the region of overlap between $u_{10} = 7$ m/s and 15 m/s or water sided friction velocity $u_* = 0.8$ cm/s and 2 cm/s, respectively, the two datasets agree. This indicates, that the shape of the wind-wave flume does not severely influence the measurements.

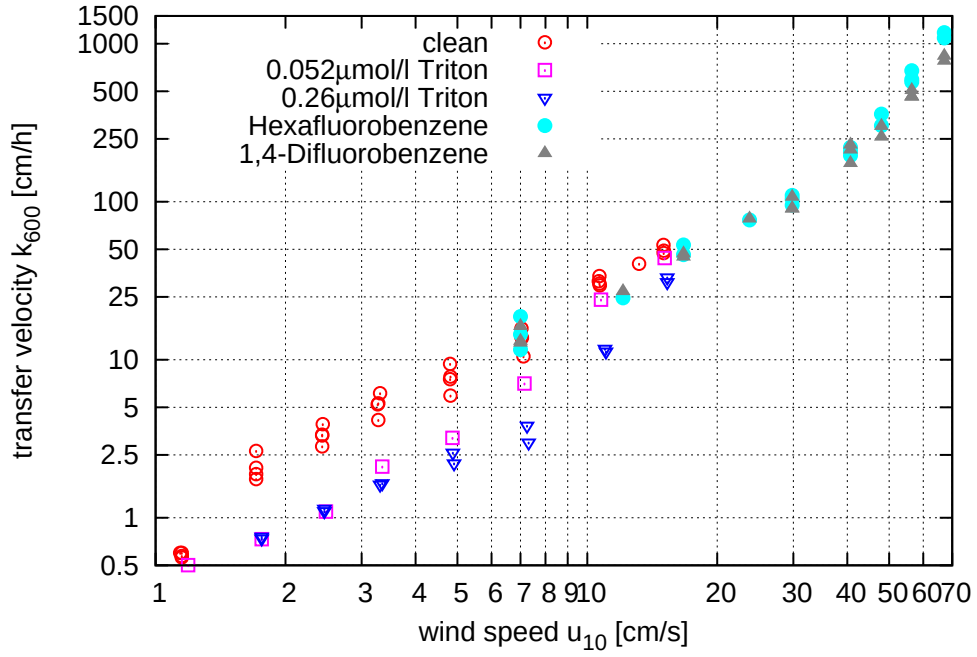

a)

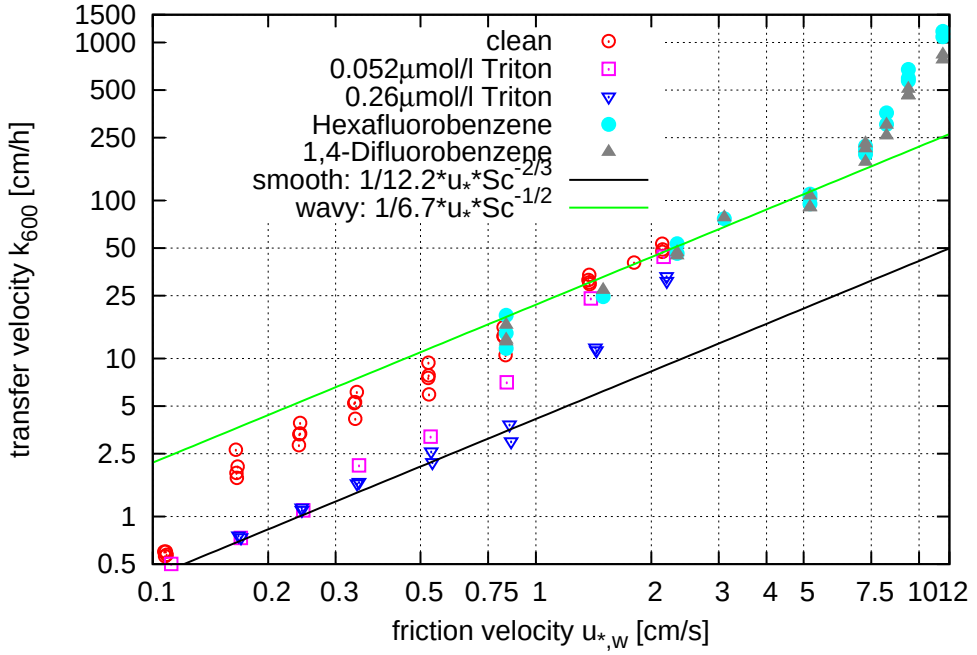

b)

Figure 7.33.: Comparison of gas transfer velocities k_{600} measured in the Heidelberg Aeolotron (open symbols), see section 7.4.2 and in the Kyoto high speed wind-wave tank (solid symbols). a) plotted against the wind speed u_{10} and b) against the friction velocity u_*.

7.5.3. Enhancement of Gas Transfer at Highest Wind Speeds

Using the theoretical prediction, equation 2.67, for a wavy water surface with the parameter $\beta_w = 6.7$ measured in section 7.4.2, the wind induced part of the transfer velocity k_w without bubbles can be estimated. The Schmidt number exponent n was not measured. The exponent is assumed to be $n = 0.5$ for a rough surface at the higher wind speeds, except for the lowest two wind speeds,

where $n = 0.55$ was chosen to compensate for the partially smooth surface at low fetches. Figure 7.34 shows the theoretically predicted and measured transfer velocities. While the theoretical prediction matches the measured values below 100 cm/h, the measured velocities are much larger than the predicted ones for larger values. This is a clear indication that additional mechanisms for gas exchange must be at work for higher wind speeds. These physical mechanisms are likely a combination of bubbles directly transporting gas out of the water, and enhanced turbulence in the air-sea boundary layer due to breaking waves and bubbles rising through the air-sea boundary. For instance, Jähne [1991] showed, that in a wind-wave tank, where mechanical waves can be generated, the transfer rate of heat, which is insensitive to direct transport due to bubbles, almost doubles in the presence of breaking waves. On the other hand, McGillis et al. [1995] were able to dissect measured gas transfer rates into gas transport in bubbles, increased transfer due to bubble mediated turbulence and wave induced transfer. They found that the turbulence partition of the total gas transfer velocity was at least a factor of 2.5 lower than the direct gas transport in bubbles.

As bubbles are the easily visible manifestation of this new gas exchange regime, it will be called the regime of bubble mediated gas transfer in accordance with literature, even though more physical mechanisms than bubbles might be at play.

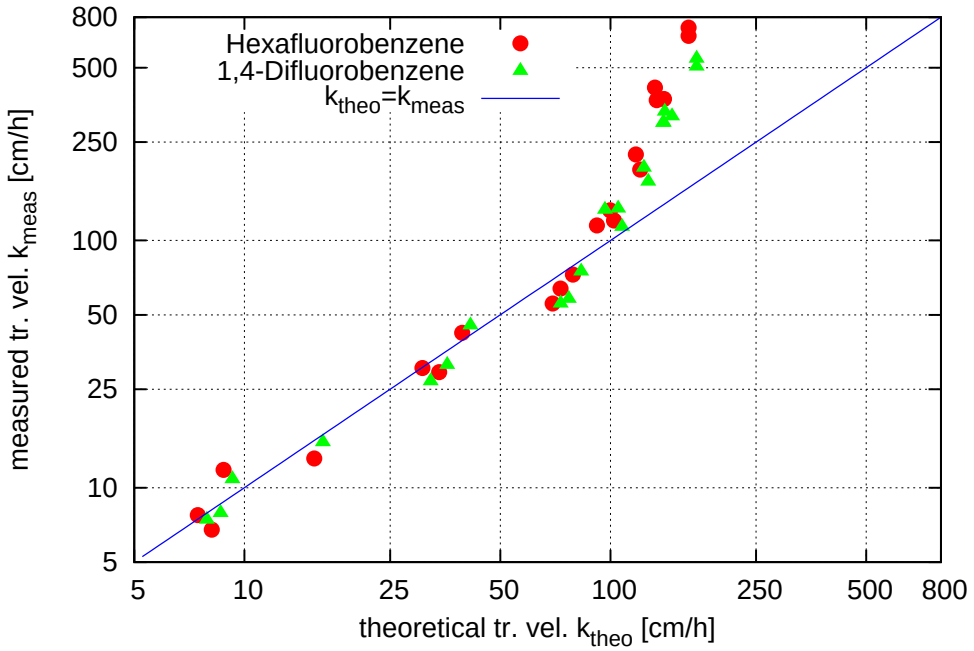

Figure 7.34.: Theoretically predicted gas transfer velocities k_{theo} and measured velocities k_{meas}

Most literature sources, including Merlivat and Memery [1983] and Woolf and Monahan [1993], assume that the total transfer velocity k can be written as

$$k = k_w + k_b, \tag{7.30}$$

with the k_w being the wind induced transfer velocity in absence of bubbles and k_b being the transfer caused in the wind regime when strong wave breaking occurs and bubbles are generated. Using this relationship, the wave breaking and bubble induced gas transfer velocity can be estimated as

$$k_b(u_*) = k - k_w = k - u_* \cdot \frac{1}{6.7} Sc^{-1/2}, \tag{7.31}$$

with the temperature dependent Schmidt number shown in section 4.2.3. However, this only works if the dimensionless parameter β, measured at wind speeds around $u_{10} = 12$ m/s to 15 m/s does not change towards higher wind speeds.

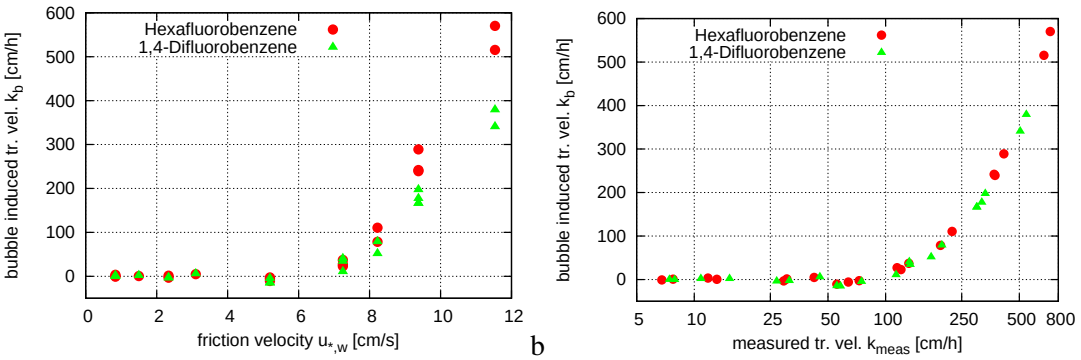

Figure 7.35.: Breaking and bubble induced portion of the gas transfer velocity measured in the Kyoto High-Speed Wind Wave Tank, a) plotted against the friction velocity u_* and b) plotted against the measured gas transfer rate.

Figure 7.35 shows the calculated breaking induced part of the gas transfer velocity. As expected, for low wind speeds when no bubbles are entrained in the water and no large scale wave breaking occurs, the bubble induced part k_b lies close to zero. At a water side friction velocity of around 6.5 cm/s, the bubble induced part starts to rise. For the tracer with the lower solubility, the bubble induced part of the transfer is higher.

An enhancement factor can be defined by

$$E_b = \frac{k_b}{k_w} \tag{7.32}$$

that describes the enhancement of the measured values over the expected purely wind induced values k_w. Figure 7.36 shows the calculated enhancement factors. At a wind speed of $u_{10} = 50$ m/s

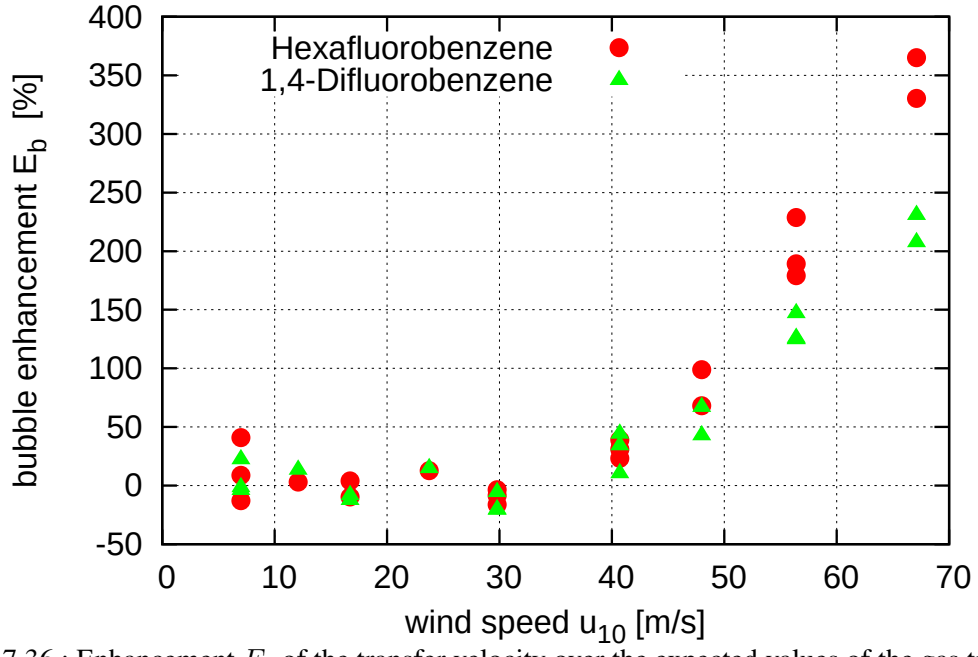

Figure 7.36.: Enhancement E_b of the transfer velocity over the expected values of the gas transfer rate due to bubbles, plotted against the wind speed.

to 55 m/s, the bubble induced portion of the measured transfer velocity is 100 %, meaning it is as large as the non-bubble influenced part. At the highest measured wind speeds, k_b makes up about

77 % of the total transfer velocity with an enhancement of 350 % for the hexafluorobenzene, and 69 % of the total transfer velocity (225 % enhancement) for the 1,4-difluorobenzene.

Attempts have been made to parameterize the bubble portion of the gas transfer. For instance, Keeling [1993] parameterizes the bubble term as

$$k_{b,k} = W_c \left(c_0 \, Sc^{-x} \alpha^{-y} \right) \tag{7.33}$$

with the white cap coverage W_c, meaning the fraction of the surface area that is covered by white caps. Keeling [1993] gives the values for the parameters x=0.35 and y=0.3. The parameter c_0 can be determined by a fit. As proposed by Monahan and Lu [1990], the whitecap coverage parameter W_c is commonly parameterized against the wind speed u_{10} by

$$W_c(u_{10}) = c_1 \left(u_{10} - u_0 \right)^3 \tag{7.34}$$

which is valid from the onset wind speed of u_0 where whitecaps start to form. This parameter as well as c_1 are typically determined empirically by a fit. Combining equation 7.33 and 7.34 yields the dependency of k_b from the wind speed u_{10},

$$k_{b,k}(u_{10}) = c \left(u_{10} - u_0 \right)^3 \cdot \left(Sc^{-0.35} \alpha^{-0.3} \right) \tag{7.35}$$

The fit parameters c_0 and c_1 were combined into the parameter c. Below the onset wind speed of u_0 the bubble term $k_{b,k}$ is assumed to be 0. The bubble term $k_{b,k}$ now depends on two more variables beside the wind speed, the Schmidt number Sc and the solubility α, which is different for both tracers and also varied from measuring day to measuring day due to different temperatures.

Equation 7.35 was fitted to the data set using temperature dependent Schmidt numbers listed in section 4.2.3. Unfortunately, no temperature dependency of the solubility of both tracers is known. Therefore, fixed solubility values of $\alpha_{\mathrm{HFB}} = 1.0$ and $\alpha_{\mathrm{DFB}} = 3.2$ were assumed, see section 4.2.

The best fit of equation 7.35 to the data was achieved with parameters $c = 0.069$ and $u_0 = 21.46$ yielding

$$k_{b,k}(u_{10}) = 0.069 \left(u_{10} - 21.5 \right)^3 \cdot \left(Sc^{-0.35} \alpha^{-0.3} \right) \tag{7.36}$$

with $k_{b,k}$ in cm/h and u_{10} in m/s. Figure 7.37a shows a comparison between the measured bubble induced transfer velocity k_b and the prediction of equation 7.36. It should be noted that the k_b values shown there were measured under different temperatures. While the fit of equation 7.35 accounted for different temperatures, the plot does not show this as it was made with mean Schmidt numbers. Also shown is equation 7.36 for mean Schmidt numbers, $Sc_{\mathrm{HFB}} = 1675$ and $Sc_{\mathrm{DFB}} = 1511$.

Figure 7.37b shows a direct comparison between the measured and the modeled transfer velocities, taking different Schmidt numbers due to different temperatures into account. The data is well represented by the model.

A different parameterization was proposed by Asher et al. [1995]. They parameterize the bubble term as

$$k_{b,k} = B_c \left(a_1 \alpha^{-1} + a_2 Sc^{-n'} \right) \tag{7.37}$$

with the fit parameters a_1, a_2 and n' as well as the bubble plume coverage B_c which is the lab equivalent to the whitecap coverage W_c. As neither bubble plume or whitecap coverage were measured, equation7.34 is used again to estimate B_c. This leads to a parameterization of the form

$$k_{b,k}(u_{10}) = \left(u_{10} - u_0 \right)^3 \cdot \left(a \alpha^{-1} + b Sc^{-n'} \right). \tag{7.38}$$

The proportionality constant c of the whitecap coverage parameterization as well as fit parameters a_1 and a_2 are condensed into the fit parameters a and b because they can not be separated with the presented data set.

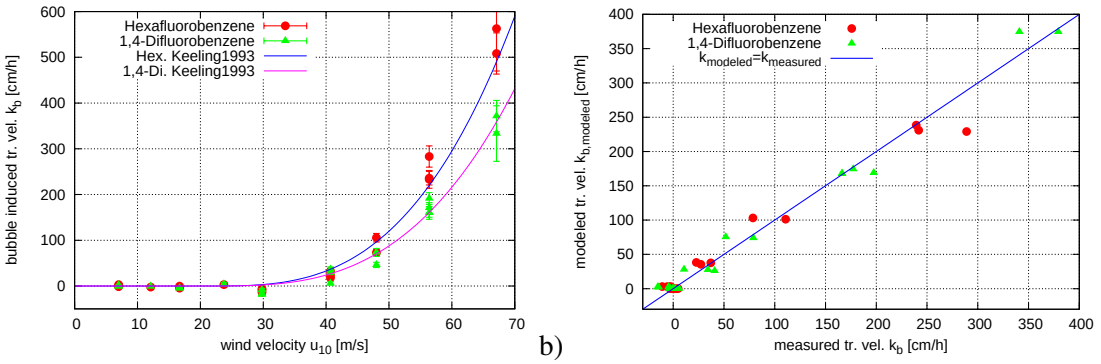

Figure 7.37.: a) Bubble induced portion of the gas transfer velocity measured for both tracers and prediction of k_b using the parameterization equation 7.36. b) Deviation between the measured and the modeled transfer velocities for the same parameterization.

To apply this parameterization to the data, the onset wind speed of u_0=21.5 m/s was chosen according to the already shown parameterization proposed in Keeling [1993]. The parameters a, b and n' were fitted. It turned out that the fit was very unstable as many combinations of b and n' yielded the same value for $bSc^{-n'}$. Therefore, n' was fixed to a value of 2/3 as proposed by Asher et al. [1995]. The fit resulted in the parameterization

$$k_{b,k}(u_{10}) = (u_{10} - 21.5)^3 \cdot \left(0.00284\alpha^{-1} + 0.368Sc^{-2/3}\right). \tag{7.39}$$

Figure 7.38a shows the bubble term for this model. Figure 7.38b shows the measured and the modeled transfer velocities. Also for this model, no systematic deviations between measured and modeled data were found. There is no obvious difference between this model and the already discussed model by Keeling [1993].

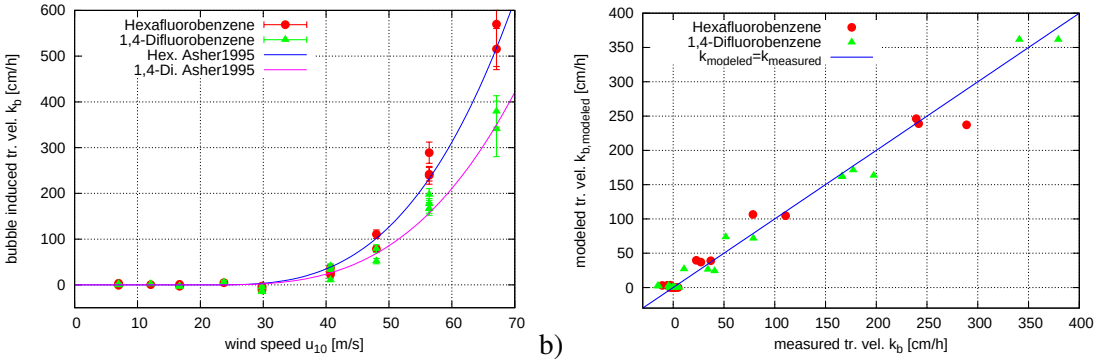

Figure 7.38.: a) Bubble induced portion of the gas transfer velocity measured for both tracers and prediction of k_b using the parameterization equation 7.39. b) comparison of measured and modeled gas transfer rate for equation 7.39.

A third parameterization, developed by Woolf [1997],

$$k_{b,k}(u_{10}) = f u_{10}^{3.41} \left(\alpha \left(1 + a\alpha Sc^{-1/2}\right)^{-1/1.2}\right)^{-1/2} \tag{7.40}$$

with the fit parameters f and a was also tested. This parameterization has a fundamentally different u_{10} dependency. Best fit parameters were found to be $f = 2.18 \cdot 10^{-4}$ and $a = 14$.

Figure 7.39a shows the fitted model curves as well as the measured bubble term. Figure 7.39b shows the deviation between modeled and measured total transfer velocity. Here, a systematic

deviation between measured and modeled transfer velocities are found. Transfer velocities around 70 cm/h are overestimated by the model, while the highest transfer velocities are underestimated. This is likely due to the different treatment of the whitecap coverage without an onset wind speed u_0. Therefore, one of the two other models is to be preferred over the Woolf [1997] model.

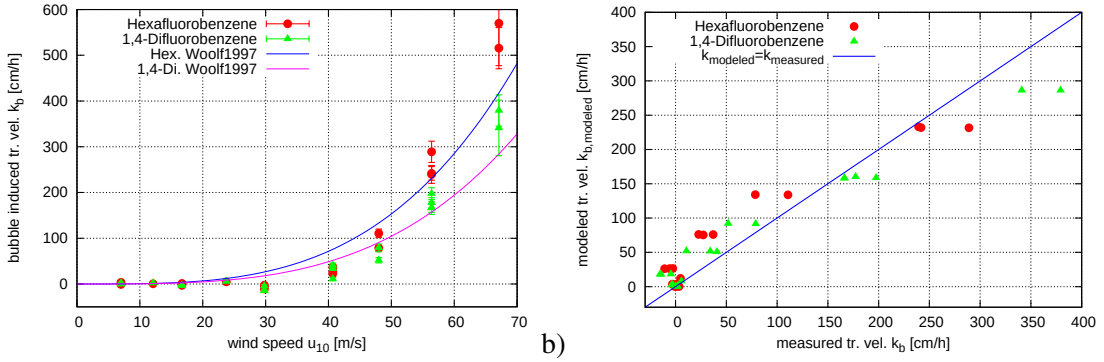

Figure 7.39.: a) Bubble induced portion of the gas transfer velocity measured for both tracers and prediction of k_b using the parameterization equation 7.40. b) comparison of measured and modeled gas transfer rate for equation 7.40.

A further test can be made which one of the two models, which were found to fit the data, is best. Figure 7.40 shows arrays of curves for both the Asher and the Keeling parameterization, see equations 7.38 and 7.39.

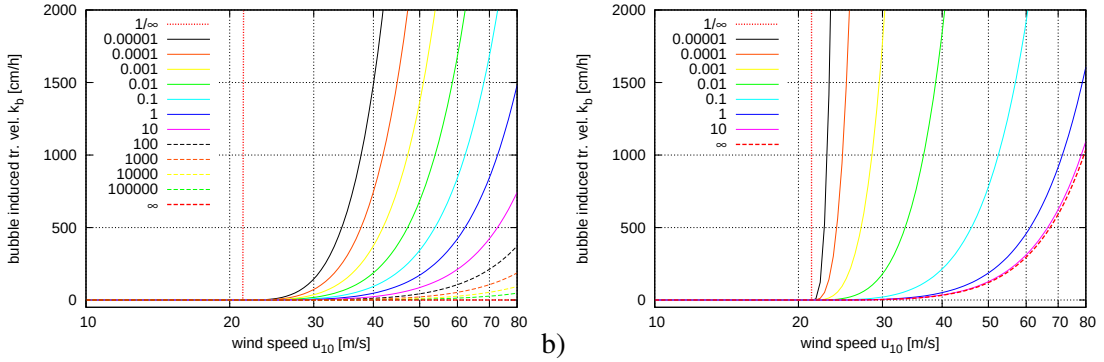

Figure 7.40.: Arrays of curves for a) the Keeling parameterization and b) for the Asher Parameterization. A Schmidt number of 600 was chosen, and the solubility was varied from curve to curve. Also shown are the upper ($\alpha = \infty$, dashed red line) and lower limits ($\alpha = 1/\infty$, dashed red line).

An interesting fact is the behavior of these arrays of curves in the case of very high or very low solubilities. For really low soluble chemicals, bubbles do have very large capacity to take up gas from the water and take part in gas exchange for a longer time than they need to rise to the water surface and burst. This means that bubbles do not get saturated and take part in gas transfer as long as they live. Therefore, their surface area can be treated just like an enlargement of the water surface area that takes part in gas exchange. This surface area is of course not dependent on the solubility. Gas transfer is, in this case, limited by diffusion across the boundary layers between the air in the bubble and the water. Neither the Keeling, nor the Asher model predict this boundary limited by the bubble surface area for low solubilities. In fact, both models predict gas transfer that converges to infinity as solubility approaches zero, which is unphysical.

The other extreme is gas transfer at higher solubilities, where all bubbles are saturated very fast.

Then, the transport is limited by the volume of the bubbles itself. Transfer of tracers with high, but differing solubilities should therefore be limited by the volume of the bubbles, and not the solubility. For the Asher et al. [1995] model, there is such a limit at high solubilities at a value of $k_{b,k} = (u_{10} - 21.5)^3 \cdot 0.368 Sc^{-2/3}$. But this limit is now determined by the Schmidt number of the tracers, which has no relation to the air volume in the bubbles. The Keeling [1993] model does not have a limit for high solubilities. As solubility approaches infinity, the bubble effect converges to zero.

However, no empirical or physical model, that limits gas transfer to the bubble surface area for low solubilities and to the bubble volume for high solubilities is available for bubble clouds produced by breaking waves. Therefore, equation 7.39 as the parameterization, that is the most physical of the presented parameterizations, is chosen to scale the bubble portion of the gas transfer from tracer 1 to tracer 2,

$$k_{b,1} = k_{b,2} * \frac{0.00284\alpha_1^{-1} + 0.368 Sc_1^{-2/3}}{0.00284\alpha_1^{-1} + 0.368 Sc_1^{-2/3}} = k_{b,2} * \frac{\alpha_1^{-1} + 129.6\, Sc_1^{-2/3}}{\alpha_1^{-1} + 129.6\, Sc_1^{-2/3}} \tag{7.41}$$

As a test, the measured transfer velocity of 1,4-difluorobenzene was scaled to that of hexafluorobenzene using this equation, see figure 7.41. The scaled transfer velocities of 1,4-difluorobenzene represent the transfer velocities of hexafluorobenzene. This is to be expected, because the scaling was developed using both tracers in the first place. Ideally, the proof that this scaling is valid would

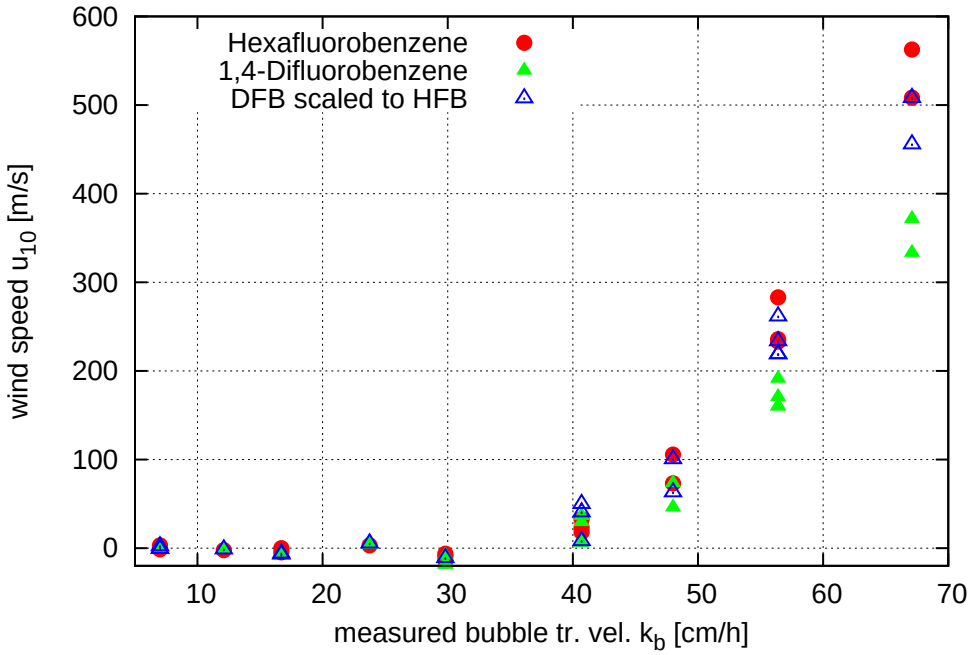

Figure 7.41.: Bubble induced transfer velocity of hexafluorobenzene, 1,4-difluorobenzene and 1,4-difluorobenzene scaled to hexafluorobenzene using equation 7.41.

need at least a third tracer. Fit parameters would be determined using two of the tracers while the prediction of the scaling for the third tracer would be compared to the measured transfer velocities. Unfortunately, only two tracers were used in this study.

Using the scaling from one tracer to another shown in equation 7.41 and the splitting of the total transfer velocity into a wave dependent and a bubble dependent part, see equation 7.30, a modified scaling of the total transfer velocity can be proposed. This can be seen as the high wind speed equivalent of Schmidt number scaling, see equation 2.68,

The wave dependent k_w part of the transfer velocity is then scaled with classical Schmidt number scaling, while the bubble part is scaled using equation 7.41,

$$k_1 = k_{w,1} + k_{b,1} = k_{w,2} \left(\frac{Sc_1}{Sc_2} \right)^{-n} + k_{b,2} * \frac{\alpha_1^{-1} + 129.6\, Sc_1^{-2/3}}{\alpha_2^{-1} + 129.6\, Sc_2^{-2/3}}. \tag{7.42}$$

As a preliminary conclusion using Schmidt number scaling, see equation 2.68 is incorrect, when bubbles have an influence on the gas transfer velocity, because it does not account for solubility effects.

7.5.4. A Model for Gas Transfer at High Wind Speeds

It has been shown, that for small wind speeds, where no bubbles are present, the Deacon [1977] formulation of gas transfer, see equation 2.67, can be used to calculate gas transfer rates, see image 7.34. It was further shown in the previpus section, that the empirical models of Asher et al. [1995] and Keeling [1993] can be used to model the bubble part of the transfer velocity. Combining both the Deacon [1977] and the Asher et al. [1995] models, a semi empirical model for gas transfer at high wind speeds can be found,

$$k(u_*, u_{10}, \alpha, Sc, n) = \frac{u_*}{\beta} (Sc)^{-n} + (u_{10} - 21.5)^3 \cdot \left(0.00284\alpha^{-1} + 0.368 Sc^{-2/3} \right). \tag{7.43}$$

In the conditions observed here, the Schmidt number exponent was $n = 0.5$ for most cases, and $\beta = 6.7$. Using the definition of the drag coefficient C_d, the friction velocity u_* can be transformed into u_{10} or vice versa,

$$u_{10}^2\, C_d = u_*^2, \tag{7.44}$$

so that equation 7.43 depends on either u_* or u_{10}. Various empirical parameterizations for the wind speed dependency exist for the drag coefficient, for instance Smith and Banke [1975] or Trenberth et al. [1998]. In the case of the presented experiment, simultaneous measurements of wind speed and friction velocity exist. Therefore, such a parameterization is not necessary here.

Figure 7.42 shows the modeled transfer velocities using equation 7.43 in comparison with the measured values. As the model was modified to fit the data, it is not surprising, that it describes the data well.

As an example, the application of the model to the common reference tracer CO_2 with a Schmidt number of $k = 600$ in fresh water at $20\,^oC$ and a solubility of α=0.68 at the same temperature will be shown. Figure 7.43a shows the modeled total transfer velocity of carbon dioxide as well as for both tracers used in this study at a temperature of $20\,^o$C. Again, the Schmidt number exponent n=0.55 was chosen for the two lowest wind speeds, and n=0.5 for the higher speeds. Unfortunately, the model's prediction can not be compared to measured data, as the transfer velocity of CO_2 was not measured in this study. Therefore, the model's predictions need to be confirmed in the future.

Figure 7.43b shows the measured transfer velocities of hexafluorobenzene and 1,4-difluorobenzene scaled to a Schmidt number of 600 without proper treatment of the bubble effects, using equation

$$k_{CO2} = k_{xFB} \left(\frac{Sc_{xFB}}{600} \right)^{-n} \tag{7.45}$$

with the Schmidt number exponent n being 0.55 for the lowest wind speeds and 0.5 for all higher ones.

Surprisingly, there seems to be only very little difference between the scaled hexafluorobenzene transfer velocities using classic Schmidt number scaling and the modeled CO_2 transfer velocities. This is due to the unique combination of Schmidt numbers and solubilities. It has been shown that

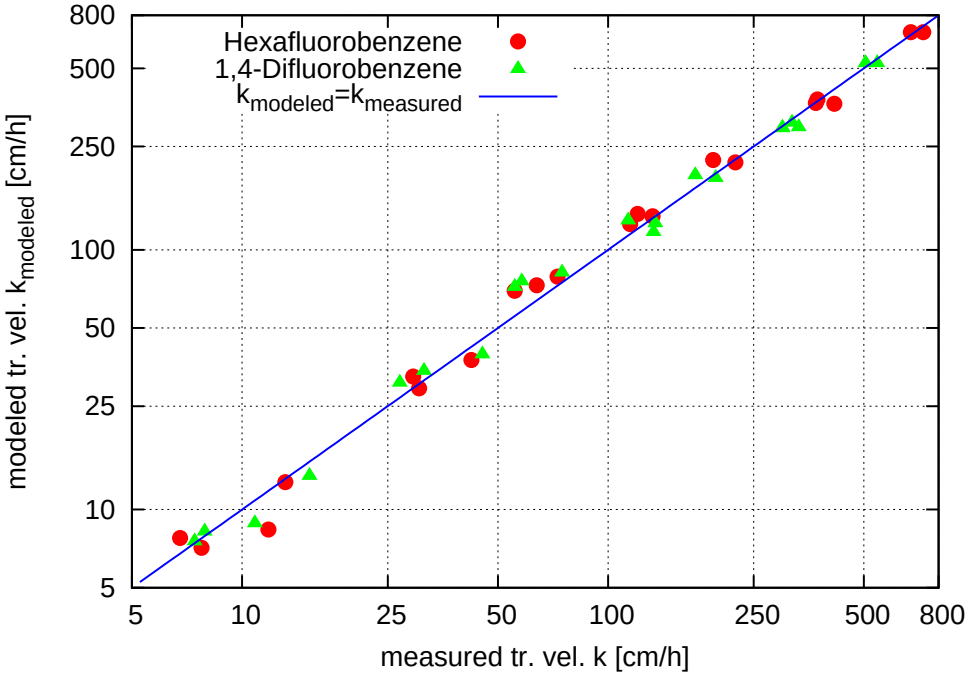

Figure 7.42.: Modeled transfer velocity for both tracers using the combined gas transfer model in equation 7.43 in dependency of the measured transfer velocity.

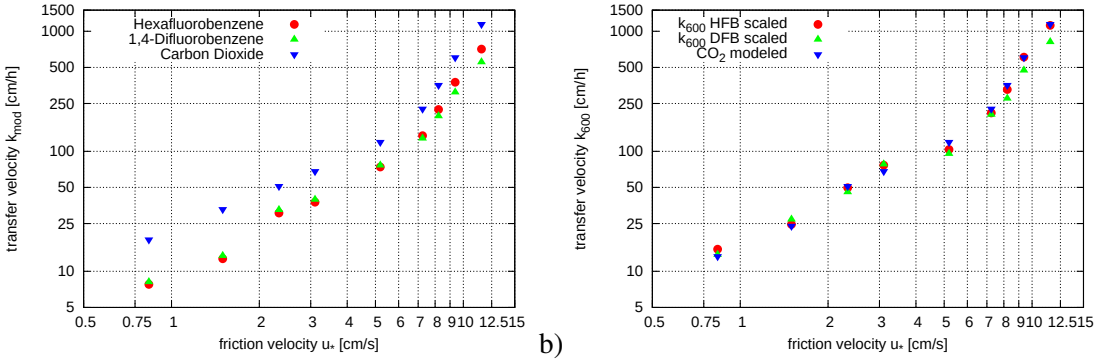

a) b)

Figure 7.43.: a) Modeled transfer velocity for both tracers at $20\,^oC$ as well as for carbon dioxide. b) Comparison of measured transfer velocities for hexafluorobenzene and 1,4-difluorobenzene which were Schmidt number scaled to Sc=600, and modeled transfer velocity for CO_2

the measured transfer velocity of hexafluorobenzene with a mean Schmidt number of 1675 and a solubility of 1.0 can be expressed using the parameterization shown in 7.43. The bubble term for hexafluorobenzene using a mean Schmidt number of Sc=1675 and solubility of $\alpha = 1.0$ is

$$\begin{aligned} k_{b,HFB}(u_{10}) &= f(u_{10})\left(0.00284\alpha^{-1} + 0.368Sc^{-2/3}\right) \approx \\ &\approx f(u_{10}) \cdot 0.00545. \end{aligned} \tag{7.46}$$

When this is scaled using classic Schmidt number scaling, equation 2.68, the multiplicative factor in the bubble term changes to

$$k_{b,600,HFB}(u_{10}) = f(u_{10}) \cdot 0.00545 \left(\frac{600}{1675}\right)^{-0.5} = f(u_{10}) \cdot \mathbf{0.00910}. \tag{7.47}$$

The same factor calculated for CO_2 is

$$\begin{aligned} k_{b,CO_2}(u_{10}) &= f(u_{10})\left(0.00284\alpha^{-1} + 0.368Sc^{-2/3}\right) \approx \\ &\approx f(u_{10}) \cdot \mathbf{0.00935}. \end{aligned} \tag{7.48}$$

Both factors are very similar. Therefore classic Schmidt number scaling of the bubble term of hexafluorobenzene gives approximately the same results like the modeled carbon dioxide. However, the preferred method to calculate gas transfer rates including the bubble/turbulence term should be the model in equation 7.43. Caution needs to be stressed again for low and high solubilities, as the model does not correctly represent those.

Summary

From the shown parameterizations it can not be concluded which is the dominant mechanism of transport, enhanced turbulence due to breaking waves and due to bubbles bursting through the boundary layer, or direct bubble transport. However, the parameters of two of the three parameterizations could be successfully modified so that the transfer velocities measured in this work are well reproduced.

For the two tracers studied here, the empirical model for gas transfer at extreme wind speeds, equation 7.43, works well in predicting air sea gas transfer. The extension of the empirical model to other tracers needs to be done with caution, because the prediction of the model could not be verified with other tracers. Limits to gas transfer velocities for low and high solubilities are expected and need to be quantified in further studies including a wider range of tracers. Also, bubble plume characteristics, i.e. bubble size and velocity distributions, are needed to interpret the data and confirm limits at high and low solubilities.

7.5.5. Uncertainties

To calculate the transfer velocity k, equation 3.21, solved for k, was used,

$$k = \frac{1}{A}\left(V_w\lambda - \dot{V}_w\right). \tag{7.49}$$

The following errors were assumed for the values entering into this equation:

error of the surface area A The water surface area A was calculated by $A = w * l_s$ using the width w and the surface length l_s. The width was assumed to have an uncertainty of 1 %. The surface area's length varied depending on the water height due to the inclined metal plate at the upstream section of the water flume. This length could be measured within an error of 10 cm, or less than 1 %, resulting in a relative error of $\Delta A = 2\,\%$.

error of the water leak rate $\dot{V}_w$ The flow rate of the clean water replacing the water lost due to spray was set using a flow meter mounted into the pipes supplying fresh water. An error of $\Delta\dot{V}_w = 5\,\%$ is assumed.

error of the water volume V_w **at below 800 rpm fan speed** The water volume was calculated as $V_w = h * w * l_w$ with the measured water height h, the width of the tank w and the length of the water flume l_w. The error of the width was estimated to be $\Delta w = 1\,\%$. The length could be measured to approximately $\Delta l_w = 0.5\,\%$. The water height was changed from day to day depending on the wind condition that was measured. An error of $\Delta h_{\mathrm{abs}} = 5$ mm is assumed. The error of the water volume can then be calculated as $\Delta v_w = \Delta w + \Delta l_w + \Delta h_{\mathrm{abs}}/h = 1.5\,\% + 5\,mm/h$.

error of the water volume V_w at 800 rpm fan speed Gas transfer at the highest wind speed was measured twice. The extra tank was used as a buffer for water entering the tank. All water was cycled through this tank, where fresh water entered. Therefore, this water has to be taken into account, too. During the experiments, the volume in this tank decreased, because more water was lost due to spray than could be replaced by fresh water. During the first experiment on Nov. 10, the water volume decreased from 14.2 m^3 to 12.0 m^3. Therefore, a water volume of $V_w = (13.1 \pm 1.2)\, m^3$ is assumed. On the second experiment at 800 rpm on Nov. 19 the water volume decreased from 14.0 m^3 to 12.9 m^3. A volume of $V_w = (13.45 \pm 0.6)\, m^3$ was used.

error of the inverse time constant of the gas exchange process λ The statistical error $\Delta\lambda$ of the fit to the exponentially decreasing data described in 5.3.4 is in the order of 0.05 % to 0.5 %, which seems unrealistically low. It was found, that small changes in the time regions chosen for the fit had a much greater impact on the fit result. Therefore, to obtain a realistic value for the error of the inverse time constant λ, another method was chosen. The fitted region was shrunk by 10 % of the length of the time interval fitted in a way that the lower fit boundary was increased by 5 % and the upper boundary was decreased by 5 %. The fit was performed again with the new boundaries, yielding a modified time constant, λ_{err}. The relative error was then calculated as $\Delta\lambda = \frac{|\lambda - \lambda_{\mathrm{err}}|}{\lambda}$. The errors obtained in that way are typically an order of magnitude larger than the standard error of the fit. If two transfer rates were measured in one experiment, the larger of the two errors is used.

The error of the transfer velocity k of each of the tracers was then calculated by

$$\begin{aligned} \Delta k &= \sqrt{\left(\tfrac{\partial k}{\partial A}\Delta A\right)^2 + \left(\tfrac{\partial k}{\partial \lambda}\Delta\lambda\right)^2 + \left(\tfrac{\partial k}{\partial V_w}\Delta V_w\right)^2 + \left(\tfrac{\partial k}{\partial \dot{V}_w}\Delta \dot{V}_w\right)^2} = \\ &= \sqrt{\left(\tfrac{\lambda}{A}\Delta V_w\right)^2 + \left(\tfrac{V_w}{A}\Delta\lambda\right)^2 + \left(\tfrac{1}{A}\Delta \dot{V}_w\right)^2 + \left(\tfrac{k}{A}\Delta A\right)^2}. \end{aligned} \tag{7.50}$$

The tracers' measured transfer velocities where scaled to a commonly used gas, CO_2 at 20^oC by Schmidt number scaling, see 2.68. This poses another source for errors discussed in the following paragraphs.

Yaws [1995], from which the diffusion coefficients were taken, lists very small errors for the diffusion coefficients. However, the diffusion coefficients are calculated from the temperature by averaging the temperature during each wind speed condition. During a single day, the temperature changed by up to 4 K. This also affects the kinematic viscosity of water, that enters into Schmidt number scaling, see 2.68. To estimate the error of k_{600}, the errors of D and ν, which are calculated from the error in temperature, are being treated as independent from each other. The error from the transfer velocity k is more than an order of magnitude larger than the errors from D and ν. Therefore, the error made by treating the errors of D and ν as independent should be negligibly small. For low wind speeds, a potential error of the Schmidt number exponent n must also be taken into account. In calculations, the Schmidt number exponent was assumed to be $n = 1/2$ which means a rough surface. Experiments in the Aeolotron suggest, that n can be different from 1/2 even at wind speeds as high as $u_{10} = 10\ m/s$, see section 7.4.3. The assumed errors in n are listed in table 7.5.

The error of k_{600} can then be calculated by

$$\begin{aligned} \Delta k_{600} &= \sqrt{\left(\tfrac{\partial k_{600}}{\partial \nu}\Delta\nu\right)^2 + \left(\tfrac{\partial k_{600}}{\partial D}\Delta D\right)^2 + \left(\tfrac{\partial k_{600}}{\partial k}\Delta k\right)^2 + \left(\tfrac{\partial k_{600}}{\partial n}\Delta n\right)^2} = \\ &= k_{600} * \sqrt{\left(n\tfrac{\Delta\nu}{\nu}\right)^2 + \left(n\tfrac{\Delta D}{D}\right)^2 + \left(\tfrac{\Delta k}{k}\right)^2 + \left(\log\left(k\tfrac{600D}{\nu}\right)\Delta n\right)^2}. \end{aligned} \tag{7.51}$$

fan rotation in [rpm]	wind speed u_{10} in [m/s]	Δn
100	7	0.16666667
150	12.1	0.13333333
200	16.7	0.1
250	23.75	0.05
300 - 800	29.8-67.1	0

Table 7.5.: Assumed errors in the Schmidt number exponent n

The uncertainties of the averaged transfer velocities $\overline{k_{600}}$ in section 7.5.1 where calculated as

$$\Delta\overline{k_{600}} = \overline{\Delta k_{600}} \tag{7.52}$$

with the average of the errors $\overline{\Delta k_{600}}$ of the single measurements.

The uncertainties of the bubble induced parts of the transfer velocities k_b in section 7.5.3 were calculated as

$$\Delta k_b = \Delta k \tag{7.53}$$

with Δk_b being the absolute error of the bubble induced part of the gas transfer velocity and Δk being the absolute error of the measured transfer velocity. The error of the wave induced part, which comes from equation 2.67, was assumed to have no error.

8. Conclusion and Outlook

Using two identical FT-IR spectrometers with differing measurement cells, the concentrations of four different tracers were monitored with a high precision directly in the air and in air equilibrated with the water of the Aeolotron simultaneously. This successful application of the FT-IR spectroscopy opens great potential for studies with more and different tracers which absorb light in the infrared range. Another setup to measure UV absorption spectra was successfully deployed at a wind-wave tank capable of producing hurricane conditions, yielding the first comprehensive laboratory study of gas transfer velocities of two different tracers at wind speeds between 7 m/s and 67 m/s. Gas transfer velocities measured in this work spanned more than 3 orders of magnitude, lying between 0.5 cm/h and 1100 cm/h.

Gas transfer velocities at low to medium wind speeds involving three different surface contamination states with a soluble surfactant were measured, see section 7.4.2. While the transfer velocities did not scale well with the wind speed, the mean square slope of the water surface was found to be a good parameter to describe the transfer velocities, except at the lowest mean square slopes. The transition of the Schmidt number exponent from 2/3 for a smooth water surface to 1/2 for a wavy water surface was measured, for the first time with three different levels of surface contamination, see section 7.4.3. Both Schmidt number exponents and transfer velocities compared well with those measured in previous studies.

The measurements at the lowest wind speeds proved to be problematic, yielding Schmidt number exponents violating theoretical constraints, which points to problems with mixing of the air or water space. Also, Schmidt number exponents calculated from transfer velocities of one of the tracers were found to be unphysical and therefore disregarded. In addition, the cut off of the measured mean square slopes towards lower slopes at 0.0025 was problematic. When using surfactants, accurate and reliable measurements of the smallest mean square slope are essential for the interpretation of the gas transfer velocities and the Schmidt number exponents.

The transition of the Schmidt number exponent was found to be gradual, rather than sudden, with the mid-point of the transition at a wind speed around 4.5 m/s for a clean water surface, and around 9 m/s for heavily surfactant covered water surface. This puts the transition region right into the wind speed regime, where field studies of air-sea gas transfer are commonly conducted. As surfactants are abundant at the open ocean surface, this stresses the importance of the measurement of the Schmidt number exponent in the field as well as in the lab. The mean square slope can be used to describe the transition of the Schmidt number exponent from 2/3 for a smooth to 1/2 for a rough water surface, see section 2.2.6, regardless of the surface contamination. In accordance with previous studies, the facet model's prediction of the transition of the Schmidt number exponent could be fitted to the data. However, the facet model could not predict correct transfer velocities, with the measured values, especially for the clean water surface, being up to almost 200 % larger than the values calculated by the facet model. This discrepancy is likely due to the scaling parameter β which is not accurately predicted by the facet model. The parameter β was found to be neither proportional to the wind speed or the friction velocity, nor to the mean square slope of the water surface. As β links gas transfer with momentum transfer, other variables, such as turbulent kinetic energy, might be better parameters to describe β.

The transfer velocities at hurricane strength wind speeds were found to be extremely large, see section 7.5.1. At the onset of strong, large scale wave breaking with bubble entrainment and

spray generation, the correlation between gas transfer velocities and wind speed was found to become steeper, indicating a new air-sea gas exchange regime. The gas transfer velocity could be dissected into a purely wave induced part and a part caused by increased wave breaking and bubble entrainment using a purely empirical partitioning equation. Assuming this partitioning into the two parts is valid, the gas transfer velocities were found to be up to 350 % larger than expected from waves alone at the highest wind speed. Several empirical models describing gas transfer at extreme wind speeds were fitted to the data with success. However, they need to be used with caution, as they lack a physical basis.

As a further point, the applicability of the fast controlled leakage method to measure gas transfer rates in the Aeolotron was tested. Due to the large inhomogeneities found in the air side concentration when the Aeolotron was flushed with large amounts of fresh air, the fast and easy controlled leakage method was found unsuitable to accurately measure gas transfer rates, see section 7.1. The existence of secondary currents could be inferred from the homogeneity study, and is in accordance with previous studies done at smaller annular wind-wave tanks.

Last but not least, a method was developed that allows the parallel measurement of the solubility and the transfer velocity of a tracer, as long as a reference tracer with known solubility is measured in the same experiment, and the observed transfer rates are rather large, see section 7.3.

Outlook

The future goal is to develop a comprehensive, physics based model for gas exchange, involving tracers of all diffusivities and solubilities, all wind speeds as well as all levels of surface contaminations and other forcing parameters such as stratification, chemical enhancement, buoyancy, water currents, wave breaking and bubble entrainment. This work, along with a number of other previous works such as Nielsen [2004], Degreif [2006] and Kräuter [2011], lays the foundation for the development of such a model. The measurement of more parameters, such as turbulent kinetic energy as well as bubble size and life time distributions needs to be incorporated into further studies.

A. Appendix

A.1. A Numerical Model for Calculating Concentration Time Series

In a first step, the box model equations, 3.5 and 3.6 are discretized,

$$V_a \frac{c_a^i - c_a^{i-1}}{\Delta t} = Ak_w(c_w^{i-1} - \alpha c_a^{i-1}) - \dot{V}_a c_a^{i-1} \tag{A.1}$$

$$V_w \frac{c_a^i - c_a^{i-1}}{\Delta t} = -Ak_w(c_w^{i-1} - \alpha c_a^{i-1}) - \dot{V}_w c_w^{i-1}, \tag{A.2}$$

with i denoting the concentration value at the i-th time step and Δt being the time difference between two discrete values. This can be solved for c_a^i and c_w^i,

$$c_a^i = \left(\frac{V_w}{V_a}\frac{1}{h_w}k\left(c_w^{i-1} - \alpha c_a^{i-1}\right) - \lambda c_a^{i-1}\right)\Delta t + c_a^{i-1} \tag{A.3}$$

$$c_w^i = -\left(\frac{1}{h_w}k\left(c_w^{i-1} - \alpha c_a^{i-1}\right)\right)\Delta t + c_w^{i-1}). \tag{A.4}$$

So, beginning from the starting points c_a^0 and c_w^0, a concentration time series can be calculated iteratively. The time steps must be kept short in relation to the other time scales given by the leak rate λ and the transfer velocity k.

A.2. Water Side FT-IR Reference Spectra

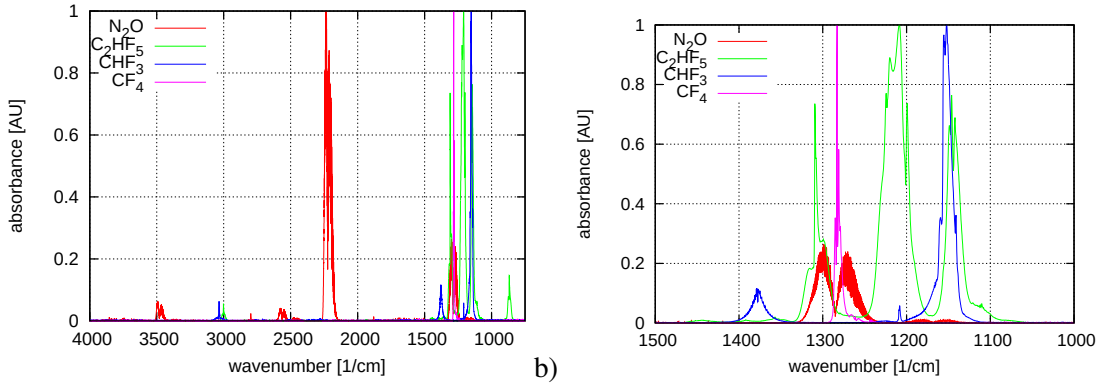

Figure A.1.: a) reference spectra measured with the water sided FT-IR spectrometer. b) enlargement of the wavenumber region between 1500 and 1000 cm^{-1}.

A.3. More on Calibration of the FT-IR Spectrometers

A.3.1. Calibration Curves with Error Bars

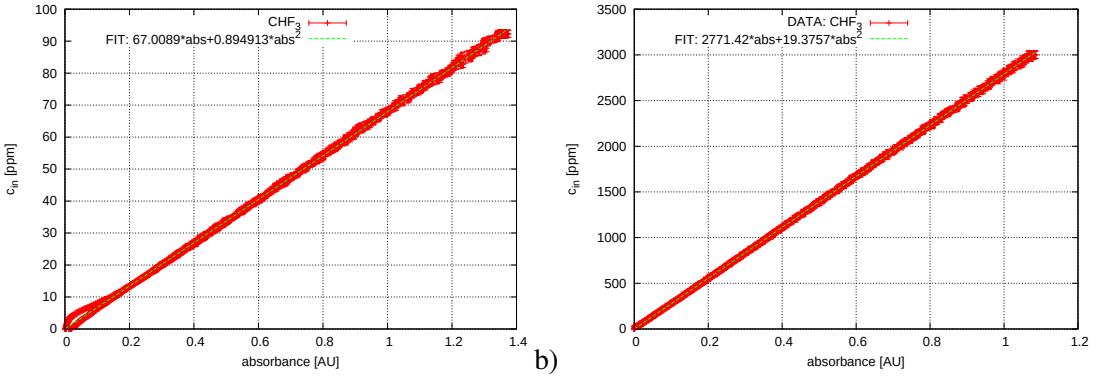

a) b)

Figure A.2.: Relationship between input concentration and measured absorbance of CHF_3 for a) the air-sided spectrometer and b) the water sided spectrometer. Also shown is a quadratic fit. In the air-sided (water-sided) fit the region between 0 and 0.2 (0 and 0.05) was omitted.

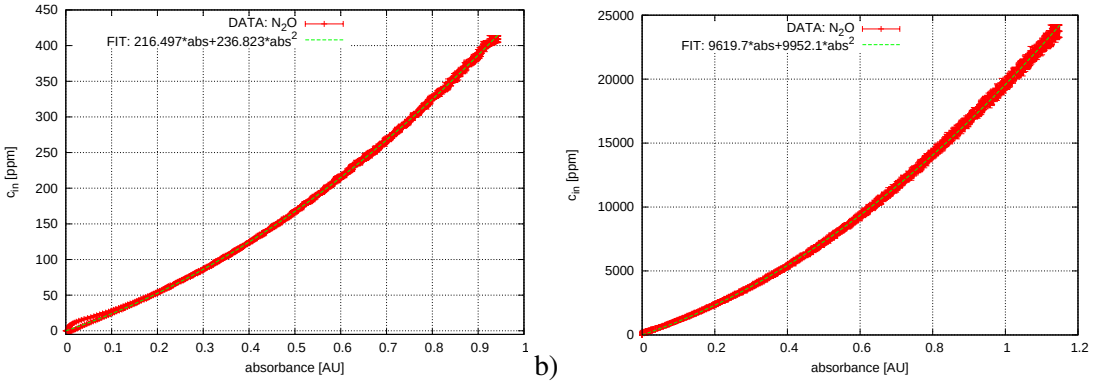

a) b)

Figure A.3.: Relationship between input concentration and measured absorbance of N_2O for a) the air-sided spectrometer and b) the water sided spectrometer. Also shown is a quadratic fit. In the air-sided (water-sided) fit the absorbance region between 0 and 0.2 (0 and 0.05) was omitted. For clarity reasons, the errorbars are not shown.

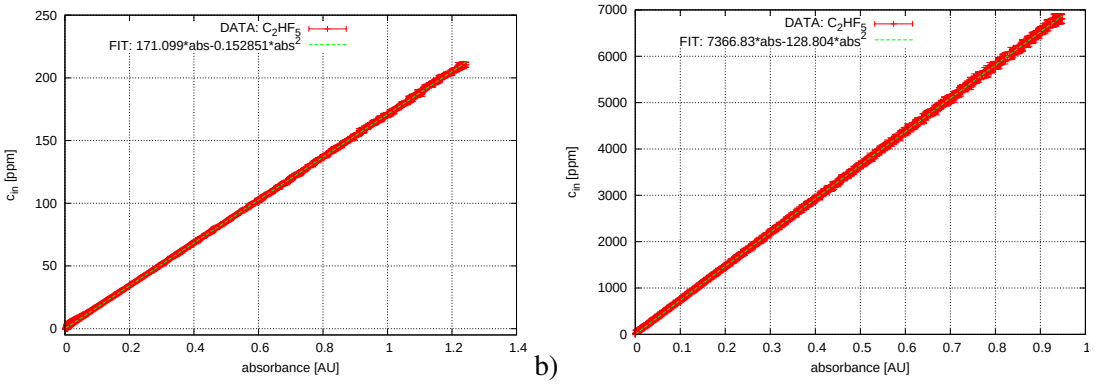

a) b)

Figure A.4.: Relationship between input concentration and measured absorbance of C_2HF_5 for a) the air-sided spectrometer and b) the water sided spectrometer. Also shown is a quadratic fit. In the air-sided (water-sided) fit the absorbance region between 0 and 0.2 (0 and 0.05) was omitted.

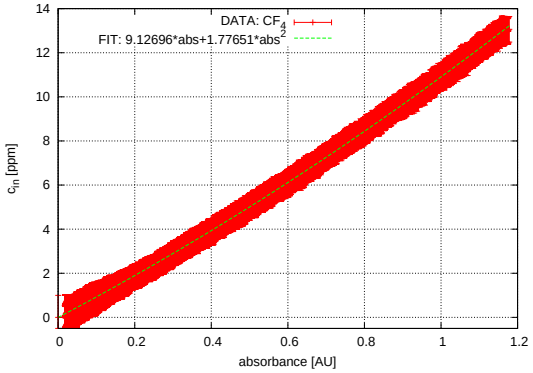

Figure A.5.: Relationship between input concentration and measured absorbance of CF_4 for the air-sided spectrometer Also shown is a quadratic fit where the absorbance region between 0 and 0.2 was omitted.

A.3.2. Alternative Calibrations

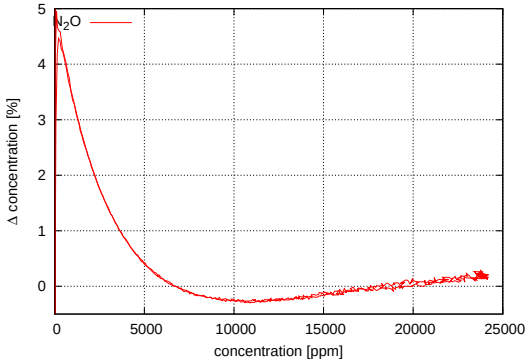

Figure A.6.: Deviation of the water sided concentration of N_2O measured using the standard calibration from the calibration with the alternative reference spectrum with a maximum absorbance of 0.2.

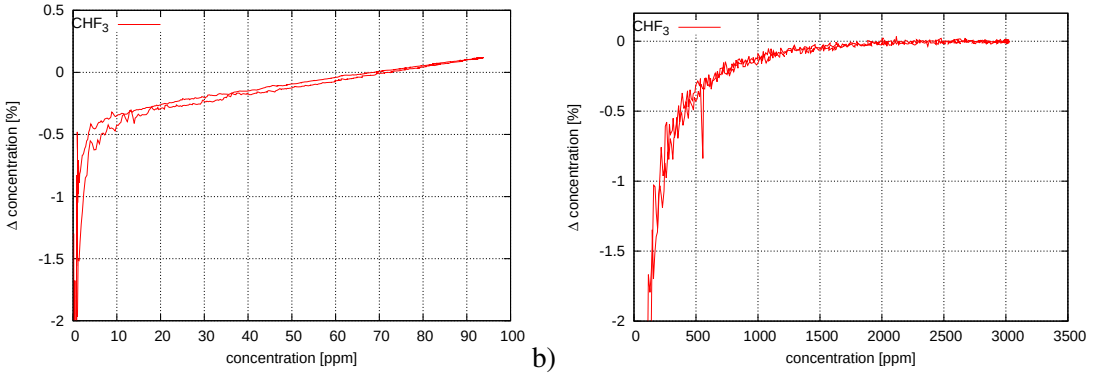

a) b)

Figure A.7.: a) Deviation of the air sided concentration of CHF_3 measured using the standard calibration from the calibration with the alternative reference spectrum with a maximum absorbance of 0.2. b) The same, but for the water side.

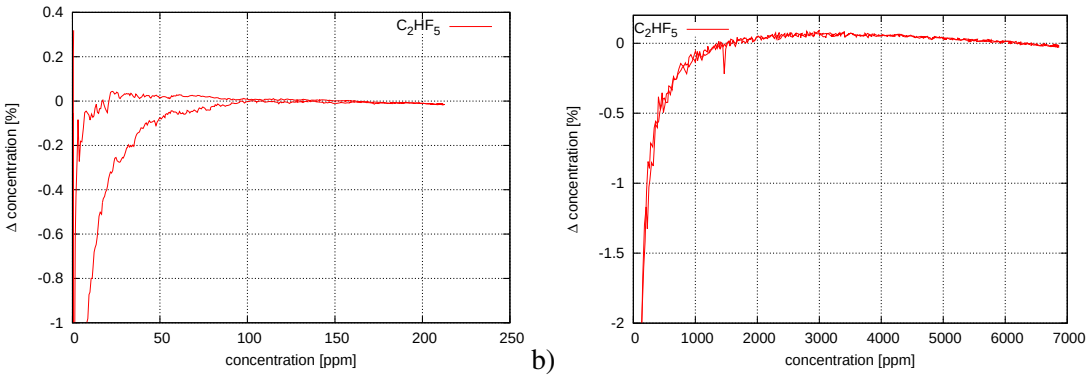

Figure A.8.: a) Deviation of the air sided concentration of C_2HF_5 measured using the standard calibration from the calibration with the alternative reference spectrum with a maximum absorbance of 0.2. b) The same, but for the water side.

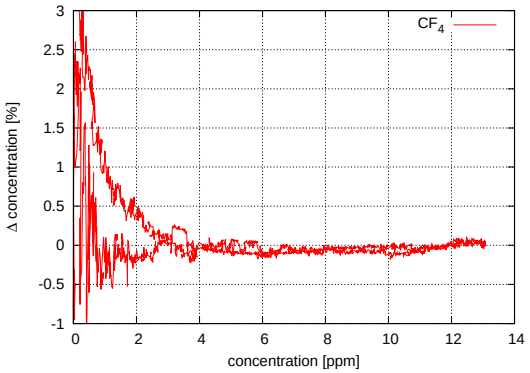

Figure A.9.: Deviation of the air sided concentration of CF_4 measured using the standard calibration from the calibration with the alternative reference spectrum with a maximum absorbance of 0.2.

A.3.3. Statistical Errors

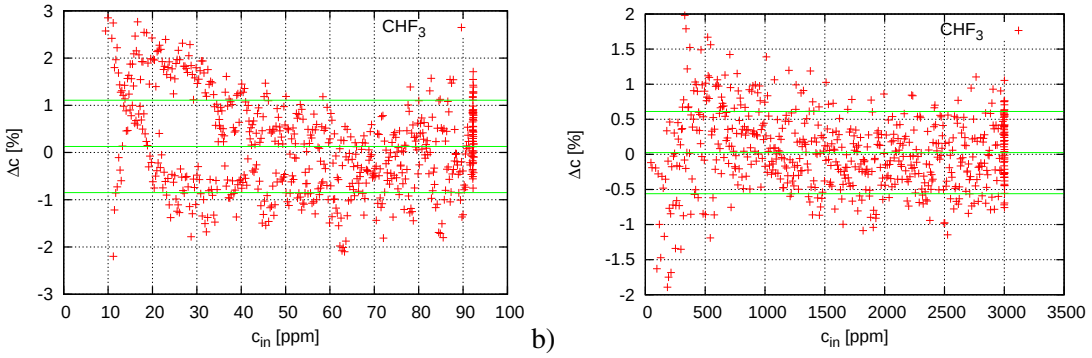

Figure A.10.: Deviation between measured concentration and input concentration for CHF_3 in a) the air and b) the water side calibration. The Standard deviation is 0.98 % (air) and 0.58 %(water).

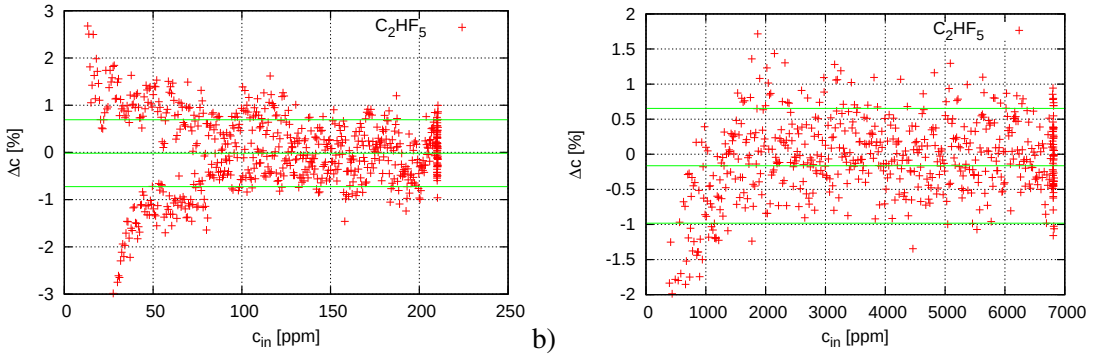

Figure A.11.: Deviation between measured concentration and input concentration for C_2HF_5 in a) the air and b) the water side calibration. The Standard deviation is 0.71 % (air) and 0.82 %(water).

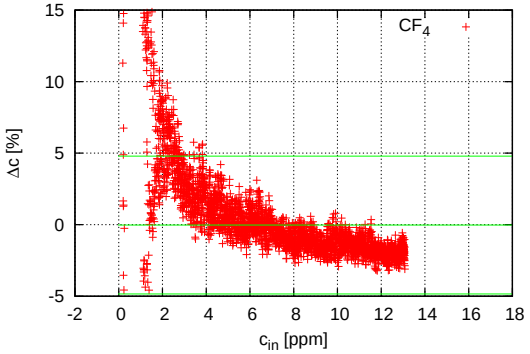

Figure A.12.: Deviation between measured concentration and input concentration for CF_4. The standard deviation is 1.23 %.

A.4. Numerical Results

A.4.1. Aeolotron

The following tables list the numerical values of the transfer velocities and Schmidt number exponents and their systematical and statistical errors measured in the Aeolotron, as well as wind speeds and mean square slopes.

day	u_{ref}	u_{*w}	u_{10}	n	k N_2O	k CHF_3	k C_2HF_5	σ_s^2	T	k_{600}	Δn syst.	Δ n stat.	Δ k N_2O syst.	Δk CHF_3 syst.	Δ k C_2HF_5 syst.	Δ k N_2O stat.	Δk CHF_3 stat.	Δ k C_2HF_5 stat
	m/s	cm/s	m/s		cm/h	cm/h	cm/h		^{o}C	cm/h			cm/h	cm/h	cm/h	cm/h	cm/h	cm/h
11/02/18	0.747	0.108	1.150	0.486	0.590	0.480	0.456	0.002281	19.400	0.600	0.056	0.009	0.026	0.055	0.054	0.082	0.065	0.066
11/02/18	1.418	0.165	1.710	0.672	1.853	1.560	1.280	n.m.	19.450	1.891	0.063	0.033	0.083	0.176	0.149	0.113	0.095	0.086
11/02/18	2.050	0.241	2.430	0.691	3.260	2.735	2.254	n.m.	19.500	3.322	0.062	0.026	0.146	0.311	0.265	0.137	0.118	0.101
11/02/18	2.662	0.336	3.270	0.620	5.142	4.449	3.694	n.m.	19.500	5.228	0.059	0.020	0.231	0.507	0.435	0.158	0.137	0.113
11/02/18	3.616	0.523	4.810	0.599	7.414	6.495	5.384	n.m.	19.500	7.533	0.058	0.033	0.337	0.745	0.638	0.177	0.154	0.122
11/02/18	4.800	0.825	7.050	0.586	13.527	11.911	9.895	n.m.	19.450	13.760	0.057	0.054	0.627	1.386	1.190	0.194	0.169	0.131
11/02/18	6.451	1.372	10.630	0.559	30.859	27.678	22.901	n.m.	19.400	31.407	0.056	0.126	1.477	3.300	2.829	0.210	0.184	0.139
11/02/18	8.261	2.142	15.040	0.489	48.298	44.870	37.208	n.m.	19.400	49.033	0.054	0.120	2.538	5.783	4.973	0.224	0.196	0.145
11/02/22	0.740	0.108	1.150	0.661	0.538	0.450	0.380	0.00222	18.800	0.562	0.061	0.254	0.026	0.051	0.046	0.055	0.052	0.053
11/02/22	1.422	0.166	1.710	0.722	1.684	1.424	1.145	0.00714	18.850	1.760	0.063	0.200	0.081	0.158	0.133	0.154	0.128	0.103
11/02/22	2.045	0.241	2.430	0.696	2.720	2.313	1.876	0.01277	18.900	2.833	0.062	0.081	0.132	0.257	0.217	0.169	0.154	0.124
11/02/22	2.673	0.338	3.280	0.649	3.999	3.448	2.828	0.01533	18.900	4.153	0.060	0.063	0.196	0.383	0.328	0.202	0.164	0.145
11/02/22	3.628	0.526	4.820	0.608	5.721	5.007	4.135	0.01751	18.875	5.931	0.058	0.058	0.285	0.559	0.483	0.264	0.192	0.184
11/02/22	4.829	0.833	7.110	0.556	10.153	9.071	7.546	0.03316	18.800	10.514	0.056	0.041	0.521	1.019	0.890	0.203	0.178	0.124
11/02/22	6.476	1.382	10.690	0.513	28.565	26.593	21.707	0.07980	18.725	29.529	0.055	0.071	1.582	3.049	2.632	1.469	1.205	0.439
11/02/22	8.257	2.140	15.030	0.461	45.982	44.454	35.944	0.12294	18.650	47.414	0.053	0.039	2.959	5.361	4.662	1.224	1.611	0.705
11/02/24	0.755	0.109	1.150	0.524	0.565	0.475	0.430	0.00231	19.500	0.573	0.057	0.303	0.028	0.053	0.051	0.055	0.061	0.065
11/02/24	1.431	0.167	1.710	0.655	2.044	1.746	1.437	0.00711	19.600	2.073	0.061	0.182	0.102	0.194	0.167	0.241	0.195	0.140
11/02/24	2.057	0.242	2.430	0.644	3.311	2.863	2.349	0.01300	19.625	3.355	0.060	0.108	0.168	0.320	0.275	0.219	0.184	0.152
11/02/24	2.671	0.337	3.280	0.601	5.237	4.587	3.802	0.01631	19.625	5.301	0.058	0.078	0.270	0.515	0.448	0.178	0.144	0.131
11/02/24	3.621	0.525	4.820	0.554	7.724	6.871	5.746	0.02396	19.600	7.816	0.056	0.065	0.412	0.778	0.686	0.277	0.201	0.146
11/02/24	4.797	0.824	7.040	0.523	13.721	12.428	10.382	0.04633	19.550	13.893	0.055	0.055	0.769	1.427	1.264	0.364	0.400	0.235
11/02/24	6.465	1.377	10.666	0.464	30.009	28.255	23.418	0.07921	19.500	30.367	0.053	0.067	1.883	3.368	2.987	1.168	0.873	0.305
11/02/24	7.516	1.803	13.172	0.454	39.990	38.254	31.379	0.10329	19.450	40.495	0.053	0.063	3.156	5.012	4.468	1.224	1.438	0.559
11/03/01	0.733	0.107	1.140	0.570	0.590	0.487	0.431	0.00226	19.500	0.396	0.058	0.260	0.027	0.055	0.048	0.120	0.093	0.062
11/03/01	1.414	0.165	1.710	0.642	2.610	2.238	1.847	0.00730	19.600	0.612	0.060	0.121	0.122	0.252	0.207	0.298	0.208	0.158
11/03/01	2.056	0.242	2.440	0.620	3.867	3.319	2.771	0.01272	19.625	0.574	0.059	0.109	0.184	0.376	0.312	0.345	0.215	0.160
11/03/01	2.691	0.341	3.310	0.599	6.070	5.264	4.411	0.01643	19.625	0.564	0.058	0.060	0.294	0.600	0.499	0.262	0.176	0.142
11/03/01	3.619	0.524	4.810	0.584	9.296	8.091	6.806	0.02472	19.600	0.551	0.057	0.057	0.460	0.932	0.776	0.378	0.187	0.139
11/03/01	4.795	0.823	7.040	0.558	15.607	13.890	11.586	0.04505	19.575	0.578	0.056	0.064	0.806	1.632	1.339	0.660	0.466	0.198
11/03/01	6.466	1.378	10.667	0.532	33.446	30.373	25.164	0.07554	19.550	0.600	0.055	0.069	1.904	3.752	2.999	1.761	1.023	0.500
11/03/01	8.251	2.137	15.010	0.505	52.658	49.813	40.176	0.11253	19.550	0.685	0.055	0.066	3.827	7.189	5.249	3.014	2.576	1.024

Table A.1.: Measured transfer velocities for the clean cases in the Aeolotron, sorted by date. *n.m.* means not measured.

day	u_{ref}	u_{*w}	u_{10}	n	k N_2O	k CHF_3	k C_2HF_5	σ_s^2	T	k_{600}	Δn syst.	Δ n stat.	Δ k N_2O syst.	Δk CHF_3 syst.	Δ k C_2HF_5 syst.	Δ k N_2O stat.	Δk CHF_3 stat.	Δ k C_2HF_5 stat
	m/s	cm/s	m/s		cm/h	cm/h	cm/h		^{o}C	cm/h			cm/h	cm/h	cm/h	cm/h	cm/h	cm/h
11/03/03	0.800	0.112	1.190	0.581	0.498	0.421	0.366	0.00201	19.800	0.501	0.058	0.203	0.024	0.047	0.041	0.041	0.040	0.039
11/03/03	1.460	0.170	1.760	0.646	0.728	0.628	0.517	0.00195	19.875	0.732	0.060	0.124	0.035	0.070	0.058	0.029	0.041	0.034
11/03/03	2.091	0.247	2.480	0.664	1.091	0.932	0.767	0.00192	19.925	1.094	0.061	0.103	0.053	0.103	0.087	0.035	0.056	0.047
11/03/03	2.717	0.345	3.350	0.686	2.100	1.784	1.458	0.00773	19.925	2.107	0.061	0.062	0.102	0.197	0.164	0.060	0.052	0.047
11/03/03	3.650	0.531	4.870	0.662	3.191	2.713	2.243	0.01019	19.925	3.201	0.060	0.059	0.157	0.301	0.253	0.080	0.090	0.066
11/03/03	4.851	0.839	7.150	0.583	7.042	6.201	5.162	0.02046	19.900	7.066	0.057	0.030	0.351	0.689	0.583	0.340	0.332	0.266
11/03/03	6.502	1.391	10.750	0.525	23.958	22.030	18.080	0.07126	19.875	24.046	0.055	0.098	1.269	2.485	2.070	1.636	1.123	0.410
11/03/03	8.288	2.154	15.105	0.506	43.913	41.473	33.451	0.11068	19.850	44.092	0.055	0.109	2.704	4.894	3.992	3.370	2.286	0.832
11/03/08	1.463	0.170	1.760	0.530	0.734	0.637	0.556	0.00194	19.750	0.739	0.056	0.203	0.037	0.071	0.065	0.046	0.059	0.065
11/03/08	2.075	0.245	2.460	0.658	1.093	0.944	0.771	0.00190	19.775	1.102	0.061	0.164	0.055	0.105	0.091	0.070	0.075	0.065
11/03/08	2.695	0.341	3.310	0.708	1.606	1.376	1.101	0.00189	19.800	1.619	0.063	0.149	0.082	0.154	0.129	0.104	0.088	0.061
11/03/08	3.675	0.537	4.910	0.715	2.191	1.872	1.499	0.00187	19.850	2.205	0.063	0.131	0.113	0.209	0.175	0.084	0.071	0.085
11/03/08	4.927	0.862	7.310	0.715	2.973	2.543	2.032	n.m.	19.850	2.991	0.063	0.094	0.155	0.286	0.241	0.087	0.074	0.092
11/03/08	6.625	1.438	11.040	0.501	11.218	10.408	8.574	n.m.	19.850	11.264	0.055	0.120	0.615	1.178	1.025	0.762	0.605	0.306
11/03/08	8.372	2.195	15.320	0.460	30.875	29.689	24.151	n.m.	19.850	30.987	0.053	0.061	1.953	3.494	3.043	1.319	1.186	0.504
11/03/10	1.438	0.167	1.760	0.612	0.756	0.655	0.549	0.00180	19.900	0.759	0.059	0.181	0.036	0.075	0.063	0.063	0.076	0.074
11/03/10	2.074	0.245	2.460	0.648	1.138	0.986	0.806	0.00180	19.950	1.141	0.060	0.115	0.055	0.114	0.092	0.083	0.089	0.064
11/03/10	2.718	0.345	3.350	0.673	1.655	1.428	1.156	0.00180	20.000	1.655	0.061	0.083	0.080	0.165	0.132	0.078	0.076	0.056
11/03/10	3.659	0.533	4.880	0.662	2.581	2.239	1.816	0.00472	20.025	2.580	0.061	0.082	0.126	0.259	0.208	0.092	0.091	0.083
11/03/10	4.898	0.853	7.250	0.617	3.828	3.349	2.756	0.00688	20.050	3.824	0.059	0.061	0.189	0.389	0.316	0.109	0.100	0.080
11/03/10	6.604	1.430	10.990	0.506	11.731	10.792	8.941	0.03986	20.050	11.720	0.055	0.110	0.606	1.274	1.037	0.806	0.412	0.266
11/03/10	8.369	2.193	15.310	0.511	33.258	30.758	25.189	0.09592	20.050	33.226	0.055	0.162	1.957	3.889	3.042	3.705	1.787	0.782

Table A.2.: Measured transfer velocities for the partial and heavy surfactant cases in the Aeolotron, sorted by date. On 11/03/03 the surfactant concentration was and on 11/03/08 as well as on 11/03/10 the concentration was . *n.m.* means not measured.

A.4.2. Kyoto High-Speed Wind Wave Tank

Mean, Schmidt number scaled gas transfer velocities are given in table A.3. All measured as transfer velocities as well as bubble induced transfer velocities are given in numerical form in table A.4.

f_f	u_{*w}	u_{10}	k_{600} HFB	k_{600} DFB	Δk_{600} HFB	Δk_{600} DFB	k_w CO_2	k_b CO_2
rpm	m/s	cm/s	cm/h	cm/h	cm/h	cm/h	cm/h	cm/h
100	0.836	7	15.28	13.77	2.583	1.554	18.35	0.00
150	1.498	12.1	24.61	27.08	3.261	2.787	32.87	0.00
200	2.335	16.7	49.74	45.82	5.664	5.181	51.22	0.00
250	3.101	23.75	76.67	78.01	10.569	7.895	68.04	0.11
300	5.193	29.8	103.38	95.56	4.530	3.921	113.91	5.44
400	7.249	40.7	208.91	202.64	11.793	8.550	159.02	66.79
500	8.225	48	326.80	275.40	13.366	11.277	180.43	175.31
600	9.375	56.4	608.66	472.80	32.228	19.598	205.65	400.01
800	11.53	67.1	1118.77	814.89	113.842	74.873	253.05	891.54

Table A.3.: Mean, Schmidt number scaled transfer velocitiesk_{600} of both tracers. The fan frequency, that was set as the main parameter, is denoted by f_f. The wind speed u_{10} and friction velocity u_*, kindly provided by the Japanese colleagues is also given. Also shown is the expected, wind induced transfer velocity k_w of CO_2 as well as the prediction of the bubble induced transfer velocity using the parameterization proposed by Asher et al. [1995], see section 7.5.3.

date	f_f	$u_{*,w}$	u_{10}	k_{600} HFB	Δk_{600} HFB	k_{600} DFB	Δk_{600} DFB	k HFB	Δk HFB	k DFB	Δk DFB	T	Sc HFB	Sc DFB	k_w HFB	k_w DFB	k_b HFB	k_b DFB
Y/M/D	rpm	cm/s	cm/h	cm/h	cm/h	cm/h	cm/h	cm/h	cm/h	cm/h	cm/h	^{o}C			cm/h	cm/h	cm/h	cm/h
11/10/27	600	9.375	56.4	594.86	26.49	507.77	21.92	369.49	14.82	332.05	12.82	17.5	1555.2	1403.1	127.73	134.48	241.74	197.56
11/10/28	400	7.249	40.7	195.97	12.59	175.48	6.93	120.40	7.21	113.50	3.62	17.1	1589.6	1434.0	97.697	102.85	22.698	10.646
11/10/28	600	9.375	56.4	675.96	40.06	462.51	23.42	415.29	23.25	299.16	13.99	17.1	1589.6	1434.0	126.34	133.02	288.94	166.13
11/10/31	200	2.335	16.7	46.24	5.62	46.99	5.60	29.35	1.67	31.40	1.00	18.3	1489.0	1343.5	32.514	34.229	-3.164	-2.827
11/10/31	500	8.225	48.0	358.66	15.41	301.11	13.30	222.77	9.42	196.90	8.57	17.5	1555.2	1403.1	112.06	117.98	110.70	78.918
11/11/02	300	5.193	29.8	109.83	4.28	107.33	4.14	72.77	2.75	74.86	2.80	19.9	1366.9	1233.5	75.471	79.445	-2.705	-4.589
11/11/02	500	8.225	48.0	303.40	11.32	257.52	9.25	193.63	6.74	173.02	5.77	18.5	1473.0	1329.1	115.15	121.22	78.484	51.794
11/11/04	100	0.836	7.0	18.77	2.38	16.30	2.04	11.80	0.56	10.84	0.42	19.5	1396.2	1259.9	8.3742	8.8607	3.4210	1.9767
11/11/04	600	9.375	56.4	573.74	30.13	464.70	16.84	373.11	19.48	318.12	11.38	19.2	1418.7	1280.2	133.74	140.78	239.36	177.33
11/11/08	300	5.193	29.8	104.23	4.58	90.11	3.13	63.86	2.58	58.13	1.75	17.0	1598.3	1441.9	69.793	73.480	-5.931	-15.35
11/11/10	800	11.53	67.1	1177.10	150.3	777.99	93.63	726.16	92.64	505.29	60.74	17.25	1576.6	1422.3	156.11	164.35	570.05	340.93
11/11/11	600	9.375	56.4	n.m.	n.m.	461.86	16.21	n.m.	n.m.	299.97	9.71	17.25	1576.6	1422.3	126.87	133.56	n.m.	166.40
11/11/14	100	0.836	7.0	11.60	3.82	12.79	1.53	6.77	2.18	7.90	0.65	17.0	1598.3	1441.9	7.7742	8.2271	-1.005	-0.330
11/11/15	400	7.249	40.7	220.84	11.14	213.25	9.10	132.35	5.91	134.56	4.79	16.2	1670.5	1506.9	95.303	100.34	37.051	34.218
11/11/16	200	2.335	16.7	53.30	5.71	44.83	4.76	30.46	1.14	26.98	1.01	14.5	1837.4	1657.1	29.271	30.821	1.1854	-3.845
11/11/16	400	7.249	40.7	208.40	11.65	229.16	9.62	114.93	6.21	133.07	5.26	13.25	1973.0	1779.2	87.692	92.343	27.234	40.729
11/11/17	150	1.498	12.1	24.61	3.26	27.08	2.79	13.13	1.35	15.29	0.48	14.1	1879.5	1695.0	12.741	13.485	0.3932	1.8089
11/11/17	250	3.101	23.75	76.67	10.57	78.01	7.90	42.34	5.34	45.37	3.71	13.3	1967.3	1774.1	37.576	39.569	4.7652	5.7966
11/11/18	100	0.836	7.0	14.50	1.55	13.11	1.10	7.75	0.65	7.42	0.34	14.15	1874.2	1690.2	7.1224	7.5386	0.6264	-0.121
11/11/19	300	5.193	29.8	95.38	4.73	90.58	4.49	55.59	2.75	55.59	2.75	15.2	1766.3	1593.1	66.392	69.906	-10.80	-14.31
11/11/19	800	11.53	67.1	1088.75	77.36	837.01	56.12	671.66	45.09	543.63	34.18	17.25	1576.6	1422.3	156.11	164.35	515.54	379.27

Table A.4.: Transfer velocities k measured in the Kyoto High-Speed Wind Wave Tank for tracers 1,4-Difluorobenzene (DFB) and Hexafluorobenzene HFB. 'n.m.' means not measured. The transfer velocity scaled to a Schmidt number of $Sc = 600$ is labeled k_{600}. Theoretically expected transfer velocities for a wavy surface for both tracers are labeled k_w. The measured bubble induced gas transfer velocity is denoted by k_b. The fan frequency, that was set as the main parameter, is denoted by f_f. The wind speed u_{10} and water sided friction velocity u_{*w}, kindly provided by the Japanese colleagues is also given.

Bibliography

D. Ambrose, M. B. Ewing, N. B. Ghiassee, and J. C. Sanchez Ochoa. The ebulliometric method of vapour pressure measurement: vapour pressures of benzene, hexafluorobenzene, and naphthalene. *.J. Chem. Thermodynamics*, 22:589–605, 1990.

W. E. Asher, L. M. Karle, B. J. Higgins, P. J. Farley, I. S. Leifer, and E. C. Monahan. The effect of bubble plume size on the parameterization of air-seawater gas transfer velocities. In B. Jähne and E. Monahan, editors, *Air-Water Gas Transfer, Selected Papers, 3rd Intern. Symp. on Air-Water Gas Transfer*, pages 351–362, Hanau, 1995. AEON.

W. E. Asher, L. M. Karle, B. J. Higgins, P. J. Farley, E. C. Monahan, and I. S. Leifer. The influence of bubble plumes on air-seawater gas transfer velocities. *Journal of Geophysical Research*, 101 (C5):12027–12041, 1996.

W. E. Asher and J. F. Pankow. The interaction of mechanically generated turbulence and interfacial films with a liquid phase controlled gas/liquid transport process. *Tellus*, 38B:305–318, 1986.

P. Atkins and J. de Paula. *Physical Chemistry*. Oxford University Press, 9 edition, 2009.

M. Aubinet, T. Vesala, and D. Papale. *Eddy Covariance: A Practical Guide to Measurement and Data Analysis*. Springer Atmospheric Sciences. Springer, 2012.

N. R. Bates, A. H. Knap, and A. F. Michaels. Contribution of hurricanes to local and global estimates of air-sea exchange of CO_2. *Nature*, 395:58–61, 1998.

M. A. Bender, T. R. Knutson, R. E. Tuleya, J. J. Sirutis, G. A. Vecchi, S. T. Garner, and I. M. Held. Modeled impact of anthropogenic warming on the frequency of intense atlantic hurricanes. *Science*, 327(5964):454–458, 2010.

M. Bopp. Messung der Schubspannungsgeschwindigkeit am Heidelberger Aeolotron mittels der Impulsbilanzmethode. Bachelor thesis, Institut für Umweltphysik, Fakultät für Physik und Astronomie, Univ. Heidelberg, 2011.

H. C. Broecker, W. Siems, and J. Petermann. The influence of wind on CO_2-exchange in an wind-wave tunnel, including effect of monolayers. *Journal of Marine Research*, 36:595–610, 1978.

R. Bösinger. Messungen zur Schmidtzahlabhängigkeit des Gasaustausches. Diplomarbeit, Institut für Umweltphysik, Fakultät für Physik und Astronomie, Univ. Heidelberg, 1986. IUP D-221.

A. H. Callaghan and M. White. Automated processing of sea surface images for the determination of whitecap coverage. *Journal of Atmospheric and Oceanic Technology*, 26:383–+, 2009.

H. D. Ceniceros. The effects of surfactants on the formation and evolution of capillary waves. 15 (1):245–256, 2003.

J. F. Clark, P. Schlosser, H. J. Simpson, M. Stute, R. Wanninkhof, and D. T. Ho. Relationship between gas transfer velocities and wind speeds in the tidal hudson river determined by the dual tracer tecnique. In B. Jähne and E. Monahan, editors, *Air-Water Gas Transfer*, pages 785–800. AEON Verlag & Studio., 1995.

M. Coantic. A model of gas transfer across air–water interfaces with capillary waves. *Journal of Geophysical Research*, 91:3925–3943, 1986.

G. T. Csanady. The role of breaking wavelets in air-sea gas transfer. *Journal of Geophysical Research*, 95(C1):749–759, 1990.

E. L. Cussler. *Diffusion - Mass Transfer in Fluid Systems*. Cambridge University Press, Cambridge, 3 edition, 2009.

P. V. Danckwerts. Significance of a liquid-film coefficients in gas absorption. *Ind. Eng. Chem.*, 43:1460–1467, 1951.

A. Dani, P. Guiraud, and A. Cockx. Local measurement of oxygen transfer around a single bubble by planar laser-induced fluorescence. *Chemical Engineering Science*, 62(24):7245 – 7252, 2007. 8th International Conference on Gas-Liquid and Gas-Liquid-Solid Reactor Engineering.

G. De Leeuw and I. Leifer. Bubbles outside the plume during the luminy wind-wave experiment. In M. A. Donelan, W. M. Drennan, E. S. Saltzman, and R. Wanninkhof, editors, *Gas Transfer at Water Surfaces*, volume 127 of *Geophysical Monograph*, pages 295–301, 2002.

E. L. Deacon. Gas transfer to and across an air-water interface. *Tellus*, 29:363–374, 1977.

K. Degreif. *Untersuchungen zum Gasaustausch - Entwicklung und Applikation eines zeitlich aufgelösten Massenbilanzverfahrens*. Dissertation, Institut für Umweltphysik, Fakultät für Physik und Astronomie, Univ. Heidelberg, 2006.

A. Dutzi. Untersuchungen zum Einfluss der Temperatur auf den Gasaustausch. Diplomarbeit, Institut für Umweltphysik, Fakultät für Physik und Astronomie, Univ. Heidelberg, 1985. IUP D-190.

A. Einstein. über die von der molekularkinetischen Theorie der Wärme geforderte Bewegung von in ruhenden Flüssigkeiten suspendierten Teilchen. *Annalen der Physik*, 322(8):549–560, 1905.

M. G. Freire, A. Razzouk, I. Mokbel, J. Jose, I. M. Marrucho, and J. A. P. Coutinho. Solubility of hexafluorobenzene in aqueous salt solutions from (280 to 340) k. *Journal of Chemical & Engineering Data*, 50(1):237–242, 2005.

N. M. Frew, J. C. Goldman, M. R. Denett, and A. S. Johnson. Impact of phytoplankton-generated surfactants on air-sea gas-exchange. *Journal of Geophysical Research*, 95(C3):3337–3352, 1990.

D. Fuß. *Kombinierte Höhen- und Neigungsmessung von winderzeugten Wasserwellen am Heidelberger Aeolotron*. Dissertation, Institut für Umweltphysik, Fakultät für Physik und Astronomie, Univ. Heidelberg, Heidelberg, Germany, 2004.

P. R. Griffiths. *Fourier Transform Infrared Spectrometry*. Wiley Interscience, 2 edition, 2007.

C. Harding. The diversity of scales for registering the force of wind. *Quarterly Journal of the Royal Meteorological Society*, 11(53):39–47, 1885.

R. Higbie. The rate of absorption of a pure gas into a still liquid during short periods of exposure. *Trans. Am. Inst. Chem. Eng.*, 31:365–389, 1935.

W. Huber. Aufbau eines gaschromatographischen Messsystems für Gasaustauschmessungen; Windkanalmessungen zur Schmidtzahl- und Wellenbildabhängigkeit des gasaustausches. Diplomarbeit, Institut für Umweltphysik, Fakultät für Physik und Astronomie, Univ. Heidelberg, 1984. IUP D-178.

J. Ilmberger. Impulsübertrag und Strömungsverhältnisse in einem runden Wind-Wasser Kanal. Diplomarbeit, Institut für Umweltphysik, Fakultät für Physik und Astronomie, Univ. Heidelberg, 1981. IUP D-167.

B. Jähne. *Zur Parametrisierung des Gasaustauschs mit Hilfe von Laborexperimenten*. Dissertation, Institut für Umweltphysik, Fakultät für Physik und Astronomie, Univ. Heidelberg, 1980. IUP D-145.

B. Jähne. *On the transfer processes at a free air-water interface*. Habilitation thesis, Institut für Umweltphysik, Fakultät für Physik und Astronomie, Univ. Heidelberg, 1985. IUP D-200.

B. Jähne. New experimental results on the parameters influencing air-sea gas exchange. In S. C. Wilhelms and J. S. Gulliver, editors, *Air-Water Mass Transfer, selected papers from the 2nd International Symposium on Gas Transfer at Water Surfaces, September 11–14, 1990, Minneapolis, Minnesota*, pages 582–592. ASCE, 1991.

B. Jähne. Air-sea gas exchange. In J. H. Steele, K. K. Turekian, and S. A. Thorpe, editors, *Encyclopedia Ocean Sciences*, pages 3434–3444. Elsevier, 2009. invited.

B. Jähne. Personal communication., 2012.

B. Jähne and E. Bock. Physically-based modelling of air-sea gas transfer. 2001.

B. Jähne and H. Haußecker. Air-water gas exchange. *Annu. Rev. Fluid Mech.*, 30:443–468, 1998.

B. Jähne, P. Libner, R. Fischer, T. Billen, and E. J. Plate. Investigating the transfer process across the free aqueous boundary layer by the controlled flux method. *Tellus*, 41B(2):177–195, 1989.

B. Jähne, K. O. Münnich, R. Bösinger, A. Dutzi, W. Huber, and P. Libner. On the parameters influencing air-water gas exchange. *J. Geophys. Res.*, 92:1937–1950, Feb. 1987.

R. F. Keeling. On the role of large bubbles in air-sea gas exchange and supersaturation in the ocean. *Journal of Marine Research*, 51:237–271, 1993.

J. Kestin, M. Sokolov, and W. A. Wakeham. Viscosity of liquid water in the range - 8°c to 150°c. *Journal of Physical and Chemical Reference Data*, 7:941–948, 1978.

S. Khatiwala, F. Primeau, and T. Hall. Reconstruction of the history of anthropogenic CO2 concentrations in the ocean. *Nature*, 462:346–349, 2009.

A. N. Kolmogorov. The local structure of turbulence in compressible turbulence for very large Reynolds numbers. *Compt.Rend.Akad.Nauk SSSR*, 30:301, 1941.

K. E. Krall. Gas exchange test campaign at the Kyoto high speed wind-wave tank 2011. Technical report, Institut für Umweltphysik, Universität Heidelberg, 2012.

C. Kräuter. Aufteilung des Transferwiderstands zwischen Luft und Wasser beim Austausch flüchtiger Substanzen mittlerer Löslichkeit zwischen Ozean und Atmosphäre. Diplomarbeit, Institut für Umweltphysik, Fakultät für Physik und Astronomie, Univ. Heidelberg, 2011.

P. K. Kundu. *Fluid Mechanics*. Academic Press, Elsevier, San Diego, CA, 4th edition, 2008.

P. Libner. *Die Konstantflußmethode: Ein neuartiges, schnelles und lokales Meßverfahren zur Untersuchung von Austauschvorgängen an der Luft-Wasser Phasengrenze*. Dissertation, Institut für Umweltphysik, Fakultät für Physik und Astronomie, Univ. Heidelberg, Heidelberg, Germany, 1987.

P. S. Liss and L. Merlivat. Air-sea gas exchange rates: Introduction and synthesis. In P. Buat-Menard, editor, *The role of air-sea exchange in geochemical cycling*, pages 113–129. Reidel, Boston, MA, 1986.

P. S. Liss and P. G. Slater. Flux of gases across the air-sea interface. *Nature*, 247:181–184, 1974.

W. McGillis. Factors affecting air-sea gas transfer. image at http://www.solas-int.org/resources/downloads.html; retrieved on 05/11/12, 2012.

W. R. McGillis, E. J. Bock, and N. M. Frew. Mass transfer from gas bubbles in fresh and seawater. In B. Jähne and E. Monahan, editors, *Air-Water Gas Transfer, Selected Papers, 3rd Intern. Symp. on Air-Water Gas Transfer*, pages 363–372, Hanau, 1995. AEON.

C. McNeil and E. D'Asaro. Parameterization of air sea gas fluxes at extreme wind speeds. *Journal of Marine Systems*, 66:110–121, June 2007.

L. Memery and L. Merlivat. Modelling of gas flux through bubbles at the air-water interface. *Tellus B*, 37B(4-5):272–285, 1985.

L. Merlivat and L. Memery. Gas exchange across an air-water interface: experimental results and modeling of bubble contribution to transfer. *Journal of Geophysical Research*, 88:707–724, Feb. 1983.

A. A. Michelson. On the application of interference-methods to spectroscopic measurements. *Phil. Mag*, Series 5, 31:191:338–346, 1891.

W. Mischler. Entwicklung eines Experiments zur Messung von Blasendichten und blaseninduziertem Gasaustausch. Diplomarbeit, Institut für Umweltphysik, Fakultät für Physik und Astronomie, Univ. Heidelberg, 2010.

E. C. Monahan and M. Lu. Acoustically relevant bubble assemblages and their dependence on meteorological parameters. *IEEE Journal of Oceanic Engineering*, 15(4):340–349, 1990.

A. S. Monin and A. M. Yaglom. *Statistical Fluid Mechanics, Volume I*. Dover Publications, 2007.

N. Mori, M. Imamura, and R. Yamamoto. An experimental study of bubble mediated gas exchange for a single bubble. In M. A. Donelan, W. M. Drennan, E. S. Saltzman, and R. Wanninkhof, editors, *Gas Transfer at Water Surfaces*, volume 127 of *Geophysical Monograph*, pages 311–313, 2002.

T. Münsterer. *LIF Investigation of the Mechanisms Controlling Air–Water Mass Transfer at a Free Interface*. Dissertation, Institut für Umweltphysik, Fakultät für Physik und Astronomie, Univ. Heidelberg, 1996.

T. Naegler. Reconciliation of excess 14C-constrained global CO2 piston velocity estimates. *Tellus B*, 61(2):372–384, 2009.

R. Nielsen. *Gasaustausch - Entwicklung und Ergebnis eines schnellen Massenbilanzverfahrens zur Messung der Austauschparameter*. Dissertation, Institut für Umweltphysik, Fakultät für Physik und Astronomie, Univ. Heidelberg, 2004.

P. D. Nightingale, G. Malin, C. S. Law, A. J. Watson, P. S. Liss, M. I. Liddicoat, J. Boutin, and R. C. Upstill-Goddard. In situ evaluation of air-sea gas exchange parameterization using novel conservation and volatile tracers. *Glob. Biogeochem. Cycles*, 14:373–387, 2000.

E. D. Palik. *Handbook of optical constants of solids II*. Academic Press, 1991.

U. Platt, D. Perner, and H. W. Pätz. Simultaneous measurement of atmospheric ch_2o, o_3 and n_2o by differential optical absorption. *J.Geophys.Res.*, 84:6329–6335, 1979.

S. B. Pope. *Turbulent Flows*. Cambridge University Press, 6 edition, 2009.

H. Reichardt. Vollständige Darstellung der turbulenten Geschwindigkeitsverteilung in glatten Leitungen. *Zeitschrift für angewandte Mathematik und Mechanik*, 31:208–219, 1951.

K. Richter. Technische Daten des Aeolotron nach dem Umbau 2007/2008. Technical report, AG Bildverarbeitung Interdisziplinäres Zentrum für Wissenschaftliches Rechnen und Institut für Umweltphysik, Universität Heidelberg, 2009.

R. Rocholz. *Spatiotemporal Measurement of Short Wind-Driven Water Waves*. Dissertation, Institut für Umweltphysik, Fakultät für Physik und Astronomie, Univ. Heidelberg, 2008.

U. Schimpf. *Untersuchung des Gasaustausches und der Mikroturbulenz an der Meeresoberfläche mittels Thermographie*. Dissertation, Institut für Umweltphysik, Fakultät für Physik und Astronomie, Univ. Heidelberg, Heidelberg, Germany, 2000.

S. D. Smith and E. G. Banke. Variation of the sea surface drag coefficient with wind speed. *Quarterly Journal of the Royal Meteorological Society*, 101:665–673, 1975.

A. Soloviev and R. Lukas. Effects of bubbles and sea spray on air-sea exchange in hurricane conditions. *Boundary-Layer Meteorology*, 136:365–376, 2010.

J. Stapf. Bestimmung der dynamischen Oberflächenspannung mit Hilfe der Blasendruckmethode. Diplomarbeit, Institut für Umweltphysik, Fakultät für Physik und Astronomie, Univ. Heidelberg, 2010.

K. Trenberth, W. Large, and J. G. Olson. The effective drag coefficient for evaluating wind stress over the oceans. *Journal of Climate*, 2:1507–1516, 1998.

Y. S. Tsai, A. J. Grass, and R. R. Simons. Experimental study of a laminar air boundary layer over a water surface. *Experiments in Fluids*, 35:472–476, 2003.

J. M. T. Vasconcelos, S. P. Orvalho, and S. S. Alves. Gas-liquid mass transfer to single bubbles: Effect of surface contamination. *AIChE Journal*, 48:1145–1154, 2002.

G. A. Vecchi and B. J. Soden. Increased tropical atlantic wind shear in model projections of global warming. *Geophyical Research Letters*, 34:L08702, 2007.

R. Wanninkhof, W. E. Asher, D. T. Ho, C. Sweeney, and W. R. McGillis. Advances in quantifying air-sea gas exchange and environmental forcing. *Annu. Rev. Mar. Sci.*, 1:213–244, 2009.

P. J. Webster, G. J. Holland, J. A. Curry, and H.-R. Chang. Changes in tropical cyclone number, duration, and intensity in a warming environment. *Science*, 309(5742):1844–1846, 2005.

F. Weißer. Verdunstungsmessungen in einem ringförmigen Wind-Wasser-Kanal mit Hilfe von Psychochrometern und einem WLD-System. Staatsexamensarbeit, Institut für Umweltphysik, Fakultät für Physik und Astronomie, Univ. Heidelberg, 1980. IUP D-159.

E. Wilhelm, R. Battino, and R. J. Wilcock. Low-pressure solubility of gases in liquid water. *Chem.Rev.*, 77:219–262, 1977.

D. Woolf. Bubbles and their role in gas exchange. In P. S. Liss and R. A. Duce, editors, *The sea surface and global change*, chapter 6. Cambridge Univ Press, 1997.

D. Woolf, I. Leifer, P. Nightingale, T. Rhee, P. Bowyer, G. Caulliez, G. de Leeuw, S. Larsen, M. Liddicoat, J. Baker, and M. Andreae. Modelling of bubble-mediated gas transfer: Fundamental principles and a laboratory test. *Journal of Marine Systems*, 66:71–91, 2007.

D. K. Woolf and E. C. Monahan. Bubbles and the air-sea transfer velocity of gases. *Atmosphere-Ocean*, 31:517–540, 1993.

J. Wu. Mean square slopes of the wind-distributed water surface, their magnitude, directionality, and composition. *Radio Science*, 25(1):37–48, 1990.

J. Wu. Bubble flux and marine aerosol spectra under various wind velocities. *J. Geophys. Res.*, 97 (C2):2327–2333, 1992.

O. Wurl, L. Miller, R. Röttgers, and S. Vagle. The distribution and fate of surface-active substances in the sea-surface microlayer and water column. *Marine Chemistry*, 115:1–9, 2009.

O. Wurl, E. Wurl, L. Miller, K. Johnson, and S. Vagle. Formation and global distribution of sea-surface microlayers. *Biogeosciences*, 8:121–135, 2011.

S.-P. Xie, C. Deser, G. A. Vecchi, J. Ma, H. Teng, and A. T. Wittenberg. Global warming pattern formation: Sea surface temperature and rainfall. *Journal of Climate*, 23:966–986, 2010.

A. M. Yaglom and B. A. Kader. Heat and mass transfer between a rough wall and turbulent fluid flow at high reynolds and peclet numbers. *J.Fluid Mech.*, 62:601–623, 1974.

C. Yaws and H.-C. Yang. Henry's law constant for compound in water. In C. L. Yaws, editor, *Thermodynamic and Physical Property Data*, pages 181–206. Gulf Publishing Company, 1992.

C. L. Yaws. *Handbook of Transport Property Data*. Gulf Publishing Company, 1995.

C. L. Yaws. *Chemical Properties Handbook: physical, thermodynamic, environmental, transport, safety, and health related properties for organic and inorganic chemicals*. McGraw-Hill, 1999.

C. L. e. Young. *IUPAC Solubility Data Series*, volume 5/6. Pergamon Press, Oxford, England, 1981.

C. J. Zappa, W. E. Asher, A. T. Jessup, J. Klinke, and S. R. Long. Microbreaking and the enhancement of air-water transfer velocity. *J. Geophys. Res.*, 109:C08S16, 2004.

C. Zülicke. Air-sea fluxes including the effect of the molecular skin layer. *Deep-Sea Research II*, 52:1220–1245, 2005.

Danksagung

Ich möchte allen danken, die direkt oder indirekt zum Gelingen dieser Arbeit beigetragen haben.
In erster Linie gilt mein aufrichtiger Dank Herrn Prof. Bernd Jähne, dem ich die Gelegenheit verdanke auf diesem interessanten und aktuellen Forschungegebiet arbeiten zu können. Ich bedanke mich für seine zahlreichen Ideen, anregenden Diskussionen sowie die Möglichkeit an einer internationalen Messkampagne teilnehmen zu können. Besonderer Dank gilt auch Herrn Prof. Werner Aeschbach-Hertig für die Übernahme des Zweitgutachtens.
Allen Beteiligten des SOPRAN-Projekts gilt mein Dank für den Blick über den Tellerrand hinaus, und die Einordnung meiner Arbeit in das große Ganze.
Prof. Jonathan Williams, Evridiki Mesarchaki und der restlichen ORSUM-Gruppe des MPI für Chemie in Mainz danke ich fuer die anregende Kooperation und die stimulierenden Diskussionen.
Dr. Roland Rocholz danke ich für das zur Verfügung stellen der Daten der mittleren quadratischen Neigung. Wolfgang Mischler danke ich für die gute Zusammenarbeit bei der Messkampagne im fernen, fremden Japan und allerlei Diskussionen darüber, was Blasen im Wasser so alles tun.
Leila Nagel und Christine Kräuter danke ich fuer das gute Teamwork, die experimentelle sowie moralische Unterstützung bei so mancher stressiger Messkampagne sowie für viele ideenreiche Gespräche über Gas- und Wärmeaustausch.
Dr. Günther Balschbach gilt mein Dank dafür, dass ich sein 'Lehrling' sein durfte; für sein Vertrauen, mich die IUP-Server co-administrieren zu lassen; für tatkräftige Hilfe beim Umbau des Aeolotron; für die Erkenntnis, dass Holz ein grossartiger Werkstoff ist; sowie dafuer, dass er immer ein offenes Ohr und guten Rat für mich hatte.
Der IUP Werkstatt, insbesondere Ralph Pfeifer gilt mein Dank fuer zuverlässige und präzise Arbeit, sowie das zur Seite stehen bei allerlei mechanischen Problemen, bis hin zur spontanen Not-OP an der streikenden Pumpe. Ich danke Karin Kruljac, Barbara Werner und Inge Clos-Lieffertz, die mir das Leben in Sachen nerviger Bürokratie sehr vereinfacht haben.
Dr. Holger Männich gilt mein Dank dafür, dass er mir gezeigt hat, wie ungeheuer spannend und interessant die Physik ist.
Dr. Alexandra Herzog danke ich dafür, dass sie die Welt ein wenig chaotischer und weniger eintönig macht, sowie für die treue Freundschaft.
Besonderer Dank gilt meiner Familie für die bedingungslose Unterstützung bei allem, was ich mir in den Kopf setze. Sowohl der 'alten Familie', meinen Eltern, als auch der 'neuen Familie', meinem Mann Heiko und meinen Schwiegereltern.

And last but not least, exceptional thanks go to Professor Satoru Komori of the Department of Mechanical Engineering at Kyoto University for the opportunity to perform experiments at the awe-inspiring high speed wind-wave tank. I cordially thank Assistant Professor Naohisa Takagaki and Koji Iwano for providing wind speed and friction velocity data, but also for their hospitality, their help with setting up my measurement devices as well as with mastering the tricky details of operating the tank. I thank all members of the Komori lab for making my stay in Japan a truly unforgettable experience.
ご支援と格別のご厚情を賜りましたことを心よりお礼を申し上げます。